

DOTTORATO DI RICERCA IN

CHIMICA

Ciclo XXVI

Settore Concorsuale di afferenza: 03/C2

Settore Scientifico disciplinare: CHIM/04

**CATALYSTS AND PROCESSES
FOR NEXT-GENERATION H₂ PRODUCTION**

Presentata da: **Rodolfo Mafessanti**

Coordinatore Dottorato

Chiar.mo Prof. Aldo Roda

Relatore

Dr. Francesco Basile

Correlatore

Chiar.mo Prof. Angelo Vaccari

DOTTORATO DI RICERCA IN CHIMICA

XXVI Ciclo - 2011-2013

Rodolfo Mafessanti

Tutor Prof. Francesco Basile

Curriculum CHIMICA INDUSTRIALE

Catalysts and processes for next generation H₂ production

Il Dott. Rodolfo Mafessanti, laureato in Chimica Industriale presso la Facoltà di Chimica Industriale dell'ALMA MATER STUDIORUM - Università di Bologna, con tesi dal titolo "Sviluppo di nuovi catalizzatori per la produzione di H₂ attraverso la reazione di water-gas-shift", ha svolto la propria attività di tesi di Dottorato presso il Dipartimento di Chimica Industriale "Toso Montanari".

L'attività svolta dal Dott. Rodolfo Mafessanti è connesso al progetto europeo "Next GTL" (7FP – NMP) e concerne lo sviluppo di un sistema catalitico e la produzione distribuita di gas di sintesi per la trasformazione in distillati medi e idrogeno che per purezza risulta particolarmente indicato per l'alimentazione di celle a combustibile.

Lo studio si è concentrato su un processo di reforming con vapore e ossigeno che consente all'unità industriale di lavorare in condizioni autotermiche a 750°C e su un processo di reforming a bassa temperatura. In entrambi i casi il processo si svolge in più stadi inframezzato da separazione di idrogeno a membrana. Lo sviluppo dei catalizzatori ha riguardato sistemi M-Ce_{1-x}Zr_xO₂ (M = Rh, Ni o Ru) preparati per microemulsione che hanno mostrato caratteristiche chimiche e morfologiche di enorme interesse per aumentare l'attività e ridurre la disattivazione da carbone. Il metodo e le competenze sviluppate nella sintesi di materiali per microemulsione hanno ampie potenzialità e un vasto campo di applicazioni, ben più estese del processo esame del progetto.

Durante il triennio di dottorato il Dott. Mafessanti ha acquisito competenze nella gestione di impianti da laboratorio per reazioni catalitiche in fase gas e nell'analisi gascromatografica e nell'utilizzo di alcune tecniche di caratterizzazione dei materiali quali: DLS (dynamic light scattering), analisi in diffrazione dei raggi X (XRD), riduzione/ossidazione in programmata di temperatura (TPR/O), porosimetria e spettroscopia Raman, microscopia elettronica a scansione e in trasmissione (SEM e TEM) accoppiata a EDX.

Al momento il candidato ha al suo attivo numerose comunicazioni orali e posters a Congressi, complessivamente sei, per la quasi totalità presentati personalmente. Alcuni manoscritti sono in fase di avanzata preparazione e saranno presto inviati a riviste internazionali. Il dottorando ha mostrato di essere in grado di illustrare efficacemente il suo lavoro a partner industriali e accademici mediante presentazioni.

Nel corso del dottorato il Dott. Rodolfo Mafessanti ha mostrato autonomia e rigore nella conduzione delle prove sperimentali associata ad una elevata capacità di approfondimento che, insieme a buone conoscenze di base, gli hanno permesso di sviluppare la sintesi in microemulsione di materiali catalitici innovativi. Il Dott. Mafessanti ha inoltre dimostrato ottime capacità di elaborazione che gli hanno permesso di collegare efficacemente le proprietà dei materiali alla reattività catalitica.

ABSTRACT

The present study is focused on the development of new VIII group metal on $\text{CeO}_2 - \text{ZrO}_2$ (CZO) catalyst to be used in reforming reaction for syngas production. The catalyst are tested in the oxyreforming process, extensively studied by Barbera [44] in a new multistep process configuration, with intermediate H_2 membrane separation, that can be carried out at lower temperature (750°C) with respect the reforming processes ($900 - 1000^\circ\text{C}$). In spite of the milder temperatures, the oxy-reforming conditions ($\text{S/C} = 0.7$; $\text{O}_2/\text{C} = 0.21$) remain critical regarding the deactivation problems mainly deriving from thermal sintering and carbon formation phenomena. The combination of the high thermal stability characterizing the ZrO_2 , with the CeO_2 redox properties, allows the formation of stable mixed oxide system with high oxygen mobility. This feature can be exploited in order to contrast the carbon deposition on the active metal surface through the oxidation of the carbon by means of the mobile oxygen atoms available at the surface of the CZO support. $\text{Ce}_{0.5}\text{Zr}_{0.5}\text{O}_2$ is the phase claimed to have the highest oxygen mobility but its formation is difficult through classical synthesis (co-precipitation), hence a water-in-oil microemulsion method is, widely studied and characterized. Two methods (IWI and bulk) for the insertion of the active metal (Rh, Ru, Ni) are followed and their effects, mainly related to the metal stability and dispersion on the support, are discussed, correlating the characterization with the catalytic activity. Different parameters (calcination and reduction temperatures) are tuned to obtain the best catalytic system both in terms of activity and stability. Interesting results are obtained with impregnated and bulk catalysts, the latter representing a new class of catalysts. The best catalysts are also tested in a low temperature ($350 - 500^\circ\text{C}$) steam reforming process and preliminary tests with H_2 membrane separation have been also carried out.

SUMMARY

Summary	1
1 Introduction	1
1.1 Synthesis gas (Syngas)	1
1.1.1 Syngas uses: a brief overview	1
1.1.2 Options for Syngas and H ₂ production	2
1.1.3 Syngas from renewable resources	4
1.1.3.1 Pyrolysis	5
1.1.3.2 Gasification	6
1.1.4 Natural gas (NG): reserves and utilization	8
1.1.4.1 Unconventional Gas	8
1.1.5 Production from Natural Gas	13
1.1.6 Membranes and Membrane Reactors (MRs)	18
1.2 Processes for H₂/Syngas production	22
1.2.1 Steam Reforming	22
1.2.1.1 Thermodynamics of Steam Reforming reaction	22
1.2.1.2 Kinetics and reaction mechanism	27
1.2.2 Catalysts for Steam Reforming	32
1.2.2.1 CeO ₂ – ZrO ₂ mixed oxide as catalytic support	37
1.2.2.2 Carbon formation on reforming catalysts	44
1.2.2.3 Sintering of Steam Reforming catalysts	49
1.2.3 Practical aspects of Steam Reformer unit plant	53
1.3 Catalytic Partial Oxidation (CPO) Process	57
1.4 Autothermal Reforming (ATR)	61
1.5 Aim of the work	62
2 Experimental Session	65
2.1 Synthesis methods followed for catalysts preparation	65
2.1.1 Water – in – oil Microemulsion	65
2.1.2 Co – precipitation method	67
2.1.3 Calcination procedure	67
2.1.4 Insertion of the active metal	68
2.1.4.1 Incipient Wetness Impregnation (IWI)	68

2.1.5	Shaping of the catalysts	69
2.2	Membranes preparation	71
2.2.1	Activation step	72
2.2.2	Electroless Plating Deposition (EPD)	73
2.3	Laboratory plant description	75
2.4	Description of the experiments	78
2.5	Dynamic Light Scattering (DLS) analysis	79
2.6	X – Ray Diffraction (XRD) analysis	81
2.7	Surface area and porosimetry analysis	82
2.8	Temperature Programmed Reduction (TPR) and Oxidation (TPO) analysis	83
2.9	Transmission Electron Microscopy (TEM)	84
2.10	Raman Spectroscopy	85
3	Results and discussion	87
3.1	Introduction by previous studies	87
3.2	W/O Microemulsion synthesis	89
3.2.1	Effect of pH	91
3.2.2	Effect of TMAH molar concentration	93
3.2.3	Effect of R_w ratio	94
3.2.4	Effect of the nature of the precipitating agent	96
3.2.5	Effect of the amount of the organic compounds	98
3.3	Characterization of the calcined CZO samples	104
3.3.1	W/O Microemulsion vs Co-precipitation	105
3.3.1.1	XRD Characterization	105
3.3.1.2	Raman Spectroscopy	108
3.3.1.3	TPR/O/R Characterization	110
3.3.1.4	TEM Characterization	111
3.3.1.5	Surface Area and Porosimetry Characterization	113
3.3.2	Effect of the Precipitating agent: TMAH vs NH_3	115
3.3.3	Effect of the Ce/Zr ratio	118
3.3.4	Insertion of the active metal	122
3.3.4.1	Impregnation vs Bulk	122
3.4	Catalytic activity of the samples prepared	140

3.4.1	Comparison with a commercial CZO-based catalyst -----	145
3.4.2	Effect of the support' Ce/Zr ratio-----	147
3.4.3	Effect of the synthesis method: w/o microemulsion vs co-precipitation-----	151
3.4.4	Effect of the nature of the active metal -----	158
3.4.5	Effect of the metal insertion method -----	163
3.4.6	Effect of the calcination temperature-----	167
3.4.6.1	Bulk samples -----	167
3.4.6.2	Impregnated (IWI) samples -----	179
3.4.7	Effect of the reduction temperature -----	186
3.4.8	Preliminary tests with membrane reactor (MBr) -----	189
4	Conclusions-----	197
5	References-----	201

1 INTRODUCTION

1.1 Synthesis gas (Syngas)

Synthesis gas (syngas), a mixture of hydrogen and carbon monoxide, can be manufactured from natural gas, coal, petroleum, biomass and even from organic wastes, potential sources of syngas are ubiquitous in nature. The availability and flexibility of the resource base are keys to the present and future uses of syngas and of its separate components, hydrogen and carbon monoxide. Syngas is a present and increasing source of environmentally clean fuels and chemicals and is also a potentially major fuel for the production of essentially pollution-free electricity, as sulfur and nitrogen in parts per million can be removed from syngas relatively easily [1].

1.1.1 Syngas uses: a brief overview

Syngas is an important building block in the energy production market because of the multitude of processes. Syngas is involved as reagent to be transformed directly into energy or into fundamental intermediate chemicals for energy and fuels production (Fig. 1.1).

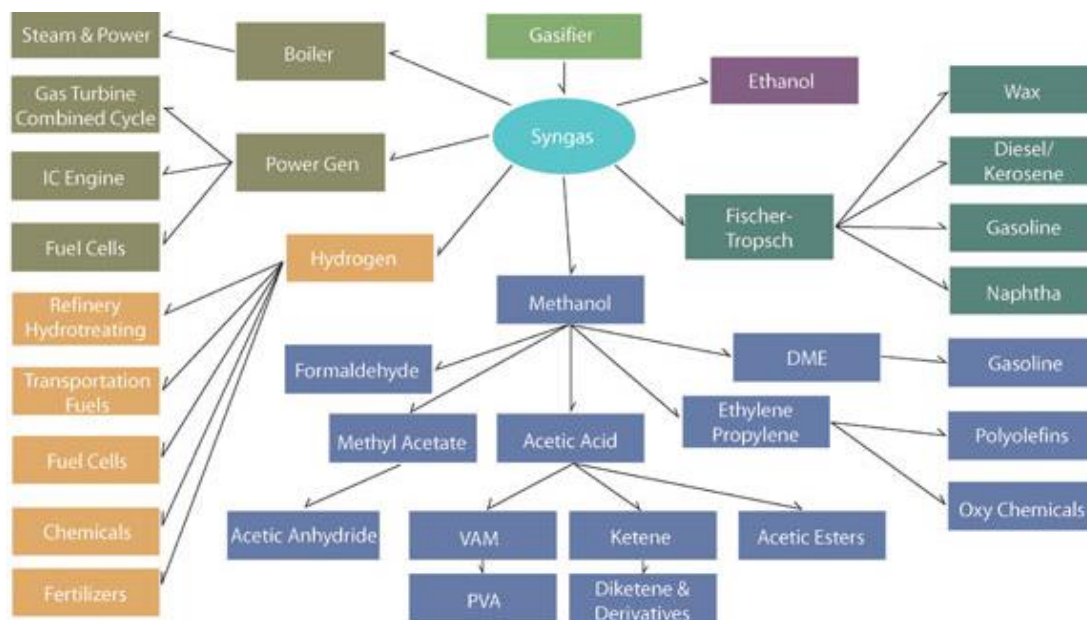


Fig. 1.1. Multitude of products that can be produced from syngas

Syngas is principally utilized for the production of H_2 , the reactant, together with N_2 , of the ammonia synthesis process, and for the synthesis of fuels through Fisher – Tropsch process.

A different set of options opens up if syngas is converted into methanol [2]. Methanol synthesis takes place over a copper zinc oxide catalyst in the temperature range 220 – 300°C at a pressure of 50 – 100 bar. The ideal molar ratio of H₂:CO:CO₂ is 11:4:1. Starting with methanol, there are Methanol To Olefines (MTO) technologies which lead to a whole series of monomers and downstream polymers (polyethylene, polypropylene, ethylene oxide, glycols, surfactants, etc.). There are also processes for converting syngas into higher alcohols, with synthesis taking place at higher temperatures (up to 425°C) and higher pressures (up to 300 bar).

Alternatively, syngas can be converted into SNG (Substitute Natural Gas, or Synthetic Natural Gas) via a methanation process [3], which opens up a whole new set of options using the natural gas grid as a chemical fuel for transportation vehicle. In the power generation sector, syngas production from coal gasification is also becoming more common. On Integrated Gasification Combined Cycle (IGCC) plants, the idea is that coal is gasified to produce a syngas which can serve as a fuel for a highly efficient gas turbine in a combined gas/steam cycle [4,5].

Syngas can also be used as a combustion fuel in a boiler for medium/high pressure steam production or in a simple gas turbine for power generation. It has already been noted that the term “syngas” is used in many different ways. At one end of the spectrum, a low purified gas can be used as a low-grade fuel. At the other end of the spectrum, a highly processed, decarbonized syngas (which is 90% hydrogen) can be used to reduce CO₂ emissions. In that case it should be noted that the decarbonized syngas has a lower energy density than natural gas and so a higher gas throughput is required. Gas turbines adapted to run in this mode have been found to produce power outputs that are 20 – 25% higher than normal due to the higher flow rate of hot combustion gases expanding through the turbine [6].

1.1.2 Options for Syngas and H₂ production

Various sources and processes for syngas production yield different ratios of H₂ to CO and the availability of source material for syngas manufacture varies at different places in the world. Matching the specific method of production of syngas with the use in a particular synthesis is an important factor in determining the technical and economic value of the various processes [7].

Both non-renewable and renewable energy sources are important for hydrogen and syngas production. As an energy carrier, H₂ (and syngas) can be produced from catalytic processing of various hydrocarbon fuels, alcohol fuels, and bio-fuels such as

oxygenates. H₂ can also be produced directly from water by electrolysis, thermochemical cycles, or photocatalytic splitting, although this process is in the early stage of laboratory research [8].

Table 1.1 show how hydrogen (and syngas in most cases) can be produced from coal (gasification, carbonization), natural gas, and light hydrocarbons such as propane gas (steam reforming, partial oxidation, autothermal reforming, plasma reforming), petroleum fractions (dehydrocyclization and aromatization, oxidative steam reforming, pyrolytic decomposition), biomass (gasification, steam reforming, biologic conversion), and water (electrolysis, photocatalytic conversion, chemical and catalytic conversion). The relative competitiveness of different options depends on the economics of the given processes, which in turn depend on many factors such as the efficiency of the catalyst, the scale of production, H₂ purity, and costs of the feed and the processing steps, as well as the supply of energy sources available [3].

H ₂ source	Energy source	Reaction Processes
1. Fossil hydrocarbons Natural Gas Petroleum Coal Tar sands, shale oil Natural gas hydrate	1. Primary Fossil energy Biomass Organic waste Nuclear energy Solar energy	1. Commercialized process Steam reforming Autothermal reforming Partial oxidation Catalytic dehydrogenation Gasification Carbonization Electrolysis
2. Biomass	Photovoltaic	2. Emerging approaches Membrane reactors
3. Water	Hydropower	
4. Organic/animal waste	Wind, wave, geothermal	Plasma reforming
5. Synthetic fuels MeOH, FTS liquid, etc.	2. Secondary	
6. Specialty areas Organic compound Metal hydride, chemical complex hydride Ammonia, hydrazine Hydrogen sulfide	Electricity H ₂ , MeOH, etc. 3. Special cases Metal bonding energy Chemical bonding energy	

Table 1.1 Options of H₂ (and Syngas) production processing regarding atomic H₂ source, Energy source for molecular H₂ production, and Chemical reaction processes [Adapted from Ref. [8]]

Current commercial processes for syngas and H₂ production largely depends on fossil fuels both as source of hydrogen and as the source of energy for the production

processing. Fossil fuels are non-renewable energy resources, but they provide a more economical path to hydrogen production in the near term (next 5 – 20 years) and perhaps they will continue to play an important role in the midterm (20 – 50 years). Alternative processes need to be developed that do not depend on fossil hydrocarbon resources for either the hydrogen source and energy source, such as alternative processes need to be economical, environmentally friendly, and competitive. H₂ separation is also a major issue as H₂ coexists with other gaseous products from most industrial processes, such as CO₂ from chemical reforming or gasification processes. Pressure swing adsorption (PSA) is used in current industrial practice. Several types of membranes are being developed that would enable more efficient gas separation. Overall, in order for hydrogen energy to penetrate widely into transportation and stationary applications, the costs of H₂ production and separation need to be reduced significantly from the current technology, for example, by a factor of 2 [3].

1.1.3 Syngas from renewable resources

Biomass is the most likely renewable organic substitute to petroleum. Biomass is a renewable material containing appreciable quantities of hydrogen, oxygen and carbon. It is available from a wide range of sources such as animal wastes, municipal solid wastes, crop residues, short rotation woody crops, agricultural wastes, sawdust, aquatic plants, short rotation herbaceous species (i.e. switch grass), waste paper, corn, and many more. For hydrogen and syngas productions, the current biomass technologies include: pyrolysis, gasification, reforming [9]. Currently, there is a wide variety of biomass resources available to be converted into energy. Ni et al. [10] classified this biomass into four general categories:

1. **Energy crops:** herbaceous energy crops, woody energy crops, industrial crops, agricultural crops and aquatic crops;
2. **Agricultural residues and waste:** crop waste and animal waste;
3. **Forestry waste and residues:** mill wood waste, logging residues, trees and shrub residues;
4. **Industrial and municipal wastes:** municipal solid waste (MSW), sewage sludge and industry waste.

As already mentioned above, the two principal processes involved in the transformation of biomass into H₂ and syngas are pyrolysis and gasification.

1.1.3.1 Pyrolysis

According to Arni et al. [11], pyrolysis is a thermal process in which biomass is converted into gas, liquid, and solid in the absence of air. The solid called char is rich in carbon and contains the ash, and has several applications such as fuel and sorbent. The condensable fraction (liquid) consists of a very complex mixture of oxygenated hydrocarbons and water, or can be used as a substitute for fuel oil in many static applications such as in boilers, or as important source of intermediate chemicals. The gas is non-condensable fraction of the pyrolysis process, consisting mainly of H₂, CO, CO₂, CH₄ and other lowmolecular weight hydrocarbons, and is used as fuel gas. Parameters such as: temperature, heating rate, residence time and type of catalyst used are important in the pyrolysis process. In order to increase gaseous products especially hydrogen production, high temperature, high heating rate and long volatile phase residence time are required. Temperature is an important variable in thermal decomposition processes of biomass, significantly influencing the product distribution [10].

Pyrolysis can be further classified into slow pyrolysis and fast pyrolysis [10]. Slowpyrolysis is normally not considered for hydrogen production. Fast pyrolysis is a high temperature process, in which the biomass feedstock is heated rapidly in the absence of air, to form vapor and subsequently condensed to a dark brown mobile bio-liquid. The products of fast pyrolysis can be found in all gas, liquid and solid phases. In particular, the gaseous product is of considerable interest due to its potential as a source of hydrogen fuel. Moreover, this process has advantages as negligible production of toxic oxidized species (e.g. dioxins), less energy consumption and the production of a disposable solid waste (char). Ni et al. [10] reported hydrogen production cost of biomass pyrolysis versus the costs of hydrogen production by electrolysis. The estimated cost for the hydrogen production from biomass pyrolysis is in the range between 8.86 US\$/GJ and 15.52 US\$/GJ depending on the facility size and biomass type. For comparison, the costs by wind-electrolysis systems and PV-electrolysis systems are 20.2 US\$/GJ and 41.8 US\$/GJ, respectively. It can be seen, at least for the economical point of view, that biomass pyrolysis is a competitive method for renewable hydrogen production.

The use of catalysts in the thermo-chemical processing of biomass can be an interesting approach for increasing the gas yield by decreasing the amount of liquid. Catalytic pyrolysis occurs at relatively low temperatures (≤ 750 °C) and the catalyst is incorporated in the same reactor where the pyrolysis of biomass is performed. Garcia et

al. [12] reported that nickel is the metal most frequently used in catalysts for biomass processing. The catalyst must have appropriate physical and chemical properties, including mechanical strength, because of its use in a fluidized bed. The thermal stability of the active phase is also very important. Ni/Al co-precipitated catalysts combine these characteristics. The calcinations and reduction conditions of the catalyst impact on the gas yield of the catalytic pyrolysis of biomass. The catalytic pyrolysis is important to reduce the tar formed during pyrolysis process. The use of dolomite or nickel oxide as catalysts in biomass pyrolysis had been attracted much attention, because it was inexpensive and abundant and it could significantly reduce the tar content of the product gas [13].

1.1.3.2 Gasification

Gasification is a thermochemical process that differently from pyrolysis, occurs in the presence of oxygen air and/or steam. Usually the biomass gasification occurs at 700 – 900°C and the products are mainly gaseous.

Hydrogen and syngas production from biomass through thermo-chemical conversion, gasification in particular, have been widely studied. According to Chang et al. [14], the temperature is the most influential factor for gasification, and increasing the temperature, resulted in increase in gas yield and more hydrogen production. Particle size is another factor that affects the gasification process, therefore carbon conversion efficiency and hydrogen yield increase with decreasing particle size. The optimization of gasification temperature is around 830°C and the oxygen content expressed as equivalent ratio with respect to the stoichiometry of combustion around 0.3. Xie et al. [15] studied syngas production by two-stage method of biomass catalytic pyrolysis and gasification. The results illustrated that higher temperature was needed in the gasification process (850°C) than in the pyrolysis process (750°C) to maximize syngas yield, and the maximum syngas yield could achieve up to 3.29 N m³/kg biomass (drywt.), much higher than previous studies. Gao et al. [16] investigated hydrogen production from biomass gasification with porous ceramic reforming. The results indicated that the hydrogen yield increased from 33.17 to 44.26 (g H₂)/(kg biomass) with the reactor temperature increase. The H₂ concentration of production gas in oxygen gasification (oxygen as gasifying agent) was much higher than that in air gasification (air as gasifying agent). The hydrogen yields in air and oxygen gasification varied in the range of 25.05 – 29.58 and 25.68 – 51.29 (g_{H₂})/(kg_{biomass}), respectively. Nipattummakul et al. [17] reported a study on syngas production from steam gasification of oil palm trunk waste and it was observed that the high initial syngas flow rate is mainly attributed to the

pyrolysis of volatile matter from the oil palm sample. Almost 50 % of the syngas is produced during the first 5 min. The results showed that there is over 60 % increase in hydrogen production with steam gasification as compared to that with pyrolysis. The increase in steam flow rate reduced the time duration of gasification, and promoted steam reforming reactions to result in increased hydrogen yield. Increase in steam flow rate provided negligible effect on the apparent thermal efficiency. Lv et al. [18] studied catalytic gasification of pine sawdust and the maximum gas yield reached 2.41 N m³/kg biomass at 850 °C.

Table 1.2 summarizes some of the most important processes of pyrolysis and gasification of biomass to produce H₂ and syngas.

Process	Biomass	Reactor	Catalyst	Products	Reference
Gasification	Glycerol with lignocellulosic	Fixed bed	-	Syngas	[19]
Gasification and Pyrolysis	Pine sawdust	Tubular	Ni	Syngas	[15]
Gasification	Sawdust	Fluidized bed tubular	Fe/CaO	-	[20]
Gasification and Pyrolysis	Rubber	Tubular	-	H ₂ and syngas	[21]
Gasification	Lignocellulosic materials	Tubular	-	H ₂	[14]
Gasification	Wood	-	-	Syngas	[22]
Gasification	Glycerol	Fluidized bed	-	Syngas	[23]
Gasification and Pyrolysis	Food waste	Tubular	-	Syngas	[21]
Gasification	Refuse fuels	Fixed bed	-	Syngas	[24]
Gasification and Pyrolysis	Pine sawdust	Fluidized bed	Dalomite and Ni	Syngas	[18]

Table 1.2. Summary of the gasification and pyrolysis processes for biomass conversion into H₂ and syngas [Adapted from Ref. [9]]

1.1.4 Natural gas (NG): reserves and utilization

Despite of the utilization of renewable resources, and the growing of more efficient processes to convert biomass into synthesis gas, nowadays it is still produced for the major part from non – renewable sources and mainly from natural gas.

From around 2001 the proven world gas reserves have overcome those of oil to reach nearly 1'200 Billion BOE (Barrel of oil equivalent), i.e. over 196 TSCM (thousand billion standard cubic meters).

The total amount of "Stranded Gas Reserves", i.e. the part which is not readily usable, has been estimated to be about 70 TSCM, about 40% of the gas proven reserves. Such an amount could, if converted to synthetic fuels, generate around 250 billion barrels of synthetic oil, a quantity equal to one third of Middle East's proven oil reserves. The possible options for remote gas monetization, when transport in pipelines is not possible, are the following:

1. LNG (Liquefied Natural Gas), i.e. cooling to about 160°C for transport followed by re-gasification and introduction in the local network;
2. GTL (Gas to Liquid), i.e. conversion of NG to liquid transportation fuels. The economics of GTL versus LNG depends on the oil to gas price relationship which depends on various aspects.

Natural gas is widely used so far as a primary energy source principally because its reserves are still very large and, especially from 2007, they even increase thanks to discovery of new technologies able to exploit parts of the enormous reserves of the so called "unconventional gas".

1.1.4.1 Unconventional Gas

Around 45% of the world's recoverable natural-gas reserves are "unconventional" The International Energy Agency [25] reckons global gas demand will increase by more than half between 2010 and 2035, and unconventional gas will make up 32% of the total supply, up from 14% today. While Russia and the Middle East hold the largest reserves of conventional gas, available sources of unconventional gas are spread across the world, and can be found in countries that are currently net importers, such as China and America (Fig. 1.2).

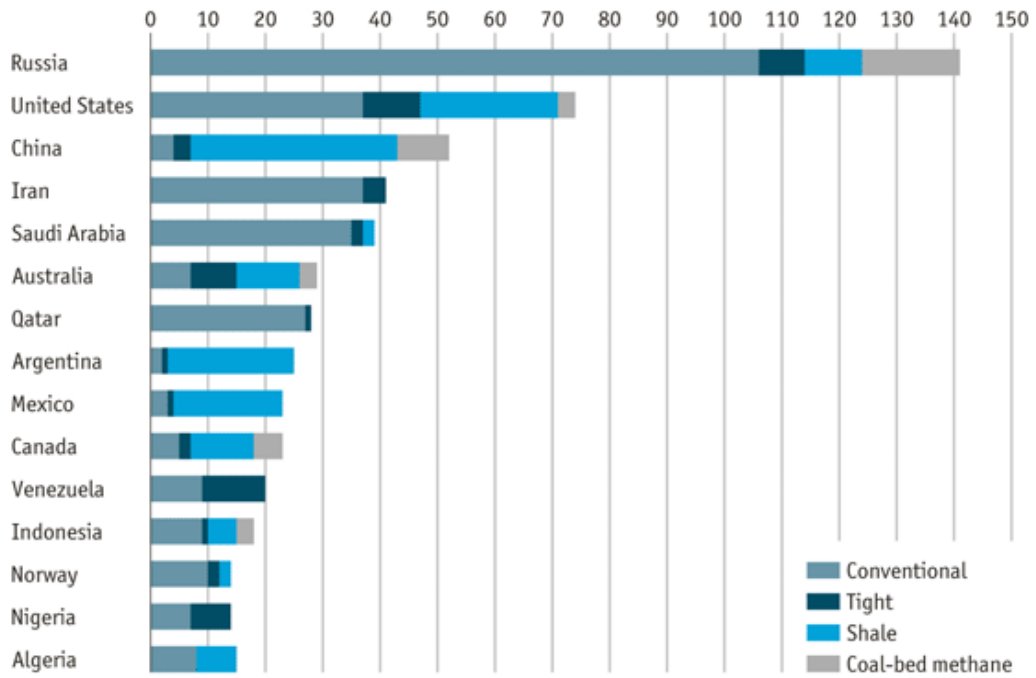


Fig. 1.2. Global conventional and unconventional Natural Gas reserves [25] (Values reported in trillion of cubic meters)

Since 2007 two significant events have changed the market developments. The first was the global economic crisis associated with the near-collapse of the financial system that led to a temporary fall in gas demand. The second was the sudden and unexpected development of unconventional gas supplies in the United States, the so-called shale gas revolution. Unconventional gas can be defined as resources that, after the initial well has been drilled, require further processing before it can flow, whereas conventional gas can be collected by simply drilling the well. Today these two factors have turned the relatively tight gas markets of 2006–2007 into a buyers' market. At the same time, many analysts have formed the view that unconventional gas is a major 'game changer' which will have significant implications for the global supply and demand balances, and for how gas markets work together with the underlying geopolitics [26, 27, 28, 29, 30, 31].

There are a number of different sources for unconventional gas [32]:

- **Gas hydrates:** These are gas deposits trapped in ice crystals in permafrost and on the ocean floor. The gas resource contained in hydrates is estimated to be larger than all other sources of natural gas combined, but most such gas is not commercially producible with today's technologies [33].
- **Coal-bed methane (CBM):** Also known as coal seam gas, this is simply natural gas contained in coal beds. Normally the coal beds are regarded as commercially sub-optimal. The International Energy Agency (IEA, [33]) estimated

CBM to be the source of 10% of total gas production in the United States in 2008, 4% in Canada and 8% in Australia. China and India, with their huge coal reserves, also have great interest in developing their CBM capability. In China, CBM has been made one of the 16 priority projects in the 11th Five-Year Plan.

- **Shallow biogenic gas:** This is gas found in coal seams generated by biogenic processes rather than the thermal maturation that produces CBM. At present it is mainly found in Western Canada.
- **Tight gas:** This refers to gas deposits found in low permeability rock formations that require fracturing to release them for production. The IEA suggests a definition that is based upon a gas reservoir that cannot be developed commercially by vertical drilling because of the lack of natural flow [33]. Also, even with horizontal drilling, hydraulic fracturing is required to produce commercial quantities.
- **Shale gas:** These are deposits trapped within shale rocks. Unusually, these rocks are both the source of the gas and the means of storing it. They also tend to overlie conventional oil and gas reservoirs. Thus if there has been extensive exploration for conventional oil and gas the existing well-cores can generate large amounts of data to locate the potential shale plays.

It is the last two categories, shale and tight gas, that are currently generating the most media interest. Such deposits have characteristics that are important for their profitability and future prospects. Compared with conventional gas reserves¹ shale and tight gas are spread over much wider areas. For example, shale gas deposits in place are around 0.2 to 3.2 billion cubic meters (bcm) per km² of territory, compared with 2–5 bcm per km² for conventional gas [33].

Table 1.3 summarize the world reserves of the main types of unconventional gas.

Country	Tight gas	Coalbed Methane	Shale gas	Total
Middle East and North Africa	23	0	72	95
Sub – Saharan Africa	22	1	8	31
Former Soviet Union	25	112	18	155
Asia – Pacific	51	49	174	274
Central Asia and China	10	34	100	144
OECD Pacific	20	13	65	99
South Asia	6	1	0	7

¹Conventional gas reserves are either those of associated gas produced as a by-product of crude oil production, or those of non-associated fields. These produce methane which is dry natural gas, although often methane is produced as part of wet gas. This includes various liquids such as condensates/ natural gas liquids which must be stripped out before the gas can be used as gas.

Other Asia – Pacific	16	0	9	24
North America	39	85	109	233
Latin America	37	1	60	98
Europe	12	8	16	35
Central and Eastern Europe	2	3	1	7
Western Europe	10	4	14	29
WORLD	210	256	456	921

**Table 1.3. Global unconventional natural gas resources in place (trillion cubic meters—Tcm)
[Adapted from Ref. [34] – Source [33]]**

The ease of accessibility will vary from well to well. Extracting shale gas and tight gas involves hydraulic fracturing of the rocks with water and chemicals, a technique known as "fracking". This is more expensive than the methods used to produce conventional gas. Costs differ between countries, too. China's shale-gas and coal-bed methane industries are subsidized to the tune of 3 cents per cubic meter. Elsewhere there is less government support. France and Bulgaria have banned fracking for environmental reasons [35].

The shale gas has already had a serious impact on LNG capacity utilization. As a result of gas market conditions around 2007, a surge in LNG export and import capacity was expected. PFC Energy has estimated that export capacity would increase from 200 Mt/y in 2008 to 285 Mt/y in 2012 and to 300 Mt/y on 2013 [36]. The IEA [33] described this as an "unprecedented period of expansion" in LNG export capacity, with the largest ever plants due to be commissioned and 147 bcm under construction in 11 countries – all due on-stream in 2013. Even more capacity was expected in the longer term. The forecast for 2020 reported by Jensen [37] suggests a 'high case' LNG capacity of 450 Mt/y and a 'low case' of 300 Mt/y. Much of this increase in capacity was expected to supply the US market. Thus in Jensen's 'low case', it was assumed that North America would account for 30% of the growth in LNG demand. This is now all looking extremely optimistic, depending upon the view taken of whether the shale gas revolution can continue in the United States. In fact recently, in the United States there was a decline in LNG imports. While this is in part due to the lower gas demand in the United States as a result of the recession, part is due to the rise in shale gas production.

The result has been a significant under-utilization of US re-gasification capacity [32]. Over the last ten years, this capacity has increased more than tenfold to reach over 100 Mt/y in expectations of domestic gas shortages; however, the increase in shale gas production by over 5.5 bcf/d is equivalent to some 41.25 Tt/y of LNG [38]. The IEA estimated that in 2008, six re-gasification plants were under construction, accounting for

69 bcm per year, and a further 19 plants with a total capacity of 280 bcm per year had received approval [33]. In 2009, the average utilization of the existing re-gasification capacity was only 9.3% [38]. The result is that a great many private investors in LNG in the United States have suffered considerable losses.

This development of over-capacity is a global phenomenon [28]. There was a general reduction in global gas demand by 70.4 bcm[39] as the result of the recession, leading to a significant over-supply of LNG capacity and supply, together with a reduction in the throughput of pipelines.

The current LNG surplus has caused gas prices generally to fall dramatically, as shown in Fig. 1.3. In Japan and the EU, the fall in gas prices was 28% and 26% respectively, while the fall in oil import costs (based upon an energy content comparison) was 38%. By contrast, the fall in the United Kingdom was 55%, in the United States 56% and in Canada 58%.

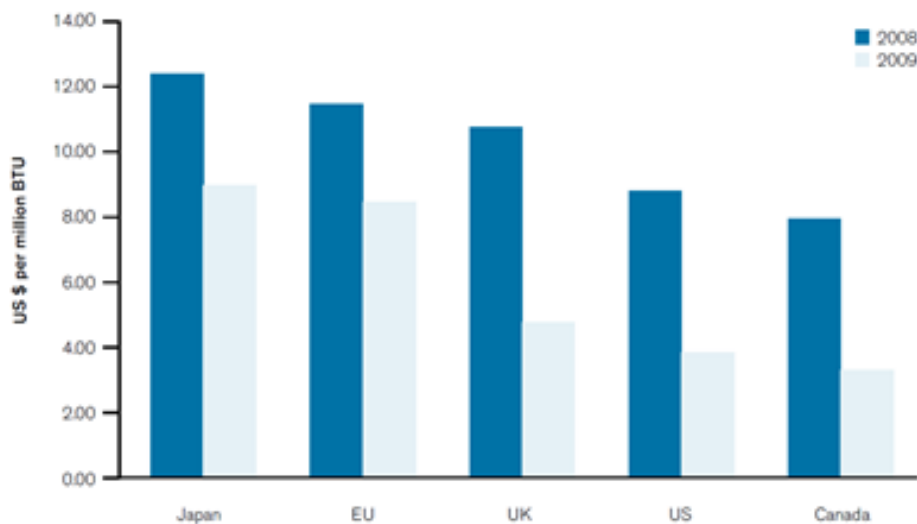


Fig. 1.3. Prices of domestic natural gas [32]

These considerations, can help to explain and illustrate the global scenario of natural gas reserves and availability in the world. The unconventional natural gas play a fundamental role on the utilization of this resources both from an economic point of view and regarding the quantity of natural that is possible to utilize. The latter point is of enormous importance regarding the fact that the discovery of new technologies and the improvement of the existing ones, lead to an increase of the exploitation capacity of all types of the natural gas reserves, with big changes on the global market of this energy resource. Therefore, is not difficult to understand why a non-renewable resources such as natural gas, is one of the most utilize so far, generally for the production of chemicals and energy.

1.1.5 Production from Natural Gas

Currently the only industrial feasible option for GTL passes through the first step of conversion of NG to syngas (CO/H₂ mixtures) followed by conversion of syngas to either hydrocarbons via Fischer – Tropsch (FT) synthesis or oxygenated products (CH₃OH/DME, or higher alcohols) via well-established technologies. The Fischer – Tropsch process is a catalyzed chemical reaction in which CO and hydrogen are converted into liquid hydrocarbons [40]. Traditionally the process has been used to synthesize long chain alkanes as a substitute for petroleum diesel [41]. The usual catalysts are based on iron and cobalt, and are vulnerable to poisoning by sulphur, chlorides and carbonyl groups. The Fischer – Tropsch process is described by the equation (1):



The reaction takes place in the temperature range 200 – 350°C at a pressure of 20 – 40 bar. As n increases, the ideal molar ratio of hydrogen to CO tends to 2:1. Some authors would reserve the term “syngas” for an ideal 2:1 mixture of hydrogen and CO. The Fischer – Tropsch process is optimized for the desired products distribution (e.g. diesel for road and rail transport, kerosene for air transport, naphtha for petrochemicals production) and is followed by cracking and separation stages as necessary. It can also be used to produce light alkenes for petrol blending [42]. A scheme of a Fischer – Tropsch process is reported in Fig. 1.4. In this process, it plays a fundamental role in terms of cost of investments, the air pre – treatment unit (unit denominated Oxygen plant in Fig. 1.4 **Errore. L'origine riferimento non è stata trovata.**), in fact the air fractioning and the syngas production units have the higher investment cost (36-48%) (Fig. 1.5) [43]. To reduce this cost, very large plants are necessary for FT production, but this is limited, because:

1. large investments and risks are necessary;
2. there are only few gas fields for which these large investments could be justified.

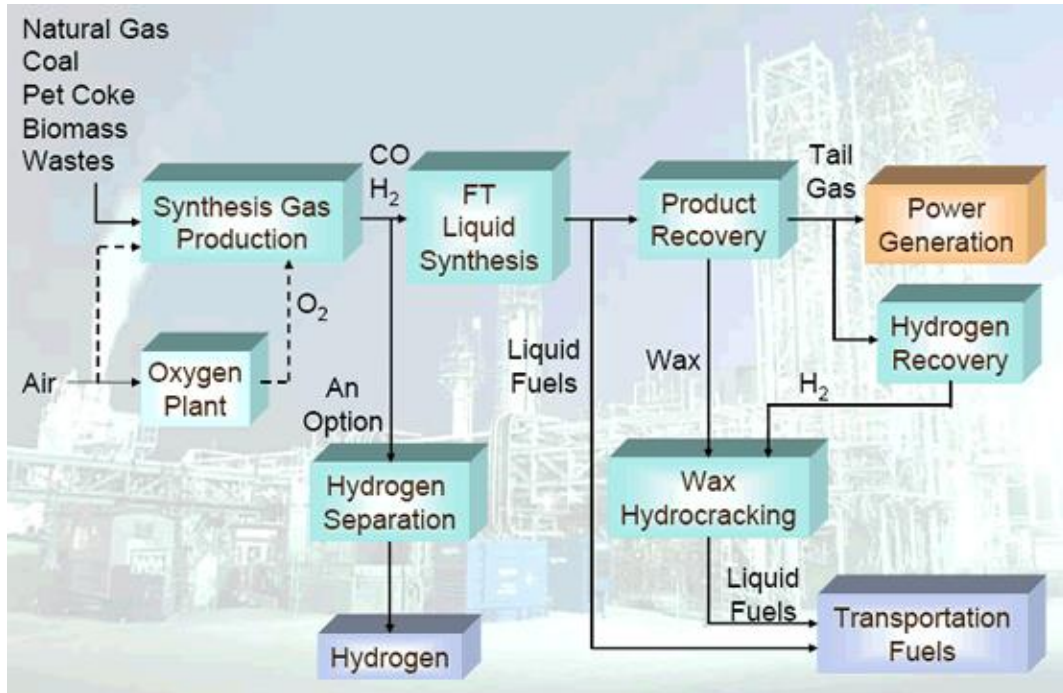


Fig. 1.4. Schematic of the Fischer – Tropsch process

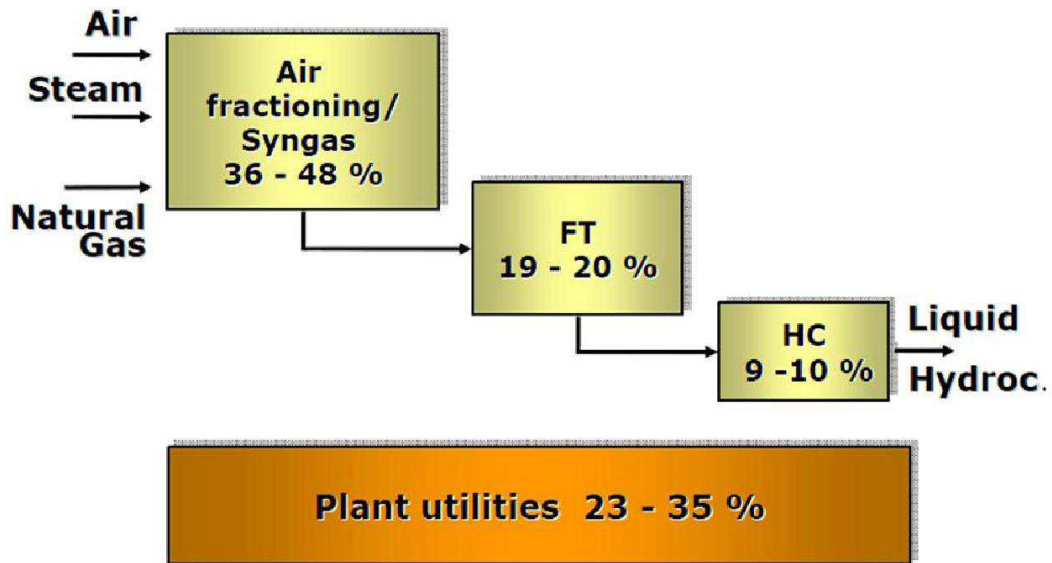


Fig. 1.5. Costs breakdown for FT process [43]

As a consequence, the valorization of small/medium size gas fields for which pipelines and LNG are not convenient, require the development of alternative syngas technologies suited for this size, and direct routes for NG conversion. With this purpose has been developed an European project called Next – GTL [44] which inspired the present work, and the overall scheme is reported in Fig. 1.6.

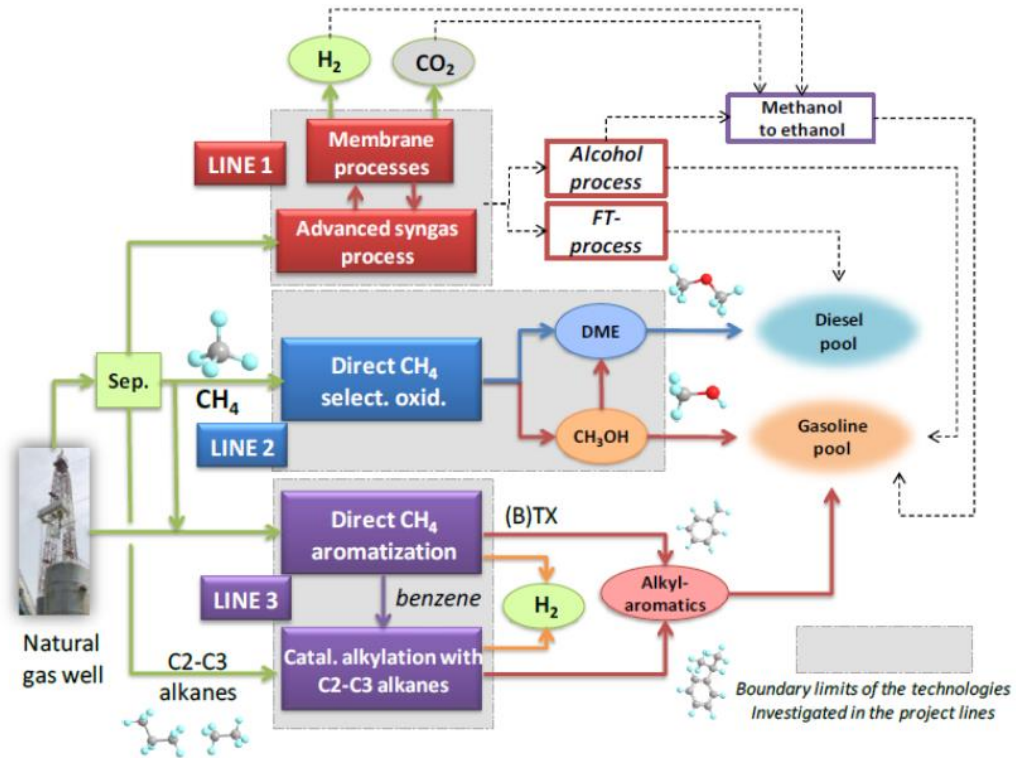


Fig. 1.6. Overall scheme of the Next-GTL Project [44]

This project addresses from one side the most critical and costly step to produce liquid fuel from natural gas using conventional routes, i.e. the stage of syngas production, and from the other side explores alternative routes (oxidative and non-oxidative) to convert natural gas to liquid transportable products for gasoline and diesel pools. The broader and ambitious organization of the project in three lines derives from the following industrial needs/objectives:

1. Reduce the cost and energy consumption (and related environmental impact) of the more costly step in the conventional GTL process, i.e. syngas production, and overcome the actual barriers in using catalysts in this process (mainly related to stability); this objective is implemented in Line 1 by developing a new low temperature catalytic syngas production based on the integration between catalysts and membranes in a multistep process.
2. Develop GTL technologies suitable for small-medium scale productions in remote NG areas; this objective is implemented in all the three lines of the project by using configurations, based on the integration with membranes, suited for this objective. Develop direct NG routes, in particular, is an important target to reach this objective. In addition, the possibility in Line 3 of using NG mixtures (instead of pure CH₄) in aromatization step and C₂-C₃ alkanes (instead of olefins)

for converting benzene to alkyl aromatics are further relevant components to reach the scope.

3. Develop processes for producing liquid fuels which can be blended in both gasoline and diesel pools, or which may be used for chemical purpose; after syngas production (Line 1) different products could be obtained, but in view of point 2, it is necessary also to develop direct conversion routes which could meet this objective. For this reason methanol, DME and alkyl aromatics are targeted as products,.

Accordingly, three development lines are followed in this project:

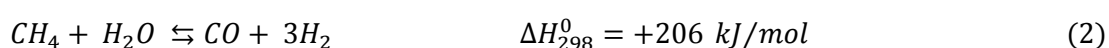
Line 1: advanced, low temperature route for catalytic syngas formation from natural gas, in which reaction steps are integrated with different types of membranes for O₂, H₂ and CO₂ separation.

Line 2: direct low temperature catalytic conversion of methane to methanol/DME, utilizing several innovative concepts to overcome the drawbacks of previous approaches including the use of supported ionic liquids/molten salts.

Line 3: direct catalytic conversion of methane to aromatics under non-oxidative conditions followed by upgrading of the products by alkylation with ethane/propane.

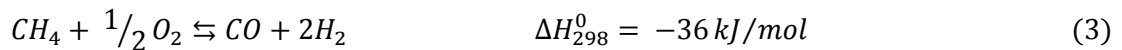
Industrially, nowadays, natural gas is converted into syngas through three main processes:

1. Steam Reforming (SR)



Steam reforming (2) is used for converting natural gas (NG) and naphtha into synthesis gas. Before being sent to SR, the hydrocarbon reagent is preheated and desulfurized; vapor is then added and the mixture is further preheated and pre-reformed to convert the C₂ and C₃ hydrocarbons. The reforming takes place in an oven in which tubes are located filled with catalyst, through which the reaction mixture flows. The synthesis gas at the outlet of the tubes is rapidly cooled and can be sent to water-gas shift processes and separation/purification. SR requires considerable quantities of vapor to reduce the formation of carbonaceous residues. Vapor is also necessary for increasing the H₂ content in the synthesis gas produced which would otherwise prevalently contain CO, in case a higher H₂/CO ratio is required.

2. Partial Oxidation (POX) or Catalytic Partial Oxidation (CPO)



A mixture of oxygen and natural gas is preheated, mixed and ignited in a burner. In the absence of catalyst, the reactor temperature must be high enough to reach CH_4 conversion. Carbon and combustion products like CO_2 and H_2O are also formed to a certain extent. Subsequently, endothermic reactions like steam reforming is also involved, which determine a decrease in the outlet temperature in the order of 100 – 150°C. At this stage, the gas composition is near thermodynamic equilibrium. According to the stoichiometry (2) the consumption of O_2 should be, in the absence of combustion products, approximately 0.5 O_2/CH_4 . However, actual use requires O_2/CH_4 ratio of about 0.7 [45]. By means of short contact time, i.e. small reactor, the catalytic process CPO is capable of transforming at lower temperature (900 – 1000°C) the NG and other hydrocarbons fractions which cannot be used by other known catalytic technologies (SR and ATR) and which can only be converted into synthesis gas by means of the PO technology but with high energy consumptions and investment costs. The control of the temperature and the catalyst stability are the main constraints of the CPO process.

3. Auto Thermal Reforming (ATR)

Autothermal reforming (ATR) is a combination of partial oxidation and steam reforming developed by Haldor Topsoe in the late 1950s with the aim of performing reforming in a single reactor [46]. Typically, the ATR operates at high temperatures of about 1300°C in the combustion zone and 900 – 1100°C in the catalytic zone. This results in a lower oxygen consumption ($\text{O}_2/\text{CH}_4 = 0.55 - 0.60$), however, with a certain amount of steam added to the feedstock to eliminate carbon formation. Carbon and soot formation in the combustion zone is an undesired reaction which leads to carbon deposition on downstream tubes causing equipment damage, pressure losses and heat transfer problems.

Fig. 1.7 schematically show the main syngas processes from natural gas.

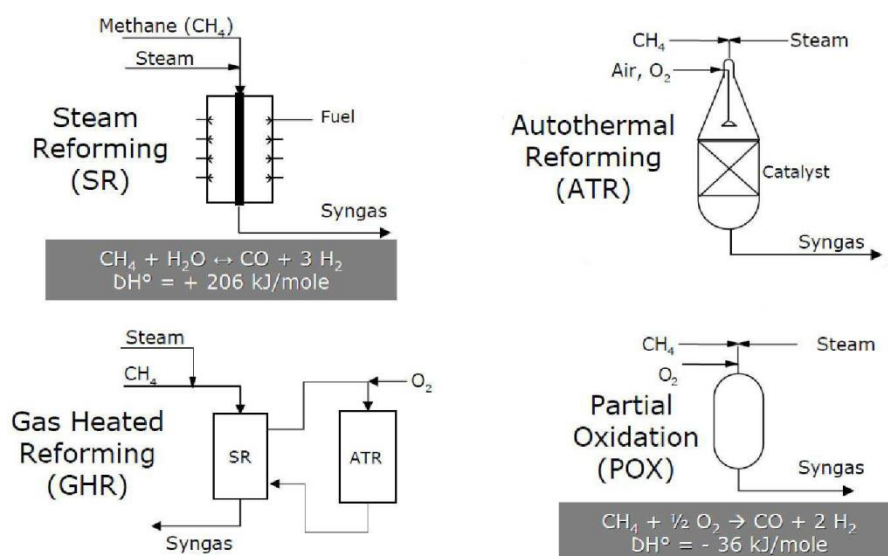


Fig. 1.7. Principal syngas production processes from natural gas

A CPO/membrane reactor can then be a valuable alternative with respect to conventional SR or CPO reactors to transform methane into syngas. No attempt was previously made to integrate CPO upstream with an O₂ membrane separator and downstream with a H₂ membrane separator [44].

1.1.6 Membranes and Membrane Reactors (MRs)

Several scientific works [47,48,49,50,51,52] have been developed this new research area, which is becoming even more of a crucial importance mainly in reactions like the reforming ones.

Considering a IUPAC definition [53], a membrane reactor (MR) is a device for simultaneously performing a reaction (SR, dry reforming (DR), autothermal reforming (ATR), etc.) and a membrane – based separation in the same physical device. Therefore, the membrane not only plays the role of a separator, but also takes place in the reaction itself.

The membranes can be classified according to their nature, geometry and separation regime. In particular, they can be classified into inorganic, organic and inorganic/organic hybrids. The choice of membrane type to be used in MRs depends on parameters such as the productivity, separation selectivity, membrane lifetime, mechanical and chemical integrity at the operating conditions and, particularly, the cost.

Regarding the inorganic type, they are commonly constituted by different materials as ceramic, carbon, silica, zeolite, oxides (Al₂O₃, TiO₂, ZrO₂) as well as Pd, Ag, and their alloys. They can operate in drastic conditions of temperature and chemical environment,

thanks to their high thermal and chemical resistance, but the costs are their main drawback.

According to Basile and Gallucci [54] inorganic membranes can be subdivided into four main groups:

1. **Metal Membranes:** dense metal membranes, are usually used for H₂ separation from gas mixture and in MR area. Pd and its alloys are the dominant materials for preparing this kind of membranes due to its high solubility and permeability of H₂. They results to be very expensive, mainly due to the low availability of Pd. Recently, supported thin metallic membranes are realized by coating a thin layer of Pd (layer thickness comprise in submicron to microns range) on a ceramic support, with the advantages to reduce the material costs, improve resistance to mechanical strength and higher permeating flux. A problem associated with this type of membranes, is the surface poisoning mainly by gases like H₂S or CO, that are adsorbed on the Pd surface, blocking available dissociation site for H₂.
2. **Ceramic Membranes:** usually made from Al₂O₃, TiO₂ or SiO₂. They have the advantages of being chemically inert and stable at high temperatures. This high stability makes this king of membranes suitable for food, biotechnology and pharmaceutical applications.
3. **Carbon Membranes:** Carbon Molecular Sieve (CMS) are porous solids containing constricted apertures that approach the molecular dimensions of diffusing gas molecules [55]. CMS can be obtained by pyrolysis of many thermosetting polymers (PVDC, PFA, PAN, etc), cellulose triacetate, phenol formaldehyde and can be divided into supported and unsupported CMS.
4. **Zeolite Membranes:** are microporous crystalline alumina silicate with an uniform pore size. One of the main drawbacks related to these membranes is represented by their relatively low gas fluxes compared to other inorganic membranes. Moreover, another important problem is represented by the zeolites thermal effect [56].

A crucial characteristic of a membrane system is its separation regime.

In porous membranes the transport mechanisms could be listed as follows [54]:

1. *Poiseuille (viscous) mechanism:* occurs when the average pore diameter is bigger than the average free path of fluid molecules. In this case, no separation takes place;
2. *Knudsen mechanism:* when the average pore diameter is similar to the average free path of fluid molecules [57];

3. *Surface diffusion*: when one of the permeating molecules is adsorbed on the pore wall. This type of mechanism can reduce the effective pore dimensions obstructing the transfer of different molecular species [58];
4. *Capillary condensation*: when one of the component condenses within the pores due to capillary forces. Generally, it favors the transfer of relatively large molecules [59];
5. *Multi-layer diffusion*: when the molecule – surface interactions are strong. It is like to an intermediate flow regime between surface diffusion and capillary condensation [60];
6. *Molecular sieving*: when pore diameters are very small, allowing the permeation of only the smaller molecules.

In dense metallic membranes, molecular transport occurs through a solution – diffusion mechanism. In particular, in Pd – based membrane, H₂ atoms interact with Pd metal. H₂ permeation through the membrane is a complex process with several stages [54]:

- Dissociation of molecular H₂ at the gas/metal interface;
- Adsorption of the atomic hydrogen on membrane surface;
- Dissolution of atomic hydrogen into the Pd matrix;
- Diffusion of atomic hydrogen toward the opposite side;
- Recombination of atomic hydrogen to form H₂ molecules at the gas/metal interface;
- Desorption of H₂ molecules

At a fixed temperature, the H₂ permeation flow through a dense Pd membrane can be expressed by means of the relation (4):

$$J_{H_2} = Pe_{H_2} \cdot \frac{(p_{H_2,ret}^n - p_{H_2,perm}^n)}{\delta} \quad (4)$$

where J_{H_2} is the H₂ flux through the membrane, Pe_{H_2} is the H₂ permeability, δ is the membrane thickness, $p_{H_2,ret}^n$ and $p_{H_2,perm}^n$ are the hydrogen partial pressures at the retentate and permeate sides, respectively, and n (in the range of 0.5 – 1.0) is the dependence factor of the hydrogen flux on the hydrogen partial pressure.

The thickness of a dense Pd membrane is very important because it represents a compromise between two factors. On one hand, a thinner membrane offers less flow resistance and, hence, a higher permeability. On the other hand, practical fabrication

technology limits the thickness of the membrane with respect to mechanical integrity and strength.

In recent decades, the alternative technology of MBRs has been applied to SRM reaction in order to produce H_2 separated from the others components of the outlet stream in the same time in which the reaction is occurring. In particular, recent reviews regarding the state of the art on the hydrogen production via SRM reaction performed by MRs have been published [61,62].

Not only H_2 can be separated adopting the membrane technology, but also other gases such as O_2 and CO_2 .

Dense ceramic membranes for the separation of O_2 are mainly based on perovskites, or O_2^- -conducting materials as used in solid state fuel cells (Y-stabilized zirconia, Ce-gadolinia, etc.). O_2 flux at a given temperature and production of crack-free thin films are the main issues.

For CO_2 separation, either nanoporous membranes (polymeric, or based on supported ionic liquids), or adsorbents based on zeolites (clinoptilolite or ion-exchanged zeolites) are utilized.

1.2 Processes for H₂/Syngas production

1.2.1 Steam Reforming

The methane steam technology was studied in the first part of 20th century by BASF who established the essential configuration of the primary steam reformer, and the technology was used in 1931 by Standard Oil of New Jersey to produce hydrogen from off-gases at its Baton Rouge and Bayway refineries.

The methane reforming process was adopted mainly in the US where natural gas was easily available as feedstock, whereas reformers in Europe were initially reduced to operate on propane and LPG [63].

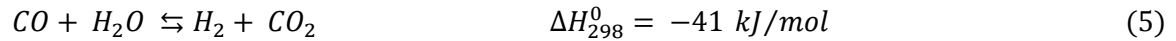
The steam reforming reaction took place over catalyst in vertical tubes, which were supported in parallel rows in a radiant furnace. The endothermic heat of reaction was supplied by burning fuel in the furnace. The process was considerably improved by ICI, who developed the fundamental engineering data for the design of the furnace, improved the catalyst formulation and introduced the desulphurization step using zinc oxide. The process was used to produce hydrogen from off gases for coal hydrogenation plants, which ICI built in 1936 and 1940.

In the 1959 ICI started up the first large scale pressure steam reformer using naphtha as a feedstock, and this became the precursor of over 400 plants subsequently licensed around the world in areas where natural gas was not available. From 1959 to date development of the catalyst continued in order to allow plants to be run at higher pressure and temperature, and with feedstock containing quantities of unsaturated and aromatics compounds to be reformed. In more recent years the increasing availability of natural gas has resulted in its use as a major source of reformer feedstock, and this is likely to remain so for some time. Development of catalyst for natural gas reforming has concentrated on extending catalyst life, improving activity, inhibiting carbon formation reactions, and by improving the physical properties.

1.2.1.1 Thermodynamics of Steam Reforming reaction

The objective of the catalytic steam reforming process is to extract the maximum quantity of hydrogen/syngas held in water and in the hydrocarbon feedstock. Thereafter the subsequent manipulation of the gas stream depends on the purpose for which the gas is intended.

The reforming process of natural gas includes two separated reactions: the steam reforming (2) and the water – gas shift (WGS) (5):



Therefore the overall reaction could be written as follows:



The reforming reaction (2) is strongly endothermic, so the reaction is favored by high temperature as well as by low pressure, while the shift reaction (5) is exothermic and is favored by low temperature but is largely unaffected by changes in pressure. To maximize the overall efficiency (and hence economics) of the conversion of carbon to carbon dioxide and the production of hydrogen, reformers are operated at relative high temperature and pressure. This is followed by the shift process that, by using two different catalysts, permits the shift reaction to be brought to equilibrium at as low temperature as possible. It can be seen in reaction (2) that SR with methane the stoichiometric requirement is 1.0. However, it has been demonstrated that these conditions are not reliable because all catalysts so far developed tend to promote carbon formation under steam reforming conditions. These reactions can be suppressed by using an excess of steam, with the results that the minimum ratio is in the region of 1.7. However, the reforming reaction itself is also promoted by an excess of steam and hence some advantage is derived from this. In practice ratios of 2.5 - 3.5 are commonly used, but in some cases, there can be economic attractions in using lower steam ratios and there is a trend in this direction. Fig. 1.8 shows how the thermodynamic parameters such as temperature and pressure together with the steam to carbon ratio (S/C), have a large influence on the reformat outlet composition.

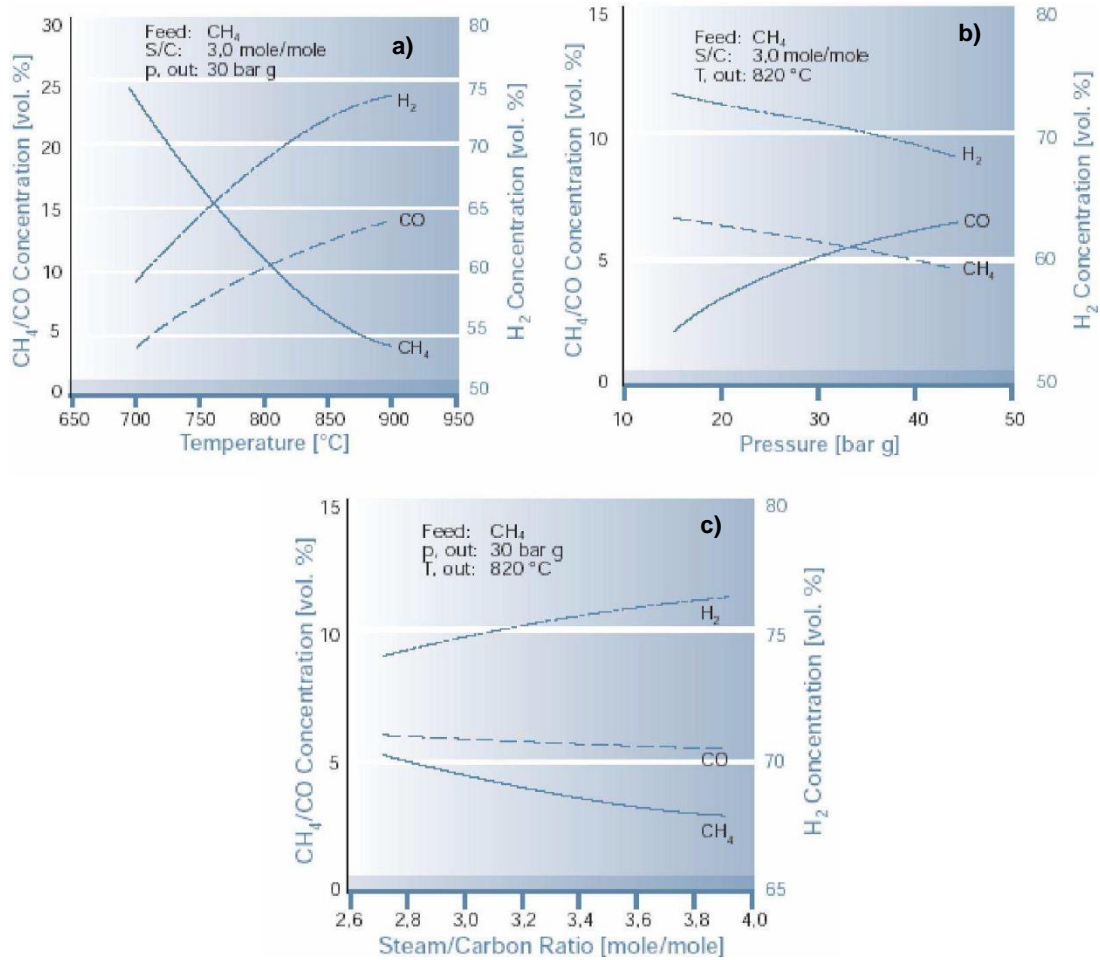
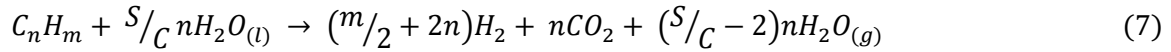


Fig. 1.8. Variation of the reformed gas in function of: a) Temperature; b) Pressure; c) S/C ratio [44]

Lutz and co-workers [64] examined the thermodynamics of the steam reforming process. The process must burn either a second fuel, a fraction of the primary fuel, or the residual fuels that remain in the reformat stream. This last option is often done in practice to recover heating value that would otherwise be wasted. The analysis presented by Lutz considers two levels of sophistication in treating the chemistry. The first uses a global species balance that assumes that the reforming reaction goes to completion. An energy balance for the reaction allows to examine the definition of thermal efficiency. This analysis provides a theoretical upper limit on the thermal efficiency that is independent of temperature or other influences on the reaction kinetics. The second analysis replaces the global reaction step with a calculation of chemical equilibrium for the reforming reaction. The equilibrium computation brings in temperature dependence, without requiring detailed information regarding the specific reactions or catalyst performance.

According to the first method of thermodynamic analysis reported by Lutz et al. [64] a global reaction balance could be written as reported by equation (7):



where n and m define the composition of the fuel, and S/C is the steam-to-carbon ratio for the mixture. The term “global reaction” recognizes that the reaction is actually the net result of a series of elementary reactions, some of which include catalytic interaction with surfaces. This balance conserves elements with two assumptions: there is sufficient steam to react with the fuel ($S/C \geq 2$), and the reaction goes to completion. Using the reaction (7), the formation enthalpies of the species can be added to determine the net enthalpy change (8):

$$\Delta H_R = nh_{CO_2}^f + (S/C - 2)nh_{H_2O_{(g)}}^f - (h_{C_nH_m}^f + h_{H_2O_{(l)}}^f) \quad (8)$$

where ΔH_R is the formation enthalpy per mole of species k at standard temperature and pressure.

In Fig. 1.9 are reported the efficiency of SRM (Steam Reforming of Methane) in function of temperature and S/C ratio, calculated through the equilibrium model (A), while (B) show the equilibrium composition of a reformat gas. Focusing on the solid curve (Fig. 1.9 (A)), for S/C=2, the effect of temperature is to increase the efficiency of the equilibrium reformer. This is simply due to the fact that at lower temperatures the equilibrium composition leaving the reformer (Fig. 1.9(B)) contains more unreacted methane and water. As the temperature increases, the equilibrium composition approaches the product stream expected from the global balance, except that there is still an excess of steam, and the CO concentration is 20% of the mixture.

The equilibrium solutions suggest that the reformer must operate at higher temperatures. There is, however, a limit to which higher temperature improves performance. The equilibrium does not shift much farther towards reaction completion as the temperature goes above 900°C. A secondary effect is that the reformat stream contains insufficient heating value, so supplemental fuel must be added prior to the burner. The effect of S/C ratio is complicated by the fact that its influence depends on the temperature. The three curves (Fig. 1.9 (A)) at S/C ratios of 2, 3 and 4 show that at low temperature, where the reaction is far from completion, the efficiency increases with excess of steam. At high temperature, where maximum H₂ is obtained, the equilibrium model behaves like global analysis. In this limit, the excess of water does reduce the efficiency. The observation that the thermal efficiency intersect at some temperature means that there is a point where the chemical benefit of extra steam is offset by the energy required to generate it.

Fig. 1.10 shows that a higher exhaust temperature reduces the thermal efficiency.

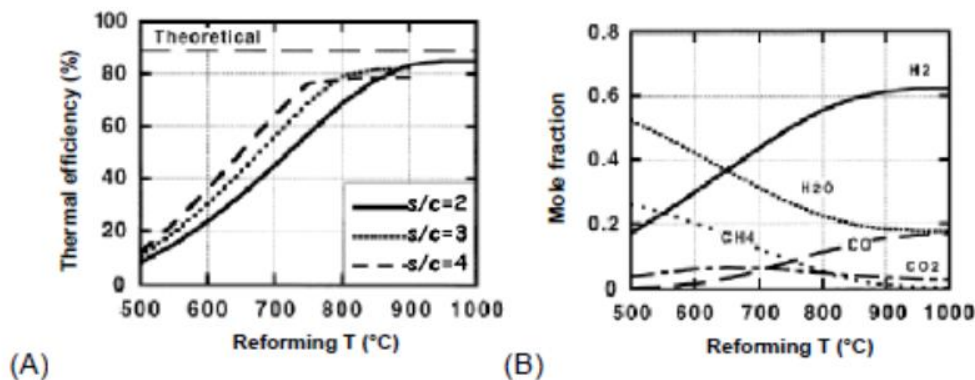


Fig. 1.9.(A) Efficiency of methane steam reforming computed in equilibrium model versus reformer temperature at pressure of 10 atm at different S/C ratios; (B) Equilibrium composition leaving the methane steam reformer for S/C = 2 and pressure 10 atm [64]

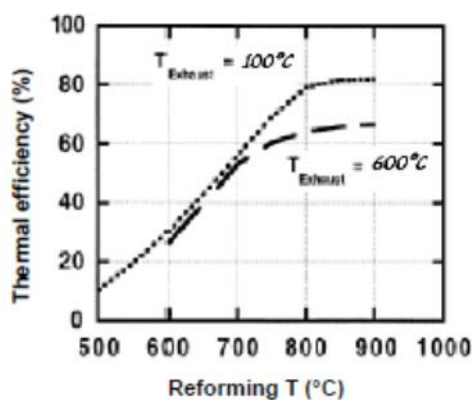


Fig. 1.10. Thermal efficiency vs. equilibrium reformer temperature for steam reforming of methane at S/C=3 and two exhaust temperatures [64]

From thermal efficiency analysis, Lutz and co-workers concluded that definitions of thermalefficiency can be misleading. The definition should be accompanied by identification of the systemboundary and the heat flows across it. The definition should include external heat addition. Comparisons of the equilibrium model for steam reforming to experimental data showed that thechemical equilibrium is appropriate for understanding the effect of temperature. Experimentalthermal efficiencies for steam reforming were significantly lower than the thermodynamic limitpredicted by the equilibrium model. Species measurements showed the deficiency was partly dueto non-equilibrium composition, but other heat transfer losses are a dominant effect, especially forcompact steam reformers. The effect of extra steam suggested by the equilibrium analysis is toincrease the H₂ conversion and thermal efficiency, at least until a high temperature limit is reachedwhere the H₂ conversion is maximized. Only in this limit is the global analysis valid.

1.2.1.2 Kinetics and reaction mechanism

The results of a number of studies on the kinetics of the methane steam reforming have been published. There is general agreement that the reaction is first order in methane, but there is less agreement with other kinetic parameters. In part, this is due to the use of different catalysts and experimental conditions, but often it has resulted from a lack of consideration of diffusion and heat transfer limitations. Thus, reported activation energies are spread in a wide range of values due to different degrees of diffusion limitation, and these can also cause misleading total pressure effect. Indeed, with the relatively large catalyst particle sizes used in industrial steam reformers, these effects result in very low effectiveness of the catalyst. Effectiveness factors (η) may, depending on conditions, only be as high as 0.3 at the inlet region, and perhaps as low as 0.01 at the exit. Because of this, apparent activity increases as the particle size is made smaller, but the increased pressure drop, which arises across the reformer, restricts the size of the catalyst that can be used in practice [65].

A wide variety of rate expressions for the steam reforming of methane have been proposed. These models range in complexity from simple first order dependency on methane, involving two parameters, to complex Langmuir–Hinshelwood models with over ten parameters [66]. It is generally agreed that the rate of methane reforming has a first order dependency on methane. Furthermore, it is also agreed that the rate-determining step in the reforming process is the formation of adsorbed carbon species which occurred through equation (9):



This mechanism leads to the formulation of rate equations (10) of the following form:

$$r_{CH_4} = -k p_{CH_4} p_{H_2}^\alpha \quad (10)$$

In equation (10), the value of α is found to depend on temperature, having a value close to -1 at low temperatures ($<700^\circ\text{C}$) and approaching to 0 at high temperatures ($>700^\circ\text{C}$).

Kinetic rate expressions for the steam reforming of methane found in the literature use the steady state approximation and take the form of the equation (11):

$$r_{CH_4} = -k p_{CH_4} \frac{f(p_{H_2O}, p_{H_2})}{[1 + f(p_{CH_4}, p_{H_2O}, p_{H_2}, p_{CO}, p_{CO_2})]} * \left(1 - \frac{p_{CO} * p_{H_2}^3}{p_{CH_4} * p_{H_2O} K_1}\right) \quad (11)$$

Reforming rates can be rigorously obtained from measured net rates using an approach to equilibrium parameter (η) evaluated from CH₄-H₂O thermodynamic reaction data and measured reactant and product partial pressures [67,68]:

$$\eta = \frac{[P_{CO}][P_{H_2}]^3}{[P_{CH_4}][P_{H_2O}]} * \frac{1}{K_{eq}} \quad (12)$$

In the expression (12), $[P_j]$ is the average partial pressure of species j (in atm); it is also used to correct for reactant depletion. K_{eq} is the equilibrium constant for CH₄ - H₂O reaction. Forward turnover rates (r_f) are given by equation (13):

$$r_f = \frac{r_n}{(1 - \eta)} \quad (13)$$

where r_n is the net CH₄ conversion turnover rate. CH₄ reaction rate increased linearly with increasing CH₄ pressure. H₂ and CO products added to CH₄ - H₂O reactant mixture influenced net CH₄ conversion rate at 600°C, but forward rates were unaffected, indicating that H₂ and CO affected only the extent to which reforming reactions approach equilibrium, but not the kinetics of CH₄ reforming reaction. Thus, previously reported inhibition of CH₄ reaction rates by products may reflect unrecognized contributions from reverse reaction rates. CO adsorption enthalpies are 135 kJ·mol⁻¹ at low coverage (<0.02) and much lower at higher coverage on Ni (100). These adsorption enthalpies indicate that CO coverage should be well below 0.01 monolayer at 600°C and even at equilibrium CH₄ conversions. The lower adsorption enthalpies typically reported for H₂ (92 kJ·mol⁻¹) would make hydrogen coverage even lower than for CO. Thus, competitive adsorption is unlikely to influence the availability of metal sites for CH₄ activation and reported inhibition effects predominately reflect contributions from reverse reactions.

These kinetic responses to reactant and product concentrations are consistent with determining CH₄ activation steps on surfaces, essentially free of reactive intermediates or co-adsorbed products. CH₄-derived chemisorbed intermediates appear to be readily removed via reactions with H₂O co-reactant; as a result, the identity and concentration of co-reactant become kinetically irrelevant and forward rate data for the steam reforming reaction is accurately described by equation (14):

$$r_f = kP_{CH_4} \quad (14)$$

Catalytic reaction of CH₄ with H₂O to form H₂-CO mixtures on Ni depends only on the rate of the initial activation of C—H bonds, catalyzed by surface Ni atoms. Co-reactant activation is easy and CH₄-derived intermediates, including reactive chemisorbed

carbon, are kept well below monolayer coverage by their rapid reactions with intermediates derived from H₂O.

Regarding the reaction mechanism, it has been demonstrated that is in accordance with the measured kinetic effects of reactant and product concentration of forward reaction rate. The various steps involve in the mechanism proposed by Wei and Iglesia [67] are schematically reported in Fig. 1.11. Methane decomposes to chemisorbed carbon (C*) via sequential elementary H-abstraction steps, which become faster as H atoms are sequentially abstracted from CH₄ reactants. Density-functional theory led to an activation energy of 142 kJ·mol⁻¹ for the first H-abstraction step in CH₄ on Ni clusters, which decreased to 25-40 kJ·mol⁻¹ for CH₂ formation from CH₃*. This cascade process leads to low CH* coverage and to C* as the most abundant carbon-containing reactive intermediate. Chemisorbed carbon is then removed using CO₂ or H₂O as co-reactants. These elementary steps are consistent also with kinetic and isotopic measurement on Ru, Pt, Ir and Rh catalysts. When exposed metal atoms (*) are the most abundant surface species, only the rate constant for the activation of the first C—H bond in CH₄ appears in the rate expression and reaction rates become first order in CH₄ and independent of the presence or concentration of H₂O or CO₂ co-reactants. These elementary steps provide pathways for reactions of CH₄ with either H₂O or CO₂ and also for water gas shift reaction which have been typically, but inappropriately and non-rigorously, treated as independent kinetic process during CH₄ reforming [67,68].

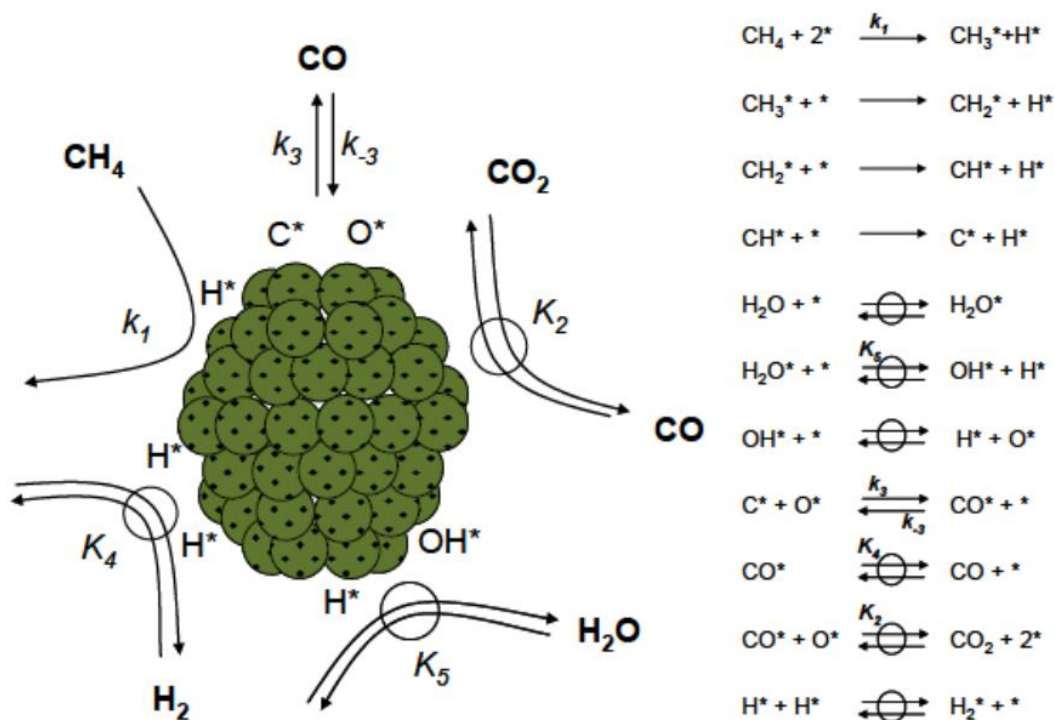


Fig. 1.11. Sequence of elementary steps for CH₄ reforming and WGS reactions on Ni based catalysts.(→irreversible step, ⇌ quasi-equilibrated step, ⇌ reversible step, ki is the rate coefficient and Ki is the equilibrium constant for a given step i) [67]

Decomposition of methane on nickel surface is believed the first step of the steam reforming of methane; then the carbon species formed on the surface react subsequently with steam or surface oxygen species. To follow the reaction steps, Matsumura and Nakamori [69] separately fed methane and steam to the catalysts at low temperature (500°C) and analyzed the mechanism at the initial stage of the reaction in which surface-active species participate. The rate of the reaction of methane in absence of steam is significantly lower than that of the steady steam reforming, suggesting that the presence of steam which can oxidize the surface of Ni accelerates the decomposition of methane to hydrogen. The formation rate of hydrogen is high at the initial stage of the reaction with methane on Ni/SiO₂ and Ni/Al₂O₃ catalysts, and formation of carbon oxides, which evidences presence of surface oxygen species, is accompanied. Carbon monoxide is selectively formed in the reaction with methane over the catalyst containing NiO. Hence, the reduction of nickel oxide results in formation of carbon monoxide [69].

In the reduction process of NiO particles, formation of hydroxyl group on the surface of nickel (Ni-OH) is hypothesized. It is also supposed that the hydroxyl group is more reactive to methane and/or carbon monoxide than the lattice oxygen of nickel oxide. Accumulation of oxygen on the surface of these catalysts can be detected at the initial

stage of the reaction with steam after methane decomposition. In this process, reaction (15) and (16) are also probable:



However, the contribution will be small because formation of carbon monoxide, which is produced in presence of nickel oxide is small in the reaction with methane after the contact with steam. Since the formation rates of H_2 and CO_2 increase gradually in the reaction with steam, carbon dioxide cannot be formed in the direct reaction between steam and surface carbon, but probably formed by the reaction with surface hydroxyl groups as reported in reaction (17), whose concentration should be saturated under the continuous feed of steam.



Little methane is formed after the formation rate of carbon dioxide is saturated, implying that the surface is mostly oxidized, because formation of methane does not proceed in absence of metallic nickel which accepts the oxygen in steam. After the feed of steam, following the reaction with methane, formation of carbon dioxide can be observed with re-feed of methane, suggesting formation of surface hydroxyl groups on the surface during the previous reaction with steam that can react with the re-fed CH_4 following the reaction (18):



In literature is reported also a study of the low temperature steam reforming mechanism on Ni/ZrO₂ [65] which confirm the hypothesis of formation of hydroxyl groups on the catalyst surface. In fact, in Ni/ZrO₂ system, accumulation of water on the support assists formation of the hydroxyl groups, and this is probably the reason why ZrO₂ is an effective support of nickel in the steam reforming at 500°C. Formation of carbon dioxide from carbon monoxide by water–gas shift reaction is possible in the reaction mechanism, but no relationship between production of carbon monoxide and carbon dioxide can be found in the reactions solely with methane or steam.

1.2.2 Catalysts for Steam Reforming

The major challenge in the research of the right steam reforming catalyst is to obtain a material that is resistant enough both towards the dramatic operative conditions in which SR is carried out (high temperature and pressure) and, especially, it must have the right resistance towards the two principal deactivation phenomena which affect this reaction: the sintering of the active particles and the carbon formation

For many years nickel has been recognized as the most suitable metal for steam reforming of hydrocarbons, other metals can be used; for example Co, Pt, Pd, Ir, Ru and Rh. Although some precious metals are considerably more active per unit weight than nickel, nickel is much cheaper and sufficiently active to enable suitable catalysts to be produced economically.

The reforming reaction takes place on the nickel surface, so the catalyst must be manufactured in a form that produces the maximum stable nickel surface area available to reactants. This is generally done by dispersing the nickel as small crystallites on a refractory support, which must be sufficiently porous to allow access by the gas to the nickel surface. This is usually achieved by precipitating nickel as insoluble compound, from a soluble salt, in the presence of a refractory support such as mixtures of Al_2O_3 , MgO, CaO and calcium aluminate cement. Alternatively, the nickel can be incorporated by impregnating a preformed catalyst support, such as alumina or an aluminate, with a solution of a nickel salt which is subsequently decomposed by heating to the oxide. Impregnated catalysts are generally stronger than precipitated catalysts, and this is one of the reasons for their widespread use.

Activity is a function of the overall nickel content. However, it has been demonstrated that with both impregnated and precipitated catalyst there is an optimum beyond which an increase in nickel content does not produce any further significant increase in activity. Typically, these optima are approximately 20% for precipitated and up about 15% for impregnated catalyst, but this depends on the nature and physical properties of the actual support.

The dissociation of methane is considered to be the rate-limiting step in SMR. This has led to a great interest in investigating the fundamental sticking process of methane on nickel single crystals. Ni single crystal studies have shown methane dissociation to be structure sensitive [70]. At a given temperature and for a given hydrocarbon feed carbon will be formed below a critical S/C ratio [71]. This critical S/C ratio increases with temperature. By promotion of the catalyst, it is possible to push this limit towards the thermodynamic limit reflecting the principle of the equilibrated gas: "Carbon formation is

to be expected on nickel catalysts if the gas shows affinity for carbon after the establishment of the methane reforming and the shift equilibria". By use of noble metals, it is possible to push the limit at lower values. A safe design criterion is to require that the actual gas shows no affinity for carbon formation. Whether carbon free operation is possible depends on the kinetic balance as illustrated in the simplified two-step mechanism (19):



For a nickel catalyst, carbon is normally formed by the whisker mechanism. Adsorbed carbon atoms that do not react to gaseous molecules are dissolved in the nickel crystal and carbon whiskers nucleate from the nickel support interface of the crystal. Carbon formation is avoided when the concentration of carbon dissolved in the nickel crystal is smaller than that at equilibrium, in other words, when the steady state activity of carbon is smaller than one. The whisker mechanism may also be blocked by use of noble metal catalysts because these metals do not dissolve carbon.

For the past decade, there has been an increased interest in the preparation of mixed oxide catalysts using hydrotalcite-like compounds (HT) as precursors for various reactions. Takehira et al [72,73,74,75] proposed a solid phase crystallization (spc) method for the preparation of well-dispersed and stable metal supported catalyst, starting from perovskite compounds (PVK) and hydrotalcite-like compounds as the precursors. Starting from Mg–Al hydrotalcite precursors containing Ni at the Mg sites, spc-Ni/MgAl catalysts have been prepared and were successfully applied in the partial oxidation, the steam reforming, and the CO₂ reforming of CH₄. Hydrotalcite is an anionic clay, layered mixed hydroxide containing exchangeable anions and affords the mixed oxide by heating; it shows an interesting property, i.e., a "memory effect". This "memory effect" allows the reconstitution of the original hydrotalcite structure under mild conditions when the product of the thermal treatment is brought into contact with aqueous solutions containing anions. By adopting this "memory effect" on the surface of Mg–Al mixed oxide particle after thermal treatment, Takehira et al. [74] have prepared egg shell-type Ni-loaded catalysts. When the Mg–Al mixed oxide particles were dipped in aqueous solution of Ni(II) nitrate, Mg–Al hydrotalcite was reconstituted on the surface of particles and Ni(II) substituted for the Mg(II) sites. After the calcination followed by the reduction of the particles, active spc-Ni/MgAl phase was formed in the surface layer of the particle, resulting in the formation of egg shell-type Ni-loaded catalyst as s-spc-Ni/MgAl (surface spc).

Other works in literature [76] reported catalyst preparation from hydrotalcite precursors. The precursors were synthesized by the traditional technique, with co-precipitation of Ni, Mg and Al nitrates with carbonate; co-precipitation of Mg and Al nitrates with pre-synthesized nickel chelate and anion-exchange of $(\text{NO}_3)^-$ of hydrotalcite with nickel chelate. The catalytic tests demonstrated high methane conversion, high activity for hydrogen production and high stability during the time of reaction for a molar ratio in the feed $\text{H}_2\text{O}:\text{CH}_4 = 2:1$. The low quantity of carbon formed on the catalysts surface confirmed the hypothesis that the structure of hydrotalcite layers leads to a homogeneous distribution of the active phase [76].

Another interesting and useful structure for reforming catalysts is the spinel – like one. Spinel is a ternary oxide with a chemical formula of AB_2O_4 , where A is a divalent metallic cation in a tetrahedral site and B is a trivalent metallic cation in an octahedral site of the cubic structure [77]. Magnesium aluminate spinel (MgAl_2O_4) has a specific combination of desirable properties such as: high melting point (2135°C), high resistance to chemical attack, good mechanical strength from room temperature to high temperatures, low dielectric constant, excellent optical properties, low thermal expansion and good catalytic properties. Conventionally, the spinel (MgAl_2O_4) is prepared through a reaction in the solid state using MgO and Al_2O_3 . In this process, the mixture is calcined at high temperatures such as $1400\text{--}1600^\circ\text{C}$. An effort to synthesize MgAl_2O_4 at lower temperatures has been reached by using chemical synthesis processes, especially chemical co-precipitation and sol–gel processes, where the spinel phase is formed at temperatures around 700°C . Due to its resistance to sintering, the magnesium aluminate spinel has been used as a catalyst support for methane reforming. It was observed a high activity and stability of a $\text{Ni}/\text{MgAl}_2\text{O}_4$ catalyst for dry reforming of methane, which was attributed to the interaction between the active phase Ni and the support, resulting in highly dispersed active Ni species.

Nickel is increasingly studied for the methane-reforming catalysis with various oxides, either classical (Al_2O_3 , SiO_2 , MgO, TiO_2) or less conventional ones (ThO_2 , CeO_2 , ZrO_2 , Cr_2O_3 , Nb_2O_5) [78]. It appears that, besides the elaboration process, the nature of the interaction between the nickel and the support, in the form of specific phases, plays a determinant role for the catalytic properties. For example, the formation of phases, such as nickel aluminate spinel, NiAl_2O_4 , on alumina leads after reduction to highly dispersed catalysts with a high selectivity and a great resistance against sintering and poisoning. Nevertheless, even though the role of the tight interaction support metal is widely studied, it is still subject to discussion and yet far from being well understood. The

catalyst properties may be due to a combination of intrinsic size effects and support effects.

Reactions used to model the steam reforming of natural gas show that the influence of the support on the performances of the metal is minimal. On the other hand, hydrogen produced during the reactions adsorbs on the metal and can spill-over to the support. The H_2 spill-over could be responsible in part for the gasification of carbonaceous residues [79].

In the industrial viewpoint, Al_2O_3 -based supports are preferred because of their easier availability in the reforming processes. As an alternative, $Ni/\gamma-Al_2O_3$ could be considered. However, it is unstable at high temperature ($>700^\circ C$) because of the thermal modification of the $\gamma-Al_2O_3$ support phase that causes sintering and leads to the reduction in porosity and surface area as well as phase transformation into $\alpha-Al_2O_3$ which changes an active surface layer and promotes a low surface area structure. Thus, Jun and coworkers [80,81,82] carefully changed $\gamma-Al_2O_3$ into $\theta-Al_2O_3$ and modified $\theta-Al_2O_3$ with $CeZrO_2$ because $Ni/CeZrO_2$ exhibited good performance in methane reforming reactions. The catalyst was remarkably deactivated by steam treatment but reversibly regenerated by H_2 -reduction. The steam treatment resulted in the formation of $NiAl_2O_4$, which is inactive for SMR, but it was reversibly converted to Ni by the reduction. The reversible oxidation-reduction of Ni state was evidenced and it was observed that the formation of $NiAl_2O_4$ is more favorable at higher temperature.

From an industrial point of view, the development of nickel catalysts with greater resistance to coking is thus an attractive research goal [83]. An effective approach to developing such nickel catalysts is to focus on the selection and modification of catalyst supports. It is widely accepted that the addition of alkali, alkali earth oxides and rare earth metal oxides to the $\alpha-Al_2O_3$ support or the use of basic metal oxides as the support improves resistance to coking. This positive effect is understood to result from the enhancement in steam adsorption, in the oxidation rate of CH_x fragments adsorbed on metallic nickel and/or the reduction of methane activation and dissociation. Although improvements of the support greatly influence catalytic activity and/or resistance to coking, limited attempts have been made to apply oxygen-ion conducting oxides, for instance CeO_2 and perovskite-type oxides, to the steam reforming catalysts.

It is mechanistically expected that oxidation of CH_x fragments adsorbed on metallic nickel would be promoted by the lattice oxygen in oxygen-ion conducting oxides and that the consumed lattice oxygen would be regenerated by steam. Such a mechanism has specifically been proposed for CO oxidation and dry reforming of methane. Huang and

coworkers [84,85,86] have evaluated the activity of nickel supported on ceria-based ion-conducting oxides for dry reforming of methane and have pointed out that the lattice oxygen in modified ceria may play some positive roles in the activation of methane and carbon dioxide. Takehira et al. [72] have reported that the perovskite-type oxides such as SrTiO₃, CaTiO₃, BaTiO₃ that contain a small amount of nickel in the titanium sites show high catalytic activities with high resistance to coking, due to the high dispersion of nickel. These researchers also examined oxygen mobility in perovskites, and found that the high resistance to coking might be partly due to the migration of mobile oxygen from the perovskite support to the metallic nickel particles.

The catalytic activity and resistance to coking of nickel catalysts supported on a variety of the perovskite-type oxides (LaAlO₃, LaFeO₃, SrTiO₃, BaTiO₃, La_{0.4}Ba_{0.6}Co_{0.2}Fe_{0.8}O_{3-δ}) were compared to those of the conventional Ni/α-Al₂O₃ catalyst for steam reforming of methane under the conditions of 800°C, atmospheric pressure and a molar H₂O/CH₄ ratio of 2 [83]. To investigate differences in catalytic activity among the Ni/perovskite catalysts examined, the dispersion and reduction properties of nickel and the roles of the lattice oxygen on the catalytic activity and carbon deposition were examined. Ni/LaAlO₃ and Ni/SrTiO₃ showed high catalytic activities among the Ni/perovskites and longer-term stabilities than the conventional catalyst. Temperature programmed oxidation of carbon deposited on used catalysts revealed that inactive carbon species detected on Ni/α-Al₂O₃ were not formed in the case of Ni/LaAlO₃. The results of temperature programmed reduction confirmed that consumption and recovery of the lattice oxygen in perovskites occurred during the reaction, and that the reducibility of perovskites had a great impact on the steam reforming activity. The lattice oxygen in perovskites is considered to play important roles in promoting the oxidation of CH_x fragments adsorbed on metallic nickel. Both the reducibility and the particle size of nickel were found to be related to catalytic activities. These results suggest that the lattice oxygen in LaAlO₃ and SrTiO₃ accesses CH_x fragments adsorbed on nickel readily due to the large amount of lattice oxygen near the surface of the perovskite, and interfaces between the nickel particles and the support. Thus, Ni/LaAlO₃ and Ni/SrTiO₃ have high catalytic activities. The lattice oxygen in LaAlO₃ and SrTiO₃, thus plays a positive role in both promoting the oxidation of CH_x fragments adsorbed on metallic nickel and in hindering the production of inactive carbon species [83].

Other materials with high oxygen mobility can improve the resistance of the catalyst towards carbon formation such as CeO₂ – based oxides, especially CeO₂ – ZrO₂ ones.

1.2.2.1 CeO₂ – ZrO₂ mixed oxide as catalytic support

CeO₂ has been extensively employed as a textural and structural promoter for supported noble metal catalysts. Its promotion effect was attributed to excellent thermal and mechanical resistance, propensity to non-stoichiometry and oxygen-storage capacity. Due to its properties, structure and capabilities of storing and releasing oxygen, CeO₂ is an important component in automotive, emission-control (oxidation) catalysts, selective oxidation in fine chemical synthesis and solid oxide fuel cell applications. However, an enhancement of the activity and more stable catalysts have been obtained if CeO₂ is present in a mixed oxide with other cations in the form of solid solutions or if it can form solid solutions interacting with the support [87,88,89,90,91,92,93]. In these systems CeO₂ contributes to metal dispersion making the catalyst more resistant to poisoning by coke and to the sintering process. In addition CeO₂ participates to the reaction mechanism as an oxygen storage component. A two pathway mechanism can be proposed for the reaction: the first step is the hydrocarbon/CH₄ decomposition into carbon; then, the carbon atoms react with oxygen coming from the ceria – based support, which is continuously replenished by the dissociation of H₂O [92]. In CeO₂ – ZrO₂ solid solutions, where the rate of oxygen transfer is greatly enhanced compared to CeO₂, this step is accelerated [90,91,92,93]. This is mainly ascribed to the synergism between ZrO₂, CeO₂ and the metal. ZrO₂ and the metal promote the reducibility of CeO₂ and therefore its oxygen storage capacity. The overall structure can be described as constituted by metal atoms at the top of the particles having a strong metallic character and behave as free metal particles. The metal present close to the surface support layers are strongly interacting with CeO₂ – ZrO₂. The reduced ceria sites in the solid solution produce active oxygen species by reacting with H₂O molecules. These species then react with the deposited carbon via oxygen spill-over from the support onto the metal. In addition, the high reducibility and Oxygen Storage Capacity (OSC) of CeO₂ – ZrO₂ provide highly mobile species via a redox cycle. This helps the oxidation of carbon through the participation of lattice oxygen which is then replenished by oxygen from H₂O.

In order to understand the oxygen mobility and storage capacity of CeO₂ and related mixed oxides in general, studies of isotopic exchange reactions have been developed [94]. On oxide – supported metals, ¹⁸O/¹⁶O exchange occurs through a sequence of well differentiated steps (Fig. 1.12):

- 1) dissociative adsorption of ¹⁸O₂ on the metal particle
- 2) transfer of ¹⁸O atoms from the metal to the support
- 3) surface migration of ¹⁸O atoms on the support

- 4) exchange of ^{18}O atoms with ^{16}O atoms of the surface
- 5) finally, every step i is coupled with step $-i$ corresponding to the reverse route for the exchanged species.

Depending on the reaction temperature, two other steps may be encountered:

- 6) internal (bulk) migration and exchange of ^{18}O with ^{16}O atoms of the support
- 7) direct exchange of $^{18}\text{O}_2(\text{g})$ with oxygen atoms of the support.

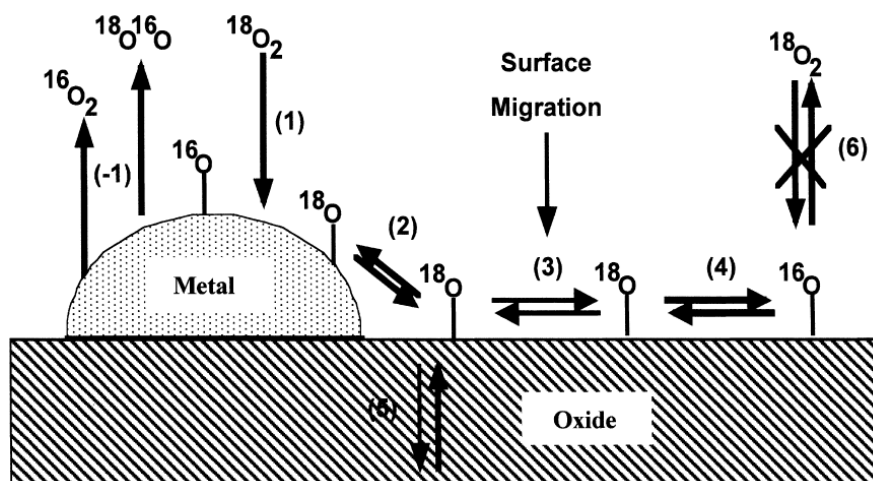


Fig. 1.12. Schematic of the isotopic exchange mechanism between $^{18}\text{O}_2(\text{g})$ and ^{16}O atoms (or ions) of an oxide-supported metal catalyst [94]

Menad et al. [95] have reported a study of comparison between different Ru – supported catalysts for dry reforming reaction, and they demonstrated how the specific $\text{Ce}_{0.5}\text{Zr}_{0.5}\text{O}_2$ phase show the highest oxygen mobility (Table 1.4), hence a very high stability of the catalyst during reaction time. Particularly they show how the synthesis method through which this support is obtained, the inverse microemulsion one, play an important role in the formation of the $\text{Ce}_{0.5}\text{Zr}_{0.5}\text{O}_2$ phase.

Oxide	$r_{\text{exchange}} (^{18}\text{O})$ [$\text{mmol g}^{-1} \text{s}^{-1}$]
SiO_2	8.91×10^{-8}
$\text{ZrO}_2 - 3.5\% \text{SiO}_2$	1.92×10^{-7}
ZrO_2 (WO)	1.04×10^{-6}
$\text{ZrO}_2 - 10\% \text{CeO}_2$	3.65×10^{-6}
Zr-Ce (WO) ($\text{Ce}_{0.5}\text{Zr}_{0.5}\text{O}_2$)	5.69×10^{-6}
CeO_2 (WO)	4.98×10^{-6}

Table 1.4. Rate of oxygen exchange of the different oxide supports. $T_{\text{exchange}} = 650^\circ\text{C}$. (WO = water-in-oil microemulsion) [Adapted from Ref. [95]]

This is a clear example from which is possible to understand how much is important the structure and the nature of a catalytic support in heterogeneous catalysis, therefore the synthesis method used to obtain the material has a crucial role on the global system.

In literature there are works [96,97,98,99] that review the use of the microemulsion method to obtain inorganic metal particles useful in the field of heterogeneous catalysis.

Microemulsion method for catalytic nanoparticles is of great interest since this system allows formation of particles in the nano-size range with narrow size distribution. Furthermore, by using the water-in-oil microemulsion route, it is possible, by varying for example the water-to-surfactant molar ratio (R_w), to influence the size of the reversed micelles and hence to control the particle size. Moreover, with the microemulsion method it is possible to control the composition of the nanoparticle in case of for example bimetallic particles, where the initial ratio of the metal precursor concentrations in the water cores of the micelles will correspond to the final composition of the particles obtained after reduction. When using microemulsions, the bimetallic particle can be formed at room temperature with a true alloy structure while conventional preparation methods usually require high temperatures which inherently will cause formation of large particles [96].

According to Schulman et al. [100], who introduced this term in 1959, a microemulsion media was formed on addition of an aliphatic alcohol (co-surfactant) to an ordinary emulsion. However, a three-component system consisting of oil, water and surfactant may analogously form microemulsions. Three factors characterize a microemulsion: transparency (optical isotropy), droplet size (6 to 80 nm) and stability (thermodynamic). There are three types of microemulsions: water-in-oil, oil-in-water and bi-continuous microemulsions. The synthesis of inorganic nanoparticles is usually carried out in water-in-oil microemulsions which consist of small aggregates (micelles) at the microscopic level. The water core of these aggregates is surrounded by the surfactant molecules which have the apolar part of their molecules towards the oil phase. In the water core of these aggregates, electrolytes may be solubilized, for instance metal salts. These metal salts will then be transformed into inorganic precipitates by using an appropriate reducing or precipitating agent. These agents can be directly added to the microemulsion containing the metal precursors, or first solubilized in a microemulsion similar to the one containing the metal precursor. The precipitating/reducing agent which will rapidly react with the metal precursors through the collision and coalescence between two aggregates containing the different reactants. The reaction (nucleation) will take place essentially at the same time in the microemulsion media which will favor the formation of a large number of nuclei inside the water cores of the micelles. These nuclei will grow through material exchange between micelles (particle growth) to give the final particle size [96].

On these bases is possible to understand clearly how in the study of Menad et al. [95] microemulsion was the most suitable preparation method in order to overcome the difficulties related to the formation of that specific $\text{CeO}_2 - \text{ZrO}_2$ phase with other classical synthesis method (precipitation, co – precipitation, sol – gel synthesis etc.). This difficulty come from the complexity characterizing the $\text{CeO}_2 - \text{ZrO}_2$ binary system.

Ivanova [101] reports an exhaustive study on the structure of CeO_2 and $\text{CeO}_2 - \text{ZrO}_2$ systems. A comparison between the ionic radii of cerium and zirconium ($r_{\text{Ce}^{4+}} = 0.88 \text{ \AA}$; $r_{\text{Zr}^{4+}} = 0.82 \text{ \AA}$) and the structural isomorphism of CeO_2 and ZrO_2 allow one to hypothesize that the introduction of zirconium into the structure of cerium dioxide will be accompanied by the formation of solid solutions. Indeed, it follows from a phase diagram [102] that three types of solid solutions (monoclinic – *m*, tetragonal – *t*, and cubic – *c*) are formed and stoichiometric compounds are absent from this system (Fig. 1.13(a)). According to a refined phase diagram [103] (Fig. 1.13(b)), a single phase region with monoclinic (*m*) symmetry occurs below 1273 K, where the mole fraction of CeO_2 is lower than 10%. Only a cubic (*c*) phase is formed at a CeO_2 content higher than 80%. The medium region of the $\text{CeO}_2 - \text{ZrO}_2$ phase diagram, where the greatest number of stable and metastable phases with tetragonal symmetry was observed, is most complicated and ambiguous [104, 105, 106]. According to published data [102] based on X-ray and Raman characteristics, three phases, *t*, *t'*, and *t''*, can be recognized. The stable *t* form results from the occurrence of diffusion processes; the formation of the metastable *t'* form is a consequence of diffusion changes, whereas the *t''* form occupies an intermediate position between *t'* and *c* forms. It is not tetragonal, and an oxygen shift with respect to the ideal fluorite structure occurs in it. The *t''* form is often referred to as cubic because, according to a diffraction pattern, it is indexed in the cubic structure with spatial symmetry *Fm3m* [107]. According to published data [103], the region of $\text{Ce}_{1-x}\text{Zr}_x\text{O}_2$ compositions in which this form occurs is broad ($0.1 - 0.2 < x < 0.30 - 0.35$). According to Vlăicet al. [108], it can be formed at a CeO_2 content of 50– 60 mol %. Thus, depending on the CeO_2 content, five modifications (one monoclinic, three tetragonal, and one cubic) can occur in the $\text{CeO}_2 - \text{ZrO}_2$ system.

Anyway, as also reported by Turko et al. [109], the occurrence of meta-stable phases in the medium part of the phase diagram essentially depends on the method of synthesis of mixed oxides and kinetic factors: the lability or inertness of the system.

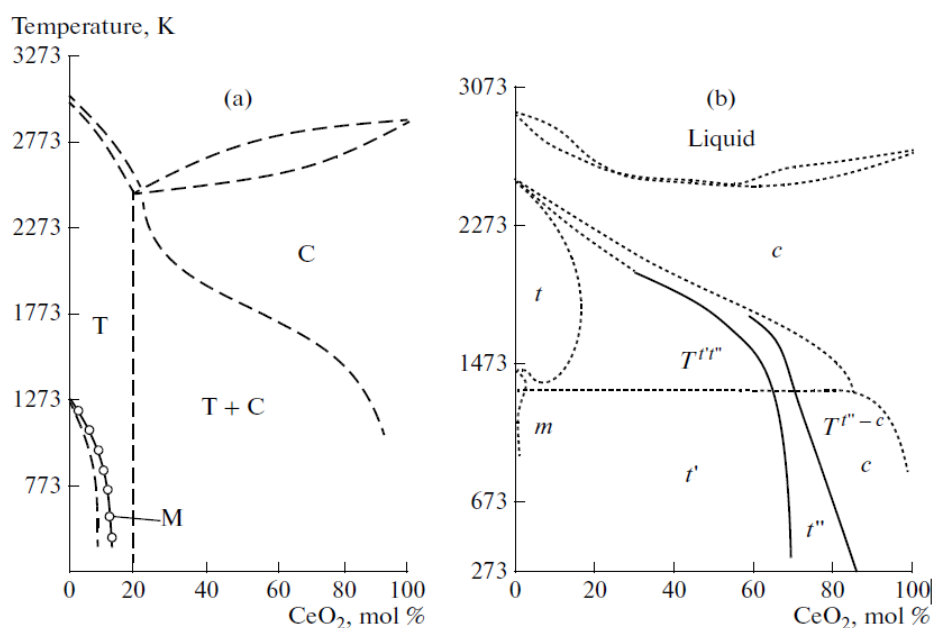


Fig. 1.13. Phase diagrams of the CeO₂-ZrO₂ system: data taken from (a) [102] and (b) [103]

A problem related to this kind of oxides is related to the reducible nature of CeO₂ which can lead to the occurrence of the so called Strong Metal Support Interaction (SMSI) effect. From a phenomenological point of view, the SMSI effect is characterized by a number of features which can be summarized as follows [110,111,112]:

1. it is associated with reducible supports;
2. it is induced by "high temperature", typically $T_{\text{redn}} \geq 723$ K, reduction treatments;
3. inherent to the onset of the SMSI state, the chemical properties of the dispersed metal phase are heavily disturbed: strong inhibition of its chemisorptive properties and significant changes in its catalytic behavior occur;
4. it is reversible, i.e., upon high-temperature re-oxidation ($T_{\text{reoxn}} \geq 723$ K) followed by a mild reduction treatment, the conventional behavior of the supported metal phase may be recovered.

The investigation of the SMSI is not easily observed through chemisorption. In fact, it is generally acknowledged that chemisorption techniques cannot be applied in the conventional way for characterizing M/CeO₂ catalysts [113,114,115,116,117,118]. Several reasons justify this statement. First, bare ceria can strongly chemisorb the most usual probe molecules like H₂ [119,120,121] or CO [122,123,124]. Second, it is known that, in the presence of highly dispersed active metal, at room temperature, large amounts of hydrogen can be transferred from the metal to the ceria support [116,117,118,125].

The metal support interaction phenomenon could be considered as a form of deactivation because the metal involved in these process become less available towards

the reactive species present on the surface of the catalyst, decreasing its activity. Even if these behavior have been extensively discussed, there are however some notable uncertainties about the precise nature of this interaction. Some authors [115,126,127,128,129] have suggested that metal/CeO₂ interactions are strongly involved in the SMSI effect. Their conclusion was mainly based on chemisorption at low temperature (- 80°C) and/or catalytic activity studies. In some cases [115], though metal decoration effects are suggested to occur, no direct proof of it could be provided. Moreover, the authors [115] acknowledge the existence of significant differences between their Rh/CeO₂ catalysts reduced at 773K and Rh/TiO₂ under SMSI state. Thus, no strong inhibition of the hydrogen chemisorption capability could be observed upon high temperature (773K) reduction [115]. This latter observation has also been reported for several different Rh/CeO₂ samples [118,130], as well as on Pt/CeO₂ catalysts [131], all of them reduced with H₂ at 773 K. In these latter cases [118,130,131], the occurrence of metal/support interaction phenomena other than the classic SMSI effect are suggested to occur. The same conclusion is arrived at in ref. [132].

The metal – support interactions are clearly dependent from the thermal treatments under that the catalysts is subjected before, during and after the reaction. Bernal et al. [133] reported that, to have available detailed information about the nano-structural evolution undergone by these catalysts when submitted to both reduction treatments at increasing temperatures, and different re-oxidation/re-reduction treatments aimed at regenerating the deactivated samples, is critically important to establish the occurrence and specific characteristics of the metal/support interaction phenomena they may exhibit. An interesting topic developed in their study [133] is the investigation of the relation between the metal particle size and the reduction temperature. They investigate the evolution with T_{red} of the metal particle size in a series of ceria-based catalysts. Data obtained for Rh and Pt catalysts supported on both pure CeO₂ and two mixed oxides have been included, and they briefly concluded that there are significant differences between the Rh and Pt catalysts, the former showing a better resistance against sintering. Likewise, the nature of the support, CeO₂, Ce_{0.80}Tb_{0.20}O_{2-x} or Ce_{0.68}Zr_{0.32}O_{2-x} does not seem to play a major role in the stabilization of the dispersed metal phase.

Another similar effect, related to the metal – support interactions phenomena is the so called decoration effect of the metal particle by the support. Through this phenomenon part of the metal surface is covered by the support which act in a sort of encapsulation of the metal particles, which is then less available for the surface reaction. This effect seem to be dependent from the temperature at which a CeO₂-based catalyst is subjected, for instance, during a reduction treatment. A lot of HREM studies have been

developed this aspect [118,134,135,136,137,138,139] but the maximum reduction temperature reached in these experiments is 773 K. Bernal et al. [140] investigate a larger range of reduction temperatures at those are subjected Rh/CeO₂ systems, reaching a temperature of 1173 K. They show, using the HREM investigation, that in the samples reduced at 973 and 1173 K are evident some significant differences in the microstructure of the metal crystallites. In these samples they observed some contrasts in the borders of the rhodium particles, the contours of which are less sharply defined. This can be interpreted as being due to the occurrence of some covering of the metal crystallites by a different phase. It has also been observed that the frequency of the decorated rhodium crystallites is much higher in the case of the catalyst reduced at 1173 K. An approximate statistical analysis suggests that no more than 30% of the metal particles appear decorated in the case of the catalyst reduced at 973 K, whereas over 90% of rhodium is covered in the case of the sample reduced at the highest temperature. The analysis of the ensemble of micrographs recorded for high temperature reduced catalysts also suggests that for the sample reduced at 1173 K the phase covering the metal particles is thicker and more crystalline. From all this evidence, they conclude that the onset of the decoration effect must occur at reduction temperatures close to 973 K [140].

1.2.2.2 Carbon formation on reforming catalysts

Deactivation of supported metal catalysts by carbon or coke formation is a problem of serious magnitude in steam reforming. Its causes are generally threefold:

1. fouling of the metal surface;
2. blockage of catalysts pores and voids;
3. actual physical disintegration of the catalyst support.

Carbon may chemisorb strongly, as a monolayer, or physically adsorb in multilayers and, in either case, block access of reactants to metal surface sites. Furthermore, carbon may totally encapsulate a metal particle, and thereby completely deactivate that particle, and plug micro- and macropores such that access of reactants is denied to many crystallites inside these pores. Finally, in extreme cases, strong carbon filaments may build-up in pores to the extent that they stress and fracture the support material, ultimately causing disintegration of catalyst pellets and plugging of reactor voids [141].

Carbon is a product of CO disproportionation while coke is produced by decomposition or condensation of hydrocarbon on metals. Nevertheless, coke forms may vary from high molecular weight hydrocarbons such as condensed polyaromatics to carbon such as graphite, depending upon the conditions under which the coke was formed and aged (Fig. 1.14).

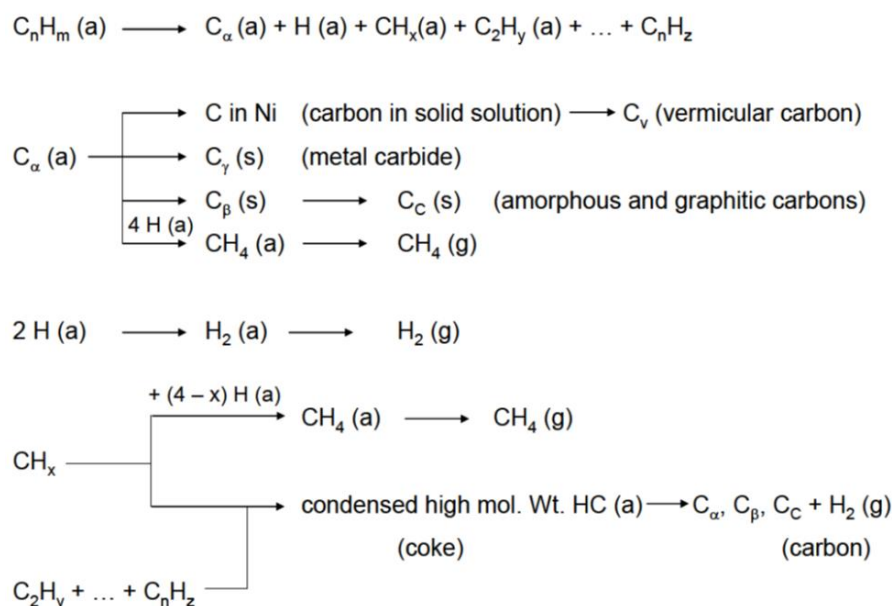


Fig. 1.14. Formation, gasification and transformation of coke and carbons on metal surfaces from hydrocarbons (a= adsorbed, g= gaseous, s= solid)

As reported by Bartholomew [142] three different kinds of carbon or coke species are observed in steam reforming (Table 1.5):

1. whiskers like carbon formed at temperature greater than 450°C;
2. encapsulating hydrocarbon films formed by polymerization at less than 500°C;
3. pyrolytic carbon from cracking of hydrocarbon above 600°C.

	Whisker like	Encapsulated film	Pyrolytic carbon
Formation	Diffusion of C through Ni crystal, nucleation and whisker growth with Ni crystal at the top	Slow polymerization of C _n H _m radicals on Ni surface into encapsulating film	Thermal cracking of hydrocarbon. Deposition of C precursors on catalyst
Temperature Range	> 450°C	< 500°C	> 600°C
Critical Parameters	High T Low H ₂ O/C _n H _m ratio No enhanced H ₂ O adsorption Low activity Aromatic feed	Low T Low H ₂ O/C _n H _m ratio Low H ₂ /C _n H _m ratio Aromatic feed	High T High void fraction Low H ₂ O/C _n H _m ratio High P Acidity of catalyst

Table 1.5. Carbon species formed in steam reforming of hydrocarbons [Adapted from Ref. [142]]

Formation of carbon deposits via CO decomposition (Fig. 1.15) may involve the production and transformation of various carbon forms, adsorbed atomic carbon (C_α), amorphous carbon (C_β), vermicular carbon (C_v), bulk nickel carbide (C_v) and crystalline, graphitic carbon (C_c), the structural reactivities of which are summarized in Table 1.6. The presence of dispersed or atomic carbon, stable below 325°C, which can be also surface nickel carbide, and polymerized carbon stable above 325°C was confirmed. Nickel carbide can be easily removed by H₂ at the same temperature.

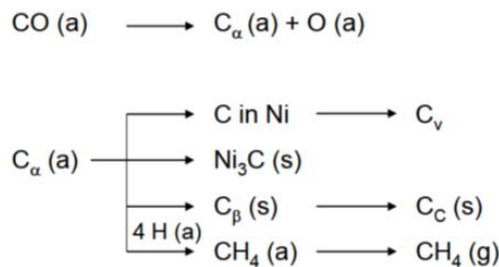


Fig. 1.15. Formation, gasification and transformation of carbon on nickel from carbon monoxide (a= adsorbed, g = gaseous, s = solid)

Structural type	Designation	Temperature formed	Peak temperature for reaction with H ₂
Adsorbed, atomic (dispersed, surface carbide)	C _α	200 – 400°C	200°C
Polymeric , amorphous films or filaments	C _β	250 – 500°C	400°C
Vermicular (polymeric, amorphous) a. filaments b. fibers c. whiskers	C _ν	300 – 1000°C	400 – 600°C
Nickel carbide (bulk)	C _γ	150 – 250°C	275°C
Graphitic (crystalline) a. platelets b. films	C _δ	500°C 550°C	550 – 850°C

Table 1.6. Forms and reactivities of carbon species formed by decomposition of CO on nickel [Adapted from Ref. [142]]

Deactivation of steam reforming catalysts at high temperature (500-900°C) may be caused by precipitation of atomic (carbide) carbon dissolved in the Ni surface layers to a depth of more than 50-70nm. If it accumulates on the metal surface, at high or low temperatures, adsorbed atomic carbon can deactivate metal sites for adsorption and/or reaction [141]. In the intermediate temperature range of 375-650°C, carbon filaments are formed by precipitation of dissolved carbon at the edge of metal crystallites causing the metal particles to grow away from the support. Filament growth stops when sufficient carbon accumulates on the free surface to cause encapsulation by a carbon layer; however, encapsulation of the metal particles does not occur if H₂/CO or H₂O/hydrocarbon ratios are sufficiently high. Thus, carbon filaments sometimes formed in CO hydrogenation or steam reforming of hydrocarbons would not necessarily cause a loss of intrinsic catalyst activity unless they are formed in sufficient amount to cause plugging of the pores or loss of metal which occurs as the carbon fibers are removed during regeneration.

A fundamental principle for coke insensitive reactions on metals (in which relatively reactive coke precursors formed on active sites are readily removed by hydrogen or other gasifying agents) is that deactivation rate, described by the equation (20) depends greatly on the difference in rate of formation and gasification of carbon/coke precursors:

$$r_d = r_f - r_g \quad (20)$$

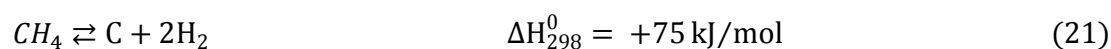
If the rate of gasification, r_g , is equal to or greater than that of formation, r_f , carbon/coke is not deposited. Rates of carbon/coke precursor formation and gasification

both increase exponentially with temperature, although the difference between them varies a great deal with temperature because of differences in pre-exponential factors and activation energies. Thus, carbon/coke formation is avoided in region of temperature in which precursor gasification rate exceeds deposition rate.

The rate at which carbon or coke is accumulated in a given reaction under given conditions can vary significantly with catalyst structure, including metal type, metal crystallite size, promoter, and catalyst support. For example, Co, Fe and Ni are active above 350 – 400°C for filamentous carbon formation from CO and hydrocarbons. Pt, Ru and Rh catalysts, on the other hand, while equally or more active than Ni, Co, or Fe in steam reforming produce little or no coke or carbon. This is attributed to reduced mobility and/or solubility of carbon in the noble metals, thus retarding the nucleation process. Thus, it is not surprising that addition of noble metals to base metals retards carbon formation; for example, addition of Pt in Ni lowers carbon deposition rate during methanation, while addition of Cu to Ni substantially lowers carbon formation in steam reforming [141].

Four reactions ((21), (22), (23), (24)) may be involved in carbon formation process:

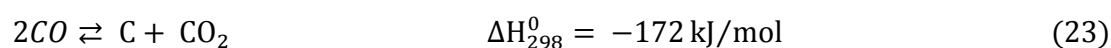
1. Thermal cracking or decomposition of methane:



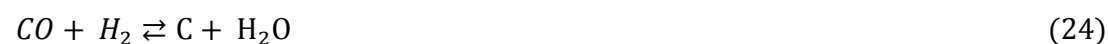
2. Thermal cracking or decomposition of hydrocarbons:



3. CO disproportionation (Boudouard reaction):



4. CO reduction:



The reduction or elimination of coke formation often results in constraints on the operating conditions to be applied. Steam and hydrogen are the most important retarding reactants. In steam reformers, carbon will be formed below a certain steam to carbon ratio which means that in many cases the steam reformer has to operate with a surplus of steam and, hence that a larger reformer is required. When using a catalyst with enhanced steam adsorption, the critical steam to carbon ratio can be reduced. This can be obtained by adding alkali to the catalyst or using active magnesia as support. In tubular reforming, no carbon is accepted because of the break-down of the catalyst will result in buildup of

pressure drop with uneven flow distribution and hot spots. The progressive deactivation can be followed by the movement of temperature profile of the catalytic bed.

Regeneration of coke deposits can be carried out in various ways depending on the reactivity of the coke. For example, the encapsulating deposits which cause deactivation of the nickel based catalysts can be removed by treatment in hydrogen at 500°C depending on the age of the carbon. Newly formed carbon in tubular steam reformers can be removed by increasing the S/C ratio or by steaming of the catalyst. However, aged coke deposits require regeneration by means of air. At sufficiently high temperatures (typically above 500°C), the regeneration process becomes limited by the diffusion of the oxygen through the carbon free pores as the burn-off progresses after a core/shell mechanism. If the carbon is highly reactive, the regeneration may easily become heat transfer limited meaning that the temperature of the catalyst pellet may be heated up to a temperature corresponding to the adiabatic temperature increase of the combustion process. In the case of a metal catalyst, the metallic phase will also be oxidized. Therefore, in many cases it is necessary to carry out the regeneration with controlled addition of air to nitrogen or steam [143].

The formation of carbon is very dependent on the system pressure. It is known that if one operates these reforming reactions at elevated pressures (≈ 12 atm), dramatic increases in the rates of coke formation are observed over most types of Ni based catalysts. Formation of carbon on a catalyst can be difficult to follow at elevated pressure running in continuous mode [144].

Carbon formation may also have an effect on construction materials. Pyrolytic coke deposited on the tube walls may lead to harmful carburization of the high alloy steel tubes. A critical phenomenon is metal dusting corrosion, which may take place if a CO-containing process gas is cooled below the equilibrium temperature of the CO-decomposition reaction. The resulting carbon will typically react with the steel forming iron carbide which will decompose and fall off leaving the construction material with heavy pitting [143].

1.2.2.3 Sintering of Steam Reforming catalysts

Sintering processes generally take place at high reaction temperatures ($> 500^{\circ}\text{C}$) and are generally accelerated by water vapor. Sintering of heterogeneous catalysts is often referred to as the loss of catalytic surface area due to growth of large particles at the expense of smaller particles. Sintering is complex and may be influenced by many parameters such as sintering time, temperature, chemical environment, catalyst composition and structure, and support morphology.

Bartholomew [141] reported three many phenomena that are induced during the catalyst deactivation induced by sintering:

- loss of catalytic surface area due to crystallite growth of the catalytic phase;
- loss of support area due to support collapse and of catalytic surface area due to pore; collapse on crystallites of the active phase,
- chemical transformations of catalytic phases to non-catalytic phases.

The most important parameters are the sintering temperature and the composition of the gas over the catalyst. Increasing temperature and the presence of steam accelerates the sintering process. High surface areas of the carrier, on the other hand, increase the stability toward sintering.

Three mechanisms for the metal particle growth have been proposed [141]:

- particle migration, where entire crystallites migrate over the support followed by coalescence;
- Ostwald ripening (atom migration), where metal atoms emitted from one crystallite migrate over the support and are captured by another crystallite;
- vapor transport between particles (at high temperatures).

In Fig. 1.16 are schematically represented two of these mechanism.

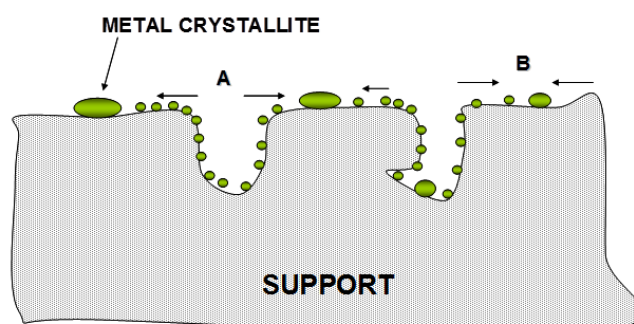


Fig. 1.16. Two conceptual models for crystallite growth due to sintering by (A) atomic migration or (B) crystallite migration [141]

The crystallite migration model postulates that metal crystallites migrate as entities along the surface of the support. Rapid diffusion of metal atoms on the surface of a metal crystallite will cause metal atoms to accumulate on one side of the crystallite by random fluctuations. This rapid, random surface diffusion will cause Brownian type motion of the particles on the support [145]. If appreciable particle migration occurs, it is restricted to metal crystallites smaller than 50 Å in diameter [145]. The model presented by Ruckenstein and Pulvermacher [as cited in [145]] is hence restricted to the early stages of sintering when crystallites are < 50 Å in size. Two limiting cases of the crystallite migration model were developed: (1) Surface diffusion controlled (i.e. the rate of migration of crystallites is the rate determining process) and (2) Sintering controlled (i.e. the merging of two metal crystallites coming into physical contact by collision is the rate-determining process).

As also reported by the studies of Campbell [146], the heat of adsorption of metal atoms to metal particles depends more strongly on the particle size than assumed previously leading to faster rates of sintering via both Ostwald ripening and particle migration and coalescence. This phenomenon is most important for small particles (diameter < 50 Å for Pb particles). A nickel particle with a diameter of approximately 36 Å contains the same number of atoms as a Pb particle with a diameter of 50 Å due to the size difference of the atoms [146]. Sehested [147] sustained that the nickel particles are generally larger than this particle size. The smallest average nickel particle diameters estimated from the nickel surface areas in the catalysts used are of the order of 75–90 Å, indicating that the effect of fast sintering of small particles can be ignored. On the contrary, ASAXS (anomalous small angle X-ray scattering) gives lower estimates of the nickel particle diameters, indicating that sintering of small particles is significant.

The atom migration model [145] envisages sintering to occur as a three-step process:

1. Escape of metal atoms or molecules such as metal oxides from the metal crystallite to the support surface;
2. Migration of these atoms along the support surface;
3. Capture of these migrating atoms by metal crystallites upon collision of these migrating atoms with stationary metal crystallites.

These processes result in the growth of the large metal crystallites and in a decrease in size of the small metal crystallites since the rate of loss of atoms is smaller than the rate of capture for large crystallites, while for small crystallites the rate of loss is greater than the rate of capture. This occurs because large crystallites are in equilibrium with a

lower concentration of migrating atoms than small crystallites (this is the two-dimensional analogy of Ostwald ripening).

Depending upon reaction or re-dispersion conditions, a few or all of the processes listed below maybe important; thus, the complexity of sintering/re-dispersion process is emphasized:

1. dissociation and emission of metal atoms or metal-containing molecules from metal crystallites;
2. adsorption and trapping of metal atoms or metal-containing molecules on the support surface;
3. diffusion of metal crystallites across support surfaces;
4. metal or metal oxide particle spreading;
5. support surface wetting by metal or metal oxide particle;
6. metal particle nucleation;
7. coalescence of, or bridging between, two metal particles;
8. capture of atoms or molecules by metal particles;
9. liquid formation;
10. metal volatilization through volatile compound formation;
11. splitting of crystallites in O₂ atmosphere due to formation of oxides of a different specific volume;
12. metal atom vaporization.

A simple expression (25) for the development of the nickel surface area as a function of time, temperature, nickel loading, and carrier surface area is recently derived by Sehested [148]. To obtain the expression it was assumed that the sintering mechanism was particle migration and coalescence, that the particle sizes were log normally distributed with constant relative standard deviation, and that the carrier acted only as an area dispersing the metal particles.

$$A_{Ni} = \pi c_{cat} d_{Ni}^2 = const. X_{Ni} d_{Ni}^{-1} \approx const. \frac{X_{Ni}^{0.86} (1 - X_{Ni})^{0.14} A_{car}^{0.14}}{K_1^{0.14} D_{Ni}^{0.14} t^{0.14}} \quad (25)$$

where:

A_{Ni} = nickel surface area

c_{cat} = number of particles per gram of catalyst

d_{Ni} = number averaged particle diameter

X_{Ni} = fractional mass of nickel (g metal/g catalyst)

A_{car} = surface area of the carrier (m^2/g of the carrier)

K_1 = equilibrium constant for the reaction: $Ni_{(111)} + Ni_{(bulk)} \rightleftharpoons Ni \text{ add-atom on } Ni_{(111)}$

D_{Ni} = diffusion coefficient of an add-atom on a Ni surface

t = time

The expression included a parameter, which depends on the atmosphere over the catalyst and the chemical environment on the catalyst. It was investigated experimentally and theoretically the effects of steam and hydrogen over nickel catalysts as a function of temperature. The relative nickel areas of Al_2O_3 and $MgAl_2O_4$ -supported nickel catalysts are determined after sintering at 1, 31, and 40 bar total pressure at various steam and hydrogen ratios. The increased rate of sintering in the presence of steam is attributed to formation of Ni_2-OH species at the surface of nickel particles. The energy of formation of this species at the nickel surface is low, compared to that of nickel atoms while the energy of diffusion is highest for the Ni_2-OH complex. It was concluded that, in the presence of steam and hydrogen, the surface transport at nickel particles will be dominated by Ni_2-OH dimers.

Sintering of the support may also occur. Single-phase oxide carriers sinter by one or more of the following processes:

1. surface diffusion;
2. solid-state diffusion;
3. evaporation/condensation of volatile atoms or molecules;
4. grain boundary diffusion;
5. phase transformation

Dispersed metals, in supported metal catalysts, can also accelerate support sintering, for example, dispersed nickel accelerates the loss of Al_2O_3 surface area in Ni/Al_2O_3 catalysts [141].

In general, sintering processes are kinetically slow at moderate reaction temperature and irreversible or difficult to reverse. Thus, sintering is more easily prevented than cured [149]. Temperature, atmosphere, metal type, metal dispersion, promoters/impurities and support surface area texture and porosity, are the principal parameters affecting rates of sintering. Sintering rates increase exponentially with temperature. Metals sinter relatively rapidly in oxygen and relatively slowly in hydrogen, although depending upon the support. Water also increases the sintering rate of supported metals. In reducing atmosphere, metal crystallite stability generally decreases with decreasing metal melting temperature,

in the order: Ru>Ir>Rh>Pt>Pd>Ni>Cu>Ag, although this order may be affected by relatively stronger metal–support interactions (SMSI).

1.2.3 Practical aspects of Steam Reformer unit plant

A typical design for a SMR reactor and a scheme for the whole process of hydrogen production are presented in Fig. 1.17. For this type of endothermic process, the catalyst is usually loaded into a number of tubes and placed inside of a furnace. There are several factors that are of fundamental importance in the reformer design: i.e., the geometry and number of single reformers; the heat transfer from the burners to the reforming units; and the catalyst design, including its intrinsic activity and physical properties (size, form, etc.) [150].

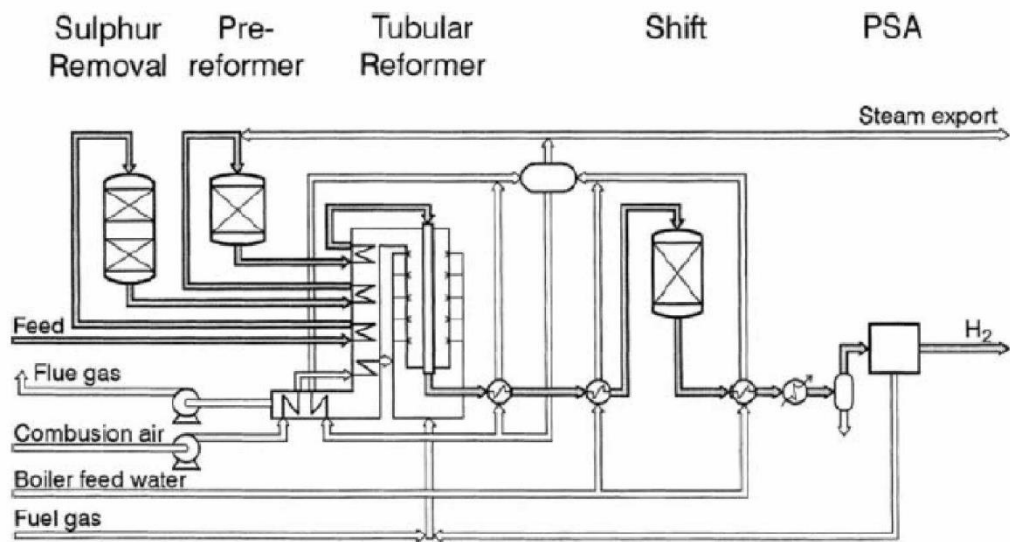


Fig. 1.17. Typical process layout for a hydrogen plant based on advanced tubular steam reforming technology [150]

The primary reformer consists essentially of two main sections: the furnace, containing the tubes charged with the catalyst, and the convection section, where heat is recovered from the flue gas by such duties as preheating feedstock, process air and/or combustion air, boiler feed-water heating and steam raising, and super heating.

The steam reforming reactions are usually carried out at a pressure up to 35 bar and temperatures of 800°C or higher, while the flue gas may reach a temperature in excess of 1000°C. Four main configurations (Fig. 1.18) could be adopted for the construction of the most suitable furnace required:

1. Top – fire;
2. Terrace wall – fire or side – fire;
3. Bottom – fire (in the case of small H₂ plants)

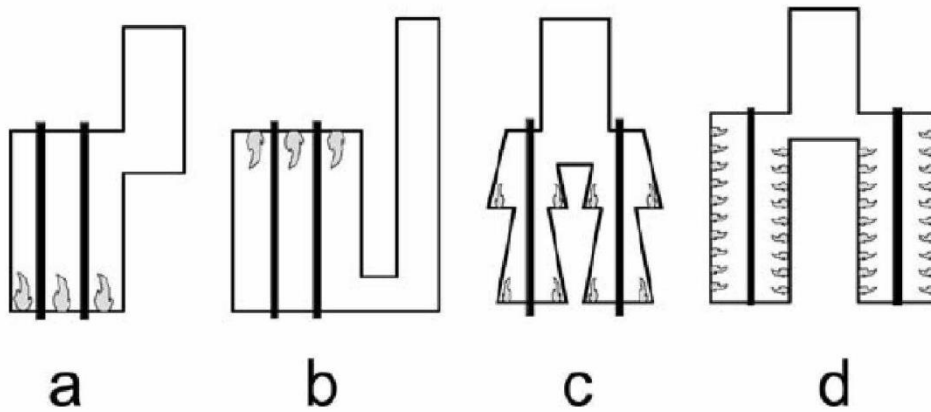


Fig. 1.18. Typical configurations of reformer furnaces: a) bottom fired, b) top fired, c) terrace wall, d) side fired [150]

Typical throughput, which is usually expressed as the amount of steam plus feedstock per hour per liter of catalyst, is in the range $2 - 7 \text{ Kg h}^{-1}\text{L}^{-1}$. The overall length of reformer tubes is usually in the range 7.5–12.0m although the heated charged length may be up to 9.0m; tube diameter usually lies between 7cm and 13cm. The number of tubes depends on output, and for a large reformer there may be as many as 650 tubes [65].

In operation, there is a gradation of temperature longitudinally from the inlet to the outlet of the tube, as well as radially across the wall of the tube. Creep occurs with time at normal operating conditions. The temperature which the tube wall experiences depends on the distribution of heat input and the heat adsorbed by the reaction taking place on the catalyst in the tubes. Uneven heat input uneven catalyst activity caused by uneven packing or catalyst poisoning will cause local overheating, resulting in excessive creep in that location, which will hasten tube rupture. Normally reformers are designed with a tube life of about 10 years using creep strength data based on creep-rupture tests of varying duration available from a number of sources [65]. The higher the temperature and pressure are, the greater the creep and the shorter the tube life. This applies to all parts of each tube, and if part of any tube is subjected consistently to higher-than-average temperatures, it will fail prematurely. It is therefore important that hot spots, due to catalyst poisoning or carbon deposition, are removed as soon as possible.

The life of a catalyst can be affected by several factors:

- a. catalyst breakdown;
- b. tube blockage;
- c. overheating of the catalyst;
- d. poisoning of the catalyst;
- e. thermal ageing.

Catalyst breakage and blockage of the tubes causes an increased pressure drop across the reformer. More fundamentally, it can lead to overheating of the catalyst, loss of activity and a reduction of throughput. All of these effects may be caused by the deposition of carbon. Overheating of the catalyst can also be caused by a not optimal reformer operation. Loss of activity through poisoning by contaminants in the process gas is important, since this can cause carbon deposition and result in overheating, catalyst breakage and, in extreme cases, even partial blocking of the tubes. Gradual loss of activity or thermal ageing caused by progressive loss of nickel surface area through sintering places a limit on the life of a catalyst charge, and for a particular catalyst, this depends on the actual operating conditions. In practice, the most important effects are catalyst sintering, catalyst poisons and carbon formation. Carbon can be deposited in primary reforming catalyst by different mechanisms and to varying degrees. Complete loss of reaction steam results in a massive deposit of carbon, and the reformer will develop a very large pressure drop within a few seconds. It will not then be possible to run the reformer again without replacing the catalyst. Running a reformer with a slightly deficient steam/carbon ratio will result in slight carbon deposition, which will slowly increase the reformer pressure drop, and the tubes will appear hotter than normal. If detected soon enough this carbon can often be removed satisfactorily, but this depends on the type of catalyst being employed. The hydrogen will keep the catalyst in a reduced form. When the carbon has been deposited within the catalyst pores by carbon monoxide disproportionation, steaming will increase the reformer pressure drop. In this case, the carbon expands within the catalyst pores and cracks the pellet and, although the carbon in situ retains the pellet strength, when the carbon is removed, the pellet collapses. If this happens, it is necessary to change the catalyst [65].

Slow deposition of carbon can occur for a number of reasons. Careful catalyst formulation is essential to maximize selectivity, and to eliminate acid sites, which can promote carbon formation. When a predominantly methane feedstock is reformed, low catalyst activity in the inlet portion of the tube can lead to carbon deposition, which restricts heat transfer and give rise to the phenomenon known as "hot bands". "Hot bands" always form at about the same position on all tubes in the furnace and approximately the same position in all reforming furnaces. As expected, heavily loaded top-fired furnaces are the most susceptible to forming "hot bands". The low catalyst activity can arise from a number of causes – catalyst may be old and at the end of its useful life, it may be poisoned or inadequately reduced. If no hydrogen is recycled with the feedstock, then the catalyst in the inlet portion remains in the oxidized state until reforming or cracking of the feedstock occurs, and produces some hydrogen. This

increases the load on the catalyst further down the tube, since the inlet portion is then functioning simply as a heat exchanger. Further, if reformer conditions change, then unreduced catalyst may be called upon to do some reforming. It will be unable to do so, carbon will be deposited and hot areas will appear at the top of the tubes.

1.3 Catalytic Partial Oxidation (CPO) Process

In the 1940s, Prettre et al first reported the formation of synthesis gas by the catalytic partial oxidation of CH₄ (reaction (3)) using a Ni – based catalyst.

In contrast to steam reforming of methane, methane partial oxidation is exothermic. However, the partial oxidation requires pure oxygen, which is produced in expensive air separation units that are responsible for up to 40% of the cost of a synthesis gas plant [151].

Several papers [149,152,153,154,155] reported that one can reach CO and H₂ concentrations in excess of those expected at thermodynamic equilibrium by operating the CH₄ oxidation reaction at exceptionally high space velocities (GHSV = 52,000 ml(g_{catalyst})⁻¹h⁻¹ in a fixed-bed reactor, employing different types of catalysts: Ni/Yb₂O₃, Co/rare earth oxide, Co/MgO, and Ni/Al₂O₃. According to the partial oxidation reaction, such a process yields the desired H₂/CO molar ratio of 2 required for methanol or Fischer-Tropsch synthesis.

From thermodynamic simulations, it is clear that the reaction is favored at T > 850°C in excess of CH₄, although both CO and H₂ selectivities are modified by the formation of CO₂ and H₂O in combustion reactions of CH₄ ((26), (27)) which are much more exothermic:



The actual reaction temperatures could be much higher than those reported. By using an optical pyrometer, it was found that, during the catalytic oxidation of methane to CO and H₂, the combination of a high space velocity, an exothermic reaction, and an active catalyst (Ni/Yb₂O₃) gave rise to steep temperature gradients (hot spots). Furthermore, the temperature of the hot spot was greater by as much as 370°C than the temperature measured with a thermocouple located at a distance of only 1 mm from the hot spot in the catalyst bed. If a temperature lower than that of the hot spot is used to calculate the equilibrium concentrations of CH₄, CO, CO₂, and H₂, one can draw the conclusion that the concentrations of CO and H₂ exceeded their thermodynamic equilibrium values. However, if the true maximum (hot spot) temperature is used in the calculation, the observed concentrations are found to be somewhat less than those predicted at equilibrium. Indeed, using a careful temperature measurement method, in which a thermocouple end contacted just the top surface of the catalyst bed, it was found

that the CH_4 conversion in the presence of $\text{Ni}/\text{Al}_2\text{O}_3$ catalyst was less than that predicted by thermodynamic equilibrium.

Hu and Ruckenstein [156] show how the temperature profile along the catalytic bed in CPO process is of a fundamental importance and also how, in some cases, it is related to the synergetic effects that can occur between support and the active phase. They observed hot layers (thinner than 1mm) in NiO/MgO solid solution catalysts and in $\text{NiO}/\text{Al}_2\text{O}_3$ and NiO/SiO_2 catalysts during the partial oxidation of methane in a fixed-bed reactor. The hottest layers were located at the top of the bed of the NiO/MgO and $\text{NiO}/\text{Al}_2\text{O}_3$ catalysts, but they were observed to move down and then up for the NiO/SiO_2 catalyst bed. The down-and-up movement resulted in an oscillatory temperature of the NiO/SiO_2 catalyst at a given position in the bed, which was absent when the catalyst was NiO/MgO or $\text{NiO}/\text{Al}_2\text{O}_3$. The different temperature behaviors of the three catalysts were attributed to the different strengths of the interactions between the metal oxide and the support. Temperature – programmed – reduction (TPR) experiments indicated that the initial reduction temperature was about 330°C for 13.6wt% NiO/SiO_2 , which is near that of pure NiO (about 300°C). In contrast, for 13.6wt% $\text{NiO}/\text{Al}_2\text{O}_3$ the initial reduction temperature was high (670°C) and no marked reduction peak could be detected even at 800°C for 13.6wt% NiO/MgO . These results clearly indicate that there are weak interactions between NiO and SiO_2 and much stronger interactions between NiO and Al_2O_3 and between NiO and MgO . The weak interactions in Ni/SiO_2 might have been responsible for the temperature oscillation by allowing a facile redox behavior of the active nickel sites, namely, the oxidation of Ni^0 to NiO by O_2 and the reduction of NiO to Ni^0 by CH_4 . In the case of NiO/SiO_2 , according to this interpretation, the freshly reduced NiO located at the inlet of the bed became highly active, causing a hot layer to be generated. The high temperature of this hot layer resulted in sintering of the nickel particles, which led to the loss of activity. Therefore, the reaction is inferred to have taken place in the neighboring section of the catalyst. As a result, a hot layer propagated downward in the reactor. However, the sintered nickel particles were re-dispersed on the SiO_2 support when they were re-oxidized by O_2 , because the oxygen concentration is high when the reaction of CH_4 with O_2 does not take place. After a certain time, the re-oxidized layer near the entrance was again reduced by CH_4 and became active again, resulting in a hot layer. The following part of re-oxidized nickel on SiO_2 can be reduced rapidly by H_2 and CO generated near the entrance of the reactor. The redox of the Ni/SiO_2 catalyst constitutes a cycle of deactivation and reactivation in each part of the catalyst. The hot layer moved downward in the bed during the time required for

the reduction of the entrance layer. Consequently, the time scale of the oscillations was determined by the time scale of the reduction–oxidation process.

Furthermore, Basile et al. [157] used IR thermography to monitor the surface temperature of the nickel foil during the methane partial oxidation reaction by following its changes with the residence time and reactant concentration. Their results demonstrate that the surface temperature profile was strongly dependent on the catalyst composition and the tendency of nickel to be oxidized in the first part of the bed can change the overall temperature profile.

The employment of noble metals has been also investigated. In 1992, Hickman and Schmidt [158] used platinum monoliths to achieve high selectivity to CO and H₂ in the partial oxidation of methane. In the following ten years, various noble metal catalysts have been examined. Compared with the non-noble metal catalysts, the noble metals exhibit high stability with excellent activity and selectivity. The major drawback of the noble metal catalysts is their high cost, which restricts their potential use in industrial processes.

Numerous attempts have been made to understand the mechanism of the partial oxidation of methane. Mechanistic investigations of the partial oxidation are still challenging, because this exothermic reaction is very fast and causes extremely high catalyst temperature rises, so that the usual methods of investigation are unsuitable.

Two kinds of pathways have been suggested:

1. a combustion – reforming pathway, schematically represented in Fig. 1.19 in which CO₂ and H₂O are the primary products, and CO and H₂ are formed by their reactions with CH₄;
2. a pyrolysis or dissociative adsorption pathway, in which CO is the primary product formed by the dissociation of methane, $\text{CH}_4 \rightarrow \text{CH}_x + (2 - 1/2x) \text{H}_2$; followed by the oxidation of carbon containing species to give CO without the pre-formation of CO₂.

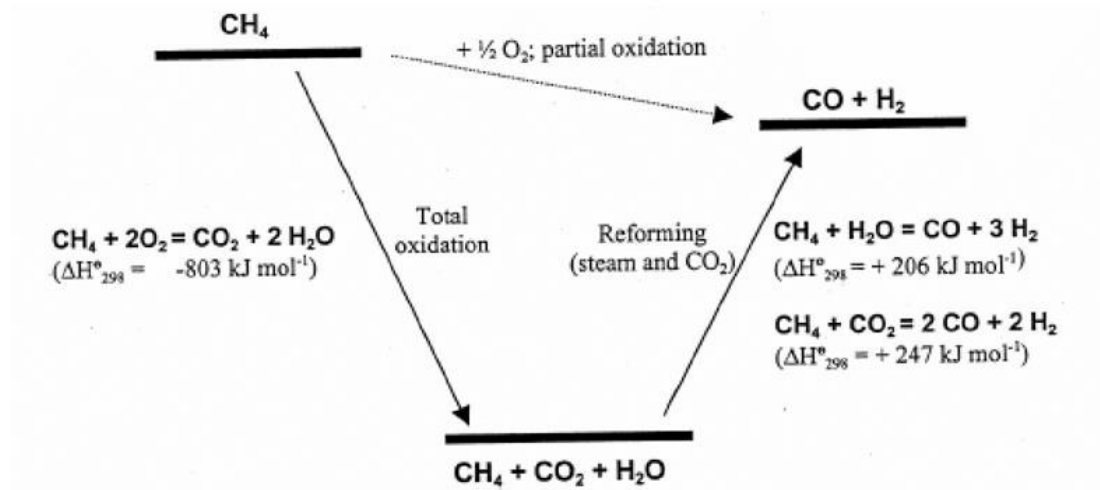


Fig. 1.19. Thermodynamic representation of the partial oxidation of methane following combustion – reforming pathway

This process is likely to become more important in the future of methane conversion due to the thermodynamic advantages which has over steam reforming that can summed up as follows:

1. partial oxidation is mildly exothermic, while steam reforming is highly endothermic. Thus, a partial oxidation reactor would be more economical to heat. In addition, it can be combined with endothermic reactions, such as steam reforming or dry reforming with carbon dioxide to make these processes more energy efficient;
2. the H₂/CO ratio produced in stoichiometric partial oxidation is around 2, and this ratio is ideal for downstream processes, in particular methanol and FT synthesis. This avoids the need to reverse shift hydrogen, which is produced in excess in steam reforming;
3. the product gases from methane partial oxidation can be extremely low in carbon dioxide content, which must often be removed before synthesis gas can be used downstream;
4. partial oxidation technology avoids the need for large amounts of expensive superheated steam. However, an oxygen separation plant, which is also costly, may be required in cases where nitrogen (from air) is undesirable in high-pressure downstream processes.

1.4 Autothermal Reforming (ATR)

Autothermal reforming (ATR) is a combination of partial oxidation (POX) and steam reforming (SR) technologies.

This process was developed by HaldorTopsoe in the late 1950s with the aim of performing reforming in a single reactor. In autothermal reforming, the energy for the production of CO and H₂ is produced by partial oxidation of the hydrocarbon feedstock. Like POX, the feeds first react in a large refractory lined vessel with O₂ for non-catalytic combustion at 1200-1250°C.

The reformer basically (Fig. 1.20) consists of a ceramic lined tube and a fixed catalyst bed for equilibration of the gas. The preheated streams (CH₄ + H₂O and H₂O + O₂) are mixed in burner placed at the top where the POX reactions take place. The final steam reforming and equilibration take place in the catalyst bed below the burner. Typically, the ATR operates at high temperatures ca. 1200-1300°C in the combustion zone and 950-1200°C in the catalytic zone. These results in lower oxygen consumption (O₂/CH₄=0.55-0.60), however, with a certain amount of steam added to the feedstock to eliminate carbon formation.

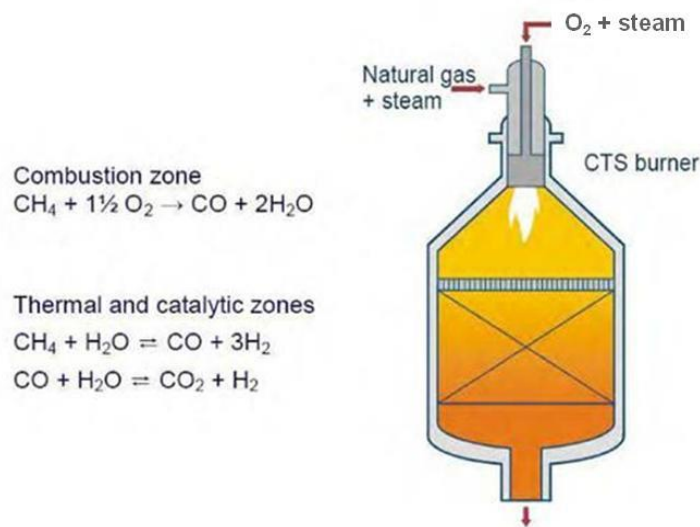


Fig. 1.20. Scheme of an autothermal reformer and reactions that take place in the two different zones inside the reformer

1.5 Aim of the work

As already mentioned in the paragraph 1.1.5, the present work is a continuation of the work of Barbera [44] developed into the NextGTL European project. Barbera developed a part of the purposes characterizing the Line 1 (paragraph 1.1.5 and Fig. 1.21) of the global European project. This research line proposed new process architecture, schematized in, to produce syngas from methane partial oxidation where reaction steps are integrated with different types of membranes for O₂, H₂ and CO₂ separation.

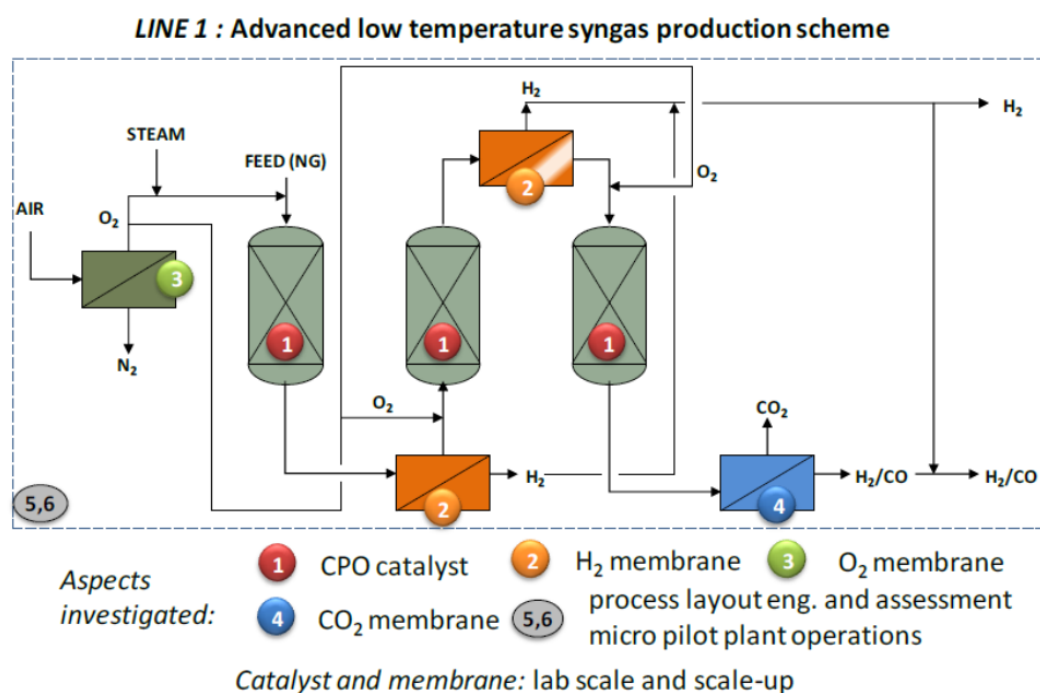


Fig. 1.21. Conceptual scheme of the proposed advanced syngas production [44]

According to the US DOE financing a large project on OTM (oxygen transport membranes), a reduction of 30% of costs is to be expected, based on such a design. The use of membrane reactors allows enhancing feed conversion at lower temperature in the range of 600 – 700°C, because the selective removal of hydrogen from the reaction environment enables the multistep integrated process to overcome the thermodynamic equilibrium conversion of single step process carried out at higher temperature. The development of the multistage reactor with only the intermediate hydrogen membrane separation can allow a reduction of operational cost of 13% with respect to the CPO process that is the best case for syngas production [44]. The new scheme allows operating at mild conditions (200 – 300°C lower than a classical CPO or SR process), with improved life-time of the catalysts, minimized overall energy consumption for syngas

production and eventually production of H₂ and CO₂ side streams which can be used for other reactions.

In this work was studied, and try to developed, the preparation of a kind of catalytic system (CeO₂ – ZrO₂ – based system), different from which used in the previous research [44], carried out through a non – classical synthesis such as the inverse microemulsion method. The catalysts obtained are employed in the same reaction conditions used by Barbera, but in this case the study has been focused mainly on the influence that the preparation route and the thermal treatments (calcination temperature, reduction temperature, etc.) can have on the catalyst and hence on the reaction. The objective is to developed a catalytic system which is able to improve its stability towards carbon formation, to be employed not only in the CPO or SR processes but also in other kinds of reforming in which the problem of carbon formation is even drastic, for example the dry methane, or CO₂ – reforming process.

Following the footprint of the project illustrated above, some tests with the use of a H₂ – membrane module are carried out studying and tuning the several operative parameters that are involved in the separation unit, with the aim to develop a system characterized by the highest grade of integration possible.

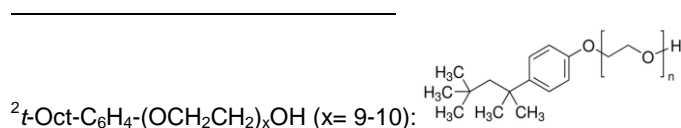
2 EXPERIMENTAL SESSION

2.1 Synthesis methods followed for catalysts preparation

2.1.1 Water – in – oil Microemulsion

CeO₂ – ZrO₂ supports are synthesized following the procedure reported by Martinez – Arias et al. [159], schematically represented in Fig. 2.1.

An aqueous solution containing the same amount (0.25 M) of both Zr (precursor: ZrO(NO₃)₂·xH₂O – 99.00%, Sigma -Aldrich) and Ce (precursor: Ce(NO₃)₃·6H₂O – 99.99%, Sigma-Aldrich) was prepared. An inverse microemulsion (water in organic) was prepared by mixing while stirring 8%wt of this aqueous solution with 58%wt of n – heptane (solvent, 99.00% – Sigma-Aldrich), 15%wt of 1 – hexanol (co-surfactant, 99.00% – Sigma-Aldrich), and 19%wt of a non – ionic surfactant (Triton X-100² (TX-100), 99.00% – Sigma-Aldrich). The cationic emulsion was mixed while stirring with another emulsion having similar characteristics, except that the aqueous solution contains 1.5 M tetramethylammonium hydroxide pentahydrate (TMAH = (CH₃)₄NOH·5H₂O), 97.00% – Sigma-Aldrich) instead of Ce and Zr salts. This approach, i.e. mixing the cationic and anionic aqueous solutions both dispersed in microemulsion is called double – mixed microemulsion method. Immediately after the mixing, a brownish turbidity appeared, denoting reaction (precipitation in the aqueous phase micelles). The fluid was stirred for 24 h, after which the resulting suspension was filtrated; the remaining solid was washed with methanol. The solid is dried at 110°C overnight then grinded to obtain a fine powder. The same procedure has been followed also using an aqueous solution of NH₃ (25% w/w – Sigma-Aldrich) instead of a TMAH one.



A wide investigation on the influence that some parameters can have on a microemulsion, have been carried out in order to study the system.

Four main parameters can be detected and modified:

1. Composition: the relative amount of the compounds involved in the system;
2. Concentration and pH of the cationic and anionic aqueous solutions;
3. R_w : the water – to – surfactant molar ratio (influence the size of micelles);
4. The nature of the precipitating agent (comparison between TMAH and NH_3)

2.1.2 Co – precipitation method

In order to compare the samples obtained through w/o microemulsion method, the same supports have been synthesized also following the classical co – precipitation procedure. This method consists in a simultaneous precipitation of metals hydroxides at controlled pH and temperature. In this case the synthesis is carried out at room temperature. The reagents used are the same already described in the paragraph 2.1.1 and the following steps are followed:

1. Preparation of aqueous solution (0.5M) of the cationic precursors (Ce/Zr molar ratio = 1);
2. Preparation of the anionic aqueous solution of NH_3 (1.5M)
3. The pH of the solution with anion is adjusted to a pH value of 9.5 with nitric acid under vigorous magnetic stirring.
4. The cations solution is slowly dropped in the anion solution keeping the pH value at 9 ± 0.5 with simultaneous dropping of a solution of concentrated NH_3 (25%wt). The system is constantly under vigorous magnetic stirring. Once the dropping of the cationic solution is finished, the dispersion is maintained under stirring at constant pH (9.5) at room temperature for about 1 hour.
5. The solid is separated from the mother liquor by vacuum filtration then washed with abundant distilled water until nitrate free. The solid is dried at $110^\circ C$ overnight then grinded in order to obtain a fine powder.

2.1.3 Calcination procedure

The fine powders obtained both through w/o microemulsion and co – precipitation is thermally treated for obtain a mixture of oxide powder. The samples are placed in a temperature programmed oven in which the samples are maintained at $500 - 700 - 900^\circ C$ for 5h. The set point is reached increasing the temperature $2^\circ C/min$. After 5h the sample is cold down to room temperature, both the weight and the volume are reduced.

2.1.4 Insertion of the active metal

Three different active metals are selected to be added to the support: Rh, Ru and Ni; all of them very active in reforming reactions. The precursors of these metals, generally the nitrate salts, are dissolved in distilled water and their addition to the $\text{CeO}_2 - \text{ZrO}_2$ medium has been carried out following two different methodologies:

- 1) **Bulk**: into the aqueous solution in which are dissolved Ce and Zr cations; then this solution is added into the organic mixture characterizing the microemulsion system described in paragraph 2.1.1;
- 2) **IWI**: after calcination of the support following the Incipient Wetness Impregnation (IWI) technique.

2.1.4.1 *Incipient Wetness Impregnation (IWI)*

The IWI is a method in which the amount of solution used for the supporting active phase is only the volume of solution corresponding to the volume of the pores of the support. The volume of solution needed to fill all the pores is called Water Uptake (WU), is different for each material and is necessary to be known before the impregnation in order to prepare the correct starting impregnation solution [160, 161]. The WU is measured by slowly dropping water (or a solvent used for the impregnation) on a known amount of support ensuring an homogeneous contact by mixing the powder. When the drop will form agglomerates, the liquid will not be absorbed and this means that the pores are filled and the volume of water used is equivalent to the water uptake. The procedure for the production of the supported catalyst is as follows [162]

1. weight the support;
2. prepare the volume of solution with the correct amount of salt containing the precursor of the active phase;
3. drop slowly the solution mixing the powder in order to impregnate homogeneously all the pores;
4. drying the solid at 110°C overnight;
5. calcining the solid for 12h at 500°C, with a ramp of 2°C/min.

During the preparation of bulk samples containing the metal, the second calcination step at 500°C is not present because the metal insertion occurred during the first steps of the synthesis.

2.1.5 Shaping of the catalysts

The calcined powders, are shaped in pellets with a granularity range between 14 and 20 mesh. The shaping procedure requires the formation of a tablet by using a device schematized in Fig. 2.3, composed by four main parts: the base (A), the body (B), two tablets (C) and a piston (D). The powder is inserted between the two tablets inside the body and with the piston on the top. The device is positioned into a small press and a pressure of 10 ton/cm² is applied to the piston. The pressure on the piston, and hence on the powder, is maintained for about 45 – 60 minutes. After this time, the pressure is realized, the powder tablet which is formed is extracted and crushed on two sieves placed one on the other. As mentioned above, a pellets granularity between 14 – 20 mesh is expected, so the 14 mesh sieve will be placed on the 20 mesh one. This procedure is followed few times until a volume of 0.5 – 0.8 cm³ of pellets is achieved.

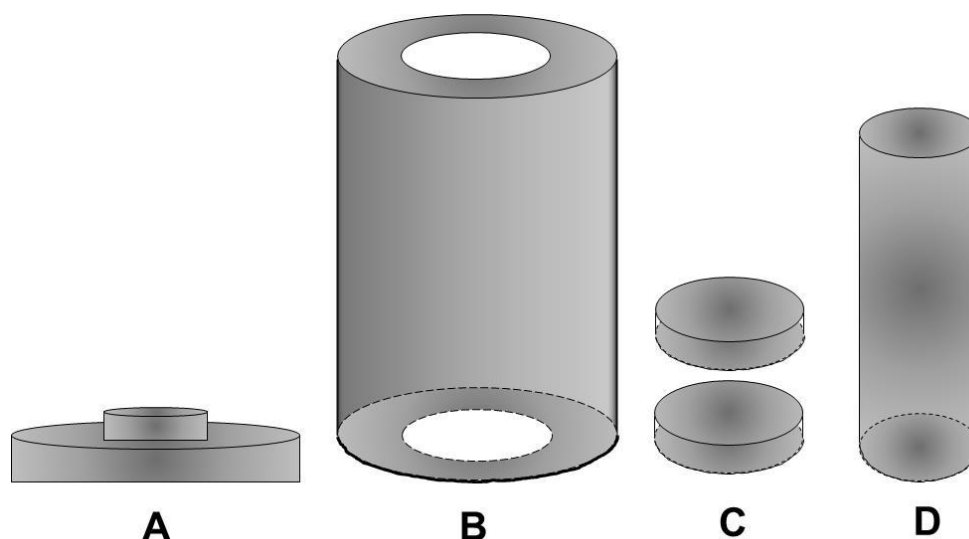


Fig. 2.3. Schematic representation of the four main parts composing the device employed for shaping the powders

An explanation of the acronyms adopted for named the catalysts prepared and tested, is maybe useful to make easier the understanding of this work. Below are reported the explanation of the various elements that compose the acronym employed for the supported impregnated samples (Fig. 2.4a) and the bulk ones (Fig. 2.4b).

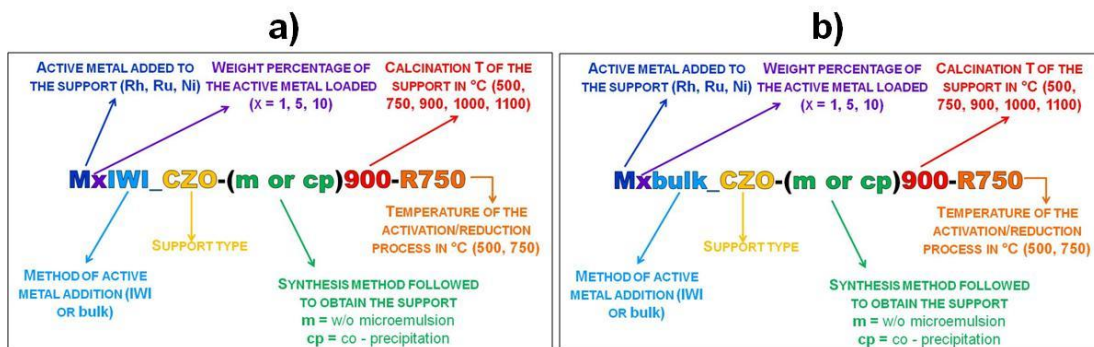


Fig. 2.4. Explanation of the samples acronyms employed in the present work. a) acronym used for the supported impregnated samples; b) acronym used for the bulk samples

2.2 Membranes preparation

In this work are involved also some preliminary tests regarding H₂ separation from the reformat outlet gas, through membrane technology, mainly following the multi-step configuration schematically reported in Fig. 1.21. In particular, this part of the research is now developing in collaboration with the University of Messina, where the actual preparation of the membrane is performed and a summary explanation is following reported.

The membranes preparation is performed following the Electroless Plating Deposition (EPD) technique, which is based on the controlled autocatalytic reduction of a metallic salt on the substrate surface, through the use of a reducing agent. This technique allows the formation of dense and thin metallic films, even on non-conductive substrate, such as ceramic materials. The permeability and selectivity performances, as well as the membranes stability, are parameters strictly dependent on the film characteristics and, hence, they vary in function of the deposition technique adopted. The surfaces utilized for the deposition of thin Pd films are asymmetric porous α -Al₂O₃ tubes characterized by the presence of a macroporous layer (thickness \approx 1.5 mm and average pores diameter \approx 3 μ m) and an internal microporous layer of a thickness at around 20 μ m with an average porosity of 70 nm. The internal diameter (ID) of the tube is 0.7 cm, the outer diameter (OD) is equal to 1 cm and the tube length is 13 cm (Fig. 2.5). The external extremities are constituted of a non-porous coating about 1.5 cm long, which guarantee the sealing with graphite rings, when the tube is finally placed into the reactor. The α -Al₂O₃ supports, before the Pd deposition, are tested in order to verify the homogeneity of the microporous layer, through the “bubbling test” procedure. This technique consists in the placement of the tubular supports inside of a plexiglass reactor, the sealing of which is guaranteed by a Viton o-ring. By means of a peristaltic pump, a liquid phase (H₂O or isopropanol) is feeded to the external side of the ceramic tube; simultaneously, a flow (\approx 180 mL/min) of an inert gas (N₂ or He) is feeded into the tube. Varying the internal pressure of the tube within a range of 1 – 4 bar, is possible to observe the formation of bubbles on the support surface, index of the presence of macroporous defects on it. These defects highlight a non-homogeneous coating, thus it is not suitable for the deposition of a dense metallic film, therefore the supports for those is observed the formation of bubbles are classified as defective and then discarded.



Fig. 2.5. α -Al₂O₃ tube inside of which the Pd active film is deposited through the EPD technique

The suitable supports are cleaned up with a pure isopropanol washing, into an ultrasonic bath for 10 minutes, then they are dried at 110°C for 1 hour and later they are weighted with an analytical balance. At this point the ceramic support is ready for the Pd deposition through the EPD technique. Before the real Pd deposition, the plating procedure requires a first activation of the support surface. Practically, the EPD technique is characterized by two consecutive phases, i.e.:

1. the activation procedure consists in the deposition of Pd nanoparticles on the support surface. It is possible to carry out this step following different methodologies, but in this specific case it is conducted through Pd/hydrazine reduction into an ultrasonic bath;
2. the out-and-out plating procedure, i.e. the Pd film deposition is carried out through the reduction of Pd ions into an aqueous solution, putted in contact with the internal wall of the tubular α -Al₂O₃ support.

2.2.1 [Activation step](#)

The activation of the internal wall of the tubular porous ceramic support is performed following an innovative seeding procedure, optimized by the research group of Messina, based on the employment of Pd complexes. The conventional seeding procedure, provided a sequence of immersions, utilizing firstly an acid SnCl₄ solution, followed by an immersion in another acid solution in which is present the Pd salt. The result of this procedure is the formation of well-dispersed Pd nuclei, but the presence of Sn particles usually caused delamination problems during the tests at high temperature. The innovative procedure, instead, allows the formation of Pd nanocrystals, avoiding the presence of Sn.

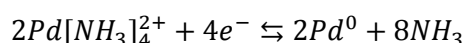
Firstly, two aqueous solutions (50 mL each) are prepared: the first one (solution A) containing HCl (0.1 N) and PdCl₂ (2% w/w), while the second (solution B) is

characterized by N_2H_4 in a molar concentration equal to 2 M. The $\alpha-Al_2O_3$ is then externally covered with a parafilm layer in order to avoid that the Pd deposition occurs also in its external surface and then it is immersed into the solution A for 3 minutes into an ultrasonic bath. After a washing with distilled H_2O , the support is immersed inside the solution B for further 3 minutes. This operation was cyclically repeated 5 times. At the end of the cycle, the support was dried at $110^\circ C$ for 1 h and it was weighted with an analytical balance in order to determine the Pd amount deposited, through a weight difference with respect to the initial weight of the support.

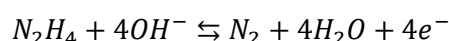
2.2.2 Electroless Plating Deposition (EPD)

The EPD is an electrochemical process which involve redox reactions, with electrons transfer at the interface existing between the surface and solution. Therefore, it is an heterogeneous reaction during which occurs the autocatalytic deposition of the metal at the solid – liquid interface. The plating bath consists in a Pd ammino – complex solution stabilized with EDTA, with hydrazine as reducing agent. Furthermore, an excess of NH_4OH is necessary in order to stabilize the bath and maintain the pH of the solution equal to 11. The reaction is carried out placing the activated support into the plating bath where the following reactions take place:

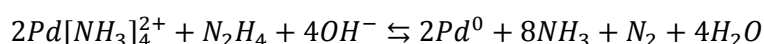
1. Cathodic metal deposition: reduction of the Pd ammino – complex:



2. Anodic reaction: hydrazine oxidation:



The overall reaction can be written:



The reaction take place on the surface of the activated support, in proximity of the Pd nuclei. The initial reaction of N_2H_4 with OH^- forms N_2 and H_2O and it is accompanied by an electrons release. These electrons are transferred to the Pd complex, allowing its reduction to Pd^0 and its consequent deposition on the support surface. The deposition velocity increase in function of the number of nuclei formed on the surface. The deposition velocity is influenced significantly by parameters such as temperature, metal concentration, presence of complexing agents and the nature of the reducing agent. If the plating procedure is carry out too quickly, it will obtain a film characterized by big grains and then with an high roughness degree, while the main objective is the formation of thick and smooth films, in order to increase the H_2 permeability which the fundamental characteristic defining the quality of a Pd membrane for the gases separation. For these

main reasons, the N_2H_4 addition is carried out very slowly, dripping its solution into the plating bath at a rate of $200 \mu\text{L/h}$ for a total time of 8 hours. At the end of this time, the membrane was washed with distilled H_2O and then dried at 110°C for 1 hour. Then, a sealing test with N_2 (180 mL/min) is carried out flowing the gas inside of the membrane until reaching a pressure of 4 bar, in order to exclude the presence of defects in the film or possible fractures of the support, that could be occurred during the preparation procedure. Finally the membrane is placed into a reactor like those represented in , and assembled downstream the reactor in which has been already placed the catalyst.

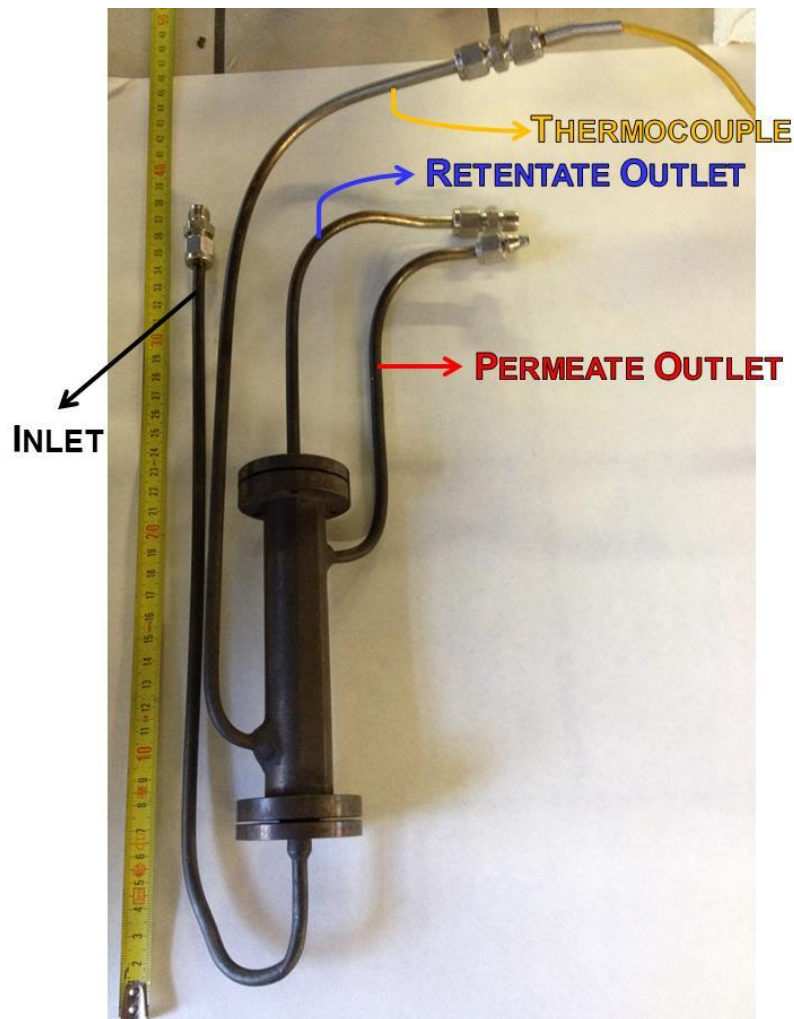


Fig. 2.6. Membrane reactor (MBr) inside of which is placed the membrane

2.3 Laboratory plant description

Catalytic tests are carried out in a laboratory plant schematized in Fig. 2.7. It is possible to subdivide this plant into three principal zones:

Zone 1 – Feeding zone: the cylinders of CH_4 and O_2 are connected to mass flow controllers by a two stage pressure regulator followed by a check valve; mass flow controllers are regulated by a central electronic unit. Deionized water is stored in a plastic vessel and pumped in a vaporizer by an HPLC pump then mixed with the hot O_2 stream. Methane is directly fed into the upper part of the reactor while the overheated vapor mixed with oxygen is fed into the reactor in the part already filled with inert, in order to avoid explosion inside. H_2 and N_2 bottles are not connected to mass flow controller, but their flows are regulated, and maintained constant, through two different low – flow metering valves placed after each check valve. N_2 flow rate is regulated at about 400 – 440 mL/min and it is fed to the reactor when the reaction is stopped in order to maintain the catalyst always under a gas flow. The H_2 flow rate is regulated in function of the N_2 one, in order to obtain a gas mixture characterized by a 10% v/v of H_2 in N_2 , to utilize for the “in – situ” reduction procedure of the catalyst.

Zone 2 – Reaction zone: the main part of this zone is characterized by the reactor, that is a 500mm long INCOLOY 800HT tube with an internal diameter of 10mm and an external diameter of 28mm; it can work up to 1000°C and 20bar. The reactor is placed inside a tubular oven regulated by an external electric unit. The desired amount of catalyst is placed into the reactor in the isothermal zone, in which the temperature of the oven is defined and constant. An inert phase is added into the reactor before and after the catalytic bed and it solves three principal roles: it is a static mixer for fuel and oxidant, it prevents explosion because it reduces the free spaces in which exist the possibility of explosive mixture formation and homogenizes the temperature of gases. Inside the reactor is also inserted a thermocouple shell; type K thermocouple is put inside rendering possible its sliding into the shell, useful for measuring the temperature along the catalytic bed. At the end of this zone, after the reactor end, it is possible to place a membrane module in order to separate H_2 from the other components of the reaction mixture. This module is maintained in temperature (400°C) through the use of electric ceramic bands controlled by two thermocouples connected to two different temperature controllers.

Zone 3 – Post – treatment and analysis zone: the outlet stream is split into two parts through a three ways valve. The system can operate with two distinct modes:

1. Reaction carried out without the membrane reactor installed;
2. Reaction carried out with the membrane reactor installed

In the first option the outlet stream is splitted into two parts, one directed to the vent, while the other part is directed to the separation and analysis zone. When the reaction is carrying out the vent valve is closed and the stream is directed to an heat exchanger maintained at 1.5°C using an ethylene glycol bath, in order to condense the major part of the vapor. Then a pressure regulator is placed on the stream way, controlled by an electric power unit, through which is possible to set and maintain constant the pressure inside the reactor. After the pressure controller the stream is at atmospheric pressure and pass into a dryer of drierite (CaSO_4) to separate possible vapor remained after the first heat exchanger. Then it is directed to a Water Gas Meter (WGM) to control the flow rate. After WGM the outlet stream pass through the final drierite dryer and finally is feeded to the analytical system.

In the second option the outlet stream is always splitted into two parts, but the flow which in the first configuration was directed to the vent, now enter into the membrane module. For this reason, during reaction, the vent valve is open and the other wayof the autoclave valve is closed. Inside the membrane the stream is separated again, in fact from the module exit two different streams, one composed only (or for the major part) by pure H_2 (Permeate stream), and the other part (Retentate stream) composed by the mixture of other reaction gases (non – converted CH_4 , CO , CO_2 and non – converted $\text{H}_2\text{O}(\text{g})$). These two streams must not mix together and so two different treatment lines are necessary for their recovery before the analysis. The permeate flow is directed to a counter – current heat exchanger maintained at 1.5°C by a recycling system of ethylene glycol, to condense possible vapor which can pass through the membrane. The condensate is collected in a little vessel, while the H_2 – rich gas is directed to a three way ball valve, from which is possible to send the flow to the vent or to the WGM and then to the analytical system. Regarding the retentate flow, instead, it is redirected to the separation system described for the first configuration, and finally to the analytical system.

The gas analysis system consist in a micro – GC composed of two modules with two different types of columns. With the first module is detected the H_2 amount, instead with the second one are detectable CH_4 , CO and CO_2 .

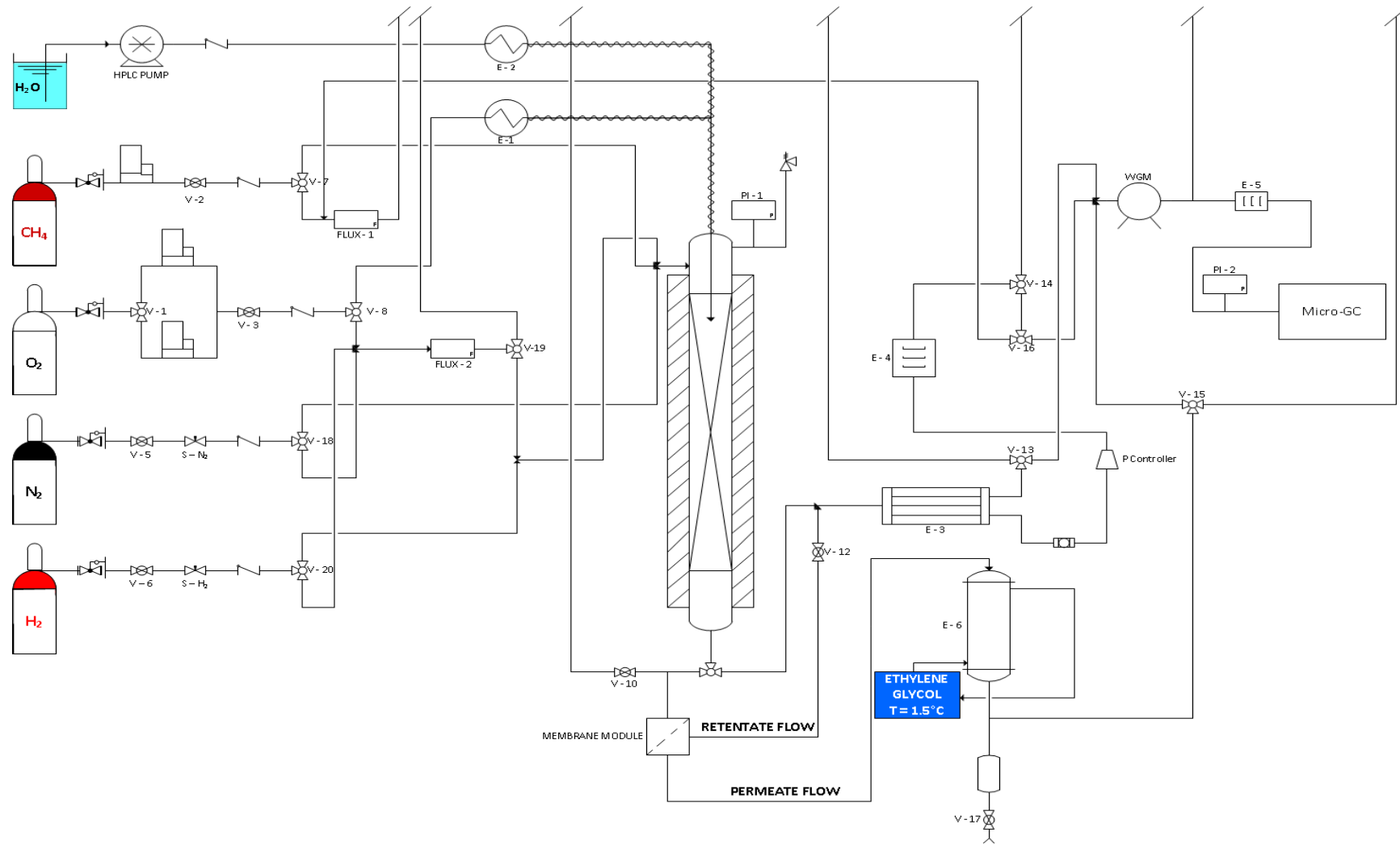


Fig. 2.7. Flow sheet of the laboratory scale plant

2.4 Description of the experiments

Two different reactions are carried out on the catalysts tested. The oxy – reforming and the steam reforming reactions. The latter is carried out only in low temperature range (350 – 500°C) in order to investigate the behavior of the catalytic systems in steam reforming conditions far from those involved in industrial plants (900 – 1000°C). Operative conditions of these two reactions are summarized in Table 2.1. The volumetric composition of the feed mixture of the oxy – reforming reaction, is decided in collaboration with Tecnimont KT simulating the real feed which will be used in the pilot plant and in the industrial plant.

Operative Parameters		Oxy-reforming			Low T SRM				
T (T _{oven}) [°C]		750			500	450	400	350	300
P [atm]		1	10	20	1				
GHSV [h ⁻¹]/τ [s]		24000/0,15	50000/0,072	100000/0,036	24000/0,15				
Feed composition [%mol]	CH ₄	52,04			25,00				
	O ₂	11,20			0,00				
	H ₂ O _(g)	36,75			75,00				
S/C ratio		0,71			3,00				
O ₂ /C ratio		0,22							

Table 2.1. Summary of the operative conditions in which catalytic tests are carried out

The O₂/C ratio is calculated considering only the free oxygen of the stream while if we take in consideration the total amount of oxygen in the stream the O₂/C ratio become 0.57, a value typical for classical CPO reaction.

Generally for all the catalysts tested, the same sequence of catalytic tests are followed, in order to have the maximum reproducibility for each catalyst. One test (reference test), generally the first one carried out on the fresh catalyst, is periodically repeated in order to evaluate the stability of the catalyst towards deactivation phenomena. For the oxy – reforming reaction the reference test is carried out at a T_{oven} = 750°C, P = 1atm and GHSV = 24000h⁻¹, while for the low temperature steam reforming the test carried out at T_{oven} = 500°C, P = 1atm and GHSV = 24000h⁻¹ is chosen as the reference one.

Before starting the reaction and proceed with all of the catalytic tests, is important to activate the catalyst, reducing the oxidized metals to its metallic active state. So after the catalyst is placed in the right position inside the reactor and it is installed in the plant inside the oven, is important to follow few rules listed below:

1. Open the vent valve placed to the exit of the reactor and close the post – treatment way

2. Feeding N₂, then start heating up to temperature of reduction
3. Open the H₂ valve and leave the reduction process go on overnight
4. Close the H₂ valve
5. Set up the reaction temperature
6. Set the values of CH₄, O₂ in the control unit and H₂O_(l) in the HPLC pump
7. Control the real flow rate of CH₄ and O₂ through two different bubble flowmeters
8. Feed to the reactor CH₄, O₂ and H₂O and close N₂ valve
9. Waiting about 10 minutes to flush all the N₂ remain into the reactor
10. Open the post – treatment valve, closing the vent one
11. Close the other vent valves and start with analysis

That just described is the standard procedure for carrying out oxy – reforming tests without the membrane module installation. When it is installed, only one points is different from those listed above:

10. close the V-10 valve

Obviously for the low temperature steam reforming tests, the procedure is the same with the difference that the O₂ valve remain close.

2.5 Dynamic Light Scattering (DLS) analysis

DLS measurements are carried out using a Malvern ZetasizerNano ZS instrument working in a size range between 0,3 nm to 10000 nm. The light source is a He – Ne laser with a wave length of 633 nm and the scattering angle θ on which is placed the fast photon detector is 173°. All the measurements on the microemulsion systems are carried out at room temperature.

Dynamic light scattering (also known as photon correlation spectroscopy or quasi-elastic light scattering) is a technique that can be used to determine the size distribution profile of small particles in suspension in a solution [163]. Typical applications are emulsions, micelles, polymers, proteins, nanoparticles or colloids. The basic principle is simple: the sample is illuminated by a laser beam and the fluctuations of the scattered light are detected at a known scattering angle θ by a fast photon detector. Simple DLS instruments that measure at a fixed angle can determine the mean particle size in a limited size range. A schematic representation of the working principle of a DLS instrument is showed in Fig. 2.8. The principle through which is determined the size distribution of the micelles, is related to the Brownian motion characterizing the micelles dispersed in the microemulsion. The Brownian motion of particles or molecules in suspension causes laser light to be scattered at different intensities. Analysis of these

intensity fluctuations yields the velocity of the Brownian motion and hence the particle size using the Stokes – Einstein relationship (equation (28))

$$D = \mu k_B T \quad (28)$$

where:

- D is the diffusion constant;
- μ is the "mobility", or the ratio of the particle's terminal drift velocity to an applied force, $\mu = v_d / F$;
- k_B is Boltzmann's constant
- T is the absolute temperature

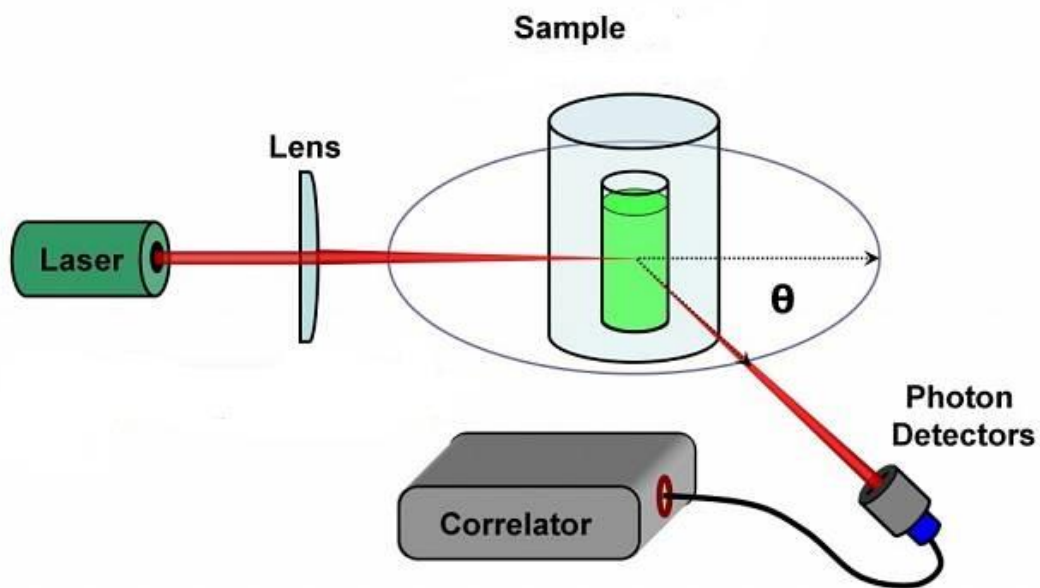


Fig. 2.8. Schematic representation of an instrument for DLS analysis

2.6 X – Ray Diffraction (XRD) analysis

In order to characterize the powders obtained in terms of structural and crystalline phase composition X – ray diffraction analysis are carried out using a Philips PW1050/81 diffractometer equipped with a graphite monochromator in the diffracted beam and controlled by a PW1710 unit (Cu K α , $\lambda = 0.15418$ nm). A 2θ range from 20° to 80° are investigated at a scanning speed of $40^\circ/\text{h}$. A small quantity of powder is necessary for each analysis (0,5 – 1 g). The working principle of an instrumentation for XRD measurements is showed in Fig. 2.9.

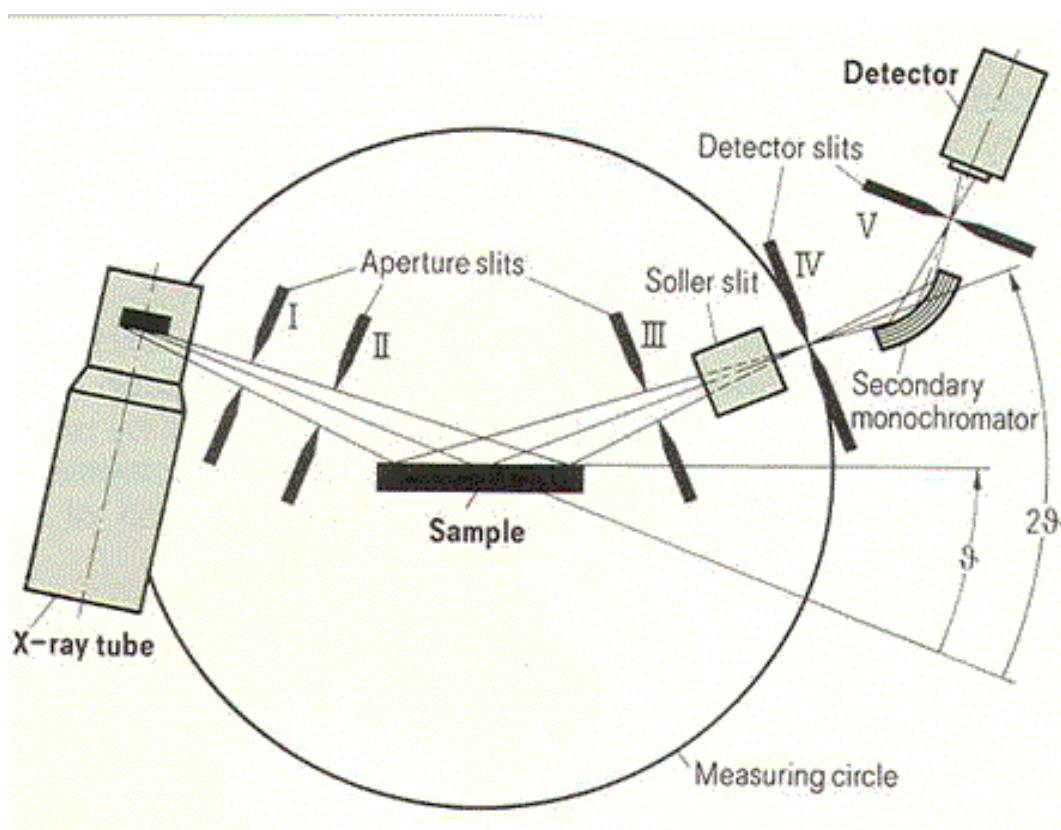


Fig. 2.9. Scheme of the working principle of the instrument for XRD analysis

The analysis of the phases present in the patterns were analyzed using the Bragg's Law (equation (29)), in order to calculate the d values to compare with those reported in the literature [164].

$$n\lambda = 2d \sin \theta \quad (29)$$

2.7 Surface area and porosimetry analysis

Specific surface area and porosimetry analysis of the calcined catalysts, were carried out in a Micromeritics ASAP2020 instrument (Accelerated Surface Area and Porosimetry System). Each analysis require about 0,2 – 0,3 grams of powder.

This analysis provide a pretreatment, which principally involve a degas under vacuum of the sample heating it up to 150°C until the pressure of 30 mmHg is reached then kept 30 min at this temperature and finally heated up to 250 °C and maintained for 30 min. The pretreatment is necessary in order to eliminate all the impurities that can be absorbed on the surface of the sample such as humidity. Afterwards the adsorption is carried out using as adsorbate molecule N₂. The adsorption and then desorption steps are carried out at constant temperature equal to the N₂ liquefaction temperature (77 K). In fact, the instrument measures the adsorption and desorption isothermal curve at 77 K by the volume of adsorbed/desorbed N₂, as a function of relative pressure (via-multi-point method).

The value of surface area is calculated by the software on the basis of the Brauner – Emmet – Teller (BET) equation [165] (equation (30)):

$$\frac{P}{V(P_0 - P)} = \frac{1}{V_m C} + \frac{C - 1}{V_m C} \cdot \frac{P}{P_0} \quad (30)$$

where:

P_0 = saturation pressure

V = gas volume adsorbed per gram of solid at a pressure P

V_m = gas volume adsorbed per gram of solid in the formation of a monolayer on the surface

C = BET constant, dependent by the net heat of adsorption

The range of linearity of equation (30) is defined in $0.05 < P/P_0 < 0.35$. Into this range, from the known values of the intercept and the slope of the isotherm curves, is possible to calculate V_m and C and through the equation (31) is possible to calculate the specific BET surface area of the sample expressed in $\text{m}^2/\text{g}_{\text{CAT}}$.

$$S_{\text{BET}} = (V_m/V_0) \cdot N_A \cdot \frac{k}{g_{\text{CAT}}} \quad (31)$$

where:

S_{BET} = surface area calculated through the BET model

V_m = N_2 volume adsorbed for the formation of the monolayer

V_0 = molar volume of the adsorbed gas

N_A = Avogadro number

g_{CAT} = weight of the catalyst analyzed

k = conversion factor which take into account the density and the molecular weight of the adsorbed gas.

2.8 Temperature Programmed Reduction (TPR) and Oxidation (TPO) analysis

The redox properties of the samples are studied using a ThermoQuestInstrument TPD/R/O 1100 Catalytic Surface Analyzer. The analysis are carried out loading about 0,06 – 0,08 grams of sample and the following steps for each calcined fresh sample are carried out:

- **Pretreatment under N_2 flow (20 mL/min)**
 - 1) Temperature increment from 60°C to 150°C with an heating rate of 10°C/min;
 - 2) Holding at 150°C for 30 minutes;
 - 3) Cooling until 60°C is reached
- **Reduction under 5% v/v H_2/N_2 mixture (20 mL/min)**
 - 1) Temperature increment from 60°C to 950°C with an heating rate of 10°C/min;
 - 2) Holding at 950°C for 30 minutes;
 - 3) Cooling until 60°C is reached
- **Oxidation under 5% v/v O_2/He mixture (20 mL/min)**
 - 1) Temperature increment from 60°C to 950°C with an heating rate of 10°C/min;
 - 2) Holding at 950°C for 30 minutes;
 - 3) Cooling until 60°C is reached

To close the cycle another step of reduction is carried out. This type of reduction/oxidation/reduction (TPR/O/R) cycle is carried out on the calcined sample before the catalytic tests, in which the metal characterizing the active phase of the catalyst is present in his higher oxidation state. The spent samples, i.e. after the catalytic tests, instead, are analyzed with the inverse cycle (TPO/R/O) because, in this case, the active phase is still reduce.

As shown in Fig. 2.10, the gas mixtures are feed to the reactor in which is placed the sample and the outlet gas stream passed firstly into a trap in order to eliminate H₂O traces developed during reduction cycles and then is analyzed by a Thermal Conductivity Detector (TCD). Through data processing, is possible to obtain reduction and oxidation profiles in function of temperature, hence the various species which are reduced/oxidized are detected, ad also their interaction with the support.

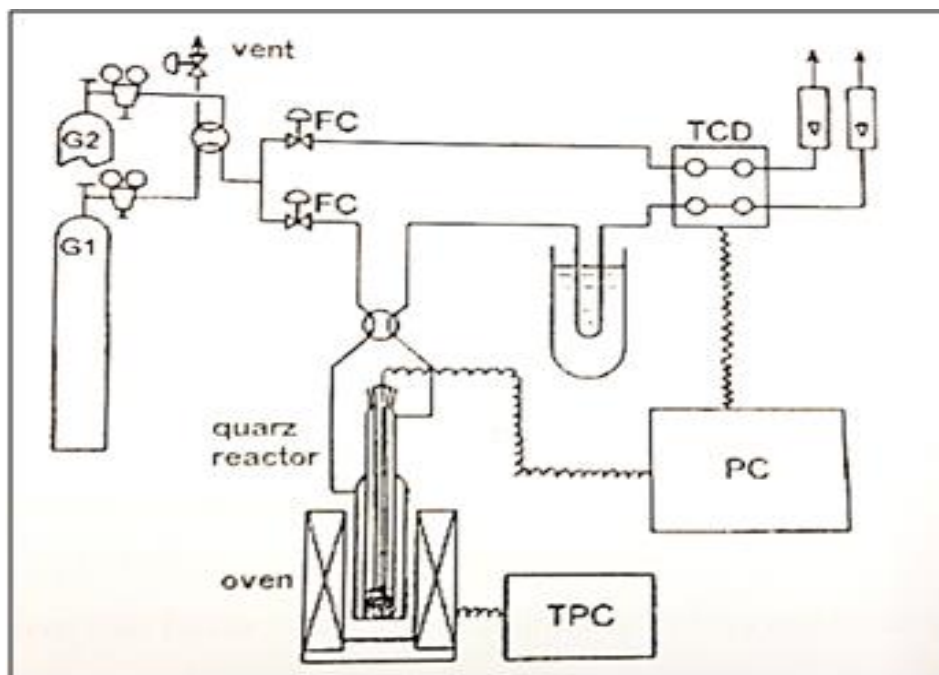


Fig. 2.10. Scheme of a TPDRO instrument

2.9 Transmission Electron Microscopy (TEM)

TEM analysis are carried out using a TEM/STEM FEI TECNAI F20 microscope combined with Energy Dispersive X – Ray Spectrometry (EDS), at 200keV. A small quantity of powder (0,3 – 0,5 g) of calcined fresh catalysts, reduced fresh catalysts and spent catalysts are investigated in order to study the morphology and the dimensions and size distribution of the active metal particles on the support and their interactions with it. The sample preparation is carried out suspending the powder in ethanol and treating it with ultrasound for 15 minutes. The suspension is deposited on a “multifoil-carbon film” sustained by a Cu grid. Then the so prepared system is dried at 100°C. With EDS is possible also to make an elementary analysis in some areas of the samples, therefore understand the real composition of the catalyst.

2.10 Raman Spectroscopy

The instrument utilized for these analysis is a micro-spectrometer Renishaw Raman RM1000 interfaced to a microscope Leica DMLM (obj. 5x, 20x, 50x). The available sources are an Ar⁺ laser ($\lambda = 514.5 \text{ nm}$; $P_{\text{out}} = 25 \text{ mW}$) and a diode laser ($\lambda = 780.0 \text{ nm}$; $P_{\text{out}} = 30 \text{ mW}$). In order to eliminate the Rayleigh scattering, the system is equipped with a notch filter for the Ar⁺ laser and an edge filter for the diode one. The network is a monochromator with a pass of 1200 lines/mm. The detector is a CCD one (Charge – Coupled Device) with a thermo-electrical cooling (203 K).

Raman is a spectroscopic technique based on inelastic scattering of monochromatic light, usually from a laser source. Inelastic scattering means that the frequency of photons in monochromatic light changes upon interaction with a sample. Photons of the laser light are absorbed by the sample and then reemitted. Frequency of the reemitted photons is shifted up or down in comparison with original monochromatic frequency, which is called the Raman effect. This shift provides information about vibrational, rotational and other low frequency transitions in molecules. Through this analysis is possible to identify the substances present in the sample, recognizing not only their chemical composition but also different molecular and crystalline structures. In fact, the vibrational spectrum reflects in the number, in the shape and in the position of the bands, the chemistry and the structure of the molecular groups that constitute the sample. Raman spectroscopy is more sensible towards structural defects present in a crystalline network, allowing, for instance, the identification of a particular distorted phase which is not detectable through XRD analysis of the same sample.

The simplify working principle of a Raman spectrophotometer is showed in Fig. 2.11.

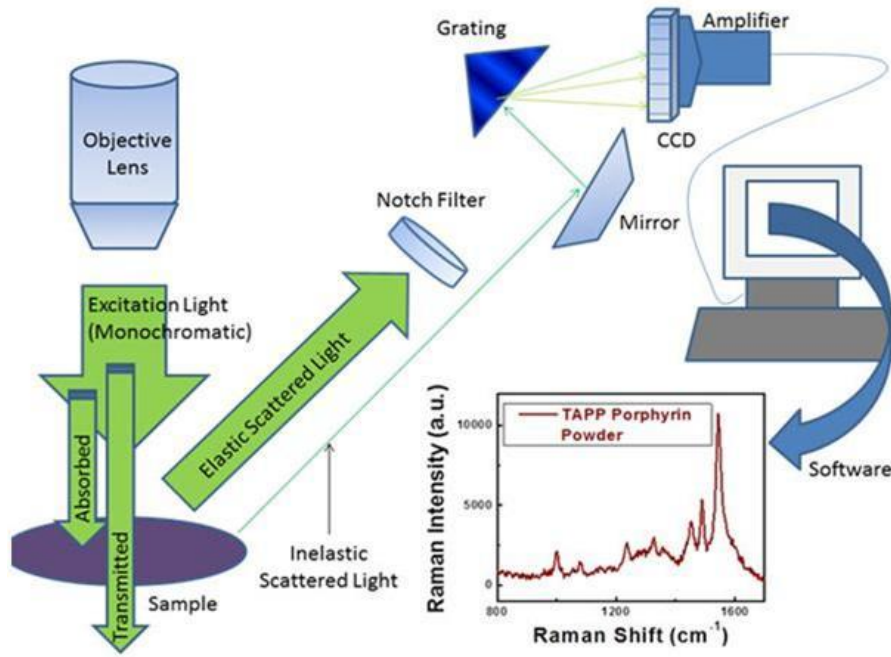


Fig. 2.11. Schematic illustration of the working principle of an instrument for Raman analysis

3 RESULTS AND DISCUSSION

3.1 Introduction by previous studies

As already mentioned, the present work is a continuation of the research work carried out by Barbera [44]. In his work, carried out into the Next-GTL European project, there a new catalyst's formulation to be employed for syngas production with a new low temperature oxy-reforming process have been developed.

Barbera studied different catalysts' formulations principally based on Mg/Al mixed oxides deriving from hydrotalcite – like precursors (see paragraph 1.2.2, page 32). Different metallic (Rh, Ru) and bi-metallic (Ni/Rh, Pt/Rh) active phases have been studied demonstrating how the nature of the support can have a relevant effect on the catalytic activity. In fact is showed [44] that between three catalysts containing the 1%wt of Rh as active phase but characterized by three different supports ($Mg_{68}Al_{32}$, $Mg_{80}Al_{20}$ and $Ce_{75}Zr_{25}O_2$) are present significant differences. The two Mg/Al – based samples are “home – made” synthesized catalysts, instead the Ce/Zr – based one is a commercial catalyst. Some results of the experiments carried out on these catalysts are showed in Fig. 3.1.

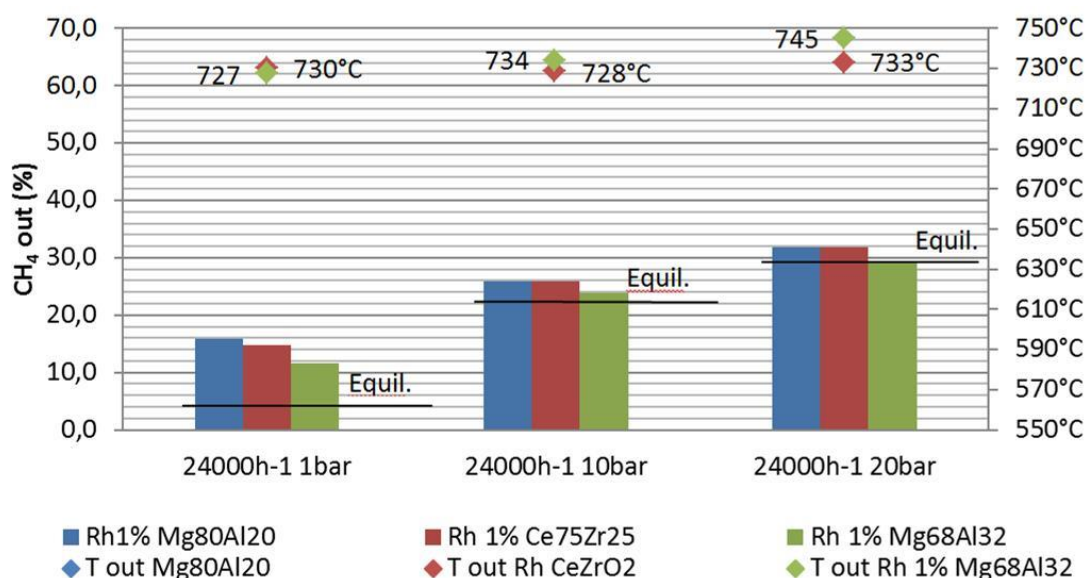


Fig. 3.1. Methane outlet composition for Rh1%Mg₈₀Al₂₀, Rh1%Mg₆₈Al₃₂ and Rh1%/Ce_{0.75}Zr_{0.25}O₂ compared at 750°C and 24'000h⁻¹. The bars are referred to the left while temperature on the right. The equilibrium lines are calculated at 730°C for tests at 1 and 10 bar while at 740°C for the tests at 20bar [44].

From these and other data [44] is clear that Rh1%Mg₆₈Al₃₂ shows the best performances in terms of CH₄ outlet dry composition, showing values close to those

calculated at the thermodynamic equilibrium. For this reason, supported by other several informations and analysis, this catalyst is chosen also to make a study of catalyst scale – up in collaboration with BASF for the pilot plant tests in Tecnimont facilities (Chieti). The catalyst was deposited on a structured support. The industrial catalytic system has an honeycomb structure on which is deposited the Rh – based catalyst through the wash coating technique (BASF). In order to obtain a final catalyst with a desired loading of Rh, the wash coating has been made using a catalyst with an higher amount of Rh (Rh3%Mg₆₈Al₃₂). The amount was decided on the bases of the required amount of catalyst to be mixed with the monolith support to have a final supported catalyst characterized by the 1%wt of Rh which is comparable with the amount of meal present in the semi industrial catalyst used in the pilot. The Rh3% catalyst shows good performances in the oxy-reforming reaction, but the main problem could derive from its stability in long terms application, because, as mentioned above, the real operative conditions are near to the limit of carbon formation phenomena. This problem become even more important if a global view of the footprint of the Line 1 of the Next-GTL project is taken into account. In fact this research Line comprise also the integration of the process with the membrane separation technique. In particular, considering the H₂ membrane separation, the second reaction step will have a decrease of the H/C ratio dramatically to a value which can lead to the carbon formation if steam is not added to increase the H/C or O/C ratio. Hence, is important to try to develop another catalytic system more stable towards the deactivation due to carbon formation, to be employed in operative conditions with the minimum H/C and O/C ratio. With the purpose to increase the stability towards coke formation and increase reactivity at lower temperature SR reaction, a new catalyst formulation, obtained through a non-classical synthesis method (w/o microemulsion), has been developed and tested in the oxy-reforming and low temperature SR reactions.

This study can be subdivided into four parts:

1. Study and characterization of the w/o microemulsion systems;
2. Characterization of the calcined CeO₂ – ZrO₂ (CZO) supports, before and after the metal insertion;
3. Discussion of the catalytic activity results;
4. Characterization of the most promising catalytic systems after reaction

3.2 W/O Microemulsion synthesis

Following the definition, a microemulsion system is thermodynamically stable and characterized by a clear optical isotropy (transparency). These issues are satisfied when the cationic microemulsion (CZ-m) is prepared, but the same behavior is not observed after the TMAH aqueous solution is added to its organic phase to form the anionic microemulsion (TMAH-m). In fact, when the CZ aqueous solution is added to the organic phase (n-heptane/1-hexanol/Triton X-100), immediately the system become slightly turbid but, after few minutes of magnetic stirring it turns to transparency. On the other hand, when the TMAH aqueous solution is added to its organic phase, a more turbid system is observed, which not turns to transparency even after some hours under magnetic stirring. The origin of this discrepancy probably reside in the different sizes of the inverse micelles that are formed into the two separated systems. DLS analysis is carried out on both of the two systems, and results are showed in Fig. 3.2. From the figure is clear how the CZ-m sample is characterized by inverse micelles with a narrow size distribution centered at a value of hydrodynamic radius of about 40nm. The hydrodynamic radius is relative to the total radius of a micelle including also the molecules of surfactant and co-surfactant placed around the water core; this mean that only the water core will be smaller. The difference between the hydrodynamic radius with which of the lonely water core, will depend by the nature of the surfactant employed, in terms of length of the aliphatic chains. In this case Triton X-100 is not characterized by a very long aliphatic chains (about 20 carbon atoms – see paragraph 2.1.1), therefore the water core radius of a micellar system like the CZ-m one, will be of about 20 nm. From DLS analysis is clear how the formation of the inverse CZ microemulsion occurred in the right way and it is stable even after long time (Fig. 3.2 – blue line). The stability is studied leaving the CZ-m sample in a vial for a long period of time (months), after which is observed if in the sample some phase separation phenomenon occurred and another DLS analysis is carried out.

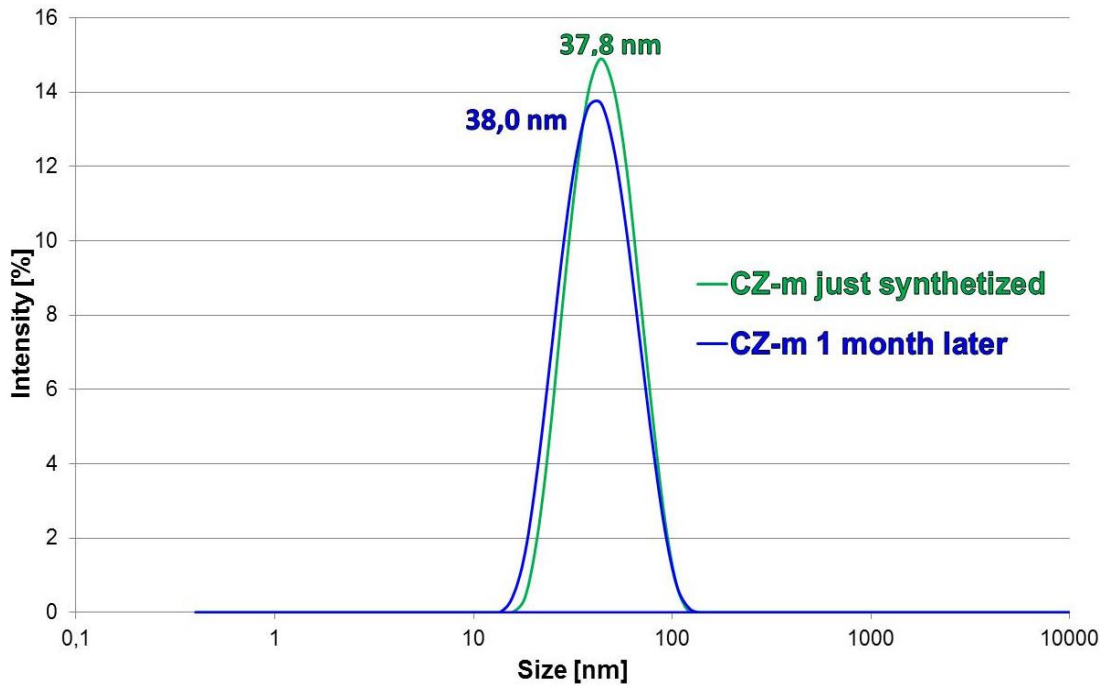


Fig. 3.2. Size distribution of micelles characterizing the CZ-m sample few minutes after the synthesis (green line) and 1 month later (blue line). $[CZ]_{aq} = 0.5M$

The same analysis is carried out also on the TMAH-m system but it is not reported because no peaks in the size range investigated is observed. This is due, indeed, to the different size of the micelles characterizing this sample. Its very turbid appearance suggested that the micelles are characterized by a larger hydrodynamic diameter than which of the CZ-m sample, having a diameter which are big enough to interfere with the wavelength of the light creating scattering phenomena that result in a high opalescence. Their size overcome the size range in which the DLS analysis is carried out, hence any distribution is detectable.

For these reasons the study is focused mainly on the TMAH-m system, modifying it trying to obtain a more stable microemulsion, like the CZ-m one for two main reasons:

1. create a real double mixed microemulsion system by having a stable TMAH microemulsion suitable for the precipitation of Ce and Zr hydroxides;
2. reach a stable microemulsion having the solid dispersed into the micelles of the microemulsion for further functionalization.

Initially this study is started from the investigation of the four following parameters:

1. pH of the aqueous solution;
2. molar concentration of TMAH aqueous solution;
3. $H_2O/Surfactant$ molar ratio (R_w);
4. nature of the precipitating agent

3.2.1 Effect of pH

This parameter is taken into account after a direct comparison between the CZ and the TMAH aqueous solutions. In fact, the former present a very low pH value (1 – 2) due to the presence of acid cations dissolved in it, instead the latter is characterized by a very high basicity (pH \approx 14). This simple consideration, suggested that a too high pH of the aqueous solution could be the responsible of the instability of the TMAH-m sample. In order to clarify this aspect, seven microemulsion systems are prepared maintaining the same proportions between water and organic phase (i.e. at constant R_w), but using different mixtures of HCl and NaOH in the right relative amount in order to obtain seven solutions in a pH range from 1 to 13. Fig. 3.3 shows the size distributions of the microemulsions prepared in the described way. In the pH range 1 – 11, the size distribution of the micelles is mono-modal and the average value is similar (between 18 and 25 nm) in accordance with the R_w value that is the same for all of the tests and equal to 14.6. This means that until a pH of the aqueous solution of 11, there is the formation of a stable microemulsion system, but when the pH is further increased to a value of 13 (violet curve), increase a population of micelles with bigger size (5115 nm), indicating an initial possible destabilization of the microemulsion. Therefore, because of the pH value measured for the TMAH solution is higher than 13, it is reasonable to think that the lack of stability observed in the TMAH microemulsion is probably due to this parameter. With this purpose, it is tried to stabilize the TMAH-m system generating a slightly decrease in the pH. In the neutralization of the OH^- is important that the pH decrease isn't too large, otherwise when the CZ-m and the TMAH-m are mixed together there aren't enough OH^- ions to precipitate all the Ce and Zr hydroxides. After stirring, it is added HNO_3 (65% v/v) to the TMAH-m opalescent system until it becomes transparent. During the acid addition, the pH is continuously monitored, and we observed that when the TMAH-m sample becomes transparent, i.e. after 300 μL of HNO_3 , the pH didn't change significantly (from 14.0 to 13.8), but now the emulsion system is transparent, stable and characterized by a single mono-modal trend (Fig. 3.4). At this point, two stable microemulsions are obtained that, mixed together, should form a final microemulsion characterized by the particles of the precipitated solid (Ce and Zr hydroxides) inside the inverse micelles. Nevertheless the resulting mixed – microemulsion is not stable and the deposition of the solid is observed. The DLS confirm the instability and the large dimension of the micelles since no constant results have been obtained during analysis.

Thus, the pH of the TMAH aqueous solution seems to have a certain influence on the stability of the TMAH-m system but not on the final mixed – microemulsion, because the separation between the solid and the liquid phase occurs after the stirring is stopped.

The final form of the solid is a precipitate which remains suspended in the liquid, in a gel-like form.

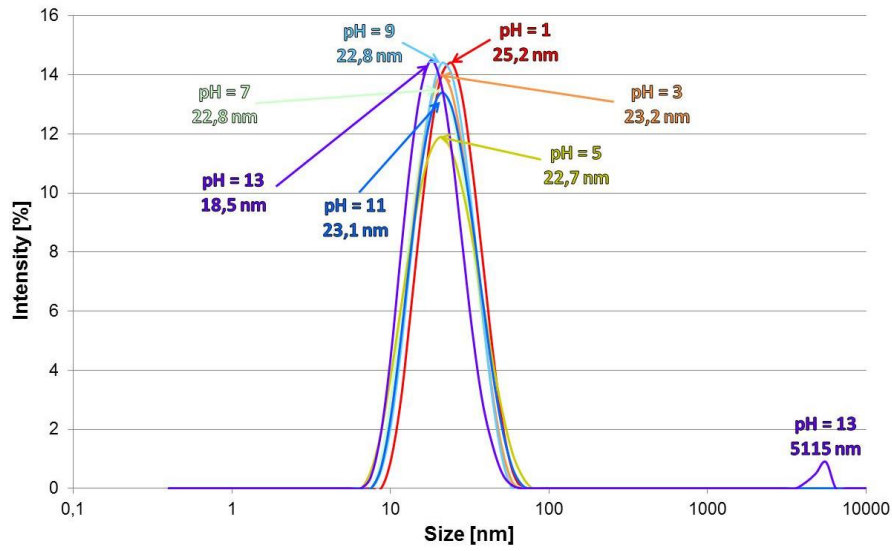


Fig. 3.3. Effect of pH on the sizes of micelles (all of the microemulsions have $R_w = 14.6$)

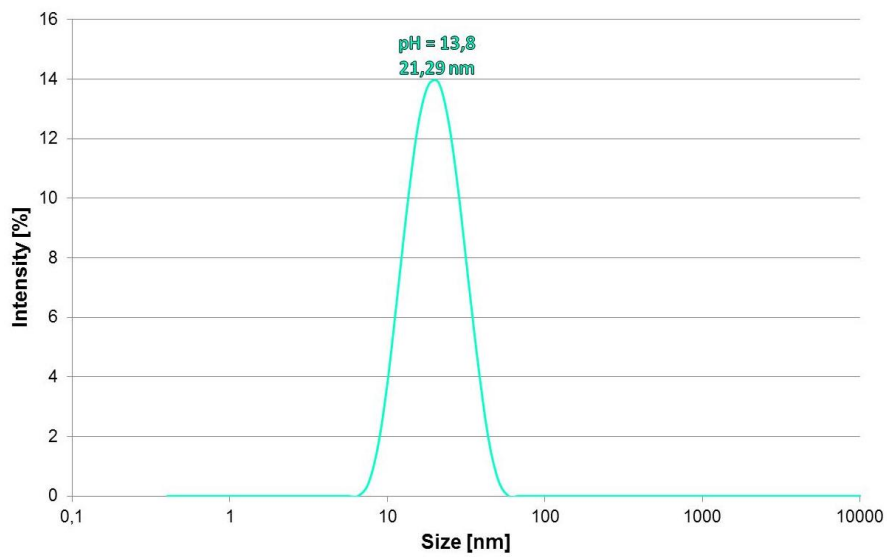


Fig. 3.4. Size distribution of the TMAH-m sample after the addition of 300 μ L of HNO₃ (65%v/v). [TMAH_(aq)] = 1.5 M; $R_w = 14.6$.

3.2.2 Effect of TMAH molar concentration

Another parameter significantly different between the CZ and TMAH aqueous solutions is their molar concentration. In fact, the TMAH has a molar concentration three times higher (1.5 M) than which of the CZ solution (0.5 M). Table 3.1 shows the main parameters investigated in the microemulsion systems prepared. Five TMAH aqueous solutions are prepared in a range of molar concentration between 1.5 M and 0.3 M (steps of 0,3 M each), starting from a reference solution divided into 5 aliquots and increasing the water content. The yellow boxes in Table 3.1 identify the values changed with respect of those relative to the initial TMAH-m, taken as the reference test and represented in the pink cells. From this investigation only the condition of the TEST 4 ($[TMAH]_{aq} = 0.6$ M) produced a transparent mixture, which remain as is, even after a long period of time (1 night).

		TEST 1	TEST 2	TEST 3	TEST 4	TEST 5	
Parameters investigated	REFERENCE TEST	H ₂ O [mL]	8,38	10,47	13,96	20,94	41,89
		TMAH [mol]	0,01	0,01	0,01	0,01	0,01
H ₂ O [mol]	2,63	0,45	0,58	0,78	1,16	2,33	
Triton X-100 [mol]	0,18	0,03	0,03	0,03	0,03	0,03	
1-Hexanol (co-surfactant) [mol]	0,87	0,15	0,15	0,15	0,15	0,15	
Heptane [mol]	3,43	0,59	0,59	0,59	0,59	0,59	
TMAH [mol]	0,07	0,01	0,01	0,01	0,01	0,01	
R _w [H ₂ O/Surf. Molar ratio]	14,63	14,63	18,85	25,14	37,71	75,42	
Heptane/H ₂ O [Molar Ratio]	1,30	1,30	1,01	0,76	0,51	0,25	
Hexanol/H ₂ O [Molar Ratio]	0,33	0,33	0,26	0,19	0,13	0,06	
TMAH/H ₂ O [Molar Ratio]	0,03	0,03	0,02	0,02	0,01	0,01	
TMAH Concentration [M]	1,55	1,55	1,20	0,90	0,60	0,30	

Table 3.1. Summary of all of the parameters changed (yellow) in the five solutions with different TMAH molar concentration (TEST 1 – 5), compared to the same parameters of the REFERENCE TEST (pink)

Thus, this system is analyzed through DLS and the results are showed in Fig. 3.5. The stability of the TEST 4 mixture, is also confirmed by DLS analysis, because it present a sharp mono-modal size distribution profile centered at about 90 nm (Fig. 3.5 a). Fig. 3.5 b, compared the size distribution profile of the TEST 4 system with that relative to the stable CZ-m microemulsion. The former profile, being centered at 90 nm, indicates that the micelles in this sample are bigger in size than those constituting the CZ-m sample, which profile is centered at about 30 nm. This result is in accordance with the different R_w values relative to each microemulsion; in TEST 4 mixture there is more water (20.94 mL) than in the CZ-m one (8.38 mL). R_w are directly proportional to the water content, therefore, an higher amount of water imply an higher R_w value (37.71 instead of 14.6) and hence bigger sizes of the micelles.

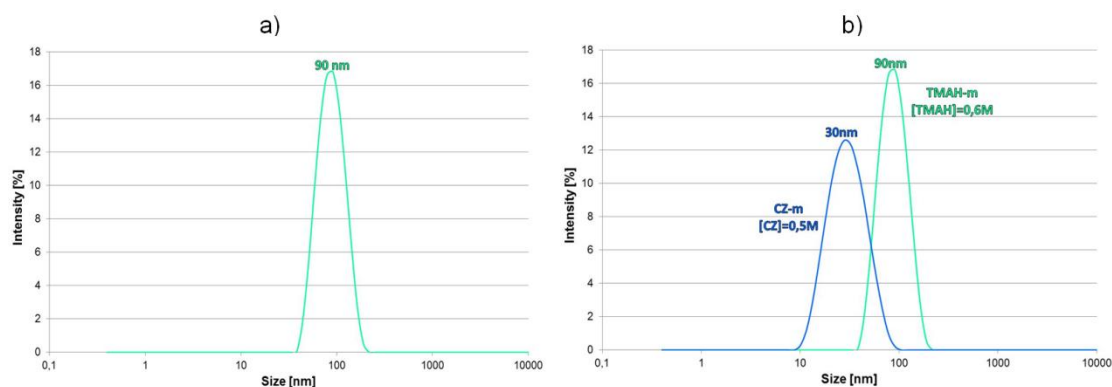


Fig. 3.5. a) Size distribution profile of the TMAH-m sample obtained in the conditions of the TEST 4 reported in Table 3.1; b) Comparison between the TMAH-m ($[TMAH]_{aq} = 0.6 \text{ M}$) and CZ-m ($[CZ]_{aq} = 0.5 \text{ M}$) size distribution profiles

Through the modification of the TMAH molar concentration, both of the microemulsion systems are now stable, and a mixture of these might allow to obtain a final stable microemulsion. Unfortunately, after the mixing, no precipitate is detected. This could be due to an excessive dilution rate of the TMAH aqueous solution inside of the micelles, resulting in an insufficient raise of the pH at the cationic/anionic micelles interface to allow the hydroxide precipitation.

3.2.3 Effect of R_w ratio

A wider range of R_w between 1 – 14 have been investigated. A unique TMAH aqueous solution with a molar concentration of 1.5 is prepared and added to the same mixture of n – heptane:1 – hexanol:Triton X-100, obtaining 8 emulsions with a difference of the R_w ratio between each mixture of 2 units. DLS analysis are carried out on each system and results are showed in Fig. 3.6. As expected, increasing the R_w , the size of micelles increase, but already at $R_w = 3$, the DLS curve shows a bi-modal trend with a population of micelles with very big size (4723 nm). This latter effect becomes relevant when R_w is increased further to 7. In this case, the first peak is centered at a value even lower (about 11 nm) than which presented in the test at $R_w = 3$ (about 14 nm), but the peak centered at higher size (2544 nm) is broader and with higher intensity value. Generally, DLS data are represented in function of the relative intensity of the scattering that a population of micelles create when gets hit by the laser beam. Bigger micelles create a more intense scattering phenomenon and this mean that even if only few micelles crossed through the laser beam, they will create an high intensity peak. In order to normalize this effect the same data are plotted in function of the Volume % (Fig. 3.7) rather than the Intensity %. In this way the scattering that is recorded, is in function of the relative volume that different populations of micelles have in the system. In other words, even if in the sample are present some biggest micelles, their weight on the final size

distribution profile is less important inasmuch, they are very big, but occupy a small volume in comparison with the volume occupied by all the other smaller micelles. In fact, by a comparison between Fig. 3.6 and Fig. 3.7, this effect is clearly visible. In the latter figure based on the volume, are not evidenced peaks in the large size region, and this means that the peaks observed in the $R_w = 3$ sample at 4000 nm can be ascribed to few micelles, not significant in terms of volume solution; actually this sample is constituted by almost all the micelles with an homogeneous size centered at about 10 nm (Fig. 3.7). $R_w = 5$ and 7 samples, have a more complex profiles with a shoulder at about 9.5 nm and 7.9 nm, respectively. This mean that these two samples are not homogeneous like those characterized by a smaller R_w ratio and this could imply that an increase of this ratio has an influence on the stability of the microemulsion system. This hypothesis may be confirmed by the fact that trends relative to measurements at $R_w = 9$ and $R_w = 14$ don't show any peak in the size range investigated because of the non-stable nature of these microemulsions. Therefore, the instability of TMAH microemulsion could depends also to R_w parameter, but it is enough unusual, considering that the CZ microemulsion is stable at a R_w value of 14.6.

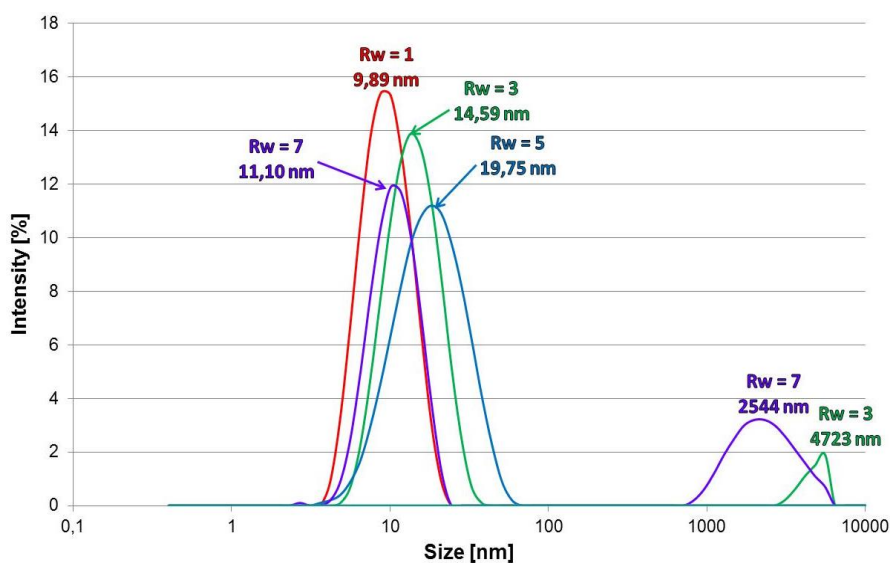


Fig. 3.6. Effect of R_w ratio on the size distribution of the TMAH-m sample ($\text{pH}_{\text{TMAHsol.}} = 14.0$ $[\text{TMAH}]_{\text{aq}} = 1.5 \text{ M}$)

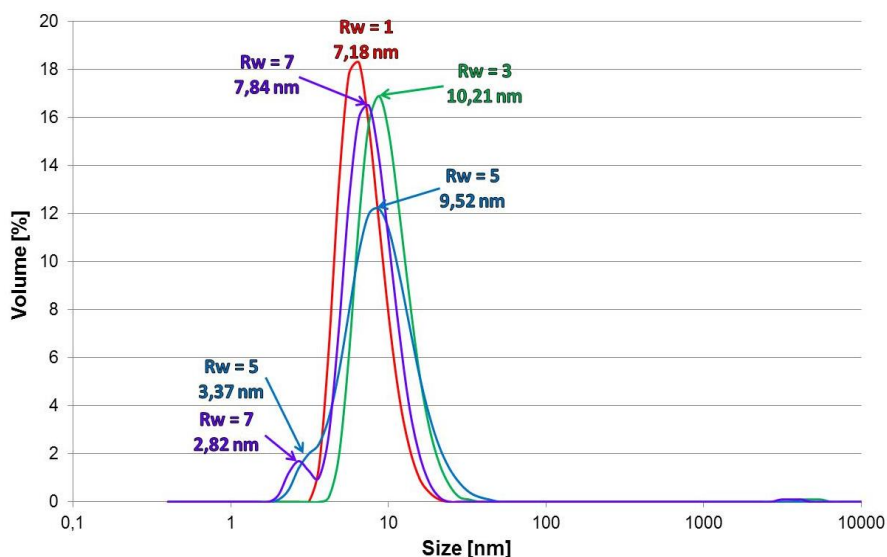


Fig. 3.7. Representation of the same data showed in Fig. 3.6 but plotted in function of the Volume [%]

3.2.4 Effect of the nature of the precipitating agent

Unfortunately, the stability of the TMAH-m and, mainly, of the final mixture is not achieved with all tests carried out so far. For this reason, it is modify the nature of the TMAH, trying to obtain a stable anionic microemulsion system with another, more classic, precipitating agent; NH_3 . Ammonia in aqueous solution forms OH^- ions and ammonio ions (NH_4^+) characterized by a less steric hindrance with respect to the TMAH cation ($(\text{CH}_3)_4\text{N}^+$) so, theoretically, could be disperse in small micelles in an easier way. However, a NH_3 solution has a pH below 12, and this could be a problem generating a non-complete precipitation of the hydroxides.

In literature [166] is reported a similar example in which is shows the difference in stability between an inverse microemulsion of iron nitrate made by tetrabutylammonium hydroxide (TBAH) and the same inverse microemulsion with NH_3 . The mixture containing NH_3 results in a stable suspension of iron hydroxide nanoparticles while the TBAH one shows an immediate settling of the precipitate. Such behavior indicates some instability mechanisms upon replacing NH_3 by TBAH. The nanoparticles suffered immediate agglomeration upon mixing the two microemulsions. This might be due to the TBA cation ($\text{N}^+(\text{C}_4\text{H}_9)_4$) favorably adsorbing on the iron hydroxide at the expense of oil/water interfacial adsorption. Such adsorption of the TBA cation is encouraged by the high pH of the water core due the presence of a high concentration of OH^- . In this case, the particles will be above their point of zero charge, and hence, become negatively charged. This causes a preferential adsorption of TBA cation and hence converts the particles from

being hydrophilic to hydrophobic. As a result, agglomeration instead of dispersion into the polar micro-water pools is expected.

The preparation of the NH_3 microemulsion system ($\text{NH}_3\text{-m}$) is carried out always in the same way in terms of molar concentration of the NH_3 aqueous solution (1.5 M) and R_w ratio, maintained at the value of 14.6. Immediately after the aqueous solution is added to the usual organic phase, the mixture became transparent suggesting the formation of a stable microemulsion system, confirmed also by the results of the DLS analysis reported in Fig. 3.8. In fact, the size distribution of the $\text{NH}_3\text{-m}$ sample is characterized by a mono-modal trend centered at about 20 nm, but the pH of this system is lower (11 – 12) than what measured for the TMAH-m mixture (about 14). In fact, after mixing this microemulsion with the CZ-m one, there isn't the formation of any precipitate, hence have been decided to increase the NH_3 molar concentration until 3 M. Also in this case the microemulsion formed show a good stability. This latter microemulsion is added again to the CZ-m and immediately the precipitation of the mixed hydroxides occurs. This mixture is leaved overnight under magnetic stirring, but when the stirring is stopped, also in this case, the precipitate settle down indicating a probable non-stable nature of the final microemulsion system.

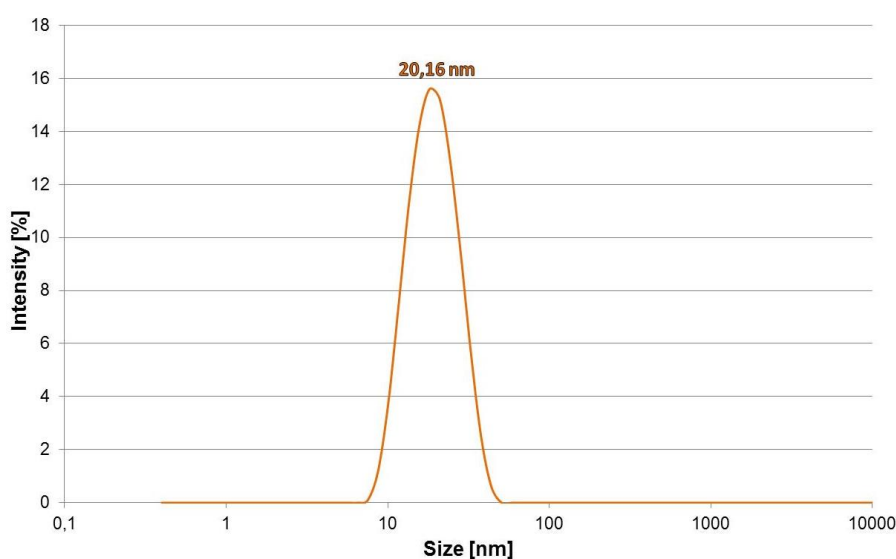


Fig. 3.8. Size distribution profile of $\text{NH}_3\text{-m}$ sample ($[\text{NH}_3]_{\text{aq}}=1.5 \text{ M}$; $\text{pH}_{\text{NH}_3(\text{sol.})}=11 - 12$; $R_w = 14.6$)

In the light of these results some conclusions can be done:

- the problem regarding the stability of the TMAH-m mixture seems depend mainly from the pH of the TMAH aqueous solution which is probably too high and affect the adsorption of the surfactant molecules around the water core. It is demonstrated that with a little addition of an acidic agent (HNO_3), from an opalescent appearance, TMAH-m turns into a transparent and stable system.

Another feature, in some way related to the pH, is the molar concentration of the TMAH in the aqueous solution which can be decreased increasing microemulsion stability. Nevertheless it is necessary to avoid an high dilution rate of the TMAH solution, otherwise when TMAH-m is mixed with CZ-m, no precipitation occurs;

- the R_w affect the stability of TMAH microemulsion, but probably it isn't the only determining factor, even because the CZ microemulsion is stable at the same R_w value of 14.6;
- the nature of the precipitating agent, in some way is related to the pH effect, because through the modification of the precipitating agent, inevitably the acid – base properties of the system are changed. It is necessary to find a precipitating agent which produced the right pH of the aqueous solution able to create stable microemulsion but also able to allow the pH increase necessary for the precipitation of hydroxides of Ce and Zr.

At this point, any TMAH-m stable systems is obtained and when they are mixed with the CZ-m sample result final mixtures that seems to be not stable due to the settle – down of a solid in a gel-like form.

3.2.5 Effect of the amount of the organic compounds

The following goal was to try to obtain a final microemulsion system in which the solid particles located inside the micelles remain in suspension, without any settling – down phenomenon. This stable situation should permits to work in a well – defined and confined environment in which is even possible to carry out further functionalization (for instance a controlled precipitation of a metal on a single particle into the micelle) in order to obtain a really tailor – made catalyst. A wide statistic study on this topic is carried out, making several series of tests in which all the component of the TMAH-m microemulsion system are modified. Until now the organic phase is maintained the same of which characterizing the CZ-m sample, but his effect on the stability of the TMAH-m mixture can't be excluded.

With this aim, starting from the standard opalescent TMAH-m mixture, the relative amount of 1-hexanol, Triton X-100 and n-heptane are modified following the same criteria adopted in the tests carried out varying the amount of water in the TMAH aqueous solution (see paragraph 3.2.2 – Table 3.1), changing consecutively 1-hexanol, Triton X-100 and n-heptane. Each addition of each component is calculated in order to obtain an increase of the moles analogous to what have been done for the addition of water (paragraph 3.2.2) to facilitate cross comparisons. Table 3.2 shows in details the

values of the parameters investigated in all of the tests carried out increasing the amount of 1-hexanol. For each TMAH-m modified mixture, the stability is observed, and the results are reported in the tables below in red boxes, if a phase separation occurs, in slightly red boxes, if the turbidity of the system is lower or in green boxes if an optical isotropy is achieved. Following the same methodology, in Table 3.3 and Table 3.4 are reported the results relative to the effect of surfactant and the n – heptane, respectively.

After all of these tests, is possible to observe how a certain phase stability is obtained for a very few mixtures. The solutions with a transparent appearance are obtained in the series of the TEST 5, mainly after the addition of Triton X-100 (Table 3.3) and n-heptane (Table 3.4). In these cases, the difference between the composition of the TMAH-m mixture and the CZ-m one become significant; therefore even if the TMAH-m is stable, the micelles that compose it, would be too different from that of the CZ-m mixture to allow the hypothesis of a formation of a non-homogeneous final microemulsion system. Furthermore also the volumes involved for the synthesis have to be taken into account. In general, the microemulsion synthesis require large volumes of solvent in order to obtain the best dispersion of the micelles; problem which become even larger if the only TMAH-m systems that are stable are exactly those obtained with the higher amount of each compounds.

RESULTS AND DISCUSSION

> Hexanol (co-surf.)										
TEST 1						TEST 2				
Parameters investigated	32,81					Parameters investigated	33,34			
	V TOT cad. [mL] Mother Sol.	TEST 1-1	TEST 1-2	TEST 1-3	TEST 1-4		V TOT cad. [mL] Mother Sol.	TEST 2-1	TEST 2-2	TEST 2-3
H ₂ O [mol]	0,113	0,113	0,113	0,113	0,113	H ₂ O [mol]	0,145	0,145	0,145	0,145
Triton X-100 [mol]	0,008	0,008	0,008	0,008	0,008	Triton X-100 [mol]	0,008	0,008	0,008	0,008
1-Hexanol (co-surfactant) [mol]	0,037	0,048	0,064	0,096	0,192	1-Hexanol (co-surfactant) [mol]	0,037	0,048	0,064	0,096
Heptane [mol]	0,147	0,147	0,147	0,147	0,147	Heptane [mol]	0,147	0,147	0,147	0,147
TMAH [mol]	0,003	0,003	0,003	0,003	0,003	TMAH [mol]	0,003	0,003	0,003	0,003
Rw [H ₂ O/Surf. Molar ratio]	14,631	14,631	14,631	14,631	14,631	Rw [H ₂ O/Surf. Molar ratio]	18,854	18,854	18,854	18,854
Heptane/H ₂ O [Molar Ratio]	1,302	1,302	1,302	1,302	1,302	Heptane/H ₂ O [Molar Ratio]	1,011	1,011	1,011	1,011
Hexanol/H ₂ O [Molar Ratio]	0,330	0,426	0,568	0,851	1,703	Hexanol/H ₂ O [Molar Ratio]	0,256	0,330	0,440	0,661
TMAH/H ₂ O [Molar Ratio]	0,028	0,028	0,028	0,028	0,028	TMAH/H ₂ O [Molar Ratio]	0,022	0,022	0,022	0,022
TMAH Concentration [M]	1,547	1,547	1,547	1,547	1,547	TMAH Concentration [M]	1,200	1,200	1,200	1,200
TMAH-m stability	Phase separ.	Phase separ.	Phase separ.	Phase separ.	Phase separ.	TMAH-m stability	Phase separ.	Phase separ.	Phase separ.	Phase separ.
Final microem stability	Phase separ.					Final microem stability	Phase separ.			
Weight of Hexanol to add [g]	0,00	1,10	2,74	6,01	15,83	Weight of Hexanol to add [g]	0,00	1,10	2,74	6,01
TEST 3						TEST 4				
Parameters investigated	34,21					Parameters investigated	35,96			
	V TOT cad. [mL] Mother Sol.	TEST 3-1	TEST 3-2	TEST 3-3	TEST 3-4		V TOT cad. [mL] Mother Sol.	TEST 4-1	TEST 4-2	TEST 4-3
H ₂ O [mol]	0,194	0,194	0,194	0,194	0,194	H ₂ O [mol]	0,291	0,291	0,291	0,291
Triton X-100 [mol]	0,008	0,008	0,008	0,008	0,008	Triton X-100 [mol]	0,008	0,008	0,008	0,008
1-Hexanol (co-surfactant) [mol]	0,037	0,048	0,064	0,096	0,192	1-Hexanol (co-surfactant) [mol]	0,037	0,048	0,064	0,096
Heptane [mol]	0,147	0,147	0,147	0,147	0,147	Heptane [mol]	0,147	0,147	0,147	0,147
TMAH [mol]	0,003	0,003	0,003	0,003	0,003	TMAH [mol]	0,003	0,003	0,003	0,003
Rw [H ₂ O/Surf. Molar ratio]	25,139	25,139	25,139	25,139	25,139	Rw [H ₂ O/Surf. Molar ratio]	37,708	37,708	37,708	37,708
Heptane/H ₂ O [Molar Ratio]	0,758	0,758	0,758	0,758	0,758	Heptane/H ₂ O [Molar Ratio]	0,505	0,505	0,505	0,505
Hexanol/H ₂ O [Molar Ratio]	0,192	0,248	0,330	0,496	0,991	Hexanol/H ₂ O [Molar Ratio]	0,128	0,165	0,220	0,330
TMAH/H ₂ O [Molar Ratio]	0,016	0,016	0,016	0,016	0,016	TMAH/H ₂ O [Molar Ratio]	0,011	0,011	0,011	0,011
TMAH Concentration [M]	0,900	0,900	0,900	0,900	0,900	TMAH Concentration [M]	0,600	0,600	0,600	0,600
TMAH-m stability	Phase separ.	Phase separ.	Phase separ.	Phase separ.	Phase separ.	TMAH-m stability	Phase separ.	TRANSP	Phase separ.	Phase separ.
Final microem stability	Phase separ.					Final microem stability	Phase separ.			
Weight of Hexanol to add [g]	0,00	1,10	2,74	6,01	15,83	Weight of Hexanol to add [g]	0,00	1,10	2,74	6,01
TEST 5										
Parameters investigated	41,19									
	V TOT cad. [mL] Mother Sol.	TEST 5-1	TEST 5-2	TEST 5-3	TEST 5-4					
H ₂ O [mol]	0,582	0,582	0,582	0,582	0,582					
Triton X-100 [mol]	0,008	0,008	0,008	0,008	0,008					
1-Hexanol (co-surfactant) [mol]	0,037	0,048	0,064	0,096	0,192					
Heptane [mol]	0,147	0,147	0,147	0,147	0,147					
TMAH [mol]	0,003	0,003	0,003	0,003	0,003					
Rw [H ₂ O/Surf. Molar ratio]	75,416	75,416	75,416	75,416	75,416					
Heptane/H ₂ O [Molar Ratio]	0,253	0,253	0,253	0,253	0,253					
Hexanol/H ₂ O [Molar Ratio]	0,064	0,083	0,110	0,165	0,330					
TMAH/H ₂ O [Molar Ratio]	0,005	0,005	0,005	0,005	0,005					
TMAH Concentration [M]	0,300	0,300	0,300	0,300	0,300					
TMAH-m stability	Phase separ.	TRANSP	Clody	Clody	Clody					
Final microem stability	Phase separ.									
Weight of Hexanol to add [g]	0,00	1,10	2,74	6,01	15,83					

Table 3.2. Parameters investigated in all of the tests carried out on the investigation of the effect related to the increase of the amount of 1-hexanol. The colors of the boxes are chosen with the same criteria discussed for the data represented in Table 3.1.

RESULTS AND DISCUSSION

> Triton X-100 (Surf.)											
TEST 1						TEST 2					
Parameters investigated	REFERENCE TEST	TEST 1-1-1	TEST 1-2-2	TEST 1-3-3	TEST 1-4-4	Parameters investigated	REFERENCE TEST	TEST 2-1-1	TEST 2-2-2	TEST 2-3-3	TEST 2-4-4
H ₂ O [mol]	2,634	0,113	0,113	0,113	0,113	H ₂ O [mol]	2,634	0,145	0,145	0,145	0,145
Triton X-100 [mol]	0,180	0,010	0,013	0,020	0,040	Triton X-100 [mol]	0,180	0,010	0,013	0,020	0,040
1-Hexanol [co-surfactant] [mol]	0,870	0,048	0,064	0,096	0,192	1-Hexanol [co-surfactant] [mol]	0,870	0,048	0,064	0,096	0,192
Heptane [mol]	3,430	0,147	0,147	0,147	0,147	Heptane [mol]	3,430	0,147	0,147	0,147	0,147
TMAH [mol]	0,073	0,003	0,003	0,003	0,003	TMAH [mol]	0,073	0,003	0,003	0,003	0,003
Rw [H ₂ O/Surf. Molar ratio]	14,631	11,353	8,515	5,677	2,838	Rw [H ₂ O/Surf. Molar ratio]	14,631	14,631	10,973	7,315	3,658
Heptane/H ₂ O [Molar Ratio]	1,302	1,302	1,302	1,302	1,302	Heptane/H ₂ O [Molar Ratio]	1,302	1,011	1,011	1,011	1,011
Hexanol/H ₂ O [Molar Ratio]	0,330	0,426	0,568	0,851	1,703	Hexanol/H ₂ O [Molar Ratio]	0,330	0,330	0,440	0,661	1,321
TMAH/H ₂ O [Molar Ratio]	0,028	0,028	0,028	0,028	0,028	TMAH/H ₂ O [Molar Ratio]	0,028	0,022	0,022	0,022	0,022
TMAH Concentration [M]	1,546	1,547	1,547	1,547	1,547	TMAH Concentration [M]	1,546	1,200	1,200	1,200	1,200
TMAH-m stability	Phase separ.	Phase separ.	Phase separ.	Phase separ.	Phase separ.	TMAH-m stability	Phase separ.	Phase separ.	Phase separ.	Phase separ.	Phase separ.
Final microem stability	Phase separ.					Final microem stability	Phase separ.				
Weight of Triton X-100 to add [g]		1,39	3,46	7,60	20,03	Weight of Triton X-100 to add [g]		1,39	3,46	7,60	20,03
TEST 3						TEST 4					
Parameters investigated	REFERENCE TEST	TEST 3-1-1	TEST 3-2-2	TEST 3-3-3	TEST 3-4-4	Parameters investigated	REFERENCE TEST	TEST 4-1-1	TEST 4-2-2	TEST 4-3-3	TEST 4-4-4
H ₂ O [mol]	2,634	0,194	0,194	0,194	0,194	H ₂ O [mol]	2,634	0,291	0,291	0,291	0,291
Triton X-100 [mol]	0,180	0,010	0,013	0,020	0,040	Triton X-100 [mol]	0,180	0,010	0,013	0,020	0,040
1-Hexanol [co-surfactant] [mol]	0,870	0,048	0,064	0,096	0,192	1-Hexanol [co-surfactant] [mol]	0,870	0,048	0,064	0,096	0,192
Heptane [mol]	3,430	0,147	0,147	0,147	0,147	Heptane [mol]	3,430	0,147	0,147	0,147	0,147
TMAH [mol]	0,073	0,003	0,003	0,003	0,003	TMAH [mol]	0,073	0,003	0,003	0,003	0,003
Rw [H ₂ O/Surf. Molar ratio]	14,631	19,508	14,631	9,754	4,877	Rw [H ₂ O/Surf. Molar ratio]	14,631	29,261	21,946	14,631	7,315
Heptane/H ₂ O [Molar Ratio]	1,302	0,758	0,758	0,758	0,758	Heptane/H ₂ O [Molar Ratio]	1,302	0,505	0,505	0,505	0,505
Hexanol/H ₂ O [Molar Ratio]	0,330	0,248	0,330	0,496	0,991	Hexanol/H ₂ O [Molar Ratio]	0,330	0,165	0,220	0,330	0,661
TMAH/H ₂ O [Molar Ratio]	0,028	0,016	0,016	0,016	0,016	TMAH/H ₂ O [Molar Ratio]	0,028	0,011	0,011	0,011	0,011
TMAH Concentration [M]	1,546	0,900	0,900	0,900	0,900	TMAH Concentration [M]	1,546	0,600	0,600	0,600	0,600
TMAH-m stability	Phase separ.	Phase separ.	Phase separ.	Phase separ.	Phase separ.	TMAH-m stability	Phase separ.	TRANSP	Phase separ.	Phase separ.	Phase separ.
Final microem stability	Phase separ.					Final microem stability	Phase separ.				
Weight of Triton X-100 to add [g]		1,39	3,46	7,60	20,03	Weight of Triton X-100 to add [g]		1,39	3,46	7,60	20,03
TEST 5											
Parameters investigated	REFERENCE TEST	TEST 5-1-1	TEST 5-2-2	TEST 5-3-3	TEST 5-4-4						
H ₂ O [mol]	2,634	0,582	0,582	0,582	0,582						
Triton X-100 [mol]	0,180	0,010	0,013	0,020	0,040						
1-Hexanol [co-surfactant] [mol]	0,870	0,048	0,064	0,096	0,192						
Heptane [mol]	3,430	0,147	0,147	0,147	0,147						
TMAH [mol]	0,073	0,003	0,003	0,003	0,003						
Rw [H ₂ O/Surf. Molar ratio]	14,631	58,523	43,892	29,261	14,631						
Heptane/H ₂ O [Molar Ratio]	1,302	0,253	0,253	0,253	0,253						
Hexanol/H ₂ O [Molar Ratio]	0,330	0,083	0,110	0,165	0,330						
TMAH/H ₂ O [Molar Ratio]	0,028	0,005	0,005	0,005	0,005						
TMAH Concentration [M]	1,546	0,300	0,300	0,300	0,300						
TMAH-m stability	Phase separ.	TRANSP	TRANSP	TRANSP	Phase separ.						
Final microem stability	Phase separ.										
Weight of Triton X-100 to add [g]		1,39	3,46	7,60	20,03						

Table 3.3. Parameters investigated in all of the tests carried out on the investigation of the effect related to the increase of the amount of Triton X-100

RESULTS AND DISCUSSION

> Heptane (solvent)											
TEST 1						TEST 2					
Parameters investigated	REFERENCE TEST	TEST 1-1-1-1	TEST 1-2-2-2	TEST 1-3-3-3	TEST 1-4-4-4	Parameters investigated	REFERENCE TEST	TEST 2-1-1-1	TEST 2-2-2-2	TEST 2-3-3-3	TEST 2-4-4-4
H ₂ O [mol]	2,634	0,113	0,113	0,113	0,113	H ₂ O [mol]	2,634	0,145	0,145	0,145	0,145
Triton X-100 [mol]	0,180	0,010	0,013	0,020	0,040	Triton X-100 [mol]	0,180	0,010	0,013	0,020	0,040
1-Hexanol (co-surfactant) [mol]	0,870	0,048	0,064	0,096	0,192	1-Hexanol (co-surfactant) [mol]	0,870	0,048	0,064	0,096	0,192
Heptane [mol]	3,430	0,189	0,253	0,379	0,758	Heptane [mol]	3,430	0,189	0,253	0,379	0,758
TMAH [mol]	0,073	0,003	0,003	0,003	0,003	TMAH [mol]	0,073	0,003	0,003	0,003	0,003
Rw [H ₂ O/Surf. Molar ratio]	14,631	11,353	8,515	5,677	2,838	Rw [H ₂ O/Surf. Molar ratio]	14,631	14,631	10,973	7,315	3,658
Heptane/H ₂ O [Molar Ratio]	1,302	1,678	2,238	3,357	6,714	Heptane/H ₂ O [Molar Ratio]	1,302	1,302	1,737	2,605	5,210
Hexanol/H ₂ O [Molar Ratio]	0,330	0,426	0,568	0,851	1,703	Hexanol/H ₂ O [Molar Ratio]	0,330	0,330	0,440	0,661	1,321
TMAH/H ₂ O [Molar Ratio]	0,028	0,028	0,028	0,028	0,028	TMAH/H ₂ O [Molar Ratio]	0,028	0,022	0,022	0,022	0,022
TMAH Concentration [M]	1,546	1,547	1,547	1,547	1,547	TMAH Concentration [M]	1,546	1,200	1,200	1,200	1,200
TMAH-m stability	Phase separ.	Slightly cloudy	Slightly cloudy	Slightly cloudy	Slightly cloudy	TMAH-m stability	Phase separ.	Cloudy	Slightly cloudy	Slightly cloudy	Slightly cloudy
Final microem stability	Phase separ.					Final microem stability	Phase separ.				
Weight of Heptane to add [g]		4,25	10,58	23,23	61,20	Weight of Heptane to add [g]		4,25	10,58	23,23	61,20
TEST 3						TEST 4					
Parameters investigated	REFERENCE TEST	TEST 3-1-1-1	TEST 3-2-2-2	TEST 3-3-3-3	TEST 3-4-4-4	Parameters investigated	REFERENCE TEST	TEST 4-1-1-1	TEST 4-2-2-2	TEST 4-3-3-3	TEST 4-4-4-4
H ₂ O [mol]	2,634	0,194	0,194	0,194	0,194	H ₂ O [mol]	2,634	0,291	0,291	0,291	0,291
Triton X-100 [mol]	0,180	0,010	0,013	0,020	0,040	Triton X-100 [mol]	0,180	0,010	0,013	0,020	0,040
1-Hexanol (co-surfactant) [mol]	0,870	0,048	0,064	0,096	0,192	1-Hexanol (co-surfactant) [mol]	0,870	0,048	0,064	0,096	0,192
Heptane [mol]	3,430	0,189	0,253	0,379	0,758	Heptane [mol]	3,430	0,189	0,253	0,379	0,758
TMAH [mol]	0,073	0,003	0,003	0,003	0,003	TMAH [mol]	0,073	0,003	0,003	0,003	0,003
Rw [H ₂ O/Surf. Molar ratio]	14,631	19,508	14,631	9,754	4,877	Rw [H ₂ O/Surf. Molar ratio]	14,631	29,261	21,946	14,631	7,315
Heptane/H ₂ O [Molar Ratio]	1,302	0,977	1,302	1,954	3,907	Heptane/H ₂ O [Molar Ratio]	1,302	0,651	0,868	1,302	2,605
Hexanol/H ₂ O [Molar Ratio]	0,330	0,248	0,330	0,496	0,991	Hexanol/H ₂ O [Molar Ratio]	0,330	0,165	0,220	0,330	0,661
TMAH/H ₂ O [Molar Ratio]	0,028	0,016	0,016	0,016	0,016	TMAH/H ₂ O [Molar Ratio]	0,028	0,011	0,011	0,011	0,011
TMAH Concentration [M]	1,546	0,900	0,900	0,900	0,900	TMAH Concentration [M]	1,546	0,600	0,600	0,600	0,600
TMAH-m stability	Phase separ.	Cloudy	Cloudy	Cloudy	Slightly cloudy	TMAH-m stability	Phase separ.	TRANSP	TRANSP	Cloudy	Slightly cloudy
Final microem stability	Phase separ.					Final microem stability	Phase separ.				
Weight of Heptane to add [g]		4,25	10,58	23,23	61,20	Weight of Heptane to add [g]		4,25	10,58	23,23	61,20
TEST 5											
Parameters investigated	REFERENCE TEST	TEST 5-1-1-1	TEST 5-2-2-2	TEST 5-3-3-3	TEST 5-4-4-4						
H ₂ O [mol]	2,634	0,582	0,582	0,582	0,582						
Triton X-100 [mol]	0,180	0,010	0,013	0,020	0,040						
1-Hexanol (co-surfactant) [mol]	0,870	0,048	0,064	0,096	0,192						
Heptane [mol]	3,430	0,189	0,253	0,379	0,758						
TMAH [mol]	0,073	0,003	0,003	0,003	0,003						
Rw [H ₂ O/Surf. Molar ratio]	14,631	58,523	43,892	29,261	14,631						
Heptane/H ₂ O [Molar Ratio]	1,302	0,326	0,434	0,651	1,302						
Hexanol/H ₂ O [Molar Ratio]	0,330	0,083	0,110	0,165	0,330						
TMAH/H ₂ O [Molar Ratio]	0,028	0,005	0,005	0,005	0,005						
TMAH Concentration [M]	1,546	0,300	0,300	0,300	0,300						
TMAH-m stability	Phase separ.	Cloudy	TRANSP & more dense	TRANSP & more dense	TRANSP & more dense						
Final microem stability	Phase separ.										
Weight of Heptane to add [g]		4,25	10,58	23,23	61,20						

Table 3.4. Parameters investigated in all of the tests carried out on the investigation of the effect related to the increase of the amount of n-heptane

Therefore, from this wide, but preliminary, statistic study is possible to conclude that a TMAH-m stable system to be added to the already stable CZ-m one, able to originate a final microemulsion in which the solid inside the micelles remains in suspension, was not found. Is possible to continue the investigation modifying other parameters such as: the nature of the surfactant and the co-surfactant; trying other precipitating agent, even of organic nature, etc.... A study also on the effect that can have the temperature on the microemulsion system could be interesting. Anyway, it is not excluded that through this synthesis method is possible to achieve the formation of solids with particular characteristics in terms of structure and surface properties. Moreover, in literature is not clearly specified if all the two microemulsion mixtures and the final one must be stable with any occurrence of precipitation phenomenon. As hypothesized before (paragraph 3.2.1) the settling – down of the solid could be due to the high specific weight of the Ce and Zr hydroxides. Anyhow, catalytic supports have been synthesized through the microemulsion method and compared with those obtained following a more classic co-precipitation route, in order to verify if the synthetic procedure influence in a relevant way the characteristics of the solid.

3.3 Characterization of the calcined CZO samples

In the studied of a catalytic process, the main role is carry out by the active phase of the catalyst, generally characterized by a VIII group metal phase. Is possible to obtain a catalyst with the active phase present in the “bulk” of it, but in general the active metal is deposited on the surface of a solid acting as a support. Two main advantages derive from the latter strategy:

1. less quantity of the active metal is required to obtain the catalyst: this aspect is of a crucial importance especially when the active metal is very expensive;
2. the exploitation of the active surface area is higher than in “bulk” catalyst, because the metal is dispersed directly on the surface of the support, is often more available towards the reactive species than that obtained by reduction from the bulk of the solid.

Usually a catalytic support is defined as inert towards the reaction in which the catalyst is involved, but. often a support plays a significant role in the system either participating or not in the reaction mechanism. Beside the physical properties due to surface area and pore volume the deposition of a metal on the support, wil generate interactions between them. These interactions can have an electronic role due to their capabability to interact with the metal electron density or can cover a stabilizing role towards the mobility of the metal, that can occur during the reaction and deactivate the active phase by sintering. Reforming processes, in general, are subjected to these thermal and deactivation problems, hence the choice of the best support able to acton these features, attenuating them, is of a crucial importance.

In addition it has to be taken into account that supported catalysts give rise usually to lower interaction between metal and support than bulk systems thererore, in order to obtain a stable and active catalyst, it is of great interest to increase the interaction without decreasing the availability and the reactivity of the active phase on the surface.

Furthermore, as reported above (paragraph 1.2.2.1) ceria – zirconia mixed oxides (CZO) has been extensively studied, mainly for their peculiar ability to provide oxygen to the metal, thanks to the high oxygen mobility capacity of CeO_2 . This oxygen exchange capacity could be exploited in order to decrease the rate of deactivation deriving from the formation of carbonaceous species that deposit on the active sites of the catalyst. In fact, taking into account the mechanism through which the oxygen mobility and exchange phenomenon take place (already explained in the same paragraph (1.2.2.1)), is possible to hypothesized that the oxygen atoms present in the superficial layers of the CZO support migrate from their position toward the surface (Fig. 3.9). Here, these atoms can

get in contact with the carbonaceous species deposited on the active metal, oxidizing and converting them to CO and CO₂. In this way the metal surface become again available for the reactive species, thanks to the establishment of a “self – regeneration” cycle which reduces the rate of the deactivation, increasing the lifetime of the catalyst. The oxygen mobility can either increase the reaction rate according to some hypothesized reaction mechanism and kinetics.

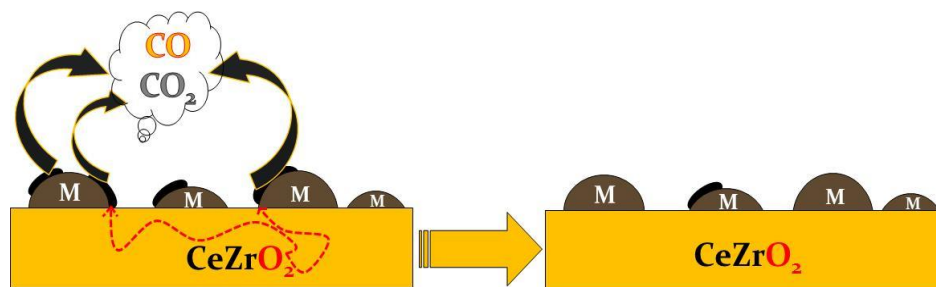


Fig. 3.9. Schematic representation of the “self – regeneration” phenomenon that take place thanks to the oxygen mobility capacity of the CZO support. M = active metal

Considering that the oxygen mobility depend in a significant way by the number and the nature of the defects characterizing the oxide framework, is clear how its value change in function of the crystalline structure of the support. For the CZO mixed oxide is demonstrated that the phase with higher oxygen exchange capacity is the Ce_{0.5}Zr_{0.5}O₂ one (see Table 1.4 – p. 38). This particular phase is not stable from a thermodynamic point of view, therefore is difficult to be formed through a classical synthesis methodology. For these reasons different comparisons will be carried out on CZO samples: i) the comparison between a classic co-precipitation route and the w/o microemulsion one has been made, pointing out the main advantages and drawbacks of each synthesis; ii) comparison among two different method for the inverse microemulsion; iii) comparison between two Ce/Zr ratio; iv) the preparation of bulk catalysts by microemulsion.

3.3.1 W/O Microemulsion vs Co-precipitation

3.3.1.1 XRD Characterization

The first comparison between the support obtained through microemulsion (CZO-m) and the co-precipitated one (CZO-cp) is carried out evaluating the nature of the crystalline phase formed by means of XRD analysis. The results are showed in Fig. 3.10, and is possible to observe how the patterns relative to the CZO-m samples are compatible with that recorded in the database list which identify the wished Ce_{0.5}Zr_{0.5}O₂ crystalline phase. The pattern, especially at high 2θ angles, is also compatible with a

slightly distorted cubic phase producing tetrahedral phase, typical of the equimolar Ce/Zr oxide. A similar pattern of the CZO-cp sample is obtained but its reflections are shifted towards lower 2θ angles. This small change in the position is an element significant enough to affirm that this sample is characterized by a phase, with a different composition than that of $\text{Ce}_{0.5}\text{Zr}_{0.5}\text{O}_2$. In fact, the reflections positions in this case correspond to the pattern that in the database list is relative to the $\text{Ce}_{0.6}\text{Zr}_{0.4}\text{O}_2$ phase, which has basically a cubic structure. Furthermore is also possible to observe that the $\text{Ce}_{0.5}\text{Zr}_{0.5}\text{O}_2$ phase is formed already at a relative low calcination temperature (500°C) and any segregation phase phenomenon is visible also at high calcination temperature (900°C), index of a good thermal stability of this phase.

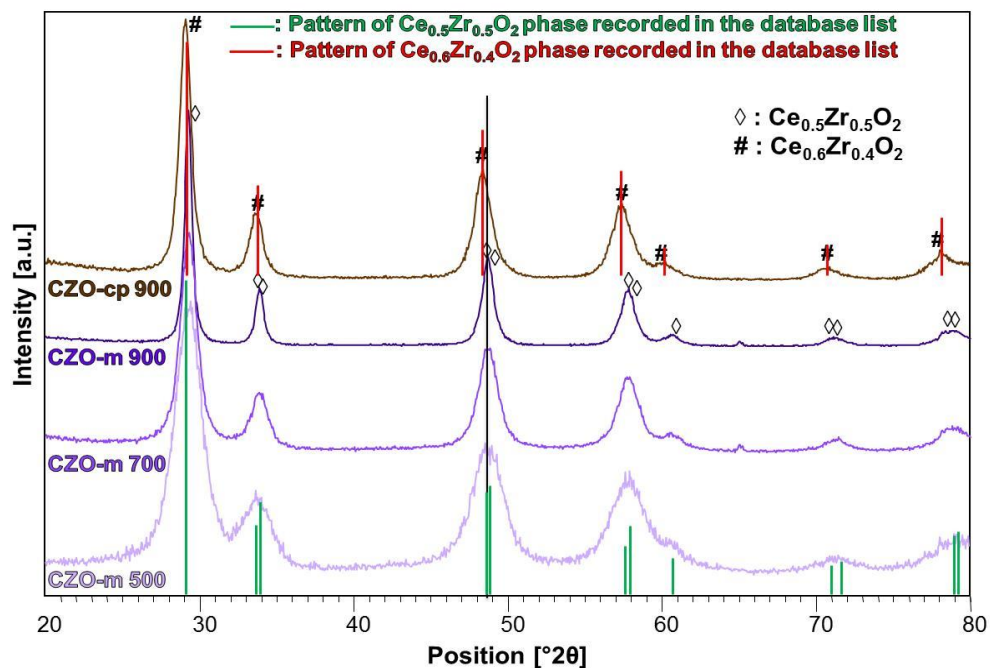


Fig. 3.10. XRD patterns of the CZO supports synthesized through microemulsion and co-precipitation method. CZO-m samples are compared also in terms of calcination temperature (500 , 700 and 900°C)

Also the thermal stability of these two supports have been investigated, calcining the samples until a temperature of 1100°C . The comparison between the patterns relative to those samples are reported in Fig. 3.11 and Fig. 3.12. From the thermal evolution can be observed that the co-precipitated support is more stable in comparison with the CZO-m one. In fact, is clear from Fig. 3.11 that increasing the calcination temperature up to 1000 (CZO-m1000) and especially 1100°C (CZO-m1100) the XRD patterns differences become less evident with respect to those relative to the samples calcined at 900°C (CZO-m900), indicating that a phase segregation phenomenon start at 1000°C , and is even more evident in the CZO-m1100 pattern. This is in accordance with literature [167,168] where is reported that under oxidizing conditions at $1000 - 1200^\circ\text{C}$ phase

separation into CeO_2 -rich and ZrO_2 -rich phases, typically occurs to give $\text{Ce}_{0.2}\text{Zr}_{0.8}\text{O}_2$ and $\text{Ce}_{0.8}\text{Zr}_{0.2}\text{O}_2$ compositions. In fact, the reflections relative to the $\text{Ce}_{0.12}\text{Zr}_{0.88}\text{O}_2$ phase and $\text{Ce}_{0.75}\text{Zr}_{0.25}\text{O}_2$ one are clearly evident in the CZO-m1100 pattern. The same behavior is not observed in the case of CZO-cp support (Fig. 3.12) in which a slight segregation phase effect is observed only in the sample calcined at the highest temperature (CZO-cp1100). Here are visible some reflections associated with the $\text{Ce}_{0.12}\text{Zr}_{0.88}\text{O}_2$ phase, in addition to those relative to the $\text{Ce}_{0.6}\text{Zr}_{0.4}\text{O}_2$ one. This behavior could be explainable considering that the CZO-cp support, already at a calcination temperature of 900°C (CZO-cp900), is characterized by a less defined XRD pattern, ascribable to the $\text{Ce}_{0.6}\text{Zr}_{0.4}\text{O}_2$ phase. Furthermore, differently from the microemulsion sample, the reflections do not become sharper after high temperature calcination. Therefore, it could be hypothesized that the segregation effect occurs with less evidence in the case of a not perfectly homogeneous systems (CZO-cp) because they are characterized by a mixture of several phases and the $\text{Ce}_{0.6}\text{Zr}_{0.4}\text{O}_2$ is actually the combination of different phases with different Ce/Zr ratio and with, most likely, a cubic structure.

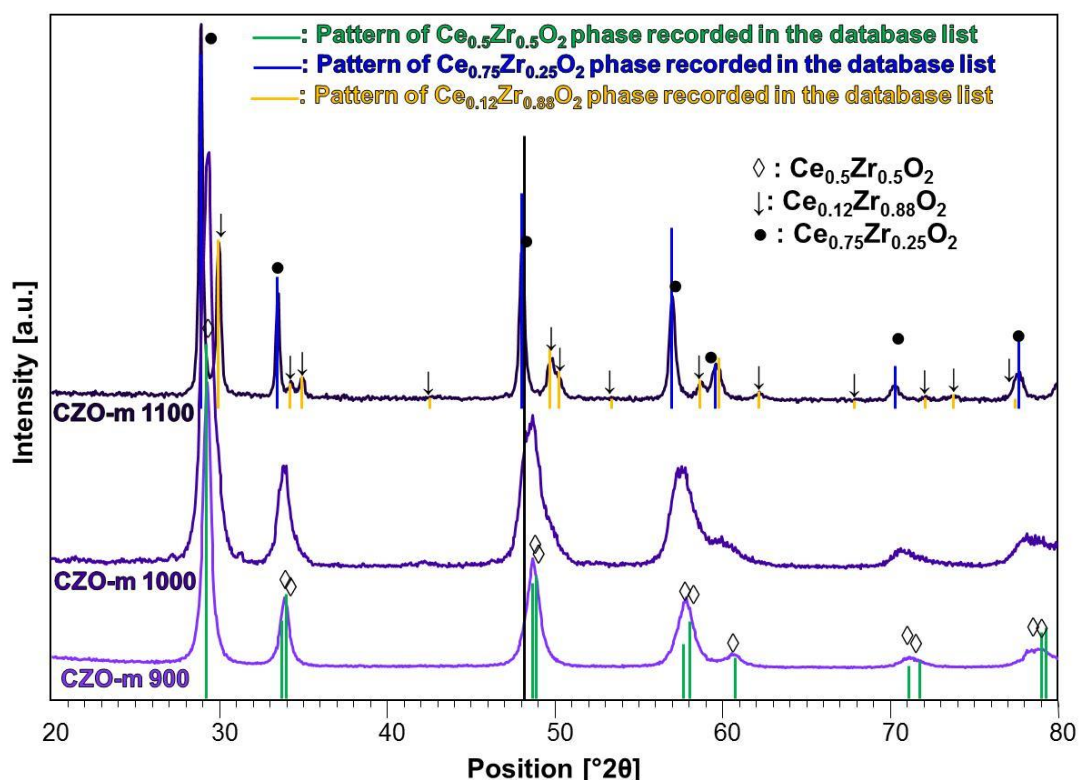


Fig. 3.11. XRD patterns of the CZO-m support calcined at different temperature

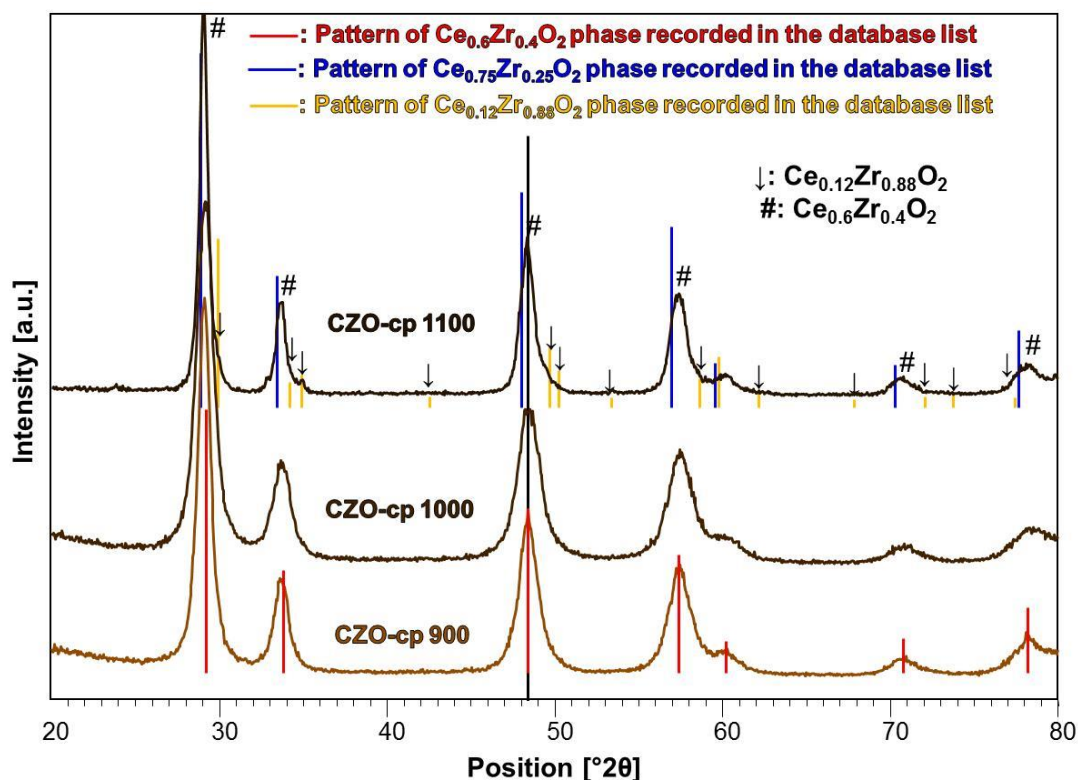


Fig. 3.12. XRD patterns of the CZO-cp support calcined at different temperatures

As mentioned above, some features of the phase diagram of the $\text{CeO}_2 - \text{ZrO}_2$ mixed system are still unresolved, due to the presence of the metastable phases (t' and t'') and the type of the distortion of the oxygen sublattice with sample origin. The differences between these tetragonal distorted phases are very small, but they could be the main reason from which depend the higher oxygen exchange capacity of the $\text{Ce}_{0.5}\text{Zr}_{0.5}\text{O}_2$ phase with respect to the other CZO compositional formulations. Hence, is very important to understand if one of the t – distorted phases characterized particularly the CZO-m sample, or it is present also in the CZO-cp sample. X – ray diffraction is not the ideal analysis useful to identify without ambiguity such a small differences between two crystalline phases, especially if dishomogeneous sample with multi-phases is hypothesized.

3.3.1.2 Raman Spectroscopy

Raman spectroscopy, is sensitive also toward small tetragonal distortions that can occur in a crystalline framework. In fact, in this technique are involved the vibrational modes of the atoms bonds, so also small displacements of some atoms can cause a disruption in a vibrational mode. Raman analysis are carried out for both the samples: CZO-m900 and CZO-cp900. The comparison between the two Raman profiles is reported in Fig. 3.13a. Zhang et al. [169] have investigated in details the transformations

that can occur in the CZO mixed system, focusing mainly on the discrimination between the cubic phase (*c*) and the *t''* phase.

For the *c* phase of pure ceria, one Raman mode is observed at 464 cm^{-1} . For the tetragonal phases *t*, *t'*, and *t''*, which all have space group $P4_2/nmc$, six Raman modes near 131 , 247 , 307 , 464 , 596 , and 626 cm^{-1} , are allowed [169]. These peaks are designated as peaks 1–6 in Fig. 3.13 b. Peaks 5 and 6 often overlap, while peak 4 of the tetragonal phase, overlaps with the strong cubic Raman peak at 464 cm^{-1} . Through these preliminary considerations, comparing between the Raman spectra of the CZO-m900 and CZO-cp900 samples (Fig. 3.13 a) with those reported by Zhang et al. (Fig. 3.13 b), is possible to affirm that each sample is in part characterized by the total symmetric stretching, detectable by the strong band centered at about 465 cm^{-1} compatible with the cubic and tetragonal phase. The Raman band in the 600 cm^{-1} range in ceria has been attributed to defects [170,171] and oxygen displacements that distort the cubic structure, breaking the cubic symmetry and selection rules of the cubic space group [172]. Raman spectra of tetragonal ZrO_2 (*t*) show this peak having the highest frequency centered at about 650 cm^{-1} accompanied by a low-frequency shoulder, centered around 620 cm^{-1} [173]. The appearance of this band for low zirconia concentration samples, its intensity increase with higher zirconia concentration, and its large width skewing towards 650 cm^{-1} with increasing zirconia content, suggest that this band is associated with *t* phase-like lattice distortions and their associated defects. Moreover, Zhang et al. [169] affirm that the most significant band which determine the presence of *t''* phase, is the band labeled with the number 3 in Fig. 3.13 b at about 300 cm^{-1} . According to this interpretation, is possible to affirm that the CZO-m sample is different from the CZO-cp one. In the CZO-m900 profile is clearly visible a band at about 300 cm^{-1} much more stronger than which detectable in the CZO-cp900 profile, indicating an higher relevance of the *t''* phase in the microemulsion sample than in the co-precipitated one. This structural difference is further confirmed by the band at about 620 cm^{-1} . As already discussed above, this band is attributable to defects relative to tetragonal lattice distortions, and the greater definition of this band in the CZO-m900 profile indicates an higher tetragonal distorted nature of this sample with respect to the CZO-cp900 one.

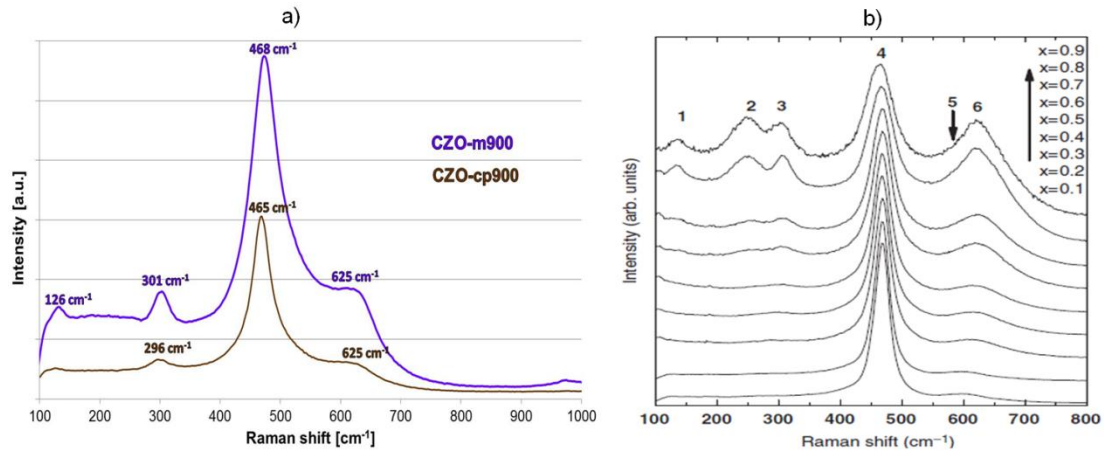


Fig. 3.13. a) Raman spectra of CZO-m900 and CZO-cp900 samples; b) Raman spectra of $(1-x)\text{CeO}_2 - x\text{ZrO}_2$ samples annealed at 800°C [169]

3.3.1.3 TPR/O/R Characterization

TPR/O/R profiles depend on many factors such as phase composition and stability, surface area, defects and phase crystal size, which are different by changing the preparation method.

Fig. 3.14 shows the comparison between the reduction profiles obtained through a Temperature Programmed Reduction/Oxidation/Reduction (TPR/O/R) cycle at which CZO-m900 and CZO-cp900 are subjected. From this kind of analysis it is clear how these two samples are different also in terms of the redox properties. All the reduction profiles recorded are characterized by a single peak centered at different temperatures. These patterns are noticeably different from that of pure ceria which are characterized by the presence of two distinct peaks at about 500°C and 900°C attributed to the reductions of the surface and the bulk, respectively [174]. The generally accepted argument to explain this profile is that the surface and bulk reduction occurs concurrently. Thus, insertion of ZrO_2 into the cubic CeO_2 resulted in a distortion on the mixed oxide which allowed a higher mobility of the lattice oxygen [175,176,177], increasing the reducibility of the mixed oxide. Anyway, the reduction temperatures of the two samples are very different; precisely CZO-cp sample reduces itself at a temperature (550°C) of about $170 - 180^\circ\text{C}$ lower compared to those at which reduces CZO-m sample (725°C). This effect could depend on the difference in the crystalline phases that characterize the two samples. This hypothesis is also confirmed by a literature study [178] in which it is reported that the substitution of zirconium by cerium ions in the oxide structure could improve the bulk reducibility of the solids and this kind of reducibility roughly increased when the cerium content in the materials increased. This is a further feature that is in agreement with the difference between the crystalline phases of the CZO-m and CZO-cp samples. In fact, the

higher reducibility of the CZO-cp900 sample probably depend by the higher Ce amount present in the $Ce_{0.6}Zr_{0.4}O_2$ phase with respect to which composing the $Ce_{0.5}Zr_{0.5}O_2$ phase.

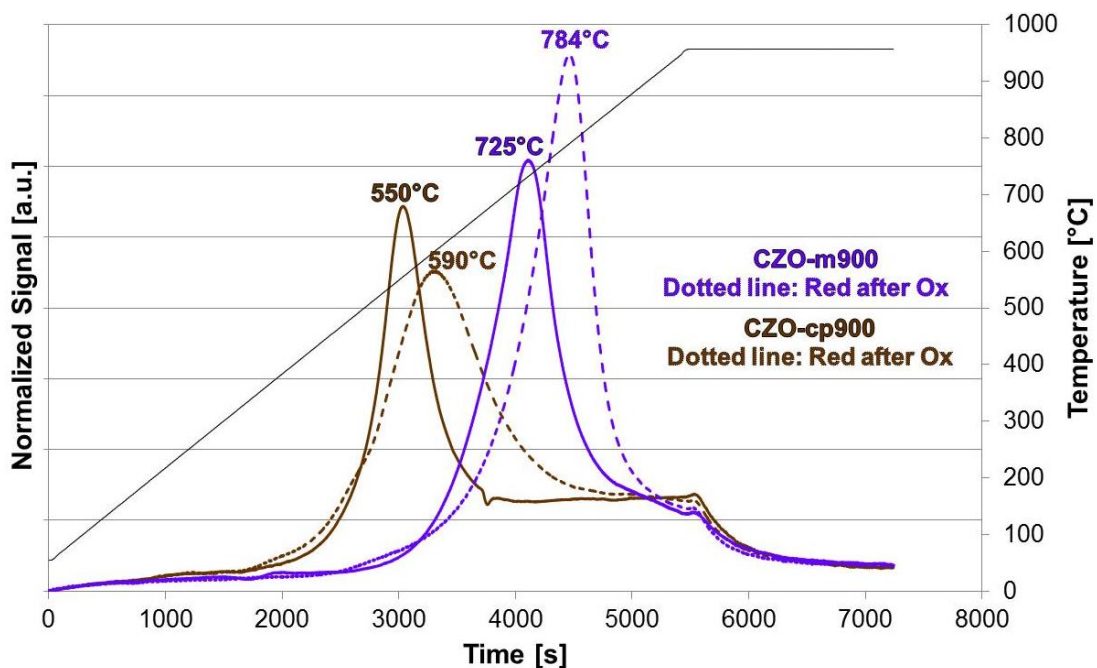


Fig. 3.14. H_2 -TPR profiles of CZO-m900 and CZO-cp900 samples

3.3.1.4 TEM Characterization

A deeper investigation on morphology can show the difference related to the synthesis procedure influencing the final solid material. It can derive from an investigation regarding the electron microscopy and imaging of the microemulsion and the co-precipitation samples, through TEM analysis. From Fig. 3.15 is clear how the CZO-m sample is characterized by a much more homogeneous particles size below around 20 – 30 nm with a similar spherical shape, while the CZO-cp sample shows agglomerates with not well – defined particles and a lower homogeneity. The difference in morphology related to the preparation method are evident notwithstanding the sample have been calcined at high temperature (900°C).

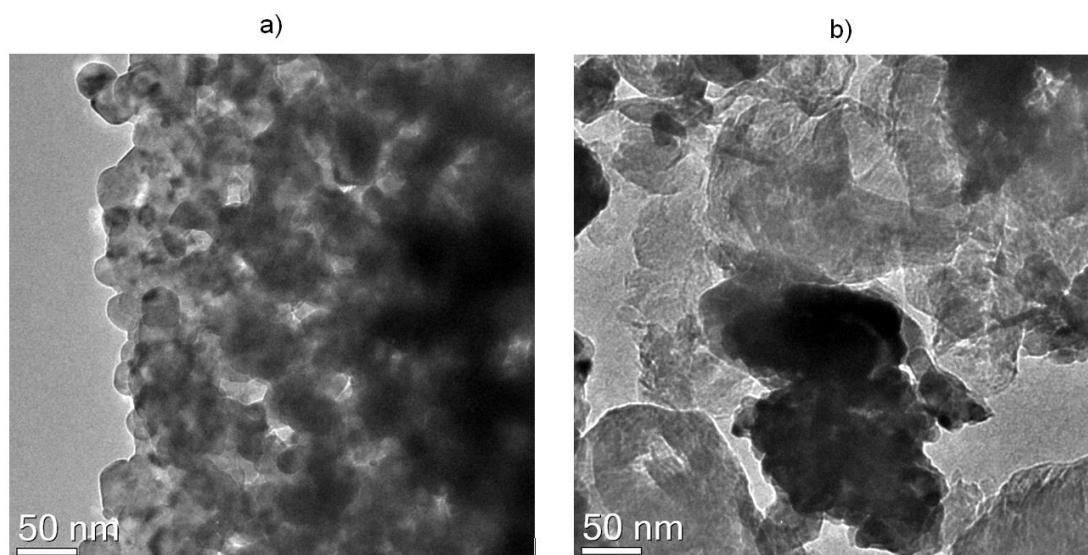


Fig. 3.15. TEM images of the samples: a) CZO-m900 and b) CZO-cp900

Furthermore, some macro zones of each sample are investigated through EDS spectrometry in order to identify if the compositional formulation of the CZO-m sample is different from which characterizing the CZO-cp one. For each zone, 3 – 5 spectra are recorded, and an average of the elementary analysis values for each zone of CZO-m900 and CZO-cp900 samples is reported in Table 3.5 and Table 3.6, respectively. These data confirm the XRD results in terms of the differences between the elementary compositions characterizing the crystalline phase of these two support. In fact, comparing mainly the atomic percentage values of Ce and Zr in the Tables below, is clear how those relative to the CZO-m900 sample (Table 3.5) are close to an ideal Ce/Zr atomic ratio of 50/50, typical of the $\text{Ce}_{0.5}\text{Zr}_{0.5}\text{O}_2$ phase, while values relative to the CZO-cp900 are more compatible with the $\text{Ce}_{0.6}\text{Zr}_{0.4}\text{O}_2$ phase, characterized by a Ce/Zr atomic ratio of 60/40.

	Element	Weight [%]	Uncertainty [%]	Atomic [%]
ZONE 1	Zr (L)	42.74	0.33	53.41
	Ce (L)	57.25	0.41	46.58
ZONE 2	Zr (L)	39.19	0.31	49.75
	Ce (L)	60.80	0.38	50.24
ZONE 3	Zr (L)	38.87	0.31	49.41
	Ce (L)	61.12	0.38	50.58

Table 3.5. Average values of elementary analysis carried out through EDX acquisition on three different macro zones of the CZO-m900 sample

	Element	Weight [%]	Uncertainty [%]	Atomic [%]
ZONE 1	Zr (L)	28.36	0.40	37.82
	Ce (L)	71.63	0.59	62.17
ZONE 2	Zr (L)	30.55	0.47	40.32
	Ce (L)	69.44	0.63	59.67
ZONE 3	Zr (L)	25.87	0.22	34.90
	Ce (L)	74.12	0.34	65.09

Table 3.6. Average values of elementary analysis carried out through EDX acquisition on three different macro zones of the CZO-cp900 sample

3.3.1.5 Surface Area and Porosimetry Characterization

Another characterization carried out to understand better the properties related to the morphological aspect of the supports is the porosimetry. The study of the acces and the area of the surface is of crucial importance in an heterogeneous catalytic process both for the impregnation procedure that produce the final catalyst, and the diffusion and reaction that take place at the surface during catalytic tests. Hence the support surface morphology could play a fundamental role regarding the dispersion of the active phase on it and, consequently, the activity of the catalyst.

From a porosimetry analysis is possible to obtain several informations about the nature of the pores characterizing the surface of a catalytic support. First of all is necessary to distinguish if the solid investigated belong to the micro-, meso- or macroporous category. These three material family are different one from each other in terms of porous size. Material with porous sizes comprise between 0 – 20 Å are microporous; mesoporous are those material with pores size between 20 – 500 Å and pores between 500 – 1000 Å are characteristic of a macroporous solid.

Is possible to understand to which class the CZO-m and CZO-cp supports belong, from the shape of N₂ adsorption – desorption isotherms. In Fig. 3.16 are showed these isotherms of the CZO-m900 and CZO-cp900 samples and their clear differences. According to the classification reported by Brunauer et al. [179] the CZO-m900 is characterized by isotherms types relative to mesoporous materials and specifically by a type-II isotherms, instead CZO-cp900 present a typical profile of type-IV isotherms. However, the main feature from which is possible to discriminate the shape of porous characterizing different samples, is the type (shape) of the hysteresis loop which forms between the two isotherms [180]. The display of a hysteresis loop in adsorption isotherms is due to occurrence of capillary condensation of the adsorbate [181,182,183], and the way in which the condensation occurs depend by the shape of the porous. Gregg at al. [180] reported a classification of the hysteresis loop types, thus according to

them, CZO-m900 present a type-H3 hysteresis, while a type-H2 characterize CZO-cp900 support. A type-H2 loop is believed to be associated with ink-bottle-like pores of varying radius, often generated by agglomerates or compacts of spheroidal particles of non-uniform size and arrangement, instead a type-H3 is attributed to adsorbate condensation in capillary spaces between parallel plates or open slit – shaped capillaries. These results confirm an higher non – homogeneous nature of the CZO-cp900 with respect to the CZO-m900 sample, already hypothesized from the TEM images reported in Fig. 3.15. Another feature to be highlighted is the higher quantity of the adsorbate that is able to adsorb the CZO-m900 in comparison with the CZO-cp900. This could be due to a significant difference between the surface characteristics and area of these two samples. In fact, observing the data reported in Table 3.7, it could be affirm that in terms of surface area, the CZO-m900 sample is even characterized by a lower value ($11 \text{ m}^2/\text{g}$) than that of the CZO-cp900 one ($13 \text{ m}^2/\text{g}$). On the other hand, the pores volume values show larger differences (CZO-m900 present an higher volume of pores), while the main difference between the two supports is the value of the average pore diameter. In the CZO-m900 are present pores with a diameter about five time bigger than those relative to the CZO-cp900 sample. The comparison between the pore size distribution profiles relative to the two samples is showed in Fig. 3.17, and is clear how the distribution profile of the co-precipitated sample present an intense peak centered at about $40 - 50 \text{ \AA}$, while the CZO-m900 profile has a bi-modal trend with the major peak centered at high diameter values ($250 - 270 \text{ \AA}$). Interestingly the differences can affect both the preparation and the activity of the final catalyst in terms of dispersion and metal accessibility.

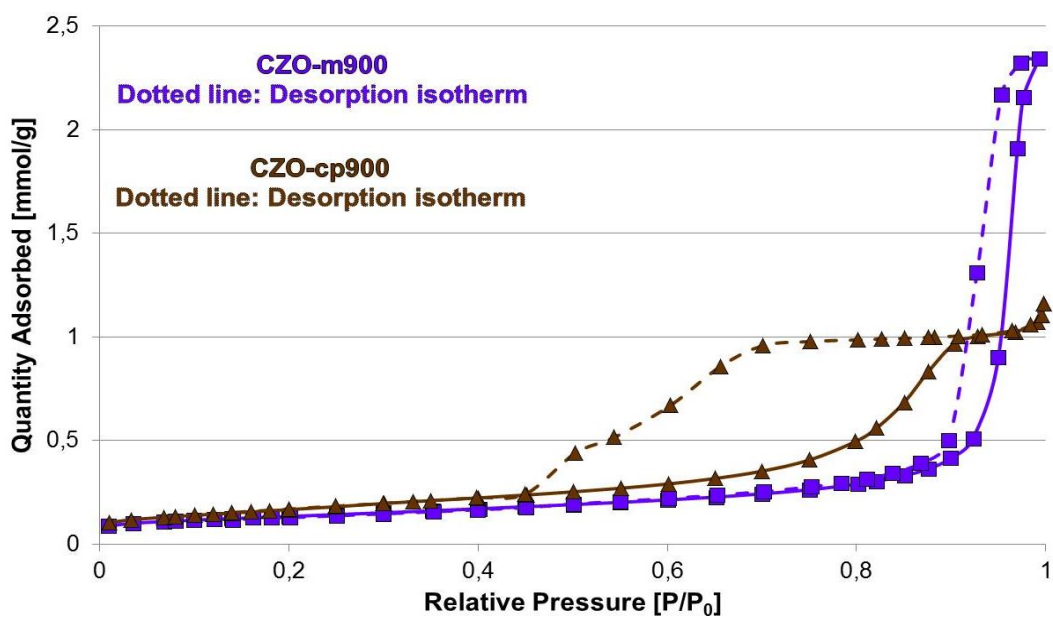


Fig. 3.16. Adsorption and desorption isotherm profiles of CZO-m900 and CZO-cp900 samples

Sample	S_{BET} [m^2/g]	Pores Volume [cm^3/g]	Avg. Pore Diameter [nm]
CZO-m900	11.5	0.06	19.7
CZO-cp900	13.7	0.04	4.4

Table 3.7. BET Surface Area, Pores Volume and Average Pore Diameter of the CZO-m900 and CZO-cp900 samples

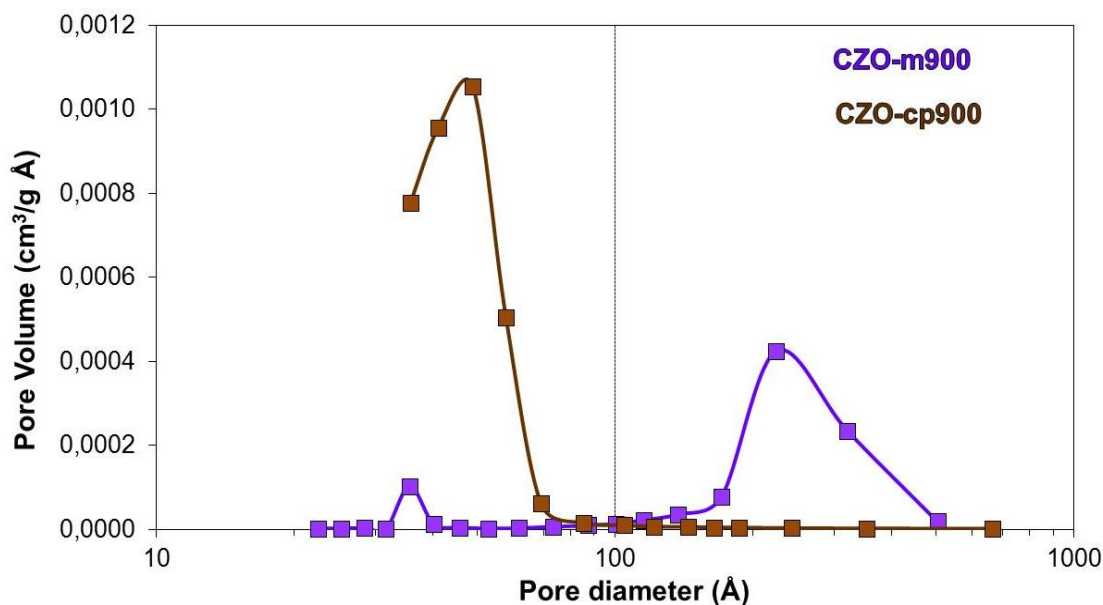


Fig. 3.17. Pore Size Distribution (PSD) of CZO-m900 and CZO-cp900 samples

3.3.2 Effect of the Precipitating agent: TMAH vs NH_3

The nature of the precipitating agent, and its effect on the microemulsion formation, is already studied in paragraph 3.2.4, where it is showed how with NH_3 , the anionic microemulsion system was transparent and stable to the contrary of the same system obtained utilizing TMAH and with a 3M NH_3 solution was possible to obtain the hydroxides precipitation. Therefore is interesting to understand if the nature of this agent and the type of microemulsion, can affect the final solid in terms of crystalline structure and stability.

Taking the CZO-m900 as the reference sample, the other supports obtained utilizing NH_3 are compared with it. At the beginning a comparison between these samples calcined at 900°C has been made (Fig. 3.18). Ammonia is added following both of the methods described in the experimental session (Fig. 2.1 and Fig. 2.2). The sample obtained through the double – mixed inverse microemulsion method is labeled CZO-m NH_3 -m900, while those obtained through the single – microemulsion method is labeled CZO-m NH_3 900. Interestingly, following the single - microemulsion method, the volume become about an half of the volume involved in the double – mixed inverse microemulsion method but, the addition of the precipitating agent not dispersed in a

microemulsion system, could change probably also the nature and stability of the final solid. Fig. 3.18 shows that the pattern of the reference CZO-m900 sample is more similar to that of the sample obtained through the single – microemulsion method (CZO-mNH₃900), while the CZO-mNH₃-m900, seems to be characterized by the Ce_{0.6}Zr_{0.4}O₂ phase. However, observing in details the pattern of the CZO-mNH₃900, it seems that some differences with the CZO-m900 one can be detected. In fact, particularly the reflection at about 58 °2θ, presents a shoulder at lower °2θ angles probably indicating a Ce-rich phase formed during the precipitation, or due to an initial segregation phase phenomenon. In order to clarify this aspect, the CZO-mNH₃ sample has been calcined also at higher temperatures (1000 and 1100°C) and the XRD patterns of these samples are compared in Fig. 3.19. Observing the black line in the figure, relative to the shoulder at about 58 °2θ, is clear how it increases, by increasing the calcination temperature, becoming a reflection in the CZO-mNH₃1000 and CZO-mNH₃1100 samples and, therefore, attributable to a segregation phenomenon with a CeO₂-rich phase and a ZrO₂-rich phase. In fact, comparing the patterns obtained with those recorded in the database list, is clear how at higher temperature the most thermodynamically stable CeO₂ – ZrO₂ phase is formed (Ce_{0.75}Zr_{0.25}O₂) and consequently a segregate ZrO₂ is also formed.

The behavior showed by the samples prepared by NH₃ imply that the nature of the precipitating agent and the way in which it is added, play a role on the characteristics of the crystalline phase of the final solid. The most homogeneous Ce/Zr mixed oxide are obtained by using highly basic precipitating agent characterized by larger micelles than that of the cation which can increase sharply the pH and induce a real homogeneous coprecipitation. A less basic precipitating agent such as ammonia, and the way in which it is added to the cationic microemulsion, seems to influence the formation of the wished Ce_{0.5}Zr_{0.5}O₂ phase. Using a microemulsion comparable with the cation micelles dimension, the Ce_{0.6}Zr_{0.4}O₂ phase is formed, probably because the raise of the pH at the cationic/anionic interface is not quick enough to permit the sudden formation of the precipitate, therefore the more stable Ce-rich phase is formed. In the case of the NH₃ addition through the single microemulsion method, the pH increase inside the micelles is probably enough to obtain the Ce_{0.5}Zr_{0.5}O₂ phase but is not homogeneous in the whole solution since the aqueous ammonia is not added in microemulsion, therefore, a solid characterized mainly by the Ce_{0.5}Zr_{0.5}O₂ phase is obtained. Nevertheless the dishomogeneity decrease the stability, since the presence of Zr- and Ce-rich zones can work as nucleation seeds and help the segregation of the Ce_{0.75}Zr_{0.25}O₂ and ZrO₂ phase. In fact, already at a calcination temperature of 900°C the NH₃-sample show a less

defined XRD pattern, differently from what happens in the CZO-m900 reference sample characterized by an high homogeneity.

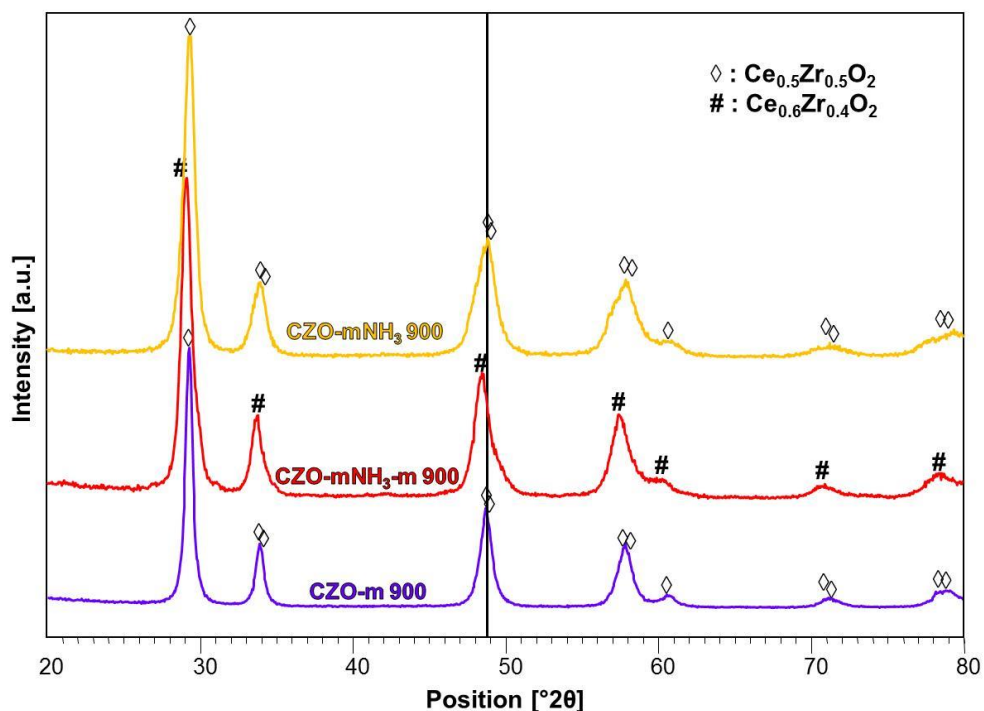


Fig. 3.18. XRD patterns of the samples obtained utilizing NH₃ as precipitating agent, calcined at 900°C. CZO-m900 is taken as reference pattern

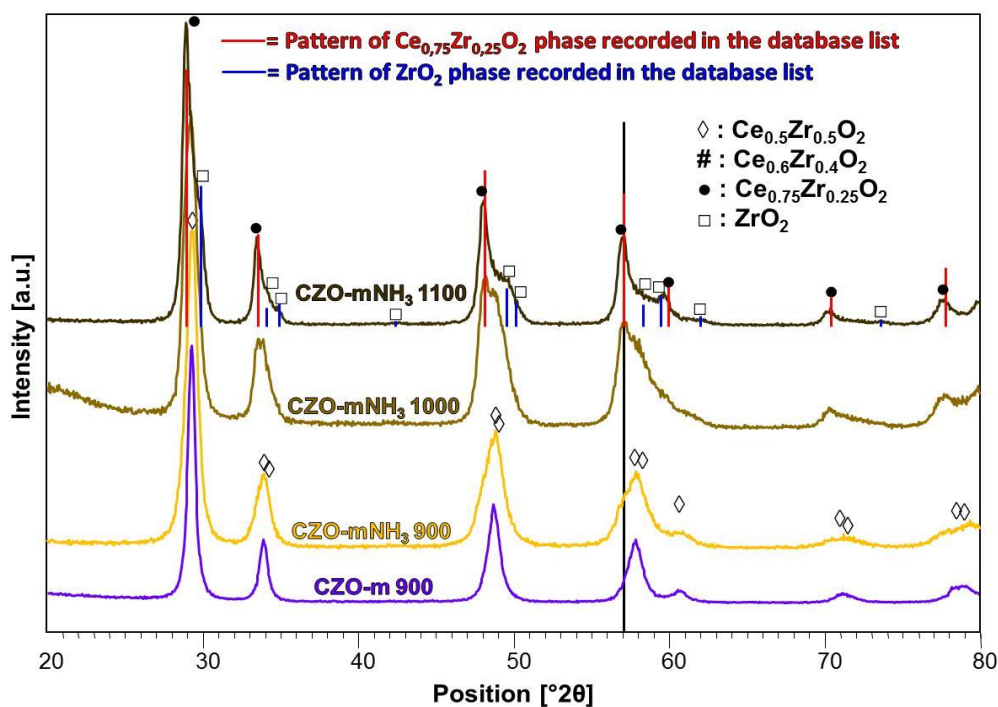


Fig. 3.19. Effect of the calcination temperature on the CZO-mNH₃ sample. CZO-m900 is taken as reference pattern

3.3.3 Effect of the Ce/Zr ratio

The effect of the Ce/Zr ratio is also studied, synthesizing a CZO support characterized by the $\text{Ce}_{0.75}\text{Zr}_{0.25}\text{O}_2$ phase. This is the thermodynamically stable phase for these kind of mixed oxides, hence it is easy to obtain it also through classical synthesis method, such as the co – precipitation one. The thermodynamic stability is the main reason for which this phase is utilized even in commercial processes that involved the use of CZO materials. The amount required at industrial level ensure that these materials are surely obtained following a classical well-known synthetic method. For these reasons could be interesting the investigation of some possible differences that can arise if $\text{Ce}_{0.75}\text{Zr}_{0.25}\text{O}_2$ synthesis is carried out following the w/o microemulsion method. This CZO support obtained through w/o microemulsion and calcined at 900°C is labeled 75/25-m900 and it is compared with a $\text{Ce}_{0.75}\text{Zr}_{0.25}\text{O}_2$ system commercially used and with the CZO-m900 and CZO-cp900 samples.

From XRD analysis (Fig. 3.20) the 75/25-m900 sample doesn't show the pattern coincident with those recorded in the database relative to the $\text{Ce}_{0.75}\text{Zr}_{0.25}\text{O}_2$ phase. This result is enough curious, also considering that a Ce/Zr ratio of 3 is the most stable from a thermodynamic point of view. The 75/25-m900 pattern is very similar to those relative to the CZO-cp900 sample, showing reflections practically at the same 2θ angles. An hypothesis which can be drawn in order to justify this behavior, could be the sequent. Following the microemulsion method probably the precipitation of the solid at the cationic/anion interface originate from the coalescence of the micelles, occurs in a so sudden way to not permit the formation of the thermodynamic stable CZO phase, but is favored a metastable phase such as the $\text{Ce}_{0.6}\text{Zr}_{0.4}\text{O}_2$. This though could be reinforced if it is considered the less defined nature of the patterns relative to the CZO-cp900 and 75/25-m900 supports, in comparison with those relative to the CZO-m900 sample. This less definition could be connected to the presence of a small part of free CeO_2 or free ZrO_2 , respectively in the 75/25-m900 and CZO-cp900 samples. In fact, the reflections relative to these crystalline phases are positioned at 2θ angles really closer to those relative to the mixed oxide phases but, being present as "impurities", are barely detectable, and they induced a lengthen of the reflections. The CZO-m900 pattern, instead, is highly defined, index of the presence of the unique metastable phase $\text{Ce}_{0.5}\text{Zr}_{0.5}\text{O}_2$.

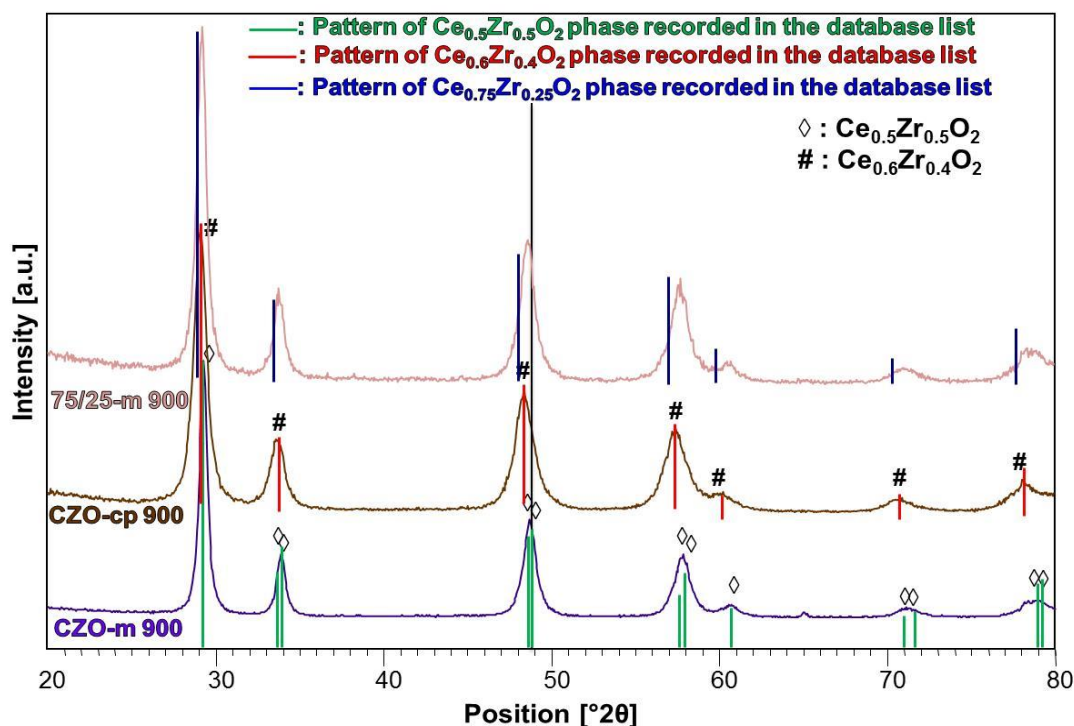


Fig. 3.20. XRD patterns of the supports CZO-m900, CZO-cp900 and 75/25-m900, compared with the pattern of the pure phases recorded in the database list

On the other hand, the XRD pattern of the commercial sample (Fig. 3.21) shows the characteristic reflections of the $\text{Ce}_{0.75}\text{Zr}_{0.25}\text{O}_2$ phase. Probably, carrying out the synthesis in a continuous phase, like following the co-precipitation procedure, there aren't problems related to the formation of the thermodynamic CZO stable phase.

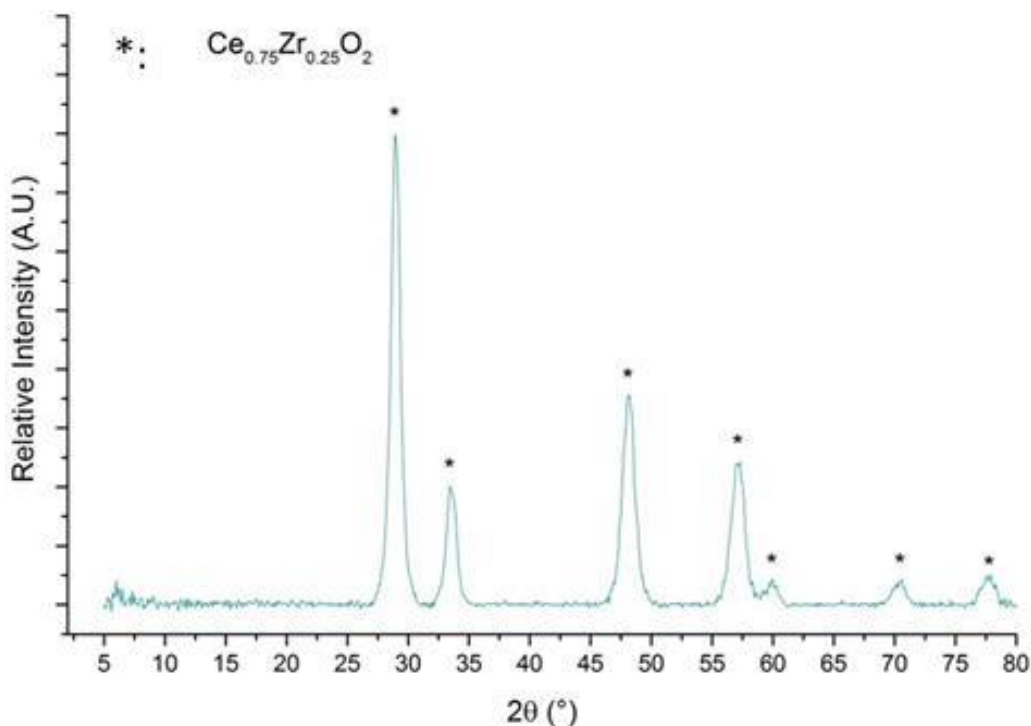


Fig. 3.21. XRD pattern of the $\text{Ce}_{0.75}\text{Zr}_{0.25}\text{O}_2$ commercial sample [44]

From TPR analysis is possible to understand the effect of the Ce/Zr ratio and of other parameters on redox properties. Comparing the reduction profiles recorded during a TPR/O/R cycle of the 75/25-m900 sample (Fig. 3.22a) with the TPR profile of the commercial support (Fig. 3.22b), are clear some different features. It is important to remind that the commercial sample is calcined at lower temperature (700°C) than the microemulsion one (900°C), (hence it will be named 75/25-cp700). This different thermal treatment could influence the properties of the final oxide in terms of surface area and crystallinity of the phases. Furthermore, on the 75/25-cp700 sample only a reduction cycle until 950°C is carried out [44]. Comparing the H₂-TPR profile of this sample with that relative to the first reduction of the 75/25-m900 sample different number and shape of the reduction peaks are present. In fact, the commercial sample present three reduction peaks at 609°C, 678°C and 867°C; the two peaks at lower temperatures are associated to the reduction of the surface CeO₂, while the 867°C peak is ascribable to the bulk reduction. The presence of a complex pattern is an indication of a non-homogeneous character of the support. The 75/25-m900 sample, instead, seems to be characterized by an higher homogeneity, showing a single reduction peak at a defined temperature of 685°C, probably due to a better interaction with Zr leading to the formation of a more uniform solid solution. Any peak over 800°C is present, indicating that there is not a distinction between surface and bulk CeO₂ may be due to the homogeneous and small size of the particles which favour a concomitant reduction of the surface and bulk. After the oxidation step, the 75/25-m900 reduction profile present a slightly undefined shape showing a shift of the main peak at higher temperature (775°C), but remain visible a very weak shoulder at about the same temperature (682°C) of the peak characterizing the first reduction profile (685°C). Probably, the temperature reached in the oxidation cycle (950°C) could be responsible of the occurrence of some thermal phenomena that can affect the Ce/Zr ratio of the phase and its sintering leading to a material with a lower reducibility.

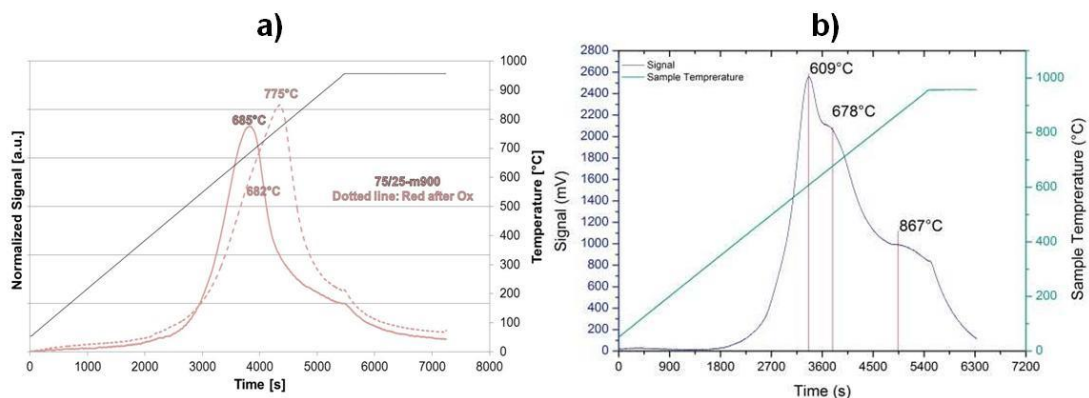


Fig. 3.22. Comparison between the H₂-TPR profiles of: a) 75/25-m900 support; b) 75/25-cp700 commercial support

In Fig. 3.23 are compared the H₂-TPR profiles of the CZO-m900 and 75/25-m900 one. The 75/25-m900 reduce itself at a temperature of about 40°C lower than that characterizing the CZO-m900 first reduction profile, in agreement with the statement that the reducibility increase as the Ce content increase.

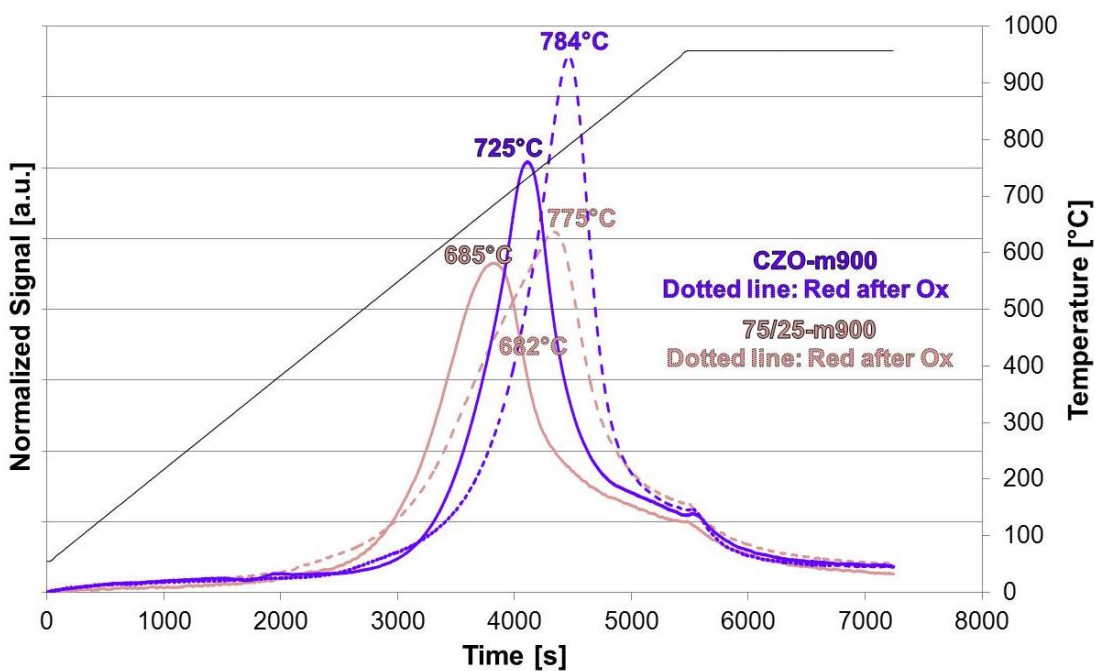


Fig. 3.23. Comparison between the H₂-TPR profiles of the CZO-m900 and 75/25-m900 supports

3.3.4 Insertion of the active metal

3.3.4.1 *Impregnation vs Bulk*

After the stabilization of the phase characterizing the support, through the calcination process, is necessary to carry out the addition of the phase catalytically active, which is generally constituted by the VIII group metals. Considering reforming reactions, it is well known that industrially Ni – based catalysts are used, thanks to the low cost of the Ni and to its high activity in the whole series of reactions involved in the process. On the other hand, Ni presents an high tendency towards deactivation phenomena deriving from both thermal effects (sintering) and carbon formation. These phenomena could be reduced, or better avoided, changing the nature of the active metal, utilizing for instance noble metals that are less sensitive towards carbon formation but characterized by a much higher cost, and/or exploiting the synergetic effect which can be established between the active metal and the support in order to avoid sintering. In this work both of the options have been adopted. In fact, on the CZO supports three different metals are added (Rh, Ru and Ni) and the effect of the methodologies used for their insertion (Incipient Wetness Impregnation (IWI) and bulk – see paragraph 2.1.4) are also studied.

3.3.4.1.1 Rhodium insertion

It is known that Rh is very active in reforming reactions but it is not widely utilized for its high commercial prize (about 100 € per gram). The addition of Rh is carried out through the IWI technique for both the two main supports, i.e. CZO-m900 and CZO-cp900, and also inserting the Rh^{3+} as cation in the Ce and Zr microemulsion, i.e. following the bulk technique. The latter insertion method is carried out with the aim to put the metal inside of the CZO lattice in order to exploit the interaction between metal and support. XRD patterns of the IWI sample (Rh1IWI_CZO-m900) and the bulk ones (Rh1bulk_CZO-900 and Rh5bulk_CZO-m900) are reported in Fig. 3.24. Comparing the Rh1IWI_CZO-m900 pattern with that of Rh1bulk_CZO-m900, only the reflections relative to the $\text{Ce}_{0.5}\text{Zr}_{0.5}\text{O}_2$ phase are detectable and no reflections ascribable to some Rh_2O_3 phase are present. In the IWI sample, Rh is surely on the surface of the CZO-m900 support, therefore the fact that are not detectable Rh-based phases, could indicates a good dispersion of the metal on the support, while in the case of the bulk sample the same consideration could be ascribable to the presence of Rh into the CZO lattice. On the other hand, these statements could be contested by the low amount of Rh present, which could be not detected from an XRD analysis, independently from its position and dispersion on the support. For this reason a small quantity of bulk sample characterized

by an higher amount of Rh (5% w/w) has been synthesized and analyzed through XRD, in order to exclude the latter hypothesis. In spite of the high amount of Rh, also in the Rh5bulk_CZO-m900 pattern are not present reflections relative to Rh_2O_3 phases, indicating that, through the bulk technique, the insertion of the metal into the CZO lattice is achieved.

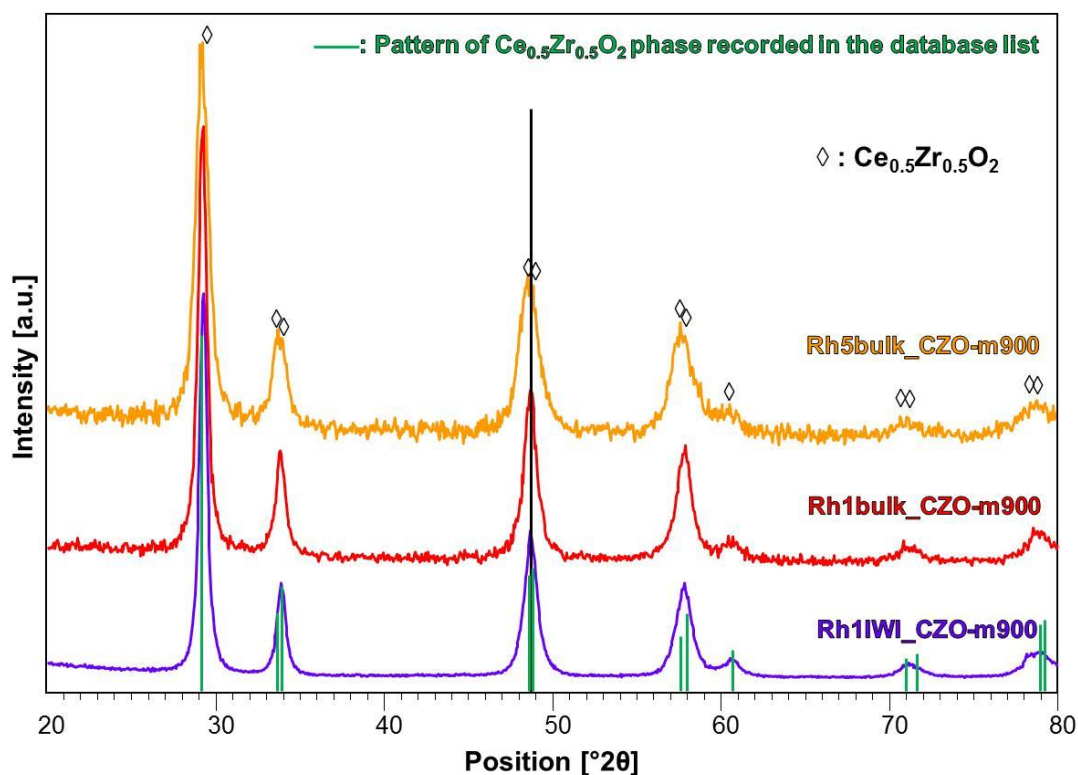


Fig. 3.24. XRD patterns of the Rh1IWI_CZO-m900 and Rh1bulk_CZO-m900

The metal insertion method could influence in a significant way the metal – support interaction (MSI), effect which is of fundamental importance in an heterogeneous catalysis, particularly when a CZO mixed oxide support is used. In fact, Ce has a certain tendency to interact strongly with the metal particles with possible drawbacks related also to the overall activity of the catalyst. These kind of interactions are mainly investigated by chemisorption which nevertheless cannot be used with Ce-containing samples. Therefore, it will be addressed through TEM analysis on the reduced samples. Some indications on the calcined samples, relative to the interaction between the metal and the support can also be evaluated through TPR/O/R analysis. In some cases, Raman spectroscopy could be also utilized in order to understand if the insertion of the active metal influence the structure of the support on which is added.

Inevitably also the nature of the support plays an important role on the interaction and the dispersion of the active metal. This is clearly visible from Fig. 3.25, where are compared the reduction profiles relative to the CZO-m900 and CZO-cp900 samples with

those relative to the same supports but with 1%w/w of Rh, added through the IWI technique (Rh1IWI_CZO-cp900 and Rh1IWI_CZO-m900). Analyzing the high temperature part of the profile related to the support, it can be stated that in both cases the Rh addition increase significantly the reducibility of the supports, shifting the reduction temperatures at lower values. Comparing the H₂-TPR profiles of CZO-cp900 support in Fig. 3.25 a, with those relative to the Rh1IWI_CZO-cp900 (Fig. 3.25 b) is possible to observe a decrease of the reduction temperature of about 100 – 150°C both in the H₂-TPR profile before (from 550 to 443°C) and after oxidation (from 590 to 438°C). This is due to the H₂ spill-over phenomenon that occurs on the metal surface. The spill-over effect permits to an adsorptive species to be indirectly adsorbed on the support surface under conditions where such adsorption is unfavorable. This is possible when a metal is disperse on the support surface, because it acts as a lower – energy pathway for gaseous species to first adsorb to the metal and then diffuse on the support surface. In particular, when the adsorptive species is molecular H₂, the spill-over effect involved the dissociative adsorption of the molecules (H₂) to atomic species (H*) on the metal surface. As a consequence, an high number of reducing species is formed and these new H* species are much more reactive and therefore have a reducing capacity higher than which relative to the molecular H₂. Therefore their migration through spill-over effect, from the metal to the support, decreases the temperature at which the reduction process occurs. The same effect occurs also in the case of the microemulsion sample. In this case a shifting of about 300°C (from 725 to 437°C) occurs, comparing the H₂-TPR profile relative to the first reduction of the CZO-m900 sample (Fig. 3.25 a) with those of the same step but relative to the Rh1IWI_CZO-m900 (Fig. 3.25 c). In the second reduction profile, after oxidation, the difference between the reduction of the metal and the support is not visible.

By taking into account the reduction of the metal, it ahs to be considered that after the metal impregnation on the calcined supports a further calcination is carried out at lower temperature (500°C), in order to stabilize the metal on the support. In this way the metal will be in its oxidized form (Rh₂O₃). Generally the metal reduction occurs at relative low temperatures, but it depends also on the interaction that the metal establish with the support; higher is this interaction, higher will be the reduction temperature. This feature is not difficult to understand, because if a metal interact strongly with support, it will be less available towards the reducing species and an higher temperature will be necessary in order to reduce the metal oxide particles. In the case of the impregnated samples this interaction is not so strong because, observing the first reduction profile of the Rh1IWI_CZO-cp900 sample (Fig. 3.25 b) the reduction of Rh occurs at about 130°C,

index of a dispersion of the metal mainly on the support surface. The peak at 245°C could be attributable to some Rh species that, interacting in a stronger way with the support, reduced themselves at higher temperature, otherwise it could be ascribable to some Rh₂O₃ particles with different size. At 433°C, instead, occurs the reduction of part of the support that interact with the metal in a so weaker way to render less important the occurrence of the H₂ spill-over effect, however, its reduction temperature is even lower than the temperature at which the reduction of the support without the metal occurs (550°C). The profile of the reduction after the oxidation step, has a different trend and three main peaks. The two peaks centered at 169 and 228°C confirm the hypothesis reported above, in the first reduction profile. This peak is relative to the reduction of Rh₂O₃ particles with different size, where larger particles request higher temperature to be reduced. In fact, is possible that during the oxidation step until 950°C, some sintering phenomenon occurs and, as a consequence, Rh particles become bigger increasing the reducing temperature. All of these considerations are valid also for the microemulsion sample, but some differences exists. Comparing Fig. 3.25 a and b, is possible to observe that the first profile relative to the Rh1IWI_CZO-m900 sample is characterized by three peaks: the first two attributable to the reduction of the Rh₂O₃ particles with different particles dimensions and the broad and weak peak at 437°C is relative to the reduction of that part of the support where the interaction with the metal is very low. The second reduction profile, recorded after the oxidation step, is very different, especially if it is compared to those relative to the Rh1IWI_CZO-cp900 sample. In fact, in this case, is present mainly one intense reduction peak at 224°C with a small shoulder at 180°C. This could imply that during the oxidation cycle an increase of the interaction among the Rh and the support occurred, originate probably by a reaction of the Rh oxide with the Ce_{0.5}Zr_{0.5}O₂ support surface, which may leads to an intermediate reduction temperature. This hypothesis is sustained mainly by two observations: the peak at 224°C is much higher in intensity with respect of those characterizing the first reduction profile, secondly the peak at 437°C practically disappeared, suggesting that Rh species is homogeneously dispersed and promote the reduction of support through H₂ spill-over effect.

From this discussion, it is possible to conclude that the metal insertion through IWI technique increased significantly the reducibility of the support because the metal is dispersed mainly on the surface where the H₂ spill-over phenomenon can occurs. The homogeneity of the metal dispersion seems to be dependent by the properties of the phase characterizing the support. The peaks at different temperatures characterizing the H₂-TPR profiles of the Rh1IWI_CZO-cp900 are index of a non-homogeneous dispersion

of Rh on the surface of the support. The same differences are also present in the first reduction profile relative to the Rh1IWI_CZO-m900 sample, but in the reduction after oxidation one is present a single intense peak. This suggests that on the CZO-m900 support the Rh is dispersed with higher homogeneity especially after the oxidation cycle, probably thanks to a reaction occurring between the metal and the oxide at the surface, especially related to the higher oxygen mobility capacity of the $Ce_{0.5}Zr_{0.5}O_2$ phase.

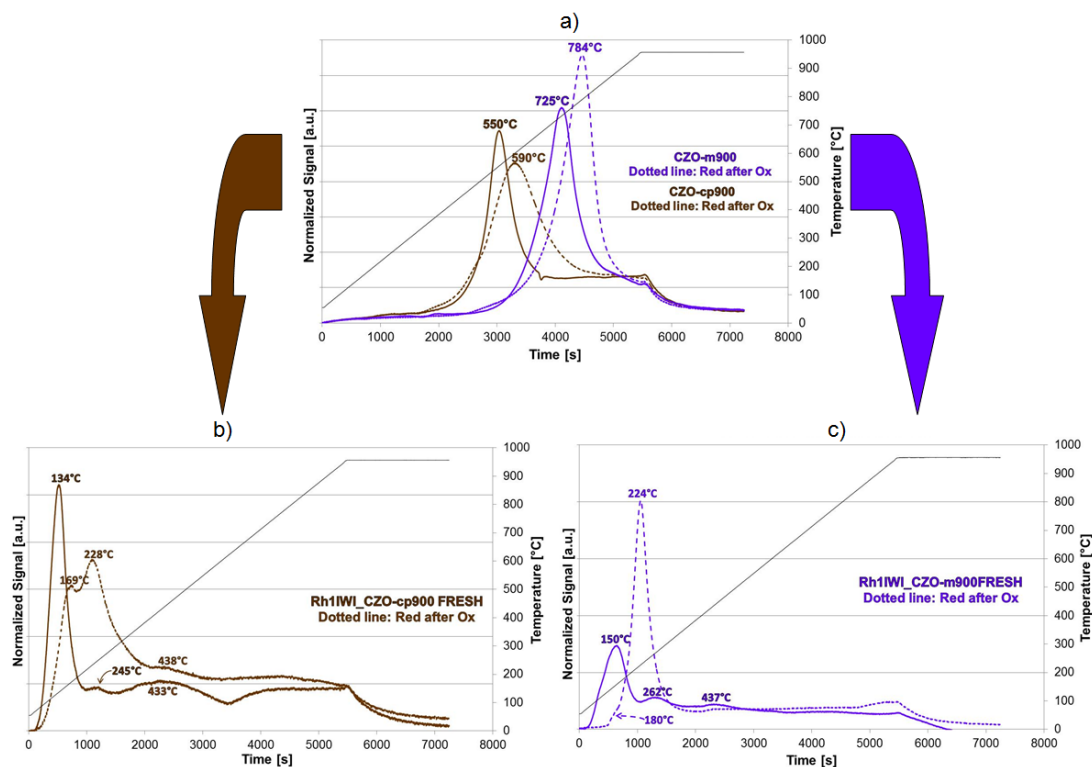


Fig. 3.25. Effect of the Rh insertion through IWI technique on the H₂-TPR profiles of CZO-m900 and CZO-cp900 supports recorded through a TPR/O/R cycle. It is clear the increase of the reducibility comparing the profiles relative to the supports without the metal (a) with those on that the metal is impregnated: b) Rh1IWI_CZO-cp900 and c) Rh1IWI_CZO-m900

The same amount of Rh (1%w/w) is added to the CZO-m support also following the bulk technique. In this case the Rh precursor ($Rh(NO_3)_3$) is dissolved in water together with the other cationic precursors ($Ce(NO_3)_3$ and $ZrO(NO_3)_2$). In this way the dispersion of the metal should be at the maximum level, but some drawbacks can exist.

Comparing the H₂-TPR profiles of the Rh1IWI_CZO-m900 sample with those relative to the bulk sample (Rh1bulk_CZO-m900) reported in Fig. 3.26, is clear that in the latter the Rh interact strongly with the support insomuch as to be not available on the surface, therefore it is unable to promote the H₂ spill-over effect. More precisely, the H₂ spill-over occurs, but with a very low rate, because from a reduction temperature of 725°C characterizing the CZO-m900 sample (Fig. 3.14) the bulk sample reduce itself at 531°C. Comparing this difference in temperature (about 200°C) with those existing between the

CZO-m900 and the Rh1IWI_CZO-m900 sample (about 300°C) is clear that the Rh dispersion and its interaction with the support is dramatically different between the impregnated sample and the bulk one. It suggests that in the bulk sample, Rh is inside the lattice of the mixed oxide material, forming a solid solution and, therefore, it is not available on the surface. As a consequence, it interacts with H₂ with more difficulty with respect to the impregnated sample, so it requires a higher temperature to be reduced. The profile after oxidation shows a similar broad peak centered at a temperature of about 100°C lower. This could be due to the fact that during the reduction step until 950°C, the Rh inside the support gets out from it, becoming more available on the surface; it reacts with the oxide being solute in the surface layer of the matrix during oxidation, and then it is reduced at a lower temperature. The broad shape of the reduction peak and the absence of other ones suggest, moreover, that the reductions of the metal and the support occur simultaneously, confirming the hypothesis according to which Rh is present into the lattice of the mixed oxide matrix.

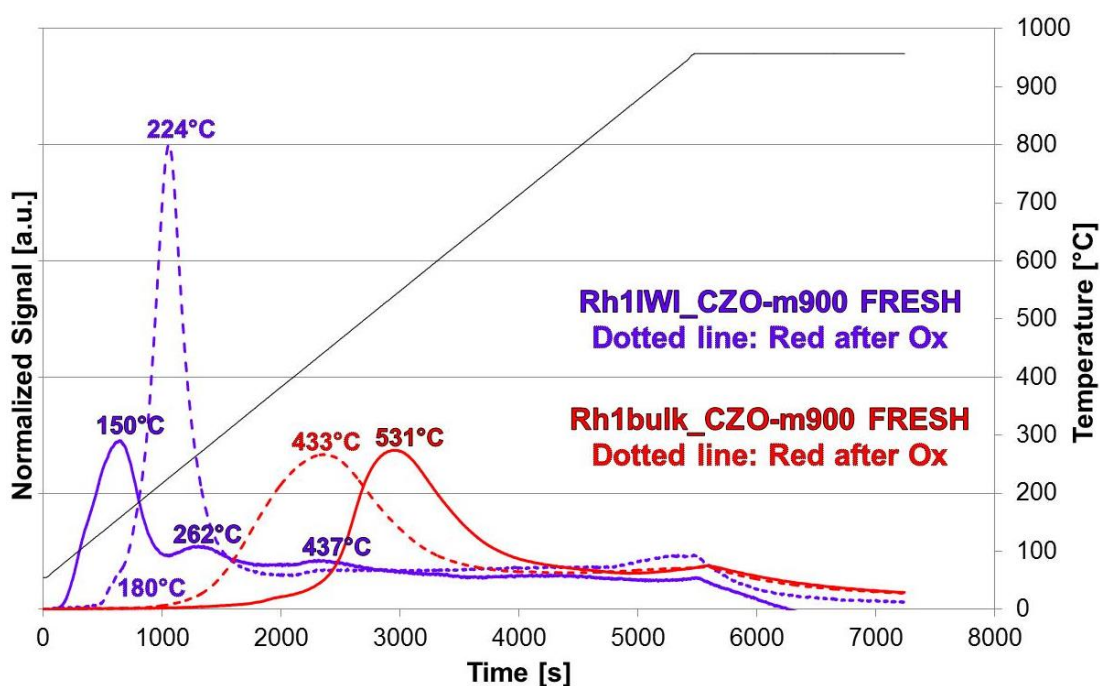


Fig. 3.26. Effect of the metal insertion method on the H₂-TPR profiles of the Rh1IWI_CZO-m900 and Rh1bulk_CZO-m900 samples recorded during a TPR/O/R cycle

In order to understand if the presence of Rh can produce a change in the vibrational structure of the support by inducing distortion of the oxygen framework, a Raman analysis is carried out both on the impregnated samples (Rh1IWI_CZO-m900 and Rh1IWI_CZO-cp900) and on the bulk one (Rh1bulk_CZO-m900). The comparison between the spectra recorded are shown in Fig. 3.27. All the Raman spectra of the Rh-based samples are compared with those relative to the CZO-m900. It is clear that both the impregnated samples (Rh1IWI_CZO-m900 and Rh1IWI_CZO-cp900) show a Raman

spectrum which is very similar to the spectrum of the support (in comparison to the CZO-m900 spectra) upon the addition of Rh, indicating that the metal doesn't have any effect regarding the oxygen lattice position in the structure of the support, but it is mainly dispersed on the surface. The bulk sample spectrum, instead, is significantly different from the CZO-m900 one, mainly regarding the relative intensities of the bands. The 465 cm^{-1} band decrease very much in intensity (about 1700) with respect to the intensity reached by the other spectra comprise between values of about 2500 – 3000. As already discussed (paragraph 3.3.1.2) this band is relative to the symmetrical stretching of the Ce–O bond characterizing the cubic *c* phase. This mean that in the bulk sample the presence of this phase is less important in comparison with the other samples. This consideration is in accordance also analyzing the band at about 600 cm^{-1} , which is attributable to defects that break the cubic symmetry rules and higher is its intensity, more predominant is the presence of a *t*-like structure. In fact, in the bulk sample this band have a slight higher intensity, suggesting that insertion of Rh influence the distortion of the CZO framework and create defects in the cubic structure. This particular band become more important in function of the amount of Zr present, which cause an higher distortion substituting itself to some Ce atoms. Comparing the ionic radii of Zr ($r_{\text{Zr}^{4+}} = 86\text{ pm}$) and Rh ($r_{\text{Rh}^{3+}} = 80\text{ pm}$) is possible to think that Rh could acts in the same way in which Zr acts, i.e. replacing some Ce atoms inducing an higher tetragonal nature to the overall structure.

With Raman analysis it is hence demonstrated that following the bulk procedure for the metal insertion, a strong interaction between the metal and support is create insomuch as the metal get into the CZO framework creating distortions, leading to a structure with a marked tetragonal nature. Regarding, instead, the impregnated samples, Rh doesn't get into the bulk of the support, but remain mainly on the surface where can also promote in a more significant way the H_2 spill-over effect, fundamental as regards the reducibility of the global system.

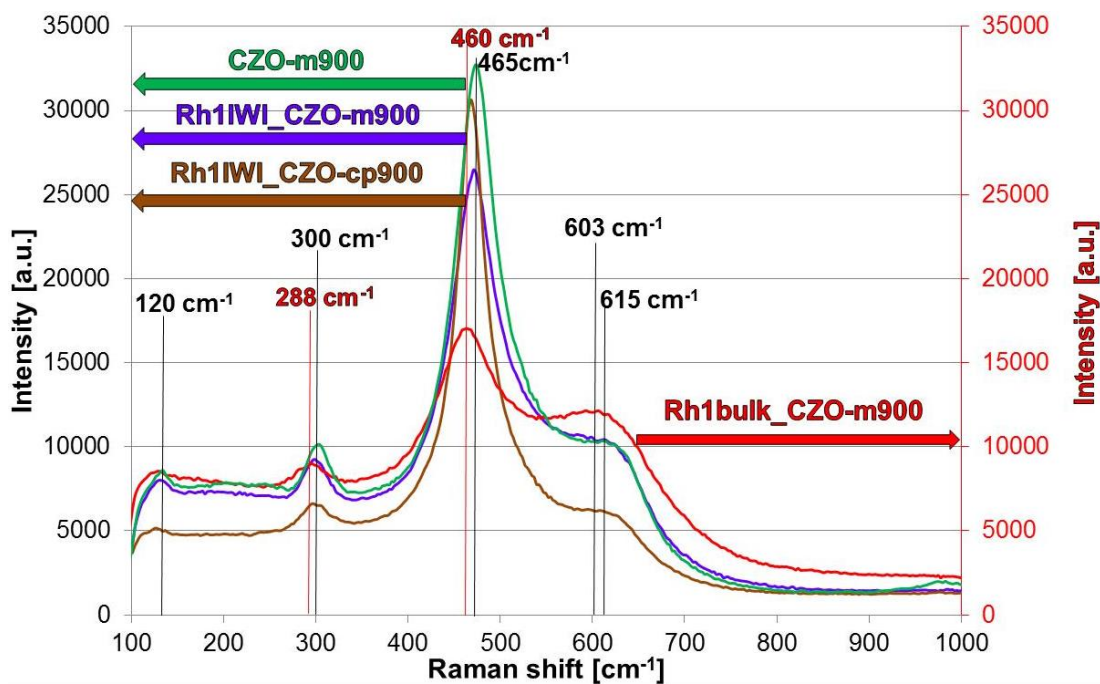


Fig. 3.27. Effect of the metal insertion method on the crystalline structure investigated through Raman spectroscopy. CZO-m900 spectrum has taken as reference

3.3.4.1.2 Ruthenium insertion

Ruthenium is another VIII group metal with an high activity in reforming reactions available with a lower price (about 20 € per gram) with respect to the Rh, but it is not easy to obtain in a dispersed form, and is affected strongly by thermal sintering deactivation. Therefore, considering the temperatures involved in reforming processes, is clear how the lifetime of a Ru-based catalyst will be shorter than that of Rh. Furthermore a suitable support which could stabilize this kind of metal is still a challenge in the research of this Ru-based systems. CZO support could be a good candidate able to stabilize the metal phase transferring in some way its thermal stability, deriving mainly from the Zr content, through a suitable interaction which could be formed between the metal and the support.

Also in this case, the Ru insertion (1%w/w) is carried out following both the IWI and the bulk technique. In Fig. 3.28 are reported the H₂-TPR profiles of the CZO-m900 support on which is deposited 1% w/w of Ru through the IWI technique. As already discussed in the case of Rh, also Ru increase the reducibility of the support through the H₂ spill-over effect. The first reduction profile is characterized by two peaks both centered at low temperatures; the main one at 160°C, with a shoulder at 175°C. This mean that the metal is mainly dispersed on the surface of the CZO support, with most likely differences in the metal particles sizes. Probably some large particles are present that require an higher temperature to be reduced. After the oxidation step this effect

increase, in fact in the second reduction profile are present three peaks at different temperatures. It seems that the first two peaks described above are slightly shifted at higher temperatures (173°C and 185°C) probably because the same particles become even larger during the oxidation until 950°C and reduced themselves at high temperature. The new peak at 248°C, instead, could be ascribable to the reduction of Ru migrated and reacted with the support surface, therefore an increase in the reduction temperature, which allows a contemporary reduction of the support can be observed.

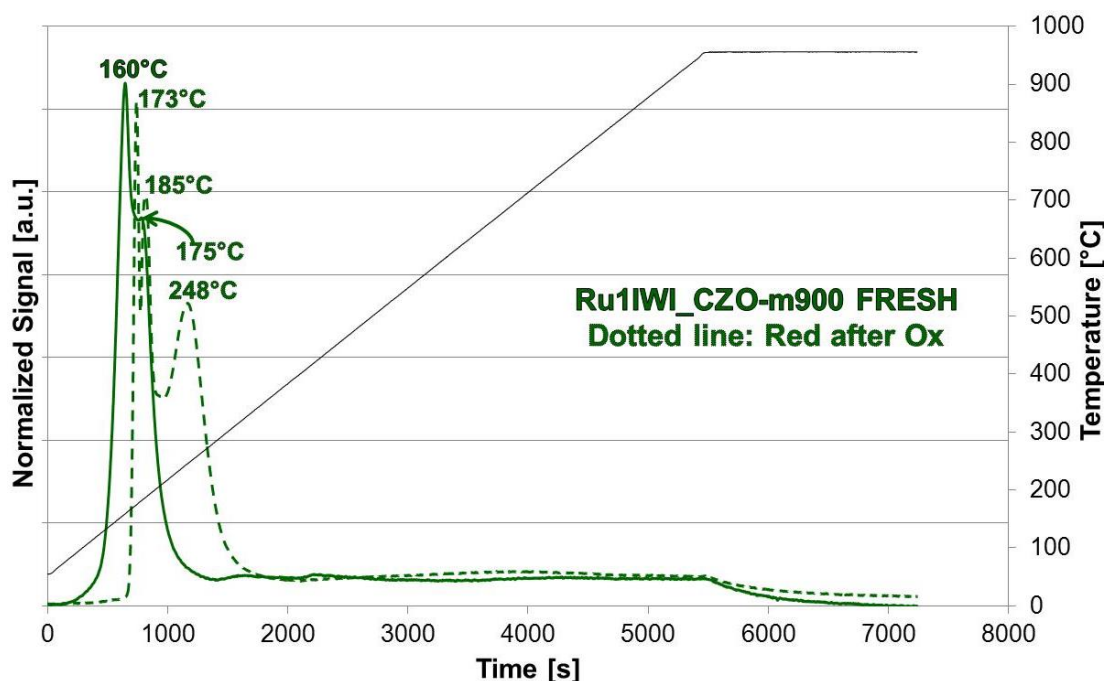


Fig. 3.28. H₂-TPR profiles of the Ru1IW1_CZO-m900 sample

Observing the reduction profiles relative to the sample obtained following the bulk metal insertion technique (Fig. 3.29), it is possible to evidence that the second mechanism hypothesized above could be the main one and it occurs in larger extent in the bulk sample. Between the IW1 samples and the bulk ones exist an important difference regarding the thermal treatment involved in the preparation procedure of each sample. In the case of impregnated samples the support calcined at high temperature (in this case 900°C) and after the metal impregnation, in order to stabilize the metal on the support, another calcination treatment is carried out at lower temperature (500°C). On the other hand, in bulk samples only one calcination treatment is involved because the metal is added to the CZO system in the microemulsion medium, during the first steps of the synthesis procedure. The TPR of this sample shows a first peak at 203°C and a series of, at least, four unresolved peaks between 300 and 630°C, demonstrating that probably the RuO₂ is present in different position inside the catalyst. In fact, analyzing the first reduction profile the peak at low temperature (203°C) can be ascribed to the surface

RuO₂ particles reduction interacting with the support and inducing the reduction of CeO₂ at a lower temperature range (569 – 629°C) with respect to the reduction temperature of the CZO-m900 (725°C – Fig. 3.14). In literature [184] is reported that TPR of pure CeO₂ generally shows two peaks at approximately 500°C and 900°C, the former (LT peak) being associated with surface reduction, while the latter (HT peak) is due to the bulk reduction. However, when a low surface area sample is employed, the LT peak is negligible and in some cases it appears as a shoulder of the peak due to bulk reduction. Furthermore Trovarelli et al. [185] reported that in the presence of a metal, the LT peak is shifted to lower temperatures and split into several peaks. In this specific case, the Ru presence is able to promote the H₂ spill-over effect which is the responsible of the reducibility increase of the CeO₂ at lower temperature which, as reported by Trovarelli, can appear splitted in two or more peaks. On the other hand a different phenomena can be used to describe the peaks at 455°C and 385°C, which similarly to Rh can be ascribed to the Ru inserted in the CZO lattice which decrease the overall reduction temperature of the mixed oxide solid. In the second reduction profile, the peak at low temperature is less intense in comparison with the 203°C peak in the first reduction profile and shifted at slightly lower temperature (177°C and 200°C). The lower H₂ consumption could depend by the fact that during the oxidation step until 950°C, some Ru particles react with the support surface leading to a more significant increase of the reducibility of the surface CeO₂ which is reduced at a temperature of about 70°C lower (506°C) than in the first reduction profile (569°C). Consequently, the amount of free Ru present on the support surface is lower than in the fresh sample, because part of it get into the first layers of the CZO support. The decrease of the free Ru and its presence in the bulk of the sample, may cause also the increase of the CeO₂ reduction temperature which, with less H₂ spill-over effect, is reduced at 745°C.

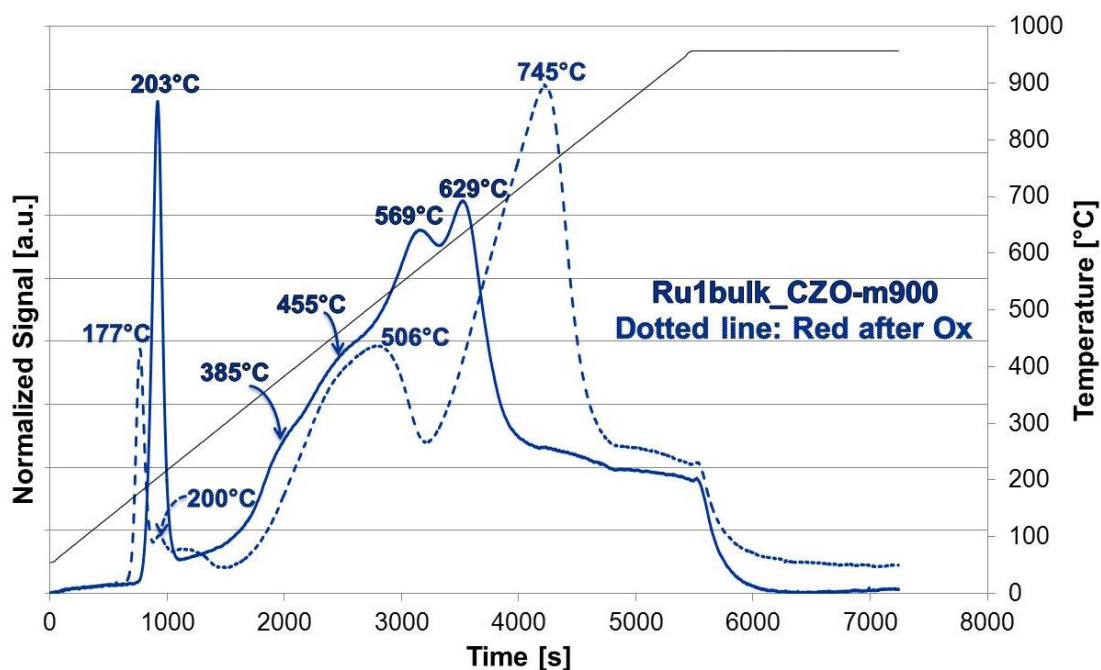


Fig. 3.29. H₂-TPR profiles of the Ru1bulk_CZO-m900 sample

3.3.4.1.3 Nickel insertion

In order to make a comparison between the noble metal – based supported systems and more classic metal – based ones, also Ni has been added to the CZO-m900 support. The high availability and the low price, make the Ni the most utilized metal in reforming processes in spite of lower activity with respect the Rh and its low stability towards deactivation deriving from carbon formation phenomena and sintering. One of the several approaches in order to contrast these kind of deactivation, is to overload the catalytic reactor by using an high metal loading (10 – 20% w/w). Therefore to have a good discrimination on the catalytic performance are prepared using two impregnated samples loading with an amount of metal (5 and 10% w/w) in comparison with the Rh and Ru percentages (1% w/w).

For both the samples (Ni5IW1_CZO-m900 and Ni10IW1_CZO-m900) TPR/O/R analysis is carried out in order to investigate if, and how, the Ni interact with the support. The reduction profiles relative to these samples are reported in Fig. 3.30 a and b. The effect of the Ni addition to CZO systems are widely investigated in literature [186,187,188,189,190,191], but there is not already a general agreement regarding the shape of the TPR profiles of similar materials and/or the ascription of their features. Comparing these two samples is possible to observe that the amount of Ni doesn't have a significant influence on the dispersion and interaction of Ni with the CZO support. Generally, in literature is reported that exist a problem to obtain an homogeneous metal dispersion on this kind of systems, detected from the presence of more peaks at different

temperatures. Montoya et al. [189] compared the redox properties of Ni/CeO₂ with Ni/CeO₂ – ZrO₂ ones, showing that already from the simplest Ni/CeO₂ system these dispersion problems are detected. TPR profiles show the first peak, centered at about 420°C, relative to the reduction of high uniform NiO species to Ni⁰ together with another high temperature peak (800°C) associated to the partial reduction of Ce⁴⁺ to Ce³⁺. Moving toward more complicated binary materials (Ni/CeO₂ – ZrO₂) the number of the reduction peaks increase and also their shape become even undefined, indicating that a non-homogeneous metal dispersion on the support is reached. Also Kambolis and co-workers [192] reported some H₂-TPR profiles relative to Ni/CeO₂ –ZrO₂ materials characterized by several peaks ascribable to different types of reducible phases. These considerations are not fully in accordance with the reduction profiles recorded for the Ni5IWI_CZO-m900 and Ni10IWI_CZO-m900 samples. In fact, in both cases the first profile is characterized by a main peak at about 400°C (415°C for the Ni5IWI_CZO-m900 and 400°C for the Ni10IWI_CZO-m900) attributable to the reduction of NiO particles with high uniformity that have a quite strong interaction with the support. This latter affirmation is made on the basis of results obtained by Tang et al. [193] that reported the occurrence of Ni reduction on a CeO₂ support occurs predominantly at 360°C. According to this interpretation, the shoulder at 365°C (Fig. 3.30 a) and 385°C (Fig. 3.30 b) can be ascribable to the reduction of a small amount of the NiO less interacting with the support, and therefore with a lower reduction temperature. In any case, problems related to a non-homogeneous metal dispersion are not identified, especially if the second reduction profile is taken into account. In fact, both the IWI samples show a sharp single reduction peak centered at about 490°C, characterized by an higher intensity in comparison to the peak at about 400°C of the first reduction profile. The shift at higher temperature (from 400 to 490°C) is probably associated to an increase of the interaction between Ni and CZO support that occurs during the oxidation step. Concurrently, the small amount of NiO species that, before oxidation, reduced themselves at about 370°C probably increase their interaction with the support, reaching the same metal – support interaction grade of those characterized by an higher interaction from the beginning, leading to a more homogeneous NiO species. This implies that from two different NiO species, one more homogeneous NiO species is formed (after the oxidation cycle) having a defined interaction with the support, hence reducing itself at a specified higher temperature. In other words the H₂ amount necessary to reduce all the NiO species is the same before and after the oxidation cycle, but in the former case this amount is used to reduce two different NiO species, while in the latter all the H₂ is utilized to reduce only one homogeneous NiO.

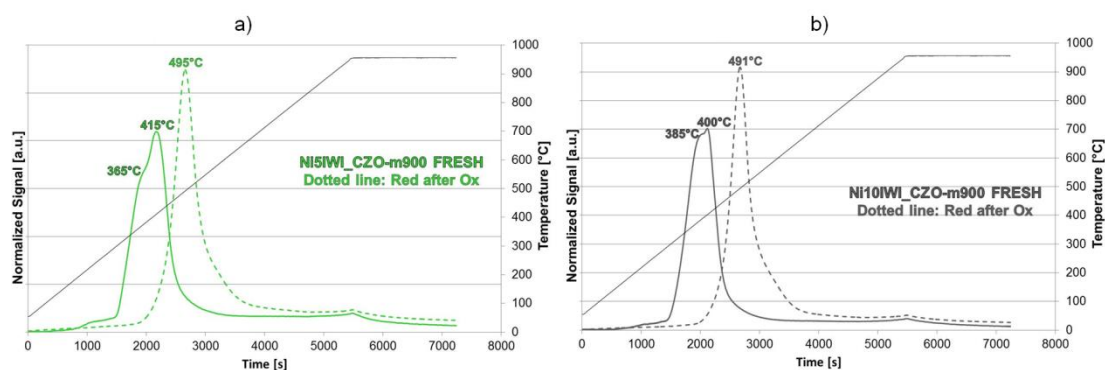


Fig. 3.30. H₂-TPR profiles recording during a TPR/O/R cycle of the: a) Ni5IWI_CZO-m900; b) Ni10IWI_CZO-m900 samples

Up to now, the XRD patterns relative to the metal loaded supports did not show any reflection ascribable to the presence of Rh or Ru species was detectable, maybe thanks to an high dispersion of the metal inside the matrix of the, or its low amount (1% w/w) and good dispersion on the surface give signal not detectable from the XRD analysis. In the case of Ni-based samples, on the contrary, the metal amount is higher (5 and 10% w/w) than the previous cases, hence is possible to detect some reflections relative to some Ni species if their dispersion is not optimal. As expected, in the patterns relative to these samples reported in Fig. 3.31 are clearly visible the reflections coincident to those recorded in the database list relative to the NiO phase and their intensities increase as the metal percentage increase, from 5 to 10%. This mean that, the homogeneity regarding the metal dispersion on the support hypothesized above during the analysis of the TPR data is not actually so good, because of the presence of NiO crystalline species that are clearly present outside of the pores of the support. This could depends on the low surface area characterizing the CZO-m900 support and, mainly, on the very low pores volume value ($\approx 0.06 \text{ cm}^3/\text{g}$). In other words, the total pores volume of the CZO-m900 support is too small and in order to impregnate all the Ni many incipient impregnation steps are required. This procedure cause a decrease in the metal dispersion. This could explain the higher reduction temperature of the NiO, which depends on the size of the crystals and could have negative consequence on the activity of this kind of catalyts.

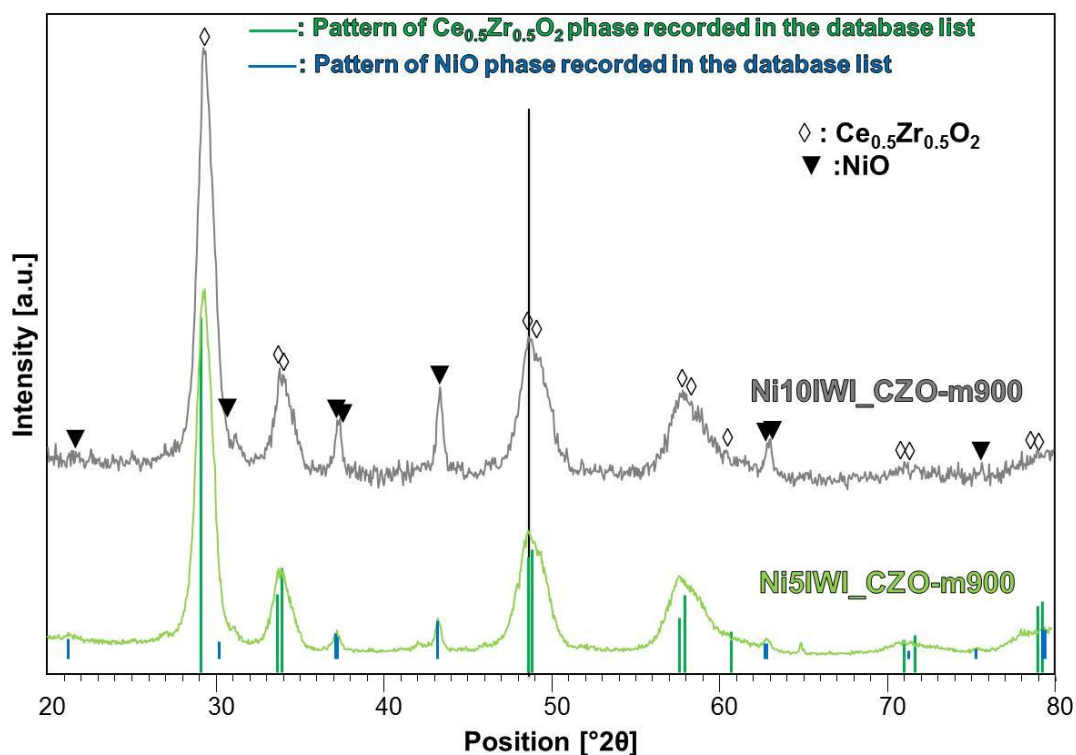


Fig. 3.31. XRD patterns of the Ni5IWI_CZO-m900 and Ni10_CZO-m900 samples

The morphology and surface properties are influenced strongly by the temperature at which the CZO supports are subjected, and conducting this treatments at milder conditions, could lead to a more defective system characterized by pores large enough to allow the impregnation of an high amount of metal, like in the case of Ni.

As expected, from the porosimetry analysis data, it is verified that the nature of the metal (Rh, Ru or Ni) doesn't influence the surface area, but the method followed for its insertion could condition it, simply because the bulk samples are subjected to only one calcination treatment, while the IWI samples undergo a first support calcination at 500, 750 or 900°C and, after the metal impregnation, another thermal treatment at 500°C occurs. The latter could affect the surface area, decreasing it slightly, as shown in Table 3.8. The surface area decrease as the calcination temperature increase and, from a comparison between the IWI samples and the bulk ones, is possible to observe that between the samples calcined at lower temperature (Rh1IWI_CZO-m500 and Rh1bulk_CZO-m500) the bulk sample has a surface area of about 25% higher than the IWI one. Increasing the calcination temperature until 750°C, this difference become of about 50% but, in the samples calcined at 900°C the differences are smoothed, and the IWI sample showing a slightly higher value of S_{BET} (11.5 m²/g) with respect to those characterizing the bulk sample (8.4 m²/g).

Anyway, as in the comparison between the CZO-m900 and CZO-cp900 supports (paragraph 3.3.1.5 – Table 3.7), also in this case the average pore diameter seems to be significantly influenced by the calcination temperature. Varying the temperature from 500 to 750°C, this value doesn't change very much both considering the IWI and bulk samples. On the other hand, increasing the temperature from 750 to 900°C, in all the cases is recorded a significant increase of the average pore diameter value. This could be explainable from the analysis of the adsorption/desorption isotherms, that are quite similar for all the samples reported in the Table above therefore, for example, are reported only those relative to the Rh1IWI_CZO-m samples calcined at 500, 750 and 900°C (Fig. 3.32). The samples calcined at 500 and 750°C are characterized by a type-H2 hysteresis loop, associable with ink-bottle-like pores of varying radius and as expected the hysteresis loop of Rh1IWI_CZO-m750 is bigger and start at P/P_0 value well above ($P/P_0 \approx 0.9$) with respect to which relative to the Rh1IWI_CZO-m500 ($P/P_0 \approx 0.6$). This mean that an higher calcination temperature lead to a change in the pores structure, rendering them larger and less homogeneous than in the case of the sample calcined at 500°C; in fact, higher is the pores homogeneity in terms of size and shape, smaller will be the hysteresis loop. Therefore, increasing the calcination temperature the pores become larger, but when the calcination temperature is pushed up to 900°C, a drastic change in the morphology of the pores occurs. The hysteresis loop manifested in the isotherms determined on Rh1IWI_CZO-m900 is type-H3, ascribable to adsorbate condensation in capillary spaces between parallel plates or open slit-shaped capillaries. Therefore, between 750 and 900°C exist a temperature at which the pores collapse and forms the so called open slits that are characterized by a larger diameter with respect to the pores present in the samples calcined at lower temperature.

Sample	S_{BET} [m^2/g]	Pores Volume [cm^3/g]	Avg. Pore Diameter [nm]
Rh1IWI_CZO-m500	97.1	0.09	3.3
Rh1IWI_CZO-m750	34.6	0.07	5.6
Rh1IWI_CZO-m900	11.5	0.06	19.7
Ru1IWI_CZO-m900	10.2	0.07	21.2
Rh1bulk_CZO-m500	130.4	0.13	3.4
Rh1bulk_CZO-m750	69.5	0.12	4.9
Rh1bulk_CZO-m900	8.4	0.08	28.7
Ru1bulk_CZO-m500	139.7	0.13	3.4
Ru1bulk_CZO-m750	66.2	0.12	5.1
Ru1bulk_CZO-m900	-	-	-

Table 3.8. S_{BET} , Pores Volume and Average Pores Diameter values of Rh-based and Ru-based IWI and bulk samples, calcined at different temperatures

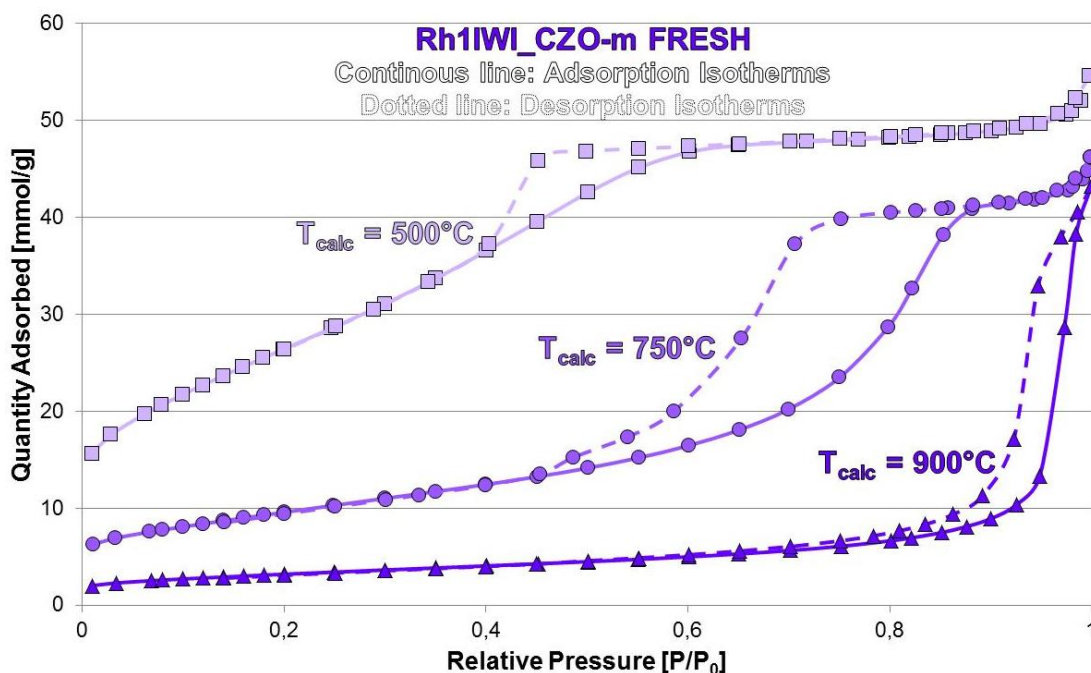


Fig. 3.32. Adsorption/desorption isotherms of the Rh1WI_CZO-m samples calcined at different temperatures

From these latest results, it is possible to conclude that a decrease in the calcination temperature of the CZO-m support until 750°C and even 500°C doesn't lead to a significant increase of the volume of pores in order to allow the impregnation of the metal amounts involved in the case of Ni. Thus, the impregnation of 5% and 10% w/w of Ni is not performed on the CZO-m750, hypothesizing the formation of a system similar to those characterized by the CZO-m900 support (Fig. 3.30 and Fig. 3.31). Therefore, it was decided to carry out the insertion of 5% and 10% of Ni following the bulk methodology, carrying out their calcination process at 750°C obtaining the Ni5bulk_CZO-m750 and Ni10bulk_CZO-m750 samples. H₂-TPR profiles of these catalysts are reported in Fig. 3.33. Making a comparison among the first reduction profiles is clear how they are similar, both showing a weak peak at about 230 – 240°C relative to the reduction of surface NiO species characterized by a weak interaction with the support. At about 400°C occurs the reduction of NiO species with a stronger interaction with the support, but still preferentially present on its surface, allowing the H₂ spill-over effect which improves the reducibility of CeO₂ in the support. Like in the case of Ru1bulk_CZO-m900 (Fig. 3.29), even if in a less marked way, it is possible to detect the splitting between the LT and the HT peaks (510°C and 660°C) relative to different positions that Ni occupy inside the CZO lattice. Concurrently to these reductions, probably occurs the reduction of part of Ni that interacts strongly with the support, reducing itself at 660°C. The higher intensity of this peak characterizing the Ni10bulk_CZO-m750 profile rather than the Ni5bulk_CZO-m750 one, indicates that Ni is preferentially in the bulk of the support while

those dispersed on the surface, that reduce itself at about 400°C, is more or less the same amount. After the oxidation step the reduction profiles are more different indicating a different behavior of Ni during the oxidation cycle. In the case of the sample with a lower Ni amount, comparing the first reduction profile with the second one is clear how the number of peaks decrease from 4 to 2; the first intense one at 560°C and a shoulder at 688°C. This could mean that during the oxidation step until 950°C, the surface Ni gets into the CZO-m750 framework rendering themselves less available on the surface, requiring more energy to be reduced. The 688°C peak is probably ascribable to the reduction of NiO species with an even higher interaction with the support probably caused by the species that already were in the bulk of the CZO-m support and during the oxidation cycle get even more in the bulk of it. In the case of Ni10bulk_CZO-m750, is again present the main peak at 560°C but the shoulder, this time, is detected at a lower temperature (510°C). Also this time the surface Ni gets in the bulk of the support reducing itself at 510°C rather than 390°C, but the bulk species that reduced themselves at 660°C in the first reduction profile, probably because of the very high amount of metal (10% w/w), seems that preferentially get out from the bulk migrating towards the surface, decreasing their reduction temperature of about 100°C. Analyzing in more details this second reduction profile, is possible to detect at higher temperatures (670 – 690°C) a not perfectly smooth trend, but a weak shoulder at about 690°C is present, relative probably to the reduction of a very low amount of Ni deeper present in the bulk of the support.

Anyway, at least from TPR analysis, the insertion of a such large amount of Ni on the CZO-m support remain a problem even if it is carried out the bulk technique, because in any case is reached a non-homogeneous dispersion of the metal phase.

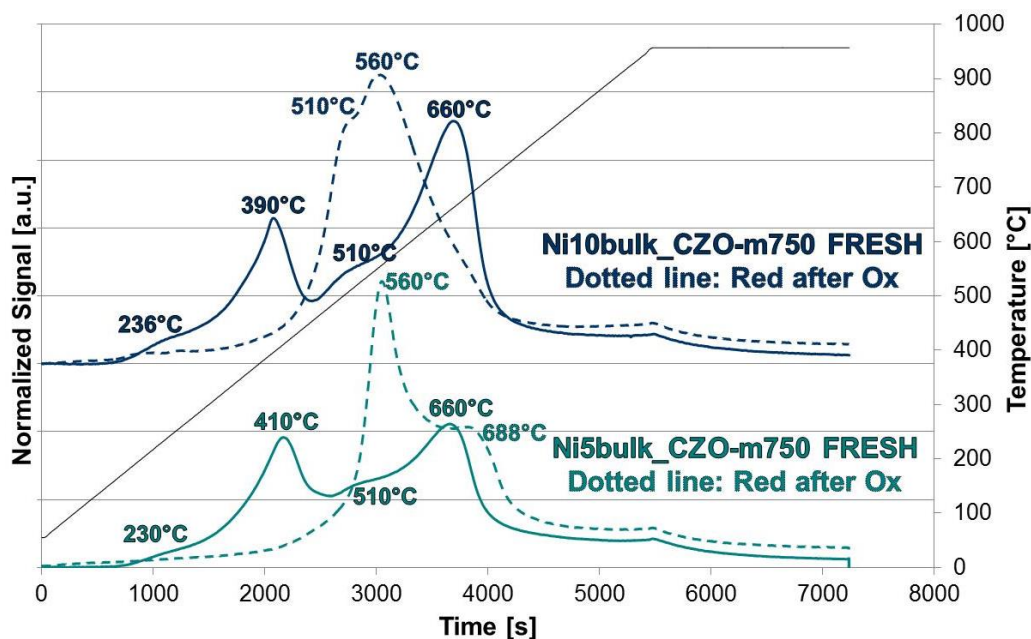


Fig. 3.33. Comparison between the H₂-TPR profiles recorded during a TPR/O/R cycle on Ni5bulk_CZO-m750 and Ni10bulk_CZO-m750 samples

A confirmation of the fact that in these samples the Ni is present in the bulk of the support, derive from the XRD patterns reported in Fig. 3.34. In contrast with the results obtained for the equivalent IWI samples (Fig. 3.31), in both of the bulk samples is not detectable any reflection corresponding with the NiO phase indicating that the metal is not revealed by the XRD, analysis in which are involved only the surface layers of the sample.

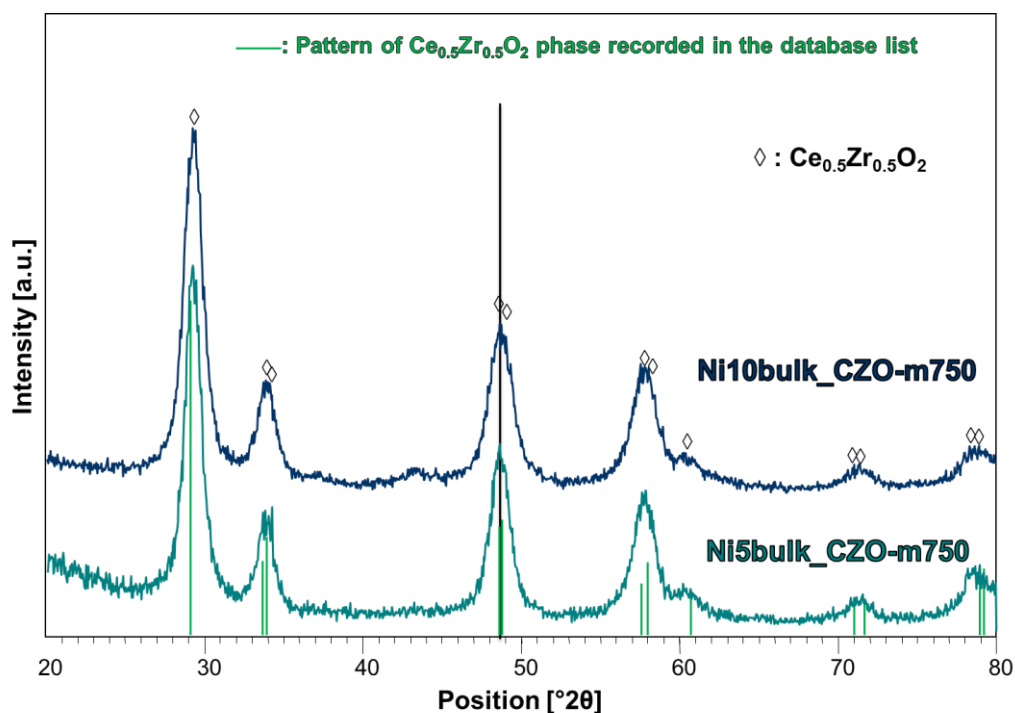


Fig. 3.34. XRD patterns of Ni5bulk_CZO-m750 and Ni10bulk_CZO-m750 samples

3.4 Catalytic activity of the samples prepared

The catalysts prepared and characterized, are tested in two different type of processes, the oxy-reforming and the low temperature steam reforming process (350 – 500°C).

Oxy-reforming is a process characterized by the contemporary presence of steam reforming and catalytic partial oxidation. H_2O and O_2 , are present in sub-stoichiometric ratio with respect CH_4 . In particular the O_2/C ratio is 0.21 while the S/C ratio is 0.7. In terms of atomic ratio the overall O/C ratio is 1.1, just above the stoichiometry for the CO formation while the H/C ratio is 5.4 which means intermediate between the CPO and reforming stoichiometry. The present conditions have two type of consequences:

1. The thermodynamic limit of carbon formation is close to the conditions utilized in the process. They have been calculated by the CEA-NASA program (Fig. 3.35). The graphs shown the equilibrium composition re-calculated on a dry bases for an easy comparison with the exit gas analysis. At 1bar the formation of carbon occur at a temperature below 710°C. The carbon formation limit became narrow at high pressure and it is present only among 600 and 700°C in low amount due to the lower conversion of methane.

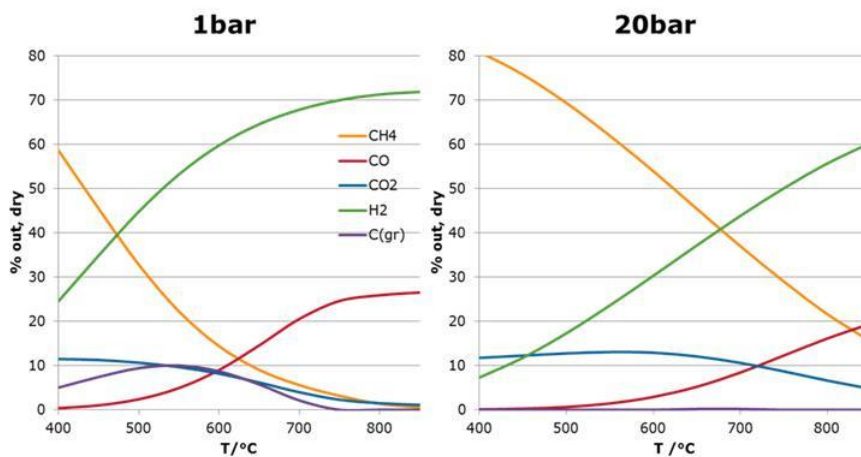


Fig. 3.35. Thermodynamic equilibrium curves calculated with CEA-NASA at 1bar (on the left) and at 20bar (on the right) with real input concentration gases [44]

2. The presence of oxygen which react very rapidly through oxidation reactions in the first zone, increasing the temperature of the bed, is compensated by the presence of water which give rise to highly endothermic reforming reaction thanks to the low amount of oxygen present in the so called oxy-reforming process (Fig. 3.36). Therefore at 1bar a small increase of temperature is present followed by a decrease of temperature of less than 50°C. The changes in

temperature are even smaller at high pressure where the overlapping between endothermic and exothermic reaction increases due to the increasing of the reaction rate (either by increase of reactant concentration and mass transfer rate). This conditions are very different from that generated in the CPO reaction where a temperature increase can easily reach 200 – 400° C and differently from reforming where a ΔT is generated radially in the bed and axially, the latter, again reaching 200°C, due to the limitation of the heat coming from external heating equipment [194]. These big differences in temperature profiles, make the comparisons between the catalysts' behavior very complicated, hence low temperatures or high dilution rates are used to limit these thermal phenomena. Furthermore, it is very difficult to have kinetically controlled performances, since by reducing the residence time the thermal profile changes dramatically. In particular in CPO if the residence time is decreased by changing the flow rate, the increase of heat produced give rise to an increase of temperature and an increase of the conversion is usually observed [195,196]. In the present conditions the axial temperature profile is much less sharp and the ΔT is limited, furthermore the presence of heat produced inside the reactor by oxidation reaction decreases a radial temperature profile usually present in the reforming reaction. In conclusion the reaction conditions are very favorable for the catalysts comparison differently from reforming and CPO and the comparison have been usually performed having the same oven temperature with a very limited shift of exit gas temperature.

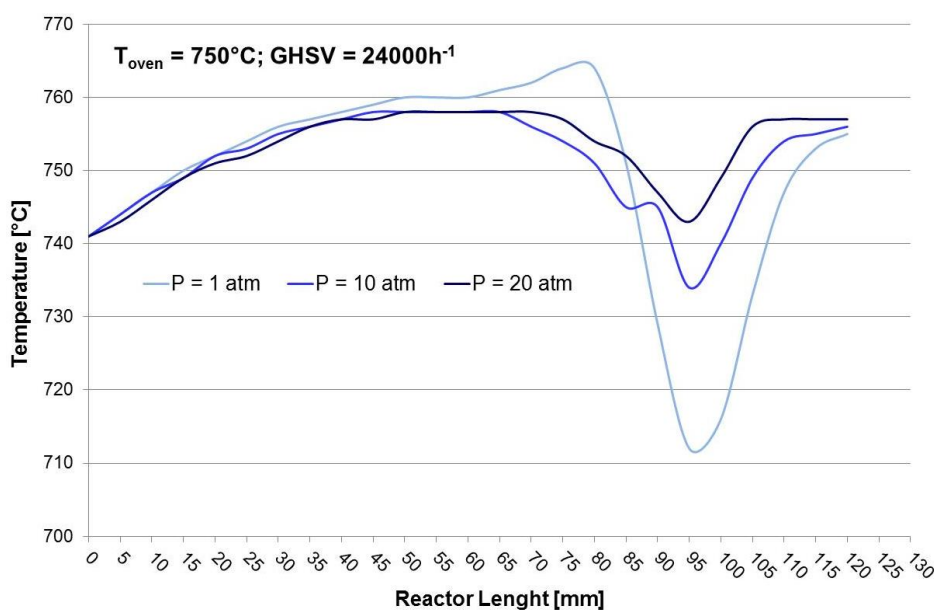


Fig. 3.36. Temperature profiles along the reactor, recorded during three catalytic tests in which the pressure parameter is changed from 1 to 20 atm at a $T_{\text{oven}} = 750^{\circ}\text{C}$ and a $\text{GHSV} = 24000\text{h}^{-1}$

With the aim to extend the research field involving the H_2 production system, the present work is moved towards a possibility to build up a system in which could be possible the occurrence of the reforming reaction together with intermediate or “integrated” separation of H_2 through selective membranes. Exist several type of membranes (see paragraph 1.1.6) but this study is mainly focused on the dense ceramic ones activated with Pd. The integrated reaction is limited to the Pd membrane maximum operative temperature, which cannot be higher than 450°C , with the difference between these temperatures and those involved in a classical steam reforming process ($900 - 1000^\circ\text{C}$) that could be cover by the continuous removal of hydrogen from the reaction zone. Nevertheless the integrated process development requires still the study on the integration between catalyst and membrane in the same reaction unit and the evaluation of its efficiency. Therefore, as starting point, a multistep H_2 membrane production and separation system could be investigated taking the scheme reported in Fig. 3.37, which is characterized by two reactors into which could occurs the oxy-reforming reaction at 750°C , spaced out by two H_2 membranes working at lower temperature ($400 - 450^\circ\text{C}$), each of which is placed at the exit of the two reactors, and a final reactor working at higher temperature to reduce the methane exit composition below 1%. This lead to a step process with the problems related to differences in terms of temperature of the gases which will be inevitably different between the reactors and the membrane ones. A further possibilities is to have the first reactor working at 500°C in the reforming configuration which leads to a decrease of oxygen consumption due to the lower diffences with the membrane operative temperature.

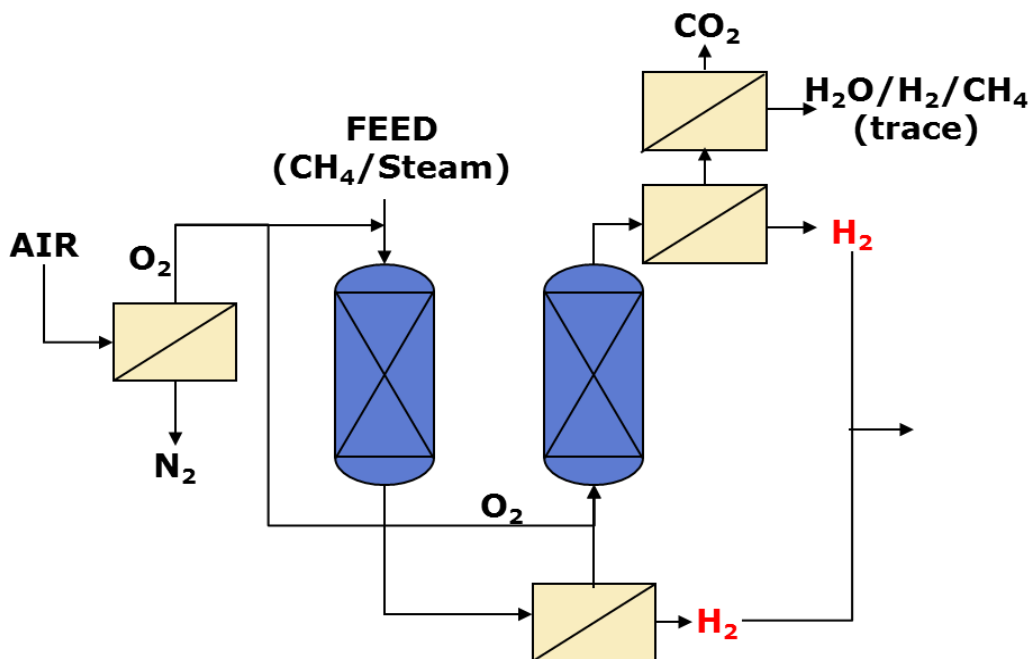


Fig. 3.37. Schematic representation of a multistep H_2 membrane production process

For these main reasons the CZO-based catalysts prepared are also tested in a steam reforming process at low temperature, investigating a temperature range between 350°C and 500°C, with the purpose to find a catalytic system active enough in these conditions, able to produce a good amount of H₂ through reforming reaction, which can be separated simultaneously.

The parameter which is taken as reference in order to compare the activities of the catalysts tested, is the CH₄ conversion, compared in all of the tests with those calculated at the thermodynamic equilibrium. This latter calculation is carried out utilizing the CEA-NASA software, which is able to give the molar gaseous mixture outlet composition (non-converted CH₄, non-converted H₂O, CO, CO₂, H₂ and C if present), knowing the feed composition in terms of molar percentage, the reaction temperature and the pressure. Some problems could exist in the choice of the right reaction temperature. In order to try to minimize the error, an average temperature is considered, calculating it from the temperature values recorded along the catalytic bed. For instance, considering the thermal profile relative to the test carried out at P = 1atm reported in Fig. 3.36, the temperature considered for the equilibrium calculation derive from the average of the values recorded between 75 and 110 mm of the reactor length, and this catalytic bed average temperature will be labeled as T_{avg}. A drawback related to this method of temperature calculation derive from the possibility that inevitably, in the same conditions some catalysts behave differently as a consequence of their specific activity. For example, a catalyst characterized by a low activity, will probably produce a thermal profile characterized by a less pronounced ΔT than those produced by an higher active catalyst. This mean that the catalytic bed average temperature could be higher in the former case with the consequence of a slightly difference in the calculation of the CH₄ conversion at thermodynamic equilibrium. Higher temperature imply higher CH₄ conversion hence, sometimes is possible to identify some different equilibrium values even if they are relative to the same operative conditions. Anyway, these differences are slightly thanks to the limited ΔT values generally characterizing the oxy-reforming process with respect to what observed in reforming and CPO processes.

The rate of deactivation of the catalysts tested has been also investigated, comparing the activity in terms of CH₄ conversion taking as reference the value obtained in the first test carried out, the so called reference test. As reference test was chose those carried out at T_{oven} = 750°C, P = 1 atm and GHSV = 24000 h⁻¹, being the most discriminating one. In fact, in these conditions is difficult to reach the thermodynamic equilibrium and this ensure that the results are obtained under a kinetic regime (hence

they are dependent by the catalyst's performances) rather than a thermodynamic one, on which the catalyst doesn't have any influence.

In the sequent sessions will be discussed the results obtained in the catalytic tests carried out trying to correlate the catalytic activity with the structural properties discussed in the previous section. A sort of a logical scheme followed in the sequent discussion could be drawn.

The main objective of this work is try to understand if the w/o microemulsion could be a valid method in order to obtain catalytic supports with peculiar characteristics that can contrast the problems related to the deactivation deriving from carbon formation and thermal sintering. With this aim, a logical scheme followed in the sequent section could be drawn proceeding with the investigations listed below:

1. **Commercial Rh1IWI_75/25-cp700 vs Rh1IWI_75/25-m900:** as starting point, is carried out a comparison between the commercial catalytic system characterized by the $\text{Ce}_{0.75}\text{Zr}_{0.25}\text{O}_2$ (obtained through co-precipitation) calcined at 700°C , on which is impregnated the 1% w/w of Rh (Rh1IWI_75/25-cp700), with the self-synthesized Rh1IWI_75/25-m900 catalysts. This first comparison permit to roughly understand if through the w/o microemulsion method increase the performances of this kind of catalytic systems, trying to understand if it's worth to continue the study and development in this direction or not;
2. **Rh1IWI_CZO-m900 vs Rh1IWI_CZO-cp900:** in order to understand if and how the support synthesis method could influence the catalytic performances, comparing two self-made catalysts deeply characterized;
3. **Effect of the nature of the active metal;** comparison of Rh, Ru and Ni will be carried out;
4. **IWI vs Bulk:** in the previous section it was observe that the method followed to insert the metallic active phase on the support play a fundamental role regarding its dispersion, feature which cover a basic role on the catalytic active;
5. **Effect of the calcination temperature:** in some way related to the previous point because the calcination temperature affect mainly the morphology of the system, influencing indirectly also the metal dispersion on the support;
6. **H₂ Membranes:** utilizing the most promising catalysts, some preliminary tests involving the H₂ membrane separation technology have been carried out, following the multistep configuration (see Fig. 3.37 and paragraph 2.3 (Zone 3)).

3.4.1 Comparison with a commercial CZO-based catalyst

A comparison between the synthesized catalyst with a commercial one with similar composition is usually carried out in order to understand if a modification of some parameter generated in the synthesized system could improve the performances of the catalyst in the perspective of an advancement of comprehension of the reactivity of the catalytic system and in the of the catalytic performances in the industrial development.

Already in the previous work carried out by Barbera [44] the commercial CZO-based catalyst was compared with other catalytic systems, showing intermediated performances between the two Rh/Mg/Al catalysts prepared through hydrotalcite precursors. In order to facilitate the comparison between the commercial sample and the prepared catalyst, the Fig. 3.1 is reported below (Fig. 3.38b) together with results relative to the catalytic activity of the Rh1IWI_75/25-m900-R750 sample (Fig. 3.38a). The data representation in these two figures is estetically different but the parameter in function of which are reported the catalytic activities, i.e. the outlet dry gas composition in terms of mol%, and the operative conditions under those the tests are carried out (T_{oven} , P and GHSV), are the same. Regarding the Rh1IWI_75/25-m900-R750 sample (Fig. 3.38a), in the graph are reported the percentages of all the gases composing the outlet mixture, while in Fig. 3.38b, the comparison between the catalysts tested by Barbera [44] is made considering only the CH₄ outlet molar percentage. Anyway, focusing on the red bars in Fig. 3.38b, relative to the commercial Rh1IWI_75/25-cp700-R750 sample, and comparing these values with the blue points (CH₄ outlet molar percentage) in Fig. 3.38a, is clear how the Rh1IWI_75/25-m900-R750 give higher performances both at P = 1 atm and 10 atm. In fact, already at lower pressure (1 atm) the experimental CH₄ outlet amount (about 8%) is very close to which calculated at the thermodynamic equilibrium (about 5% - represented by the continuous blue line), until becoming coincident with the latter at higher pressure (10 atm). On the contrary, the commercial sample show at 1 atm an outlet CH₄ amount of about 14%, very far from the value calculated at the equilibrium which obviously remain similar, equal to an outlet CH₄ amount of about 6%. Even at a pressure of 10 atm, the commercial sample doesn't reach the equilibrium, showing a distance from the equilibrium data of about 4 percentage points (experimental CH₄ out = 26% vs equilibrium CH₄ out = 22%). Unfortunately, in the case of the Rh1IWI_75/25-m900-R750 catalyst it was not possible to carry out the test at 20 atm due to some problems related to the pressure controller which doesn't permit a regulation of a constant pressure inside of the reactor. Apart from this, is possible to hypothesized that the Rh1IWI_75/25-m900-R750 sample would reach the thermodynamic equilibrium also at 20 atm given that it satisfy this purpose already at 10 atm, condition at which is more

difficult to reach the equilibrium, being the conversion of methane at the thermodynamic equilibrium lower at high pressure. In the light of these results it is possible to affirm that the self-made microemulsion sample (Rh1IWI_75/25-m900-R750) is characterized by a higher activity in the oxy-reforming conditions with respect to which relative to the commercial similar catalyst. Furthermore, making a wider comparison considering also the other two catalysts prepared by Barbera (Rh1%Mg₈₀Al₂₀ and Rh1%Mg₆₈Al₃₂) it is possible to establish the higher activity of the Rh1IWI_75/25-m900-R750 catalyst, even in the direct comparison with the Rh1%Mg₆₈Al₃₂ catalytic system, which has been selected as the best one in the NextGTL project and the work carried out by Barbera.

Therefore, from these data, seems that the synthesis method followed for the preparation of the catalytic support, its phase and morphology, play a fundamental role on the catalytic performances, probably because through the inverse microemulsion a higher morphological homogeneity is obtained, feature that can help a more uniform dispersion of the active metal on the support rendering it more available towards the reactive species increasing the activity of the overall system.

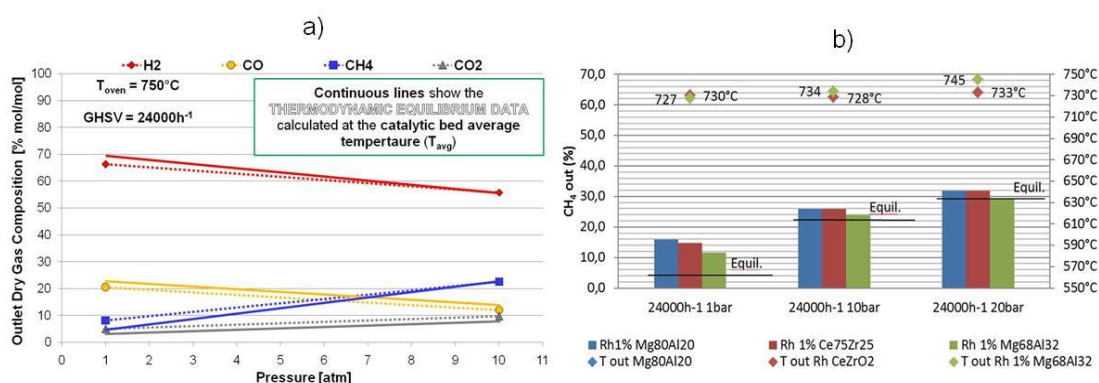


Fig. 3.38. a) Catalytic activity in function of the outlet dry gas composition of the Rh1IWI_75/25-m900-R750 sample, compared with; b) same data reported in Fig. 3.1[44]. The commercial Rh1IWI_75/25-cp700-R750 sample is labeled in this case as Rh1%Ce₇₅Zr₂₅ and represented by the red bars

Hence, the Rh1IWI_75/25-m900-R750 could be a good starting system which could be taken as reference in order to investigate other parameters more strictly related to the objective of the present work, such as the influence that could have a different phase composition, pores volume and redox properties on the catalytic performances of this CZO-based systems, mainly in terms of activity and stability towards deactivation phenomena by sintering and carbon formation. With this aim, in the following section will be discussed the comparison between the catalytic activity obtained with the Rh1IWI_75/25-m900-R750 sample and those relative to the Rh1IWI_CZO-m900-R750 catalyst.

3.4.2 Effect of the support' Ce/Zr ratio

The previous comparison have been carried out changing the preparation method which also affect the phase composition, distribution and the solid morphology. It is important to understand if the differences observed in the previous section regarding the Rh1IWI_75/25-m900-R750 sample with respect to the commercial one, are due simply to the preparation method or also dependent on the phases differences. It can be evaluated by comparing the previous catalyst (Rh1IWI_75/25-m900-R750) with Rh1IWI_CZO-m900-R750, having a Ce/Zr ratio equal to 50/50, in order to understand if the specific $\text{Ce}_{0.5}\text{Zr}_{0.5}\text{O}_2$ phase characterized by an high oxygen mobility have a significant effect on activity and/or stability of the catalyst.

In Fig. 3.39 are reported the catalytic activity results of the Rh1IWI_75/25-m900-R750 catalyst in function of pressure and GHSV. In all of the conditions tested the experimental CH_4 conversion value is compared with those calculated at the thermodynamic equilibrium represented in the graph with the transparent bars. The results obtained in the same oxy-reforming conditions for the Rh1IWI_CZO-m900-R750 are reported, instead, in Fig. 3.40. Considering the most discriminating condition ($P = 1$ atm and $\text{GHSV} = 24000 \text{ h}^{-1}$) the activities of these two catalysts are not significantly different observing in both cases a CH_4 experimental conversion of about 76%, far from the equilibrium value (about 85%) of less than 10 percentage points, indicating a good activity for both the fresh catalysts. The Rh1IWI_75/25-m900-R750 sample seems to have high activity at higher pressure (10 atm) even slightly better than the Rh1IWI_CZO-m900-R750 sample, showing at lower GHSV (24000 h^{-1}) a CH_4 conversion (48,7%) practically coincident with the calculated equilibrium value (49%), with the Rh1IWI_CZO-m900-R750 which shows, in the same conditions ($P = 10$ atm and $\text{GHSV} = 24000 \text{ h}^{-1}$), an experimental CH_4 conversion ($\approx 46\%$). Increasing the GHSV until 50000 and 100000 h^{-1} a drastic decrease of the activity for both the catalyst is observed, but the Rh1IWI_CZO-m900-R750 system show an higher activity than the system characterized by a Ce/Zr molar ratio 75/25. In fact, at 50000 h^{-1} the former (Fig. 3.40) show a CH_4 conversion of about 50%, which further decrease reaching a value of about 45% at 100000 h^{-1} ; value, the latter, which is not reach neither at 50000 h^{-1} in the case of the Rh1IWI_75/25-m900-R750 catalyst, which indeed show CH_4 conversions of about 37% and 35% at 50000 and 100000 h^{-1} , respectively. Anyway, those are very small differences being the results close to the thermodynamic equilibrium.

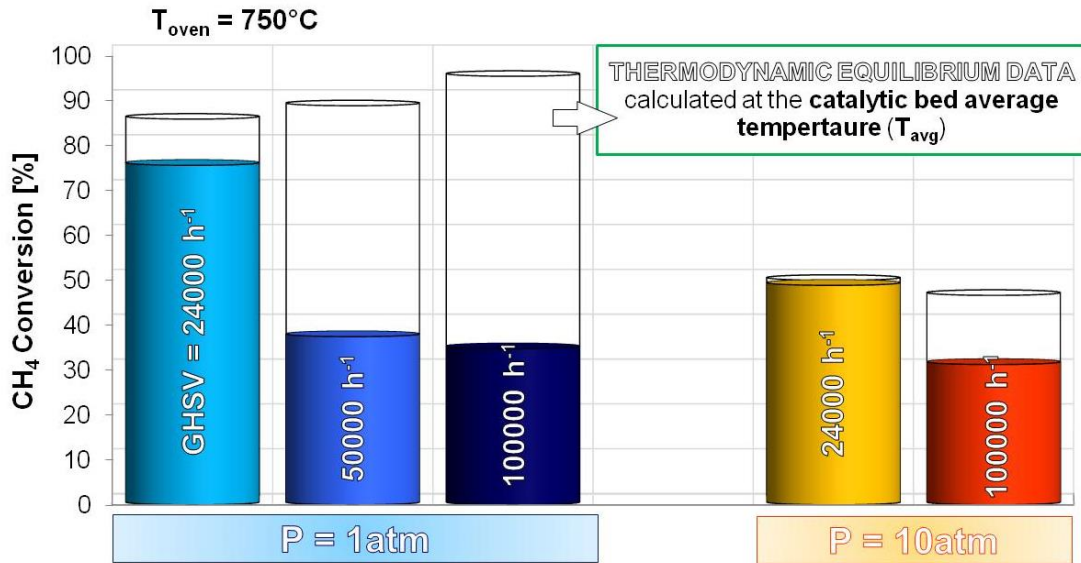


Fig. 3.39. Catalytic activity of the Rh1WI_75/25-m900-R750 in function of pressure and GHSV. All the experimental CH₄ conversion values are compared with those calculated at the thermodynamic equilibrium represented by the transparent bars

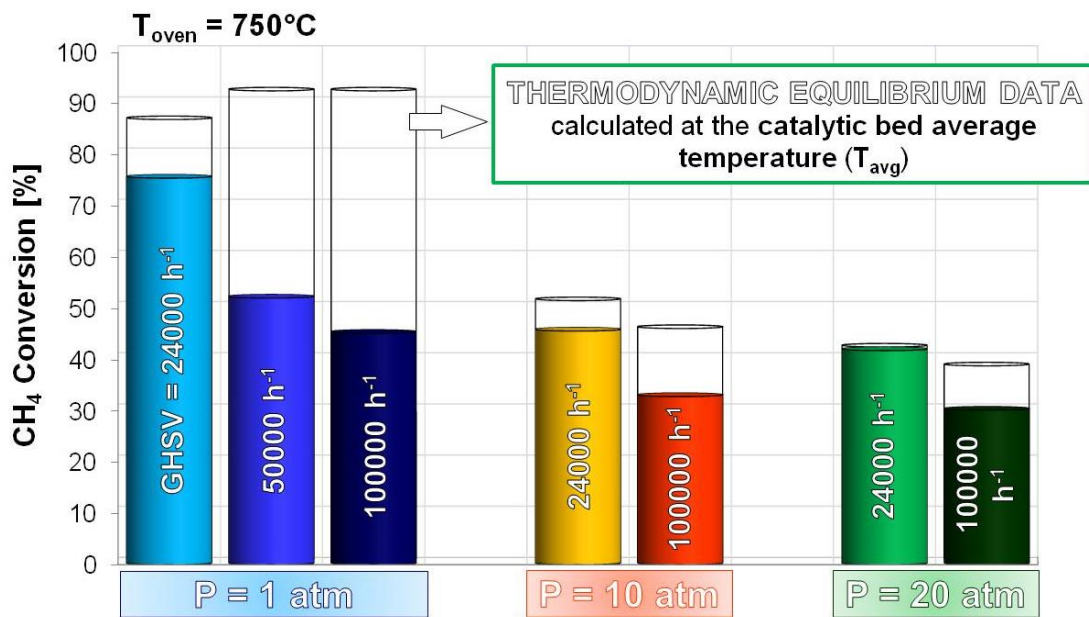


Fig. 3.40. Catalytic activity of the Rh1WI_CZO-m900-R750 sample in function of pressure and GHSV

On the other hand, the differences deriving from the change in the GHSV value are more significant and, from these, is possible to draw some hypothesis. The GHSV is indirectly proportional to the contact time. For example, a GHSV = 24000 h⁻¹ correspond to a contact time value of 0,15 s which decrease to 0,072 s considering a GHSV = 50000 h⁻¹, finally reaching 0,036 s if a GHSV value of 100000 h⁻¹ is considered. Therefore, the higher activity at 50000 and 100000 h⁻¹ observed in the case of the Rh1WI_CZO-m900-R750 system could depends on an higher dispersion of the active metal phase or could derive from an higher stability. In fact, the Rh1WI_75/25-m900-R750 lower stability with

respect to the Rh1IWI_CZO-m900-R750 sample have the consequence that the activity decrease observed in the former case depends on the occurrence of some deactivation phenomenon during the tests carried out before those at 50000 and 100000 h⁻¹. The control of the stability is carried out repeating the test at 24000 h⁻¹ after the study of the effect of each parameter related to the catalytic activity (P and GHSV). After these tests the CH₄ conversion data are reported in function of the time-on-stream of the catalyst under the gaseous reactive mixture (TOS). In Fig. 3.41 and Fig. 3.42 are reported the CH₄ conversion values recorded during the return tests carried out on the Rh1IWI_75/25-m900-R750 and Rh1IWI_CZO-m900-R750, respectively. The CH₄ conversion values obtained in the return tests are compared with those corresponding to the first test carried out on the fresh catalyst, taken as reference. In this way is possible to calculate the deactivation degree occurs during the reaction. The data reported in the figures below, lead to the conclusion that the lower activity of the Rh1IWI_75/25-m900-R750 sample at 50000 and 100000 h⁻¹ depend mainly by a lower stability of this catalytic system with respect to that characterizing the Rh1IWI_CZO-m900-R750 sample, in accordance with the second hypothesis taking into account a deactivation phenomenon. In fact, already after 13 hours of reaction the Rh1IWI_75/25-m900-R750 sample show a decrease of the CH₄ conversion of about 13% (Fig. 3.41), deactivation degree that, in the case of Rh1IWI_CZO-m900-R750 (Fig. 3.42) is not reached even after 34 hours of reaction (7%). After the same time of reaction (about 30 hours) the Rh1IWI_75/25-m900-R750 sample show a deactivation degree about four times higher (≈ 28%) than those recorded in the Rh1IWI_CZO-m900-R750 case (7%). This significant difference in terms of stability towards deactivation is a first indication of the role of the surface lattice oxygen mobility related to the Ce_{0.5}Zr_{0.5}O₂ phase, which is probably able to inhibit carbon formation phenomenon of the catalytic system, thanks to the oxygen available for the carbon oxidation. Another hypothesis is that this deactivation could be related to sintering phenomena but, even if it were, the Rh1IWI_CZO-m900-R750 remain the best catalytic system probably thanks to the higher interaction between Ce and Zr in the Ce_{0.5}Zr_{0.5}O₂ single phase characterizing the CZO-m900 support rather than those involved in the phase relative to the 75/25-m900 support. In fact, connecting with the discussion regarding the XRD and TPR analysis reported in paragraph 3.3.3, the 75/25-m900 support doesn't seem to be composed by a unique phase like in the CZO-m900 case. This non-homogeneity could also lead to the occurrence, of some segregation phenomena that can decrease the activity of the overall system.

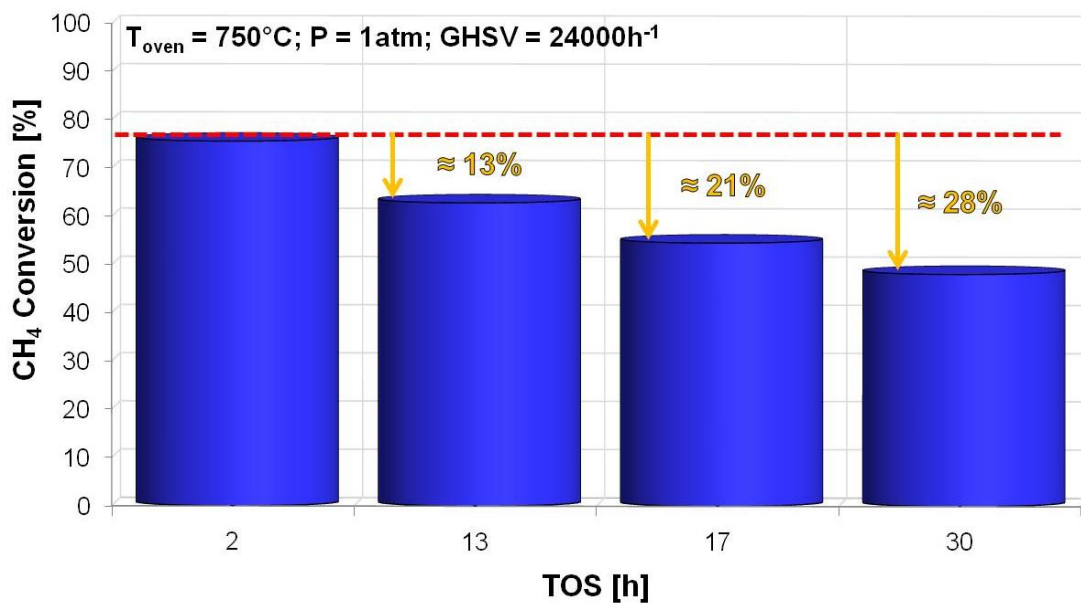


Fig. 3.41. Deactivation degree of the Rh1IWI_75/25-m900-R750 sample in function of the time on stream

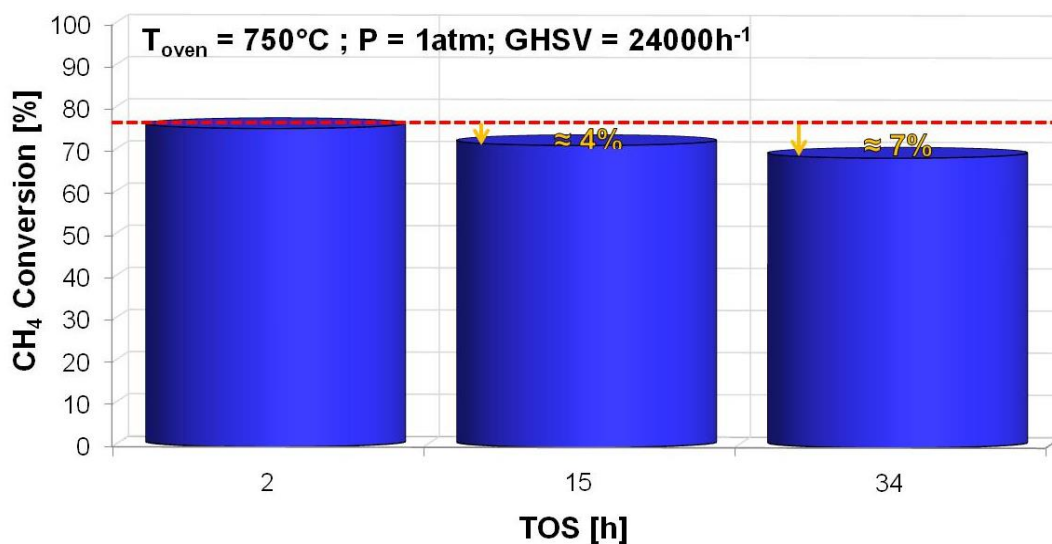


Fig. 3.42. Deactivation degree of the Rh1IWI_CZO-m900-R750 sample in function of the time on stream

3.4.3 Effect of the synthesis method: w/o microemulsion vs co-precipitation

The best Rh1IWI_CZO-m900-R750 catalyst is compared also with a catalyst synthesized by co-precipitation, i.e. Rh1IWI_CZO-cp900-R750, in order to understand if the differences observed in the characterization analysis discussed in the previous section (paragraph 3.3.1) can be confirmed by the effect observed in terms of catalytic behavior.

In Fig. 3.43 is reported a global comparison between the catalytic activity of the Rh1IWI_CZO-m900-R750 sample and the Rh1IWI_CZO-cp900-R750 one. It is enough evident the higher activity of the microemulsion sample in all of the conditions tested, especially at a pressure of 1 atm. This confirms the enhanced activity of the sample prepared by microemulsion already observed comparing it with the Rh1IWI_75/25-m900-R750 sample. In fact, considering the data recorded at the lowest pressure, already at a GHSV value of 24000 h^{-1} the Rh1IWI_CZO-m900-R750 catalyst shows an experimental CH_4 conversion ($\approx 76\%$) of about 15% higher than those observed in the Rh1IWI_CZO-cp900-R750 case ($\approx 61\%$). This difference maintains itself more or less constant also increasing the GHSV until 50000 ($\approx 52\%$ vs $\approx 36\%$) and 100000 h^{-1} ($\approx 45\%$ vs $\approx 32\%$). At higher pressures (10 and 20 atm), as expected, the differences become more subtle, but it's still possible to observe a slight higher performance of the Rh1IWI_CZO-m900-R750, which shows CH_4 conversion values closer to those calculated at the thermodynamic equilibrium than in the case of the co-precipitated supported catalyst.

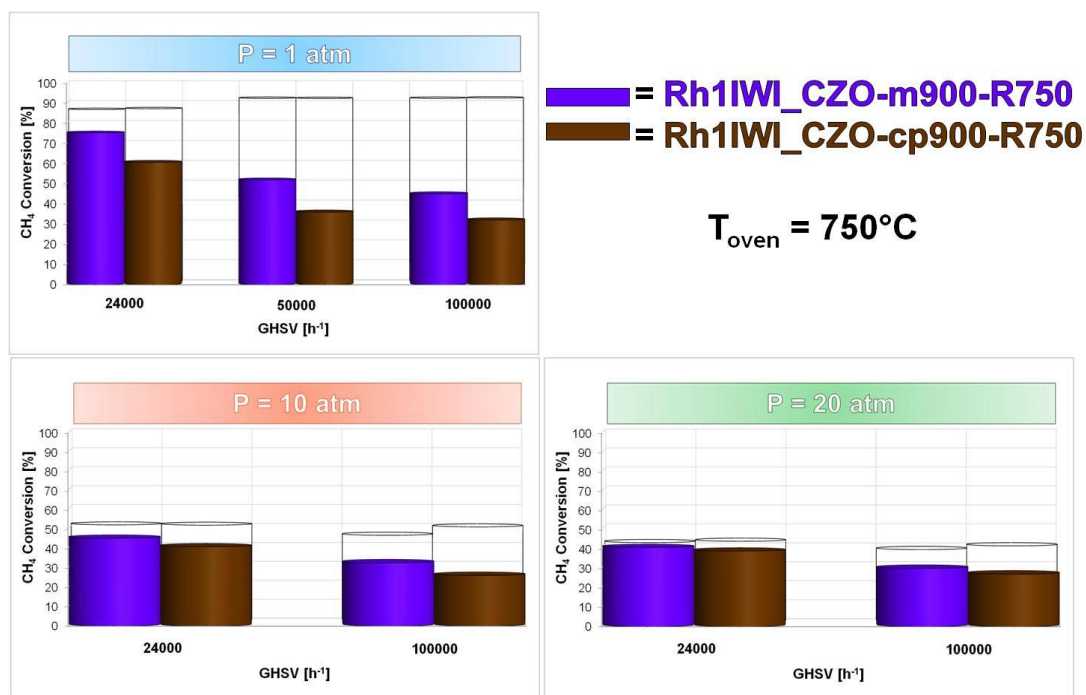


Fig. 3.43. Comparison between the catalytic activity of the Rh1IWI_CZO-m900-R750 sample and the Rh1IWI_CZO-cp900-R750 one in all of the oxy-reforming conditions of pressure and GHSV

The higher activity showed also in this case by the Rh1IWI_CZO-m900-R750 catalyst could be in ascribable to the differences listed above (paragraph 3.3.1) in terms of the nature of the support crystalline structure related to its redox and morphological properties. Probably the less homogeneous metal dispersion characterizing the co-precipitated sample rather than the microemulsion one, detected mainly through the TPR analysis (Fig. 3.25), is one of the features that are responsible of the lower activity of the Rh1IWI_CZO-cp900-R750 catalyst. This parameter can be connected also with the morphological properties (see paragraphs 3.3.1.4 and 3.3.1.5) which could deeply influence the catalytic performances and the impregnation procedure. Therefore, especially the different nature of the pores characterizing these two supports in terms of shape and dimensions (Fig. 3.16) could plays an important role always related to a better or worst Rh dispersion on the support. On the other hand, the surface cannot be responsible of the difference, being very similar for the two preparation methods ($\approx 12 \text{ m}^2/\text{g}$ for the CZO-m900 and $\approx 14 \text{ m}^2/\text{g}$ for the CZO-cp900). In particular, it is possible, that in the larger pores characterizing the CZO-m900 support ($\approx 20 \text{ nm}$) the metal could be better and more uniformly dispersed through impregnation, drying and calcination, than what it able to do in the smaller pores of the CZO-cp900 support ($\approx 4 \text{ nm}$). This could lead to an higher availability of the Rh active species on the CZO-m900 support surface causing the higher activity observed.

The effect of the different crystalline structure, instead, could influence the catalytic stability in terms of deactivation phenomena. Like have been observed in the comparison of the Rh1IWI_CZO-m900-R750 system with the Rh1IWI_75/25-m900-R750 one, also in this case is showed a lower stability of the CZO-cp900 supported catalyst characterized by the $Ce_{0.6}Zr_{0.4}O_2$ phase rather than the $Ce_{0.5}Zr_{0.5}O_2$, present in the CZO-m900 support. In Fig. 3.44 is reported the deactivation degree relative to the Rh1IWI_CZO-cp900-R750 catalyst and comparing it with those relative to the microemulsion sample (Fig. 3.42) is clear how the latter catalyst is less sensitive towards deactivation. This result is a further confirmation of the fact that the $Ce_{0.5}Zr_{0.5}O_2$ probably is the real responsible of an higher stability, for the same reasons already mentioned above. The behavior towards deactivation of the co-precipitated sample is very similar to those observed in the Rh1IWI_75/25-m900-R750 one, even if slightly better data are showed by the former system inasmuch, after about 30 hours of reaction the deactivation degree of the Rh1IWI_75/25-m900-R750 sample was 28%, while those relative to the co-precipitated catalyst is 19%. These considerations are in line with XRD results reported in Fig. 3.20 that showed a similar characteristics between the phases characterizing the supports composing these two latter catalysts.

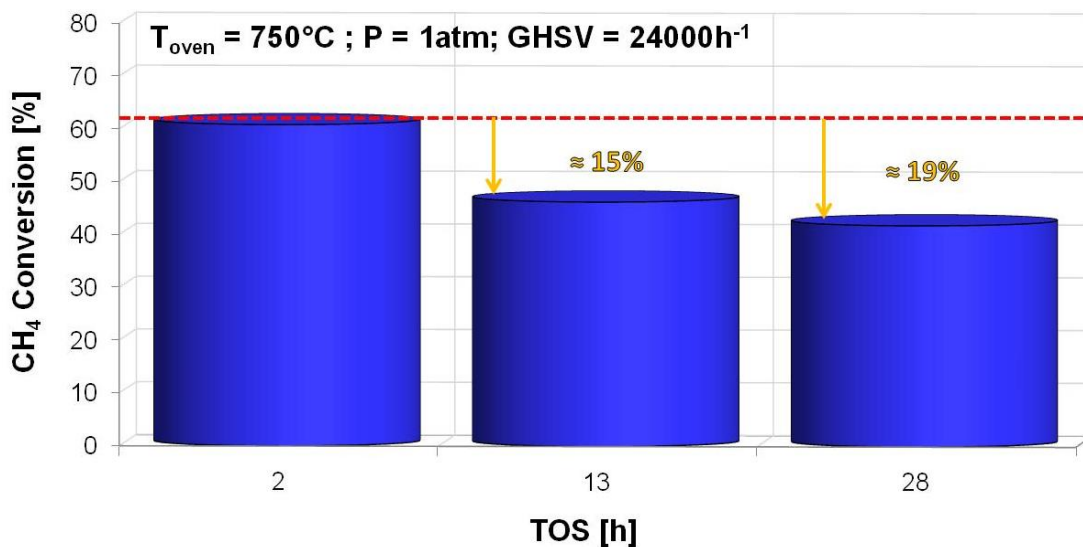


Fig. 3.44. Deactivation degree of the Rh1IWI_CZO-cp900-R750 sample in function of the time on stream

Considering the good performances of the Rh1IWI_CZO-m900-R750, it was decided to test this system also under the low temperature steam reforming (LT-SRM) conditions. In order to have a comparison parameter, the same tests are carried out also on the Rh1IWI_CZO-cp900-R750 catalyst. As mentioned above, considering that in these conditions is particularly important to know the H_2 amount produced, the comprehension of these data is probably better if they are reported in function of the outlet dry gaseous

mixture composition, as showed in Fig. 3.45 (Rh1IWI_CZO-m900-R750) and Fig. 3.46 (Rh1IWI_CZO-cp900-R750). Also in these conditions, better performances are identified in the case of Rh1IWI_CZO-m900-R750 which show experimental CH_4 outlet concentrations very close to those calculated at equilibrium even at very low temperature ($\approx 330^\circ\text{C}$) where the difference between the experimental data ($\approx 73\%$) and the calculated one ($\approx 64\%$) is less than 10%. This deviation decrease further at even higher temperatures, becoming close to zero at the highest temperature of about 480°C , where is produced a gaseous mixture with an H_2 amount equal to 60%. On the other hand, the Rh1IWI_CZO-cp900-R750 catalyst shows experimental outlet concentrations far from those calculated at the thermodynamic equilibrium in all of the temperature range investigated. Comparing the catalytic bed average temperature values (T_{avg}) for the two catalysts, is possible to notice that those recorded for the Rh1IWI_CZO-cp900-R750 are of about 10 degrees higher than those calculated for the microemulsion sample. This value derive from the thermal profile recorded during each test, hence an higher T_{avg} means a less pronounced ΔT which, in turns, is symptom of a lower activity. Even at the highest investigated temperature ($T_{\text{oven}} = 500^\circ\text{C}$) the co-precipitated supported sample shows an experimental CH_4 outlet concentration ($\approx 33\%$) almost 10% higher than those calculated at equilibrium ($\approx 23\%$), i.e. the same difference observed in the worst reaction condition ($T_{\text{oven}} = 350^\circ\text{C}$) for the Rh1IWI_CZO-m900-R750 catalyst.

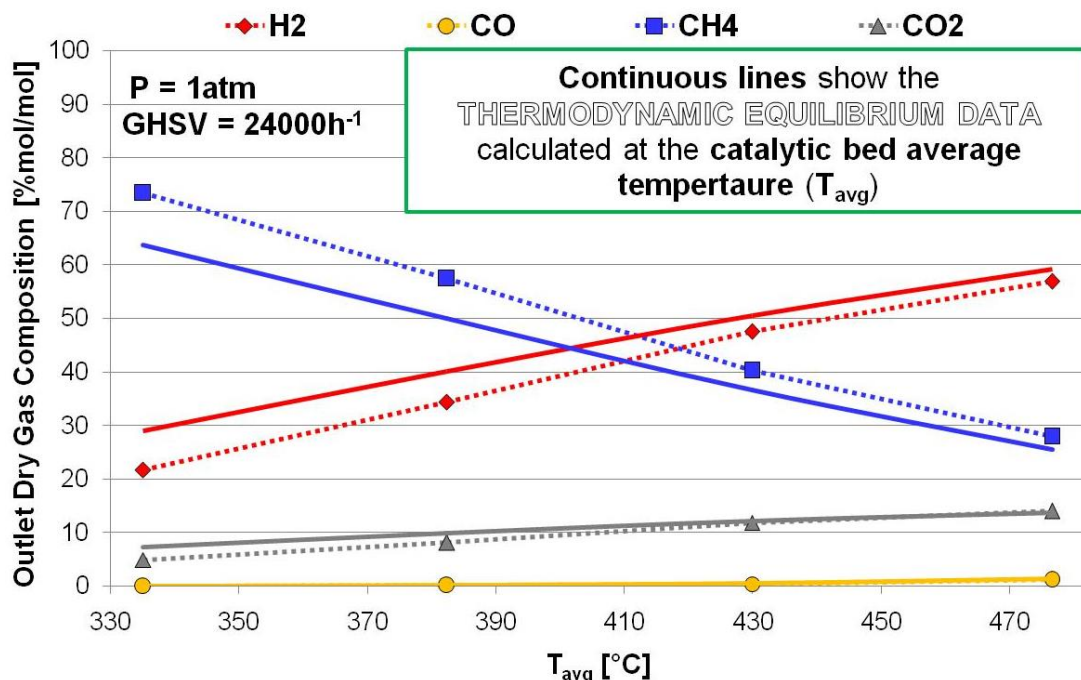


Fig. 3.45. Catalytic activity of Rh1IWI_CZO-m900-R750 in the LT-SRM conditions

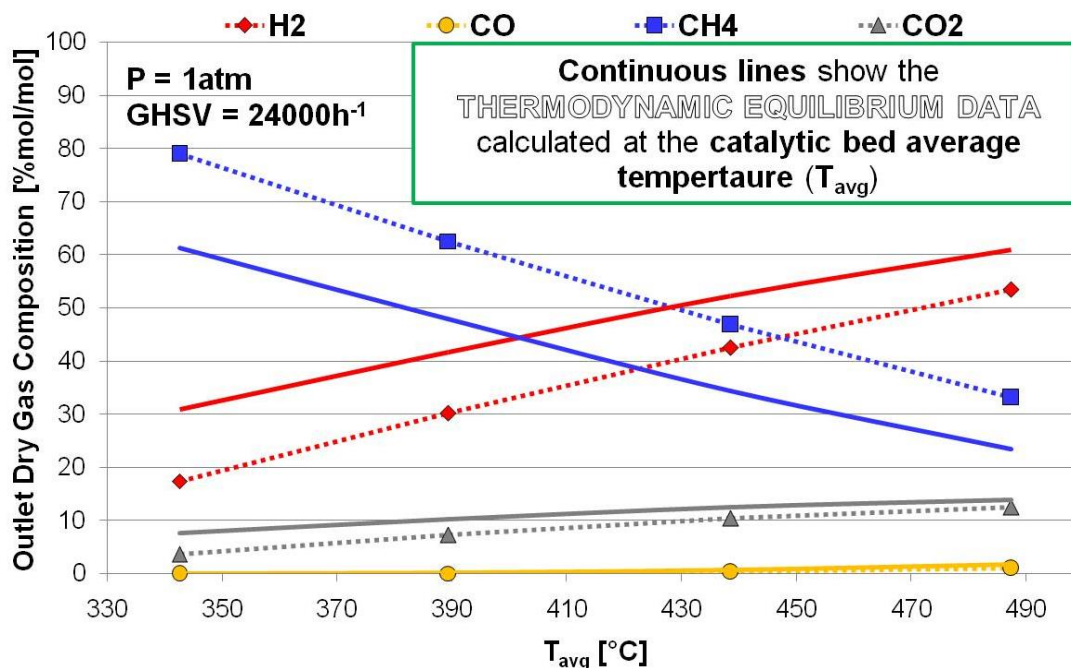


Fig. 3.46. Catalytic activity of Rh1IWI_CZO-cp900-R750 in the LT-SRM conditions

On these samples after reaction (spent catalysts) other investigations are carried out in order to identify some differences mainly related to the tendency to form carbon deposits or not, trying to understand if the $Ce_{0.5}Zr_{0.5}O_2$ phase has a relevant impact on it, rather than the $Ce_{0.6}Zr_{0.4}O_2$ one.

A TPO/R/O analysis is firstly carried out and the results are reported in Fig. 3.47 a and b. Focusing on the first oxidation profile, the first positive peak ascribable to the concurrent oxidation of Ce^{3+} to Ce^{4+} and Rh^0 to Rh^{3+} , is centered at about 140°C for both of the samples but a negative peak at about 650°C is present only in the co-precipitated catalyst and not in the microemulsion one. The temperature at which this latter peak is centered and its negative nature, are two features that permits to attribute this peak to the oxidation of some carbonaceous deposits that under oxidizing atmosphere at high temperature are eliminated from the catalyst surface in the form of CO and CO₂, compounds detected with a negative trend from the instrument. In fact, in the second oxidation profile, after reduction, this peak is not visible also regarding the co-precipitated spent catalyst, index of the absence of carbon deposits, eliminated in the first oxidation step.

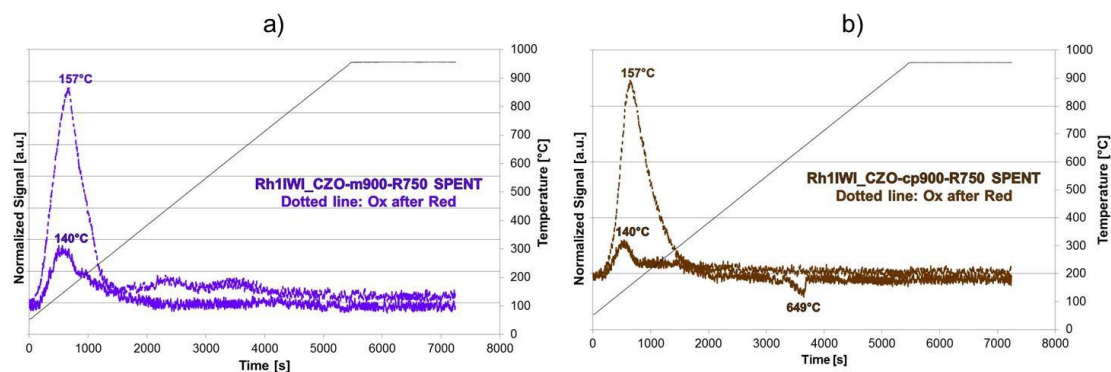


Fig. 3.47. O₂-TPO profiles recorded during a TPO/R/O cycle on the: a) Rh1IWI_CZO-m900-R750 and b) Rh1IWI_CZO-cp900-R750, after the catalytic tests

TEM micrographs on the same spent catalysts confirm the presence of carbonaceous deposits on the Rh1IWI_CZO-cp900-R750 (images on the right in Fig. 3.48) rather than on the Rh1IWI_CZO-m900-R750 (images on the left in Fig. 3.48). In the former case is clearly visible amorphous material on the support surely ascribable to some carbonaceous species that are not detectable in the microemulsion sample. The presence of carbon cause also a more difficult the identification of the metal particles on the support that are, instead, distinctly detectable in the Rh1IWI_CZO-m900-R750 case.

These results could further confirm the relevant influence that the higher oxygen mobility of the $\text{Ce}_{0.5}\text{Zr}_{0.5}\text{O}_2$ phase than the $\text{Ce}_{0.6}\text{Zr}_{0.4}\text{O}_2$ one, can have regarding the deactivation phenomena related to the carbon formation.

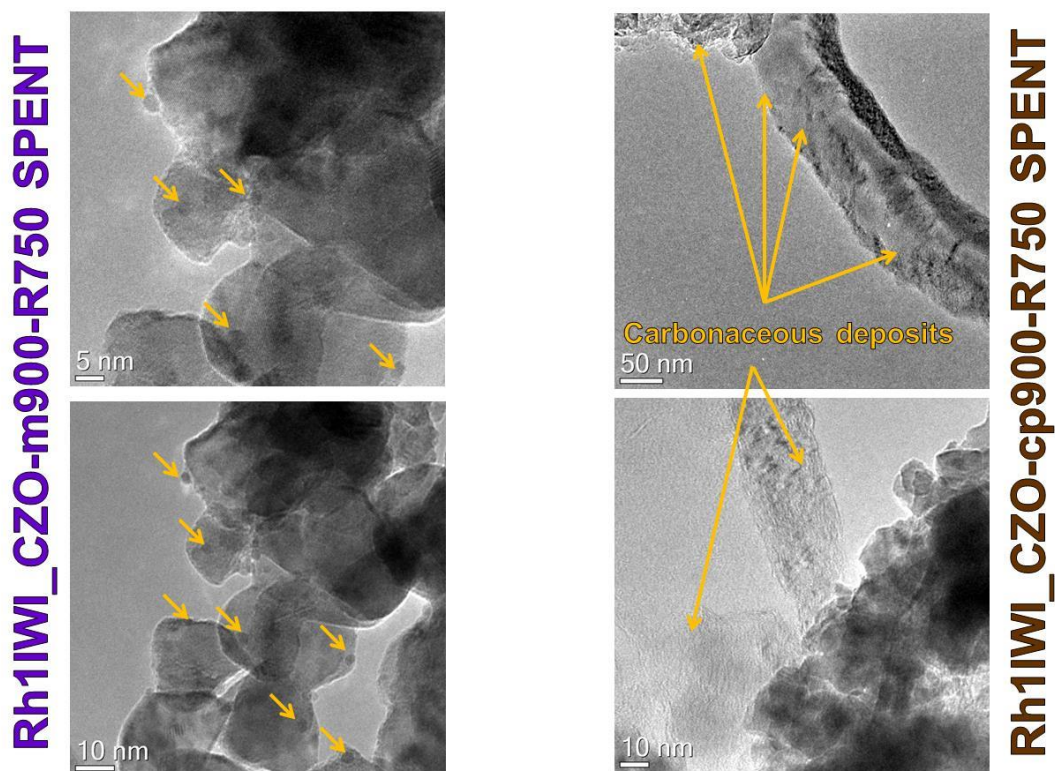


Fig. 3.48. TEM micrographs recorded on Rh11WI_CZO-m900-R750 (on the left) and Rh11WI_CZO-cp900-R750 (on the right) samples after catalytic tests. In the case of Rh11WI_CZO-m900-R750 the arrows indicate the well dispersed Rh particles on the support

Another feature deriving from the analysis of the TEM images, mainly relative to the microemulsion supported sample, is the metal – support interaction, clearly visible in the image reported in Fig. 3.49. A surface reaction of the support with the Rh particle which generate a partially incorporation of Rh particles by the support seems to take place. As a drawback, this effect lead to a consequent decrease of the metal surface active area which could negatively influence the activity of the catalyst and explain the differences in the activity also present in the the Rh11WI_CZO-m900-R750 sample prepared by microemulsion. As mentioned in the introduction session (paragraph 1.2.2.1) the SMSI phenomenon strictly depend on the thermal history followed by the sample, hence a study relative to the effects that can have the calcination and reduction temperatures on these kind of systems could be very useful in order to understand if and how the SMSI phenomenon can be limited or, better, avoided.

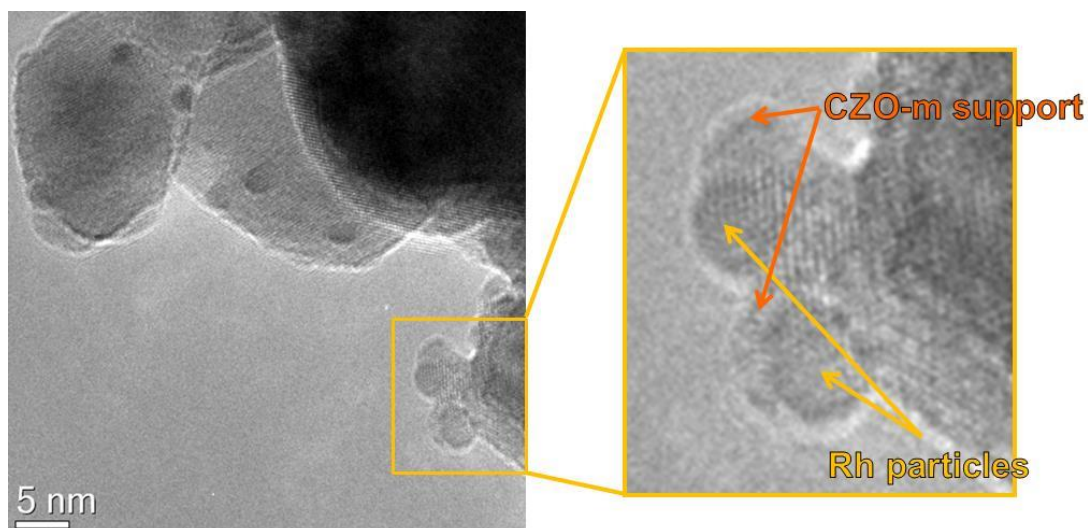


Fig. 3.49. Enlargement of a zone of a TEM micrograph relative to the Rh1IWI_CZO-m900-R750 spent catalyst, where is clearly visible the interaction between metal and support

3.4.4 Effect of the nature of the active metal

Demonstrated the better performances of the Rh1IWI_CZO-m900-R750 catalyst, it has been taken as reference in order to study the effects that could derive from the different nature of the active metal.

The main problem related to Ru-based catalysts used in reaction like the reforming ones is the high degree of thermal sintering from which this metal is strongly affected. In fact, Ru is even active enough in reforming reactions, but the conditions involved in these processes are the responsible of the very short lifetime of these kind of catalysts deriving also from the high tendency of Ru to oxidize itself also in mild oxidative conditions. Considering these problems, the CZO-m support could improve the stability of Ru-based system, thanks to its very high thermal stability (deriving from the presence of Zr) and the peculiar redox properties deriving from the presence of Ce.

The catalytic activity of the Ru1IWI_CZO-m900-R750 catalyst in the oxy-reforming conditions is summarized in Fig. 3.50. If a direct comparison between these data with those relative to the Rh1IWI_CZO-m900-R750 sample (Fig. 3.40) is made, become clear how the Ru-based system has a catalytic activity fully comparable with those relative to the best Rh-based system obtained so far. In fact, at 1 atm and 24000 h⁻¹ the experimental CH₄ conversion sowed by the Ru catalyst ($\approx 71\%$) is slightly lower than those relative to the Rh one ($\approx 76\%$), difference which practically become null at higher GHSV values, where the Ru1IWI_CZO-m900-R750 show conversions of about 55% (at 50000 h⁻¹) and 44% (at 100000 h⁻¹), against 52% (at 50000 h⁻¹) and 45% (at 100000 h⁻¹) relative to the Rh1IWI_CZO-m900-R750 catalyst. In more drastic conditions (P = 10 and 20 atm) at 24000 h⁻¹ the Ru catalyst seems to have even better performances than the

Rh one, reaching at both pressures the thermodynamic equilibrium, feature satisfied only at 20 atm considering the Rh1IWI_CZO-m900-R750 catalyst. The conversions recorded at 100000 h⁻¹, instead, practically assume the same values for both catalysts (≈ 33% at 10 atm and ≈ 30% at 20 atm).

Therefore, at high temperature, under oxy-reforming conditions, the Ru1IWI_CZO-m900-R750 catalyst have a really good activity, comparable with the Rh1IWI_CZO-m900-R750 system considered, until now, the best one. Furthermore, extended the comparison even between the other catalysts tested (Rh1IWI_75/25-m900-R750 and Rh1IWI_CZO-cp900-R750) is possible to state the higher activity of the Ru impregnated sample, more or less in all of the conditions tested.

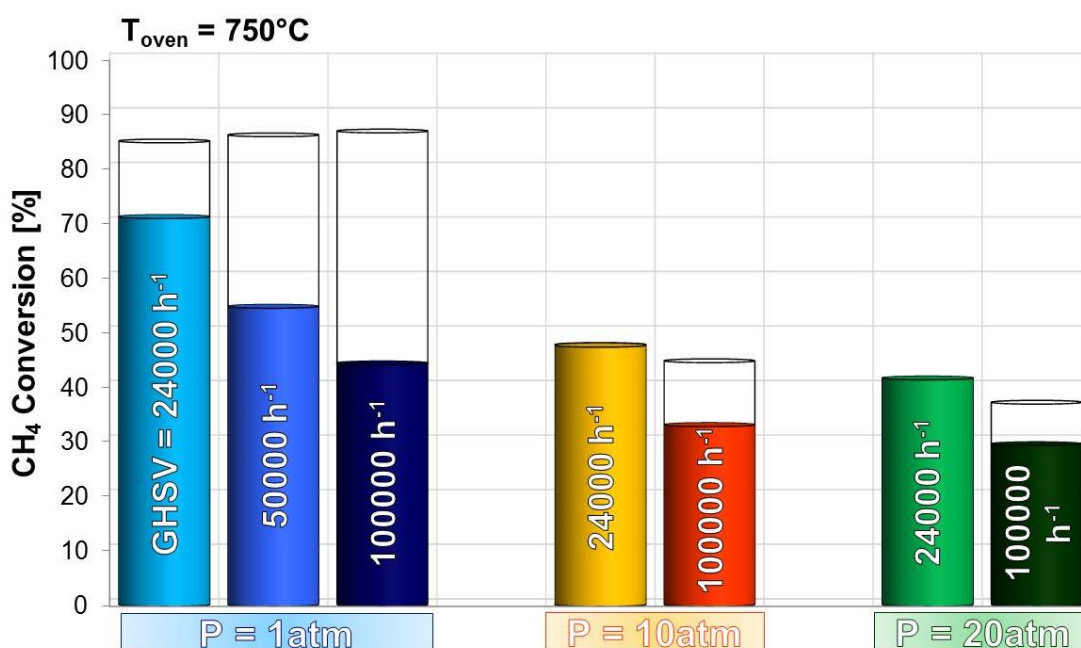


Fig. 3.50. Catalytic activity of Ru1IWI_CZO-m900-R750 in function of pressure and GHSV

Considering that weak point of the Ru-based systems, its stability towards deactivation, is possible to say that the Ru1IWI_CZO-m900-R750 catalyst is characterized by an high degree of stability as shown in Fig. 3.51. After 14 hours of reaction presents a CH₄ conversion decrease of only 3%, reaching a value of about 10% after 24 hours. As expected, regarding the stability, the Rh1IWI_CZO-m900-R750 catalyst (Fig. 3.42) remain still the best, but considering the other Rh-based systems characterized by a different support's crystalline phase (mainly Ce_{0.6}Zr_{0.4}O₂ instead of Ce_{0.5}Zr_{0.5}O₂) (Fig. 3.41 and Fig. 3.44), the Ru1IWI_CZO-m900-R750 is better showing a deactivation degree in function of time on stream significantly lower than both Rh1IWI_75/25-m900-R750 (28% after about 30 hours of reaction) and Rh1IWI_CZO-cp900-R750 (19% after about 28 hours of reaction).

Even in this case, hence, the $\text{Ce}_{0.5}\text{Zr}_{0.5}\text{O}_2$ phase characterizing the CZO-m900 support seems to play a fundamental role in terms of activity and stability, improving these important features also in systems characterized by an active metal particularly sensitive towards deactivation phenomena like Ru.

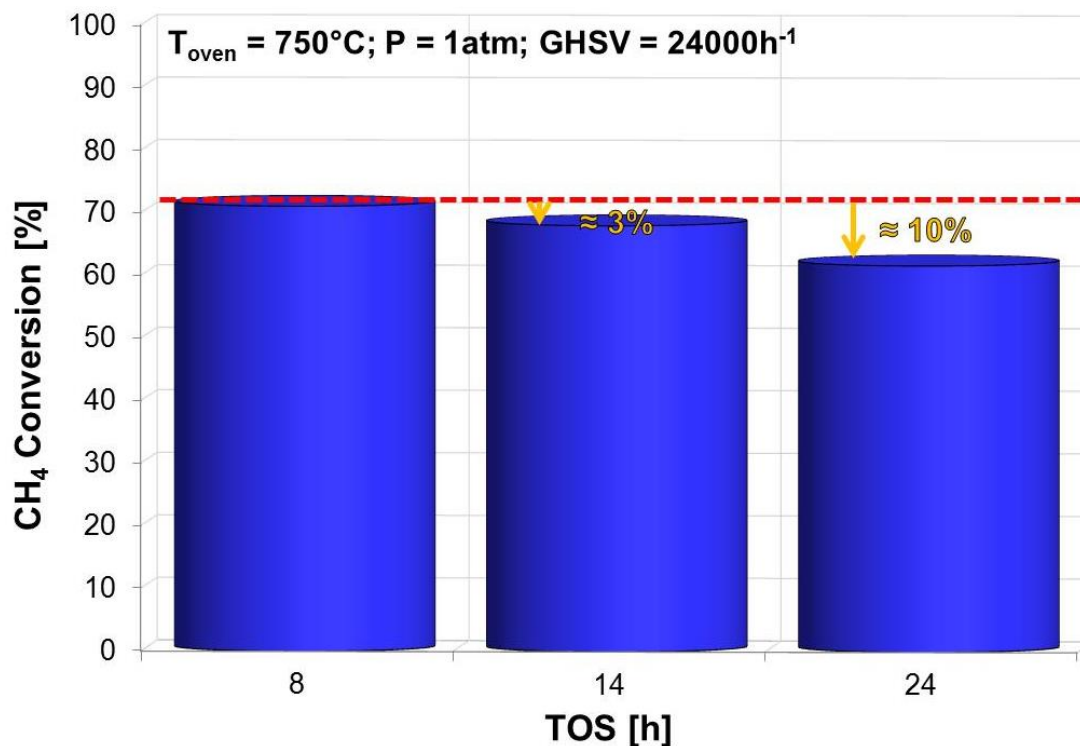


Fig. 3.51. Deactivation degree of the Ru1IW1_CZO-m900-R750 sample in function of the time on stream

The good activity showed by Ru1IW1_CZO-m900-R750 lead to the investigation of its performances also at low temperature steam reforming, conditions at which, it shows the activity results reported in Fig. 3.52. In this conditions is present an higher amount of H_2O ($\text{S/C} = 3.00$) in comparison with the oxy-reforming conditions ($\text{S/C} = 0.71$) Even in these drastic conditions the Ru1IW1_CZO-m900-R750 sample shows a very good activity comparable again with those obtained through the Rh1IW1_CZO-m900-R750 system (Fig. 3.45) and the Rh1IW1_CZO-cp900-R750 (Fig. 3.46). The Rh-based microemulsion supported system remain in any case the best one, but it is important to notice that the Ru-based catalyst shows an activity very similar to the Rh-based co-precipitated system and, in some cases, even better. At the lowest temperatures values ($T_{\text{avg}} \approx 350^{\circ}\text{C}$ and 390°C) these two samples practically show the same deviation between the experimental CH_4 outlet amount and the value calculated at the thermodynamic equilibrium; 18% against 20% at 350°C for Rh1IW1_CZO-cp900-R750 and Ru1IW1_CZO-m900-R750, respectively and 15% in both cases at about 390°C . At about 440°C instead, this trend starting to change showing a deviation of about 13% for

the co-precipitated sample against one of about 9% relative to the Ru-based catalyst. The same four percentage points of difference are still identified at about 490°C where the Rh1IW1_CZO-cp900-R750 shows a deviation of about 10% while 6% is the deviation exhibited by the Ru1IW1_CZO-m900-R750. This slight higher activity of the latter sample in comparison with the co-precipitated one, could derive again from an higher degree of homogeneity relative to the CZO-m900 support which can permits a better dispersion of Ru with respect to those of the Rh on the CZO-cp900 support (see Fig. 3.25). At very low temperatures (350°C and 390°C) the differences between these two samples are not visible probably thanks to the fact that a better dispersion of the Ru balance the lower activity of Ru also caused by the oxidation occurring at low temperature due to the excess of steam in the system. With the increase of the temperature these two features continue to influence the activities of the two samples in different way. Probably Ru become more active at a temperature higher than 400°C, while the effect of the dispersion remain the same. In fact, the temperatures involved are too low in order to influence the metal dispersion on the support but high enough to cause a slight increase of the activity of the Ru metal particles by increasing the reductive potential of the reaction mixture which increase with temperature.

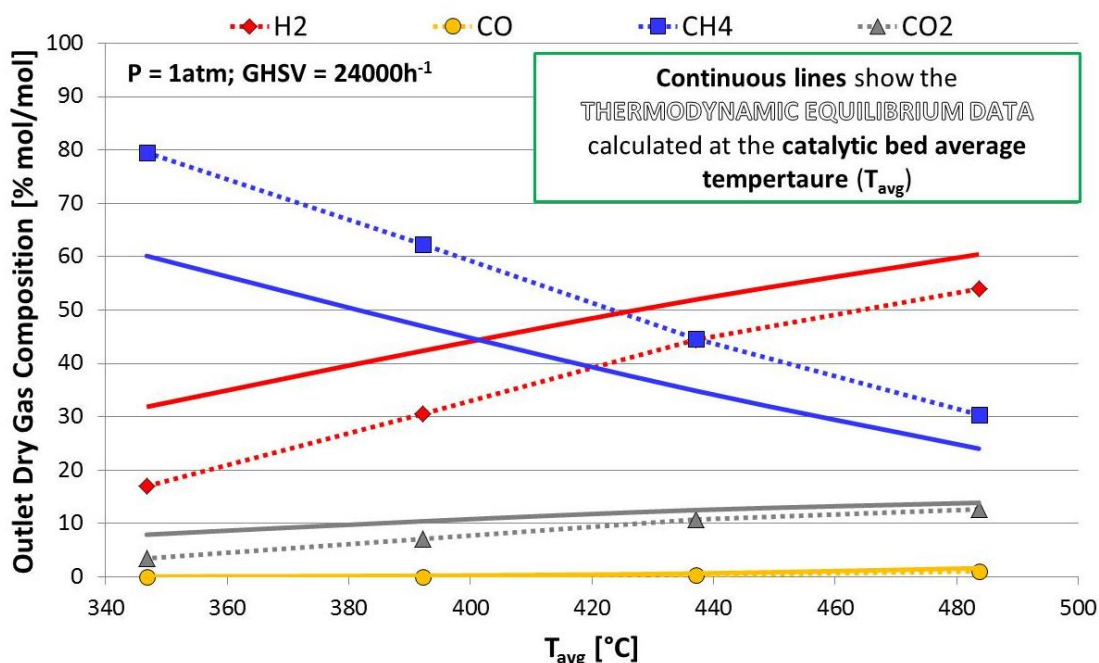


Fig. 3.52. Activity of Ru1IW1_CZO-m900-R750 sample at LT-SRM conditions

Regarding the Ni-based impregnated catalysts (Ni5IW1_CZO-m900-R750 and Ni10IW1_CZO-m900-R750), their catalytic activities in the oxy-reforming conditions are compared in Fig. 3.53 a and b. As expected, in accordance with the results deriving from XRD analysis (Fig. 3.31), these two samples show a significant lower activity with

respect to the Rh- and Ru-based impregnated catalysts discussed above. In the case of Ni5IWI_CZO-m900-R750 the CH₄ conversion at 1 atm and 24000 h⁻¹ doesn't even reach a value of 60% (≈ 56%), while at 50000 and 100000 h⁻¹ the conversion values are comparable to those obtained in general with the other catalysts (≈ 50% at 50000 h⁻¹ and ≈ 40% at 100000 h⁻¹). At higher pressure (10 atm) even at low GHSV value (24000 h⁻¹) the experimental conversion doesn't coincide with those calculated at the equilibrium, which is reached only at 20 atm at 24000 h⁻¹. Increasing the metal loading until 10% w/w (Ni10IWI_CZO-m900-R750) the performances don't increase significantly but remain, more or less, the same. A slight improvement can be observed if are considered the conversion values relative to the tests carried out at 50000 and 100000 h⁻¹ at a pressure of 1 atm. In fact, these values (≈ 55% at 50000 h⁻¹ and ≈ 50% at 100000 h⁻¹) are similar, or even slightly higher, to those showed in the case of Rh1IWI_CZO-m900-R750 (52% and 45%). Anyway, this data are a further confirmation that a so high amount of metal cannot be impregnated properly on a CZO-m900 support having a too low pores volume. In fact, in spite of the active metal amount (five and ten times higher than Rh and Ru catalysts) in this kind of reaction, the activity of these two samples is lower and this is surely due to the presence of crystalline Ni-based species not well dispersed on the support, already detected in the XRD patterns relative to the calcined fresh catalysts.

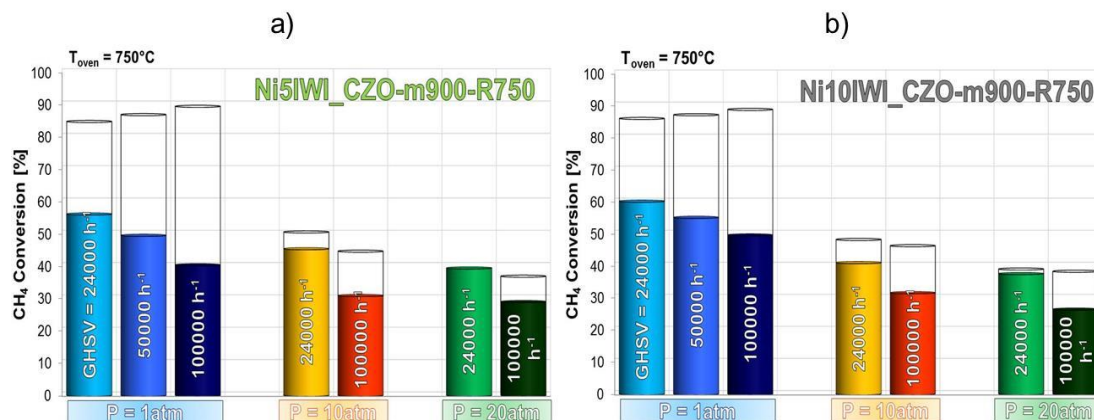


Fig. 3.53. Catalytic activity in function of pressure and GHSV of: a) Ni5IWI_CZO-m900-R750; b) Ni10IWI_CZO-m900-R750

3.4.5 Effect of the metal insertion method

This type of investigation is started from the comparison between Rh1IWI_CZO-m900-R750 and Rh1bulk_CZO-m900-R750. Beyond the difference relative to the metal insertion method, it is useful to remind that the impregnated samples and the bulk ones are inevitably different also in terms of thermal treatments. In this case, the bulk sample is calcined at 900°C already with the metal inserted, while in the case of the IWI sample, only the support is subjected to the calcination at 900°C and, after the metal impregnation, a milder calcination occurred at 500°C. This could imply important differences in terms of metal dispersion on the support, as already discussed in the previous characterization section (paragraph 3.3.4.1), that could have a significant role on the catalytic activity.

The catalytic activity data relative to the Rh1bulk_CZO-m900-R750 sample are reported in Fig. 3.54. The activity of this sample is really lower than all the other samples tested so far. In fact, at 1 atm the CH₄ conversion is barely higher than 30%, enormously different value if compared to those relative to the Rh1IWI_CZO-m900-R750 sample (≈ 76% – Fig. 3.40) and this is also the reason for which it is decided to proceed quickly to the test at 20 atm neglecting those at 10 atm, reasonably not useful in order to obtain important informations, just established the low activity at 1 atm. Furthermore, even at 20 atm the equilibrium is not reached, showing an experimental CH₄ conversion of about 32% against of a calculated thermodynamic value of about 40%. This behavior is in accordance with the characterization data stated above (Fig. 3.26 and Fig. 3.27) from that it was observed that Rh in the bulk sample calcined at 900°C get into the CZO framework, not rendering itself available on the support surface for the reaction like, on the contrary, happened in the case of the impregnated catalyst.

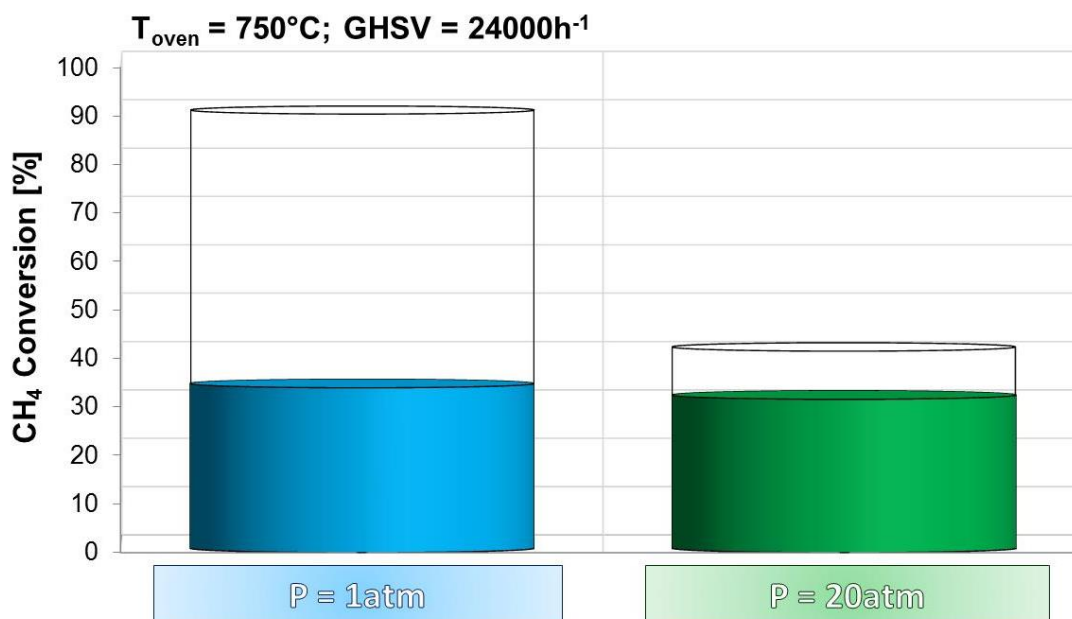


Fig. 3.54. Catalytic activity of Rh1bulk_CZO-m900-R750 sample

This statement is further confirmed if the results in Fig. 3.55 are considered. In fact, as detected from the TPR analysis (Fig. 3.26), an increase in the operative temperature could be the responsible of a sort of increase of the reduction grade of part of the metal from the bulk to the surface, leading to a consequential increasing of the activity. In fact, observing the very low activity at $T_{\text{oven}} = 750^{\circ}\text{C}$ it was tried to carry out a test at an oven temperature of 100°C higher and, as predicted, the CH_4 conversion increase of about 23 percentage points, from a value of about 34% at 750°C to about 57% at 850°C . This “activation effect” is visible also considering the data recorded in the return tests, showed in Fig. 3.56. Regarding the stability, this sample shows a decrease in CH_4 conversion of about 11% already after only 9 hours of reaction, a value that the Rh1IW1_CZO-m900-R750 catalyst didn't reach even after more than 30 hours of reaction (Fig. 3.42). Nevertheless, the last return test carried out after about 20 hours of reaction and after the test at higher temperature, result in a CH_4 conversion value higher ($\approx 40\%$) than those relative to the first test ($\approx 30\%$) carried out on the fresh catalyst. Result which confirm that during the test carried out higher temperature (850°C) some metal migration effects from the bulk to the surface of the support occurs, leading to a slightly higher percentage of Rh available on the surface which entail an higher activity.

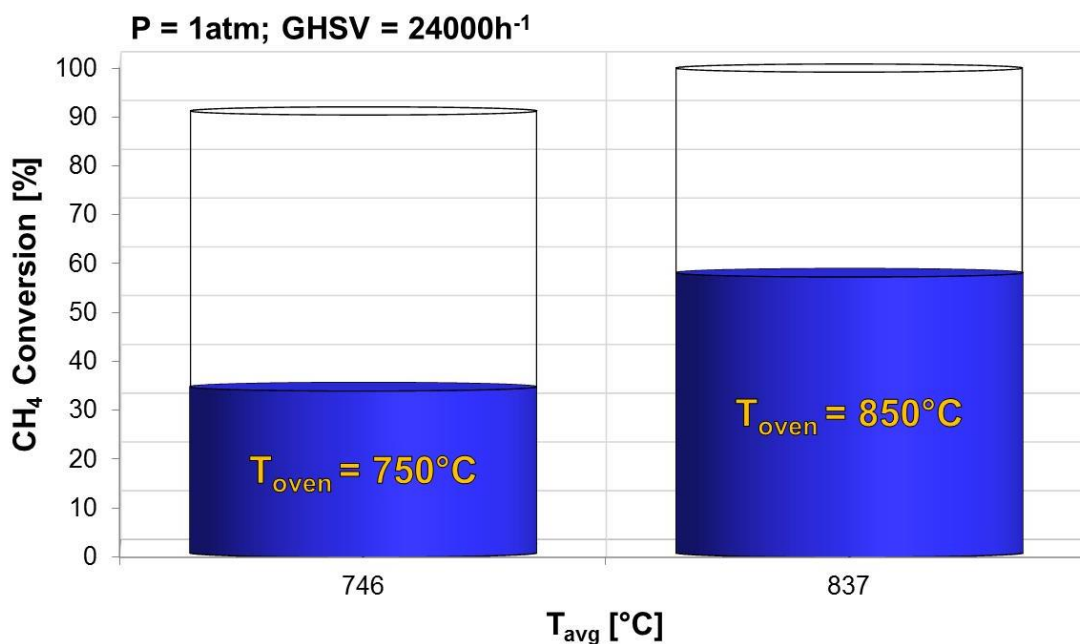


Fig. 3.55. Catalytic activity of Rh1bulk_CZO-m900-R750 sample at different temperatures

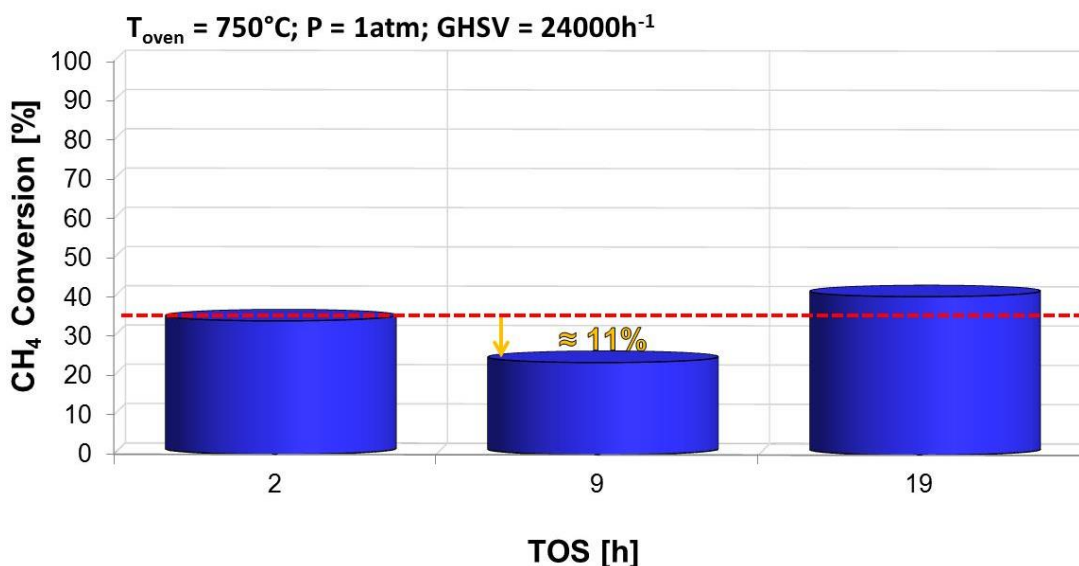


Fig. 3.56. Deactivation degree of the Rh1bulk_CZO-m900-R750 sample in function of the time on stream

Even worst results are obtained testing the bulk catalyst containing Ru as active phase (Ru1bulk_CZO-m900-R750) which showed a very low CH₄ conversion (≈ 14%) already in the first catalytic test at the reference conditions. In this case, the non-activity could be in accordance with the awful degree of dispersion of the Ru particles ascribable to this sample from the TPR data already discussed and reported in Fig. 3.29.

Concerning the Ni-based bulk samples, only the Ni5bulk_CZO-m750-R750 sample was tested in the oxy-reforming conditions and its catalytic activity is reported in Fig. 3.57. At the beginning (P = 1atm; GHSV = 24000 h⁻¹) it exhibits a good activity, showing

a CH₄ conversion value ($\approx 74\%$) higher than those relative to the IWI sample containing the same amount of Ni but characterized by the CZO-m900 support (Fig. 3.53 a), which showed a CH₄ conversion, in the same conditions of about 56%. Even at higher pressures the bulk sample behave better, reaching the thermodynamic equilibrium already at 10 atm and maintaining this trend also at 20 atm. This better performances derive from different way in which Ni is present on the support. In the IWI sample, NiO crystalline phases detected from XRD analysis (Fig. 3.31) are the responsible of the low activity of this sample since the first catalytic test. In the bulk catalyst, instead, Ni is preferentially into the bulk of the support, avoiding the formation of NiO crystalline species on the surface. After the tests at 24000 h⁻¹ and 1, 10 and 20 atm, was carried out those at 1 atm and 50000 h⁻¹, identifying a drastic decrease in the activity of the bulk sample (CH₄ conversion $\approx 33\%$) probably due to some deactivation effect occurred during the tests at high pressures. The same sequence of tests were followed in the case of the Ni5IWI_CZO-m900-R750 catalyst but it didn't show a so significant drop regarding the CH₄ conversion value (from 56% to 50%). In fact, comparing the deactivation degrees of these two samples reported in Fig. 3.58, is evident how the bulk one is more sensitive towards deactivation. The latter sample, already after about 20 hours of reaction shows a decrease in the CH₄ conversion at around 17 percentage points, while the IWI one, even after 23 hours of reaction, exhibits a catalytic activity drop of 7%. The results relative to the IWI sample (Fig. 3.58 a) could be a further confirmation of the peculiar oxygen mobility of the Ce_{0.5}Zr_{0.5}O₂ phase characterizing the CZO-m900 support, which probably avoid the occurrence of carbon formation phenomena also on metal very sensitive to this kind of deactivation like Ni. This results allow also to think that the higher deactivation degree showed by the bulk sample (Fig. 3.58 b) doesn't depend on carbonaceous deposits on the active sites, but probably sintering phenomena are the responsible. In order to understand which effect cause the deactivation, after the last return test the bulk catalyst was subjected for a short period of time (about 2 hours) to a regeneration process feeding the H₂/N₂ (H₂ = 10%v/v) reducing mixture at T_{oven} = 750°C. If carbonaceous deposits are the cause of the high deactivation degree observed, during this treatment they should be removed and then, carrying out again the reference test at 1 atm and 24000 h⁻¹, the activity should arises again reaching similar CH₄ conversion values detected in the first test carried out on the fresh sample. The reference test carried out after this 2 hours, showed a CH₄ conversion of about 56%, confirming the second hypothesis stated above, i.e. the deactivation of the Ni5bulk_CZO-m750-R750 sample depends on the occurrence of sintering phenomena during reaction at high temperature and pressure, and not on carbonaceous deposits on the Ni active sites.

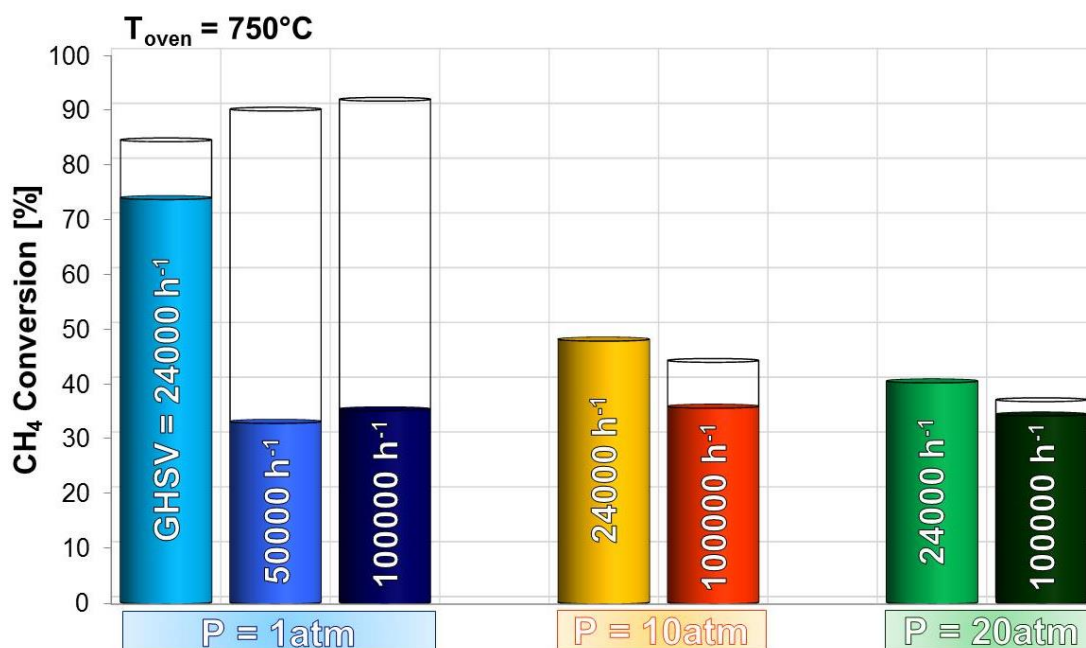


Fig. 3.57. Catalytic activity of the Ni5bulk_CZO-m750-R750 sample at the oxy-reforming conditions

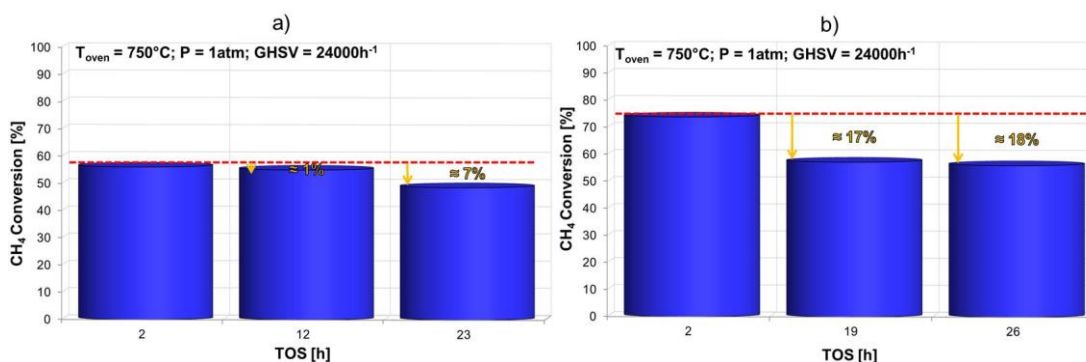


Fig. 3.58. Comparison between the behavior towards deactivation of the catalyst: a) Ni5IWI_CZO-m900-R750; b) Ni5bulk_CZO-m750-R750

3.4.6 Effect of the calcination temperature

3.4.6.1 Bulk samples

It is clear how the method of insertion of the metal plays a fundamental role on its dispersion on the support, which in turn is a feature strictly related to the catalytic activity. The dispersion of Rh and Ru in the lattice of the CZO mixed oxide in the Rh1bulk_CZO-m900-R750 and Ru1bulk_CZO-m900-R750 catalysts, their mobility and reducibility, are features that strictly depend on the temperature, therefore they could be limited modulating the calcination and/or the reduction temperature. TPR/O/R characterization is utilized in order to understand the magnitude of these effects on the samples calcined at lower temperature.

In Fig. 3.59 are reported the H₂-TPR profiles of the Rh1bulk_CZO-m sample calcined at 750°C and 500°C. These profiles are very different if compared with those relative to the equivalent sample calcined at 900°C (Rh1bulk_CZO-m900 – Fig. 3.26). In fact, keeping in mind the broad shape of the peaks characterizing the Rh1bulk_CZO-m900 and the temperature at which Rh is reduced, especially in the first reduction step (531°C), is clear that decreasing the calcination temperature the stability of the CZO framework is lower and the defects increase, giving higher mobility to the Rh inside the lattice, rendering the metal more available on the support surface. Considering the Rh1bulk_CZO-m750 sample, it presents the first reduction profile characterized by three peaks at 204, 415 and 580°C. The low temperature peak is associated to the reduction of the Rh oxide present in the CZO surface layers, while the second and third peaks can be attributable to some Rh species preferentially located in the bulk of CZO framework, rendering themselves more difficult to be reduced. After the oxidation cycle, the redox properties of the sample change in a very similar way to which observed in the Rh1IWI_CZO-m900 case (Fig. 3.14). The second reduction profile is in fact characterized by a single peak at 283°C, indicating that the Rh oxide species, formed during the oxidation at 950°C, react with the support surface forming an homogeneous surface mixed oxide.

More or less, the same considerations could be drawn for the Rh1bulk_CZO-m500, but with some inevitably differences, mainly considering the first reduction profile. In fact, in this case any peak over 300°C is present but, a combination of two peaks at lower temperature composed by the main one at 150°C with a shoulder at 111°C, is present. This is in accordance with the fact that 500°C is a calcination temperature relatively low and the metal distributed on the support surface is reduced at low temperature. The same “metal redistribution effect” which takes place during the oxidation cycle hypothesized for the Rh1bulk_CZO-m750, occurs also for the Rh1bulk_CZO-m500 sample, which shows a second reduction profile characterized mainly by a single intense peak centered at 300°C, index of an high metal dispersion homogeneity also in this sample.

In the light of these results and comparing them with those characterizing the Rh1bulk_CZO-m900 sample, seems that exists a sort of a transitional calcination temperature over which the reduced Rh on the surface become able to diffuse into the CZO framework and this temperature value is located below 950°C. In fact, between 500 and 750°C there aren't so significant differences in terms of metal dispersion on the support, especially in the reduction profile recorded after the oxidation cycle, which in both cases is characterized by a single peak centered at about 300°C.

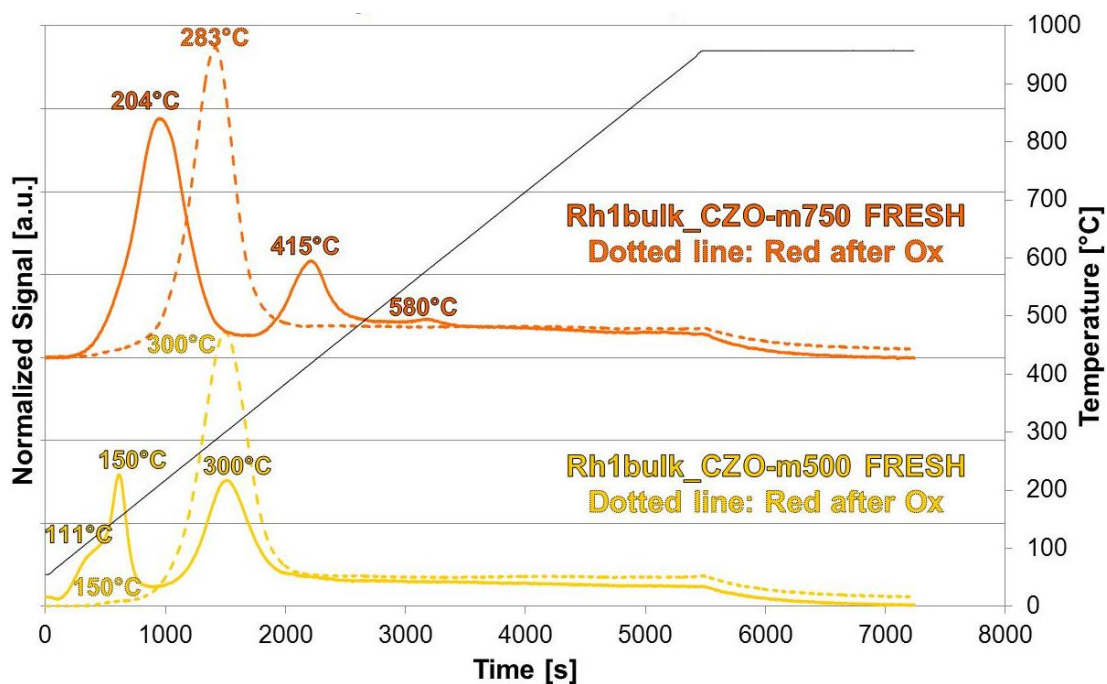


Fig. 3.59 . Comparison between the H₂-TPR profiles of Rh1-bulk samples calcined at 750°C (Rh1bulk_CZO-m750) and 500°C (Rh1bulk_CZO-m500)

The same study is carried out also on the Ru-based bulk catalysts and their reduction profiles are showed in Fig. 3.60. Comparing these H₂-TPR profiles with those relative to the Ru1bulk_CZO-m900 sample (Fig. 3.29), it could be affirmed that even in this case, the reducibility of these systems improves following a decrease in the calcination temperature but, in terms of metal dispersion homogeneity, Ru-based samples remain worse than the Rh-based ones. As mentioned above (paragraph 3.3.4.1.2), Ru is a metal very sensitive towards thermal sintering, and even in the samples calcined at low temperatures, these phenomena plays a crucial role. Decreasing the calcination temperature, sintering effects should be less important, furthermore the presence of several Ru species, which inhibit a reaction between Ru and support, is confirmed using low calcination temperature. In fact, several peaks at 126, 166, 307 and 440°C characterized the first profile of the Ru1bulk_CZO-m750 sample. Especially in the second reduction profile, only one peak is present at high temperature (268°C), ascribable to the reduction of oxidized Ru species reacted with the surface lattice of the support. This reduction occurs together with that relative to the CeO₂ present in the support.

Regarding the Ru1bulk_CZO-m500 sample, is possible to observe how the structural homogeneity is higher than in the other Ru-based bulk samples (calcined at 750°C and 900°C), particularly considering the reduction profile recorded either before or after the oxidation step. Actually, a shift towards lower temperatures of the peak at about 300°C characterizing the first reduction profile of both Ru1bulk_CZO-m750 and Ru1bulk_CZO-

m500 samples (307°C for the Ru1bulk_CZO-m750 sample and 334°C for the Ru1bulk_CZO-m500 one) with respect to the second reduction profile is observed.

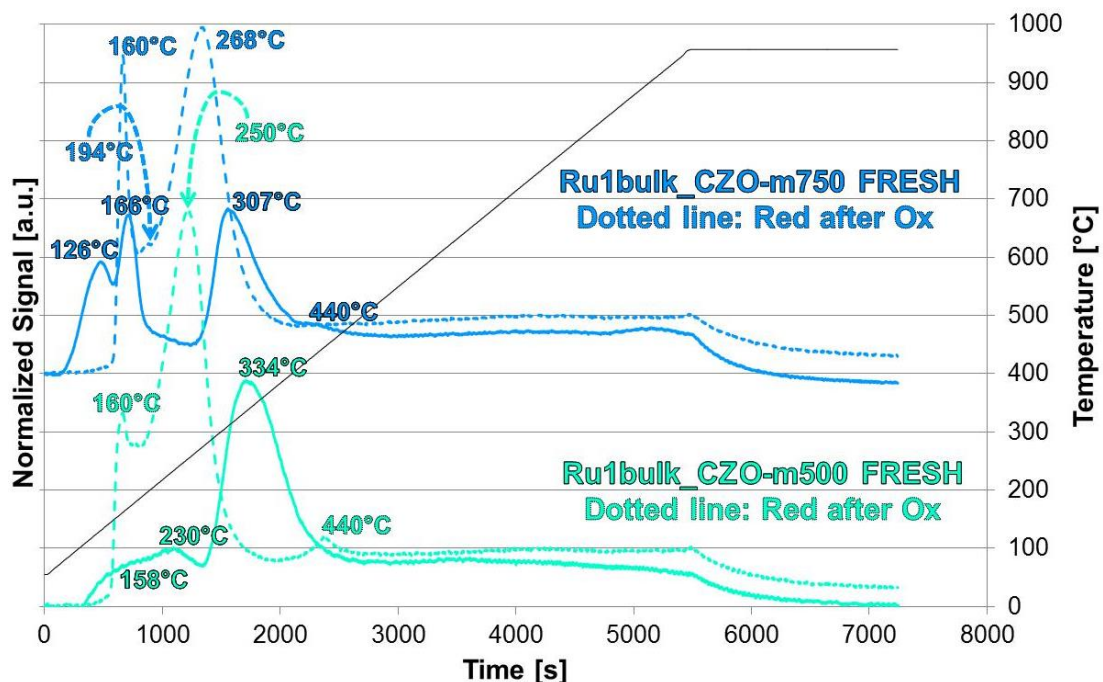


Fig. 3.60. Comparison between the H₂-TPR profiles of Ru1-bulk samples calcined at 750°C (Ru1bulk_CZO-m750) and 500°C (Ru1bulk_CZO-m500)

The catalytic activity of these samples are compared with the same systems calcined at 900°C and also with the equivalent impregnated catalysts, taken as reference; Rh1IWI_CZO-m900-R750 in the case of Rh and Ru1IWI_CZO-m900-R750 in the Ru case. A first comparison between these systems is carried out at the most discriminant conditions, maintaining a pressure of 1 atm, studying the effect of the GHSV.

Concerning the Rh-based samples (Fig. 3.61) following a calcination temperature decrease of 150°C, an increase of about 38% in the activity at 24000 h⁻¹ is observed, moving from a CH₄ conversion of about 34% in the case of Rh1bulk_CZO-m900-R750 (labeled bulk-m900 in Fig. 3.61) to a value of about 72% showed by Rh1bulk_CZO-m750-R750 (bulk-m750 in Fig. 3.61), which is fully comparable to those relative to the reference impregnated system (\approx 75%). A further decrease of the calcination temperature until 500°C lead to a drop in the CH₄ conversion to a value of about 65%, which is slightly lower than those relative to the bulk sample calcined at 750°C and to those concerning the impregnated system calcined at 900°C, but, in any way, it is significantly higher (\approx 31%) than the CH₄ conversion showed by the Rh1bulk_CZO-m900-R750 sample. At higher GHSV values (50000 h⁻¹ and 100000 h⁻¹) the activity improvement deriving from the decrease of the calcination temperature is more evident, in fact a transition from a not active Rh1bulk_CZO-m900-R750 system in these

conditions to one (Rh1bulk_CZO-m750-R750), even more active (CH_4 conversion $\approx 60\%$) than the reference Rh1IWI_CZO-m900-R750 catalyst (CH_4 conversion $\approx 52\%$), is observed. This different behaviors at high GHSV (hence low contact time) could depend probably on the metal support interaction effects that can affect the surface active area of the metal useful for the occurrence of the reaction. The variation of the GHSV value could have some important effect regarding the occurrence of the two different reactions that compose the oxy-reforming process. In fact, the CPO reaction is characterized by a slight exothermicity and very low contact time values (milliseconds), while the opposite conditions are peculiar of the SR process which require higher contact time values (seconds) and endothermicity. Maintaining the volume of the catalytic bed constant, the increase of the GHSV values are carried out by increasing the flow rates of the gaseous reagents, with the result that at higher GHSV the gaseous mixture linear velocity is higher, the heat produced and exchanged are higher and the reforming and oxidation reaction zone can overlap. Furthermore the differences in the oxidation and reforming reaction can generate difference in the reaction thermal profile, in the reaction rate and in the methane conversion. Many reason can be at the base of this differences such as the change in the thermal conductivity and heat capacity, differences in interpore and intrapore diffusion or differences in the reaction rate between exothermic and reforming reaction. Considering that the samples have the same nature, one difference can be attributed to kinetic factor due to the Rh particles. From TEM analysis carried out on these spent samples (Fig. 3.62) are visible some important differences regarding the way in which the Rh particles are dispersed on the support. In fact, in the impregnated sample the contact angle between a Rh particle and the support is lower than those observed in the case of a Rh particle characterizing the bulk system, which seems more flat and "spread" on the support surface. This different behavior is schematically represented in Fig. 3.63 where, on the right, is highlighted the different number and nature of the defects (steps and edges) that is possible to imagine that are characteristics of these two samples. It is possible to imagine to represent the circumference of a spherical particle composed by atomic steps that represent the coordinative insaturations of the metal surface. An higher number of coordinative insaturations imply a greater catalytic activity and this mean that the active sites characterizing the impregnated sample are more active than those of the bulk sample. this higher reactivity can increase the extent of the oxidation related with the contact of molecular oxygen present at higher GHSV, related to the oxy-reforming conditions. Generally at the very beginning of the catalytic bed occurs the CPO reaction and immediately after the steam reforming take place. The distinction between these two reactions can disappear in drastic conditions (high GHSV). From the analysis of the

thermal profile recorded during reaction, is possible to observe different behavior among the two catalysts (Fig. 3.64). In the figure are compared the thermal profiles recorded during the tests at 50000 h⁻¹ and 100000 h⁻¹ and 1 atm, carried out on both the impregnated and bulk samples. Considering the profiles recorded at 50000 h⁻¹ (continuous lines in Fig. 3.64) is clearly visible a slight temperature increase at the beginning of the bed (at about 70 mm) in the case of Rh1IWI_CZO-m900-R750 sample, attributable to the CPO occurrence, not detectable in the bulk case, which presents a unique endothermic peak deriving mainly from the SR occurrence, since the CPO take place slightly ahead on the catalytic bed where occurs concurrently with the SR reaction. In this way, the first part of the catalytic bed is utilize for the CPO reaction with the consequence that remain less volume of catalyst on which can occurs the SR reaction. Comparing the sub-stoichiometric amount of the oxygen involved in the oxy-reforming process (11% v/v) with the vapor content (≈ 37), is possible to assert that the CH₄ conversion deriving only from the CPO reaction is probably lower than those deriving from the SR. In this way, the remaining part of the Rh1IWI_CZO-m900-R750 catalytic bed where is possible the occurrence of the SR become shorter than in the case of the Rh1bulk_CZO-m750-R750 one, which is characterized by active sites with a lower defectivity. This less defectivity lead to the occurrence of the CPO reaction a little bit ahead on the catalytic bed where is already possible also the occurrence of the SR process. Therefore these two reactions take place simultaneously on the Rh1bulk_CZO-m750-R750 case, with the consequence of a slight higher CH₄ conversion deriving from a major volume of catalytic bed available for the SR reaction. At 100000 h⁻¹ (dotted profiles in Fig. 3.64) the slight differences deriving from the nature of the defects characterizing the surface of the active sites are not even visible because the flow rates are so much higher to not allow the simultaneous occurrence of CPO and SR, but, a clear distinction among them are clearly detectable in both of the thermal profiles. In fact, at 100000 h⁻¹ also the CH₄ conversion (Fig. 3.61) relative to these samples are very similar from each other, assuming a value around the 50%.

Also the bulk sample calcined at 500°C (Rh1bulk_CZO-m500-R750) shows a good performances in the oxy-reforming conditions, even if its activity remain lower than those exhibit by the bulk catalyst calcined at 750°C. In some way, this result confirm the data obtained with the TPR characterization (Fig. 3.59) where it was highlighted the lower metal dispersion homogeneity in the sample calcined at 500°C, which can induce the lower activity, especially at 24000 h⁻¹, where the latter shows a CH₄ experimental conversion ($\approx 65\%$) of about 7% lower than those observed for the Rh1IWI_CZO-m750-R750 sample ($\approx 72\%$). The problem which could exist in the case of the bulk sample

calcined at 500°C is relative to the fact that if it is reduced and tested at higher temperatures (750°C) the stability of the phase could be influenced and probably could change under reduction and/or reaction conditions. Therefore is probably better to reduce these kind of sample at lower temperature (500°C), testing them only in the low temperature steam reforming conditions.

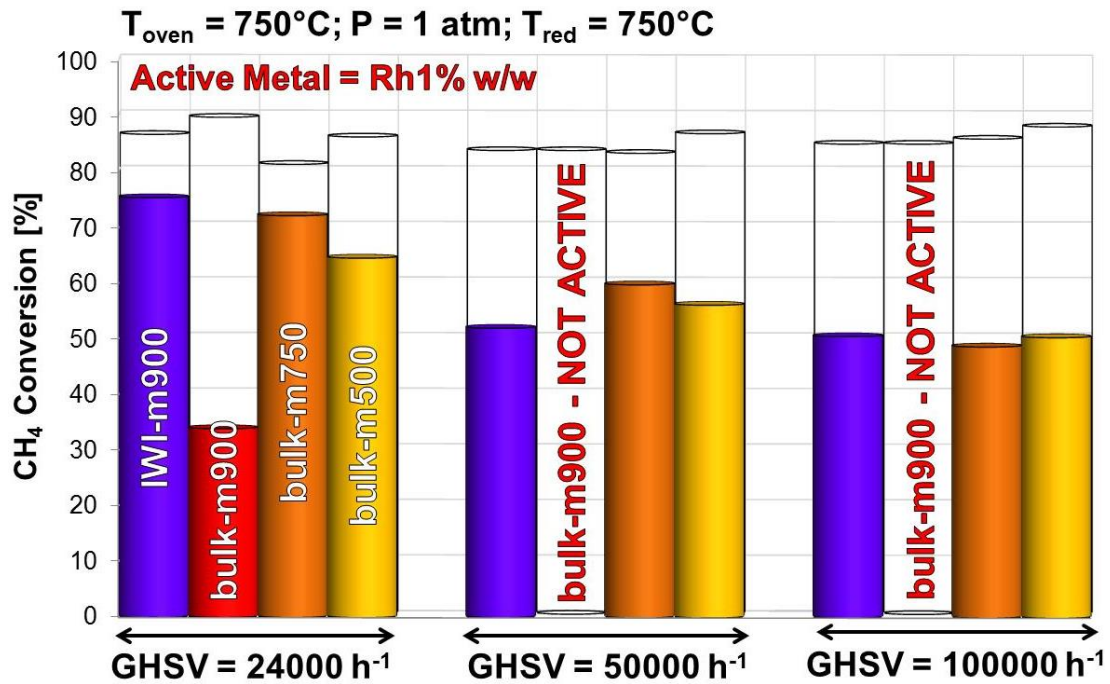


Fig. 3.61. Comparison between the catalytic activities of Rh-based bulk samples calcined at different temperatures in function of the GHSV. The activity relative to the Rh1IWI_CZO-m900-R750 (represented as IWI-m900 in the graph) is taken as reference. All the samples are reduced at a $T_{\text{red}} = 750^{\circ}\text{C}$

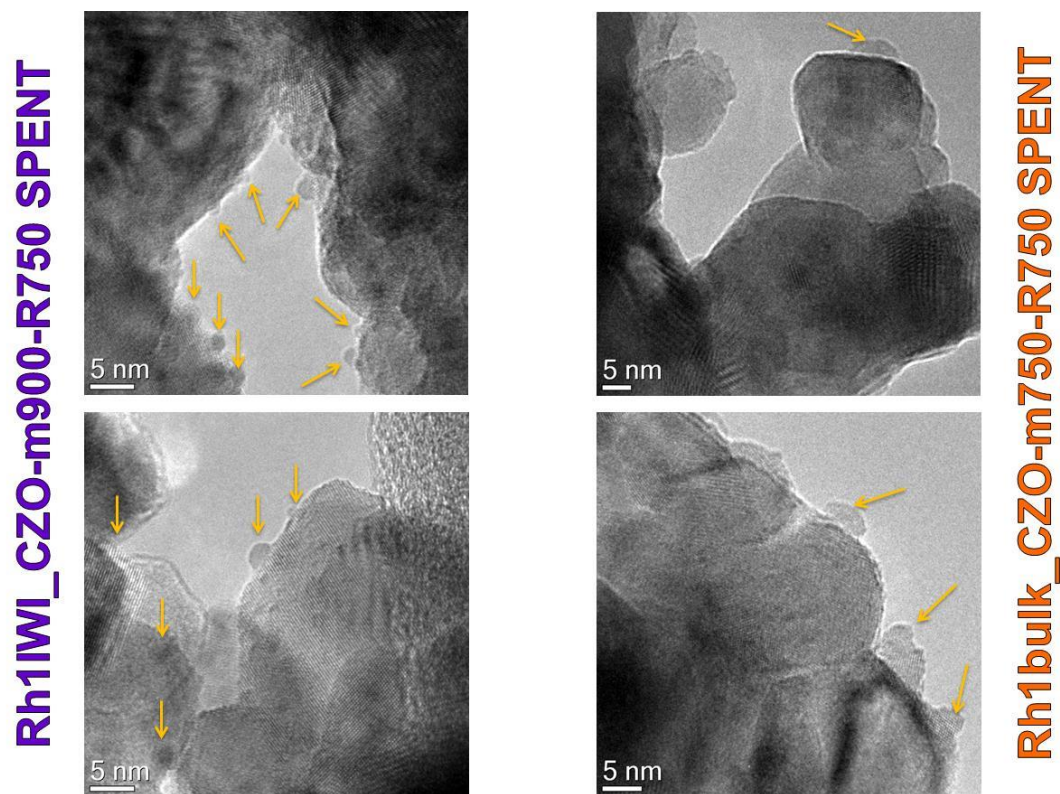


Fig. 3.62. TEM micrographs recorded on Rh1WI_CZO-m900-R750 (on the left) and Rh1bulk_CZO-m750-R750 (on the right) samples after catalytic tests

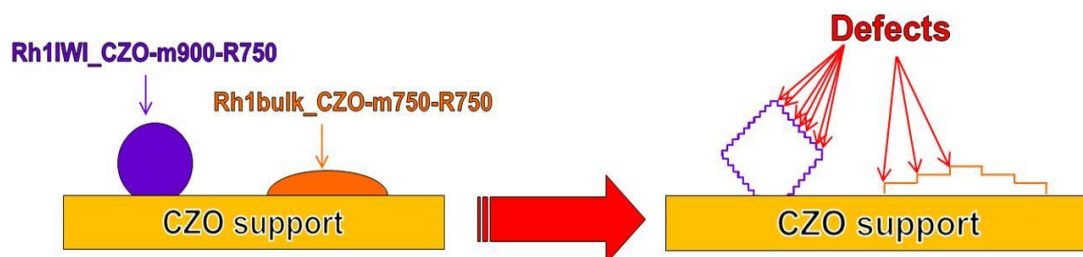


Fig. 3.63. Schematic representation of the different way in which a Rh particle is present on the Rh1WI_CZO-m900-R750 sample (violet particle) and Rh1bulk_CZO-m750-R750 one (orange particle)

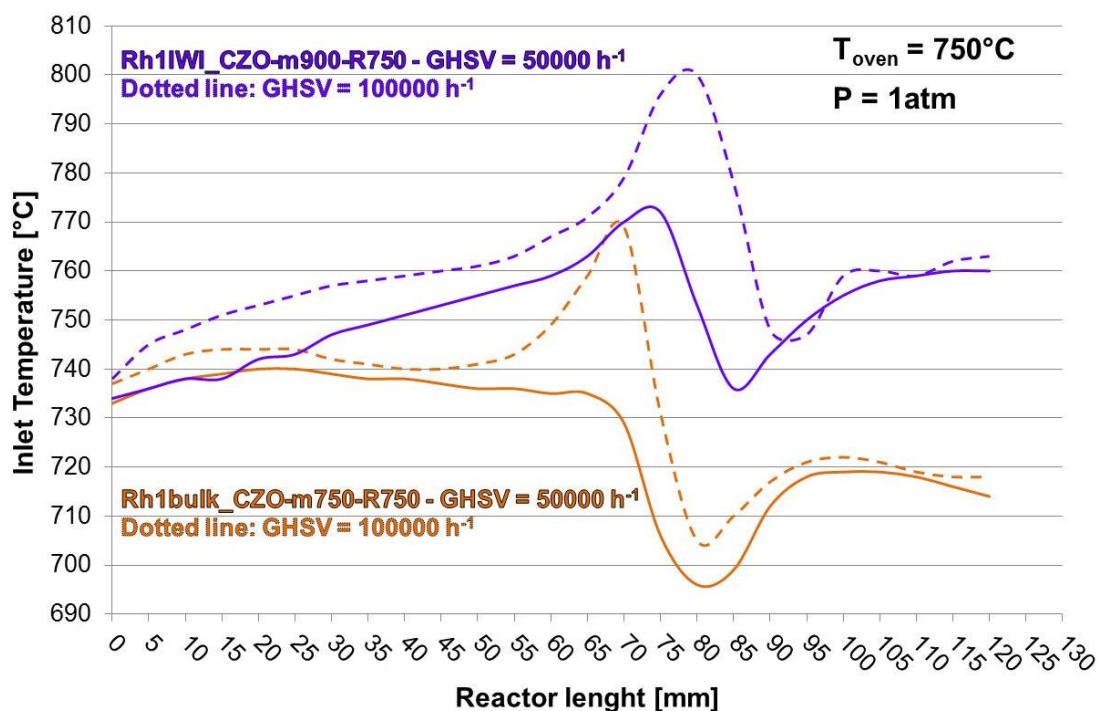


Fig. 3.64. Comparison among the thermal profiles recorded during the catalytic tests at 50000 h^{-1} and 100000 h^{-1} on the Rh1IWI_CZO-m900-R750 catalyst and the Rh1bulk_CZO-m750-R750 one

Considering the really interesting activity of Rh1bulk_CZO-m750-R750, it is tested also in have been tested in the oxy-reforming conditions at high pressure (Fig. 3.65) and in LT-SRM conditions. As shown in Fig. 3.65 it reveals a very good activity also at 10 and 20 atm, reaching the equilibrium CH_4 conversion in both the cases. At 24000 h^{-1} and even at 100000 h^{-1} the experimental conversions are really close to those calculated at the equilibrium. Thus, it is possible to affirm that the Rh1bulk_CZO-m750-R750 catalyst behave better than the Rh1IWI_CZO-m900-R750 in more drastic conditions (high P and GHSV) and probably this difference derives from the different nature of the active phase characterized by Rh sites highly interactive with the surface, which probably give rise even to higher stability which is maintained in severe reaction conditions. These described characteristics are further confirmed if some result of the tests carried out in the LT-SRM conditions is considered. The activity of the bulk catalyst, here not reported, shows low activity in these conditions. At the highest temperature ($T_{\text{oven}} = 500^\circ\text{C}$) it shows an outlet CH_4 concentration of about 54%, against one of about 28% relative to the same test carried out on the Rh1IWI_CZO-m900-R750 sample. Decreasing the oven temperature until 400°C the CH_4 outlet concentration value become even higher ($\approx 75\%$) and far from those calculated at the thermodynamic equilibrium ($\approx 50\%$) and those relative to the impregnated sample ($\approx 57\%$). At low temperature become even more important the nature of the sites characterizing the catalyst, in fact a less defective surface (Rh1bulk_CZO-m750-R750) require higher activation energy in order to convert

the methane with respect to one characterized by much more edges and steps like those typical of the active sites composing the Rh1IWI_CZO-m900-R750.

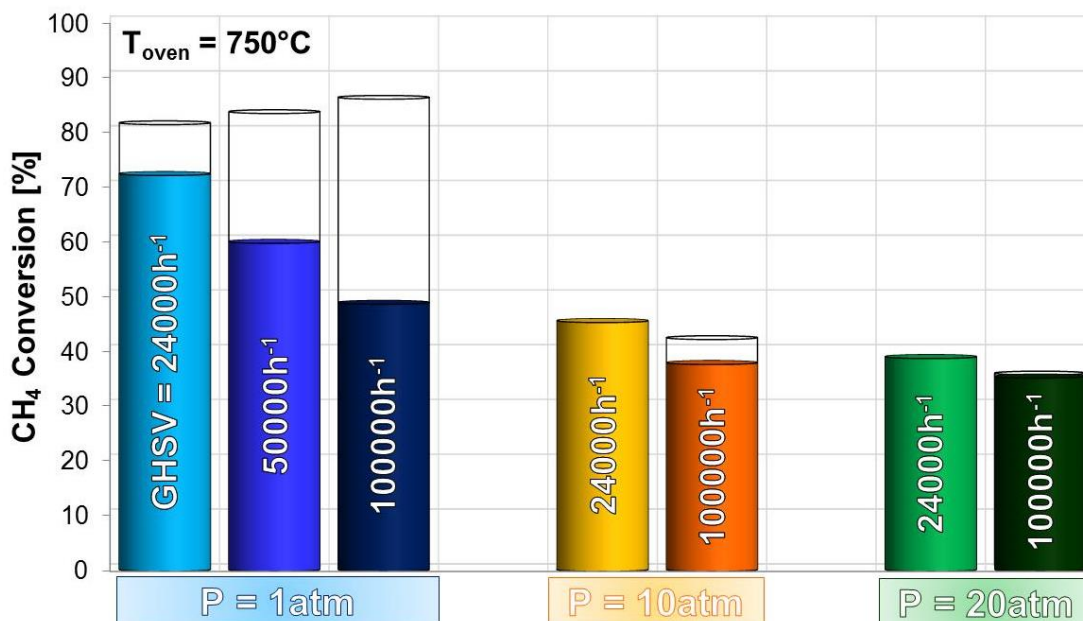


Fig. 3.65. Catalytic activity of Rh1bulk_CZO-m750-R750 in function of pressure and GHSV in the oxy-reforming conditions

The same study on the calcination temperature is carried out also on the Ru-based bulk samples, and the positive effect of a decrease in the thermal treatment is also observed in this case (Fig. 3.66). The Ru1bulk_CZO-m900-R750 catalyst give rise to a lower activity than the equivalent Rh-based catalyst, showing at 24000 h⁻¹ and 1 atm an experimental CH₄ conversion of about 14% with respect that of Rh bulk sample of about 34%. Decreasing the calcination temperature until 750°C the conversion, at 24000 h⁻¹ increase significantly reaching a value of about 61%, and decreasing of about 6% when the calcination is carried out at 500°C (≈ 55%). Similarly to the Rh sample, also in more drastic conditions (higher GHSV), the Ru1bulk_CZO-m750-R750 catalyst exhibits a good activity showing experimental conversion fully comparable to those relative to the impregnated sample calcined at 900°C (Ru1IWI_CZO-m900-R750).

The comparison of the Rh and Ru bulk catalysts calcined at 750°C show lower activity of Ru with respect to Rh, in all the reaction conditions tested. At low temperature, during SR tests, the Ru bulk systems show practically a null activity, probably related again to lower activity of the sites produced by the reduction of the bulk catalyst with respect to the impregnated samples, that show much more higher activity (Ru1IWI_CZO-m900-R750 was active in LT-SRM conditions – see Fig. 3.52) than those characteristics of the bulk ones.

In both the bulk samples the calcination temperature plays a fundamental role. Decreasing the calcination temperature (from 900°C to 750°C) the activity of the Rh- and Ru-based bulk samples considerably improve. This is probably due to a more defective structure of the support which allows an higher mobility and a higher degree of reducibility of the metal from the lattice of the $Ce_{0.5}Zr_{0.5}O_2$ matrix, producing metal sites flatter than the one obtained with the impregnation procedure. The overall results of these two parameters allow to reach very interesting activity at high temperature and especially in more severe reaction conditions, and a low deactivation degree (deriving mainly from the wider MSI). In fact, as reported in Fig. 3.67 a and b, both the bulk samples calcined at 750°C exhibit a good stability in the reaction environment, showing a decrease in the CH_4 conversion of about 7% after around 20 hours of reaction in the case of Rh (Fig. 3.67 a) and of 5% after about 14 hours in the Ru case. Especially this latter result is very interesting, considering the high sensibility of Ru towards deactivation phenomena mainly related to thermal sintering.

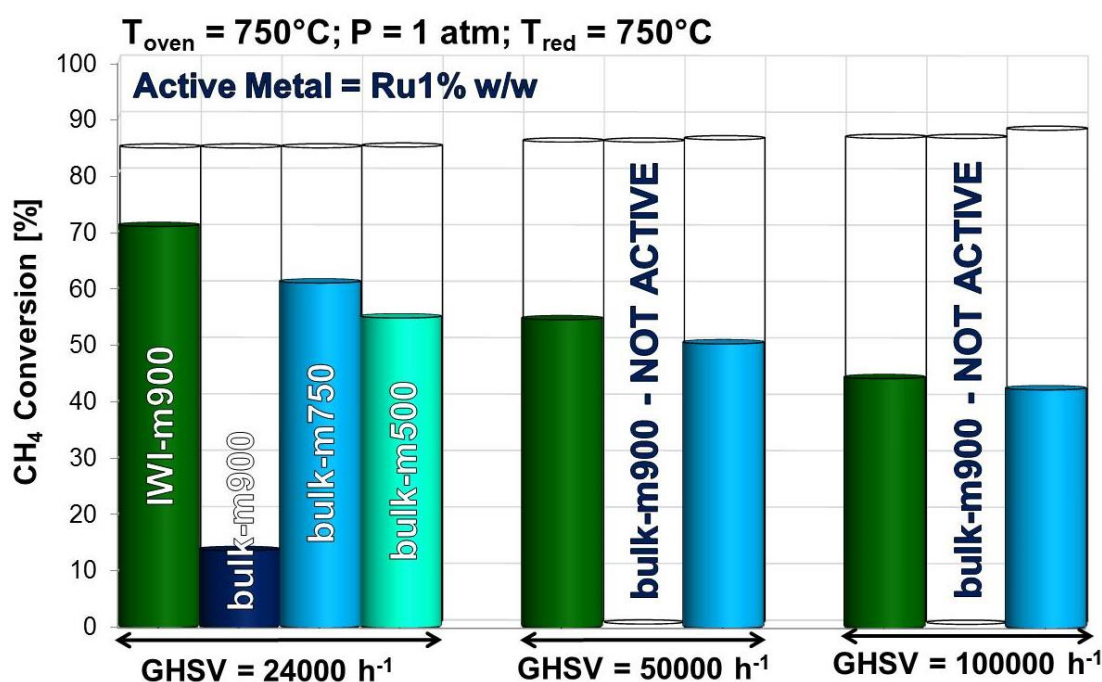


Fig. 3.66. Comparison between the catalytic activities of Ru-based bulk samples calcined at different temperatures in function of the GHSV. The activity relative to the Ru1IWI_CZO-m900-R750 (represented as IWI-m900 in the graph) is taken as reference. All the samples are reduced at a $T_{red} = 750^\circ C$

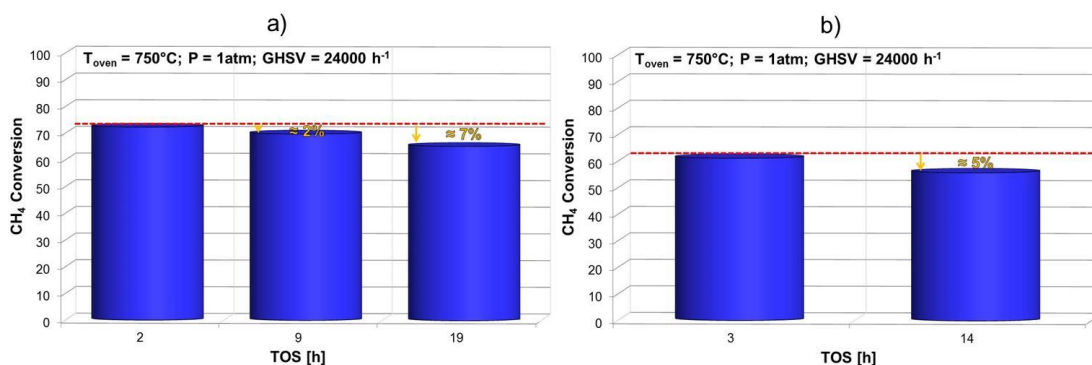


Fig. 3.67. Deactivation degree of the catalyst: a) Rh1bulk_CZO-750-R750; b) Ru1bulk_CZO-m750-R750 in function of the time on stream

3.4.6.2 Impregnated (IWI) samples

The significant improvement observed in the case of the bulk samples deriving from the decrease of the calcination temperature, suggest to investigate its effect also regarding the impregnated systems by calcining the CZO-m support at 750°C and 500°C. In the whole series of samples, the thermal treatment after the impregnation step is maintained constant (from $T = 120^{\circ}\text{C}$ to $T = 500^{\circ}\text{C}$ with a ramp of $2^{\circ}\text{C}/\text{min}$ and an isothermal step at 500°C , 5 hours long). The results can be affected by the differences of the support porosity and defectivity, which can change the impregnation and dispersion of the metal.

The H₂-TPR profiles of Rh1IWI_CZO-m750 and Rh1IWI_CZO-m500 are respectively showed in Fig. 3.68 a and b. Comparing these profiles with those relative to the Rh1IWI_CZO-m900 sample (Fig. 3.26) can be noticed that there aren't differences so significant like those existing between the bulk catalysts. This mean that the calcination temperature have an higher effect on the metal dispersion rather than on the structural properties of the CZO system, even if these latter are also significantly influenced, and could play an important role on the activity of the overall system. Anyway, one difference is evident, mainly in the Rh1IWI_CZO-m750 sample. The peak at about 180°C is higher with respect to the sample calcined at 900°C while the peak at temperature above 220°C is less intense. This can be due to a difference between the Rh which have reacted with the surface layer of a defective support during oxidation at 950°C and which, nevertheless, remains more reducibile than the analogous sample calcined at 900°C . This effect could derive from a defectivity and an higher oxygen mobility characterizing the $\text{Ce}_{0.5}\text{Zr}_{0.5}\text{O}_2$ phase, peculiar of the CZO-m supports, as also reported in literature [197,198]. Furthermore the increase of hydrogen uptake between the first and second cycle of the sample calcined at 750°C can be ascribed to the phenomenon described by Fornasiero et al. [197] which have observed the reduction peaks of $\text{Ce}_{0.5}\text{Zr}_{0.5}\text{O}_2$ at lower

temperature in the reduction/oxidation cycle, and the amount of H₂ consumption increased after the reduction/oxidation cycle.

As discussed for the bulk samples, the calcination temperature affects the metal distribution on the support also in the IWI samples. In other words, increasing the calcination temperature the Rh dispersion become even more homogeneous. In fact, the Rh1IWI_CZO-m500 sample reduction profiles (Fig. 3.68 b) are characterized by more than one peak (127°C, 250°C and 600°C) and this is probably due to the fact that at 500°C the support is not yet fully stabilized and homogeneous and its affect the homegneity of the impregnation.

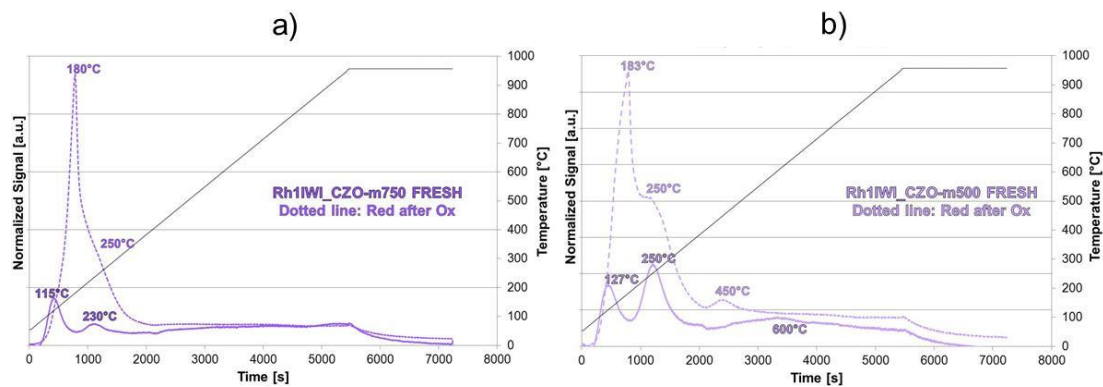


Fig. 3.68. Comparison between the H₂-TPR profiles of Rh1IWI samples calcined at: a) 750°C (Rh1IWI_CZO-m750) and b) 500°C (Rh1IWI_CZO-m500)

Regarding the catalytic activity, in order to avoid some deactivation effects that can occurs during the tests carried out in the oxy-reforming conditions at high temperature ($T_{\text{oven}} = 750^{\circ}\text{C}$), it was decided to change the order of the catalytic tests, carrying out those at LT-SRM conditions before of those at high temperature. The performances in these latter conditions of the Rh1IWI_CZO-m750-R750 sample are reported in Fig. 3.69. The trends of the concentrations of the gases composing the outlet mixture are slightly better than those obtained in the case of Rh1IWI_CZO-m900-R750 (Fig. 3.45), which is, up to now, the best catalyst in these conditions. Nevertheless it has to be noted that a comparison between the T_{avg} values recorded in the Rh1IWI_CZO-m900-R750 case and those relative to the Rh1IWI_CZO-m750-R750, is possible to notice that in the latter case these values are higher, especially considering the tests carried out at very low temperature ($T_{\text{oven}} = 350^{\circ}\text{C}$ and 400°C), where the difference is of about 11°C and 9°C , respectively. This difference is not negligible at this temperature and can be responsible of increasing the methane conversion. At very low temperature, difference become less evident by increasing the oven temperature at 450°C ($\approx 6^{\circ}\text{C}$) and 500°C ($\approx 3^{\circ}\text{C}$). However, is possible to affirm the really good activity also of the Rh1IWI_CZO-m750-R750 catalyst, which shows experimental CH₄ outlet concentration not far from those

calculated at the equilibrium. The differences are about 13% in the data collected at $T_{\text{oven}} = 350^{\circ}\text{C}$, which are reduce at a value around of 11% at 400°C , and 7% at 450°C , reaching a value of about 4% at the highest temperature (500°C). Also the H_2 outlet percentage is very higher, considering the relative low temperature, especially in the tests at 450°C and 500°C , which show respectively, a value of about 46% and 57%. In the same conditions, thanks to the activity of the water-gas-shift reaction, the CO is below 1%.

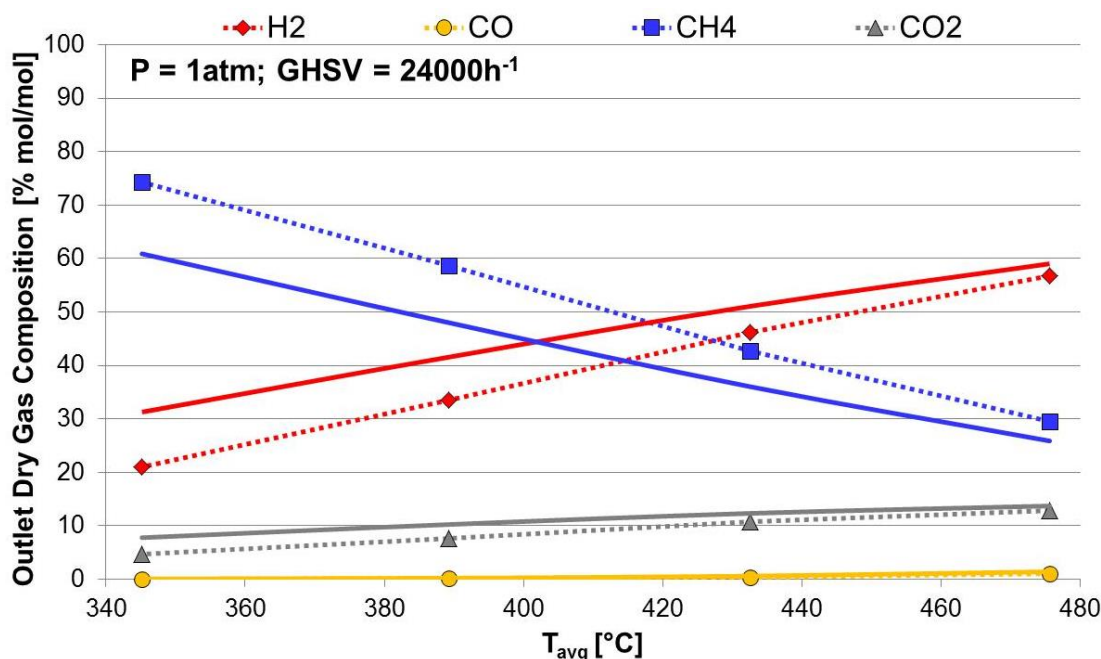


Fig. 3.69. Activity of the Rh1IWI_CZO-m750-R750 sample in function of the catalytic bed average temperature (T_{avg}) in the LT-SRM operative conditions

From these first data, seems that the temperature at which the CZO-m is subjected in the calcination procedure, doesn't influence significantly the activity, at least that at low temperature. At higher temperature, under oxy-reforming conditions instead, the effect of the calcination temperature appears more significant. Comparing the CH_4 conversions exhibit by the Rh1IWI_CZO-m900-R750 (Fig. 3.40) with that of the Rh1IWI_CZO-m750-R750 catalyst (Fig. 3.70), is clear how the performances of the latter are better in all of the conditions tested. At 24000 h^{-1} and 1 atm it shows an experimental CH_4 conversion ($\approx 80\%$) really close to the equilibrium one ($\approx 84\%$); the high activity is also confirmed at 50000 h^{-1} ($\approx 64\%$) and 100000 h^{-1} ($\approx 50\%$) and the conversions are higher than in the case of the impregnated sample calcined at 900°C which showed conversion values respectively around 52% and 45%. Increasing the pressure (10 and 20 atm) the trend is confirmed, and the sample calcined at 750°C reach the equilibrium practically at all of the GHSV tested, indicating a really high activity also in more drastic conditions. This significant improvement at high temperature deriving from a lower calcination

temperature could probably depend on a higher surface area of the support ($\approx 35 \text{ m}^2/\text{g}$ against $\approx 11 \text{ m}^2/\text{g}$ – see Table 3.8) which can improve the Rh dispersion during impregnation and the defectivity. As shown by TPR characterization (Fig. 3.68 a) the Rh is homogeneously dispersed on the CZO-m750 support surface.

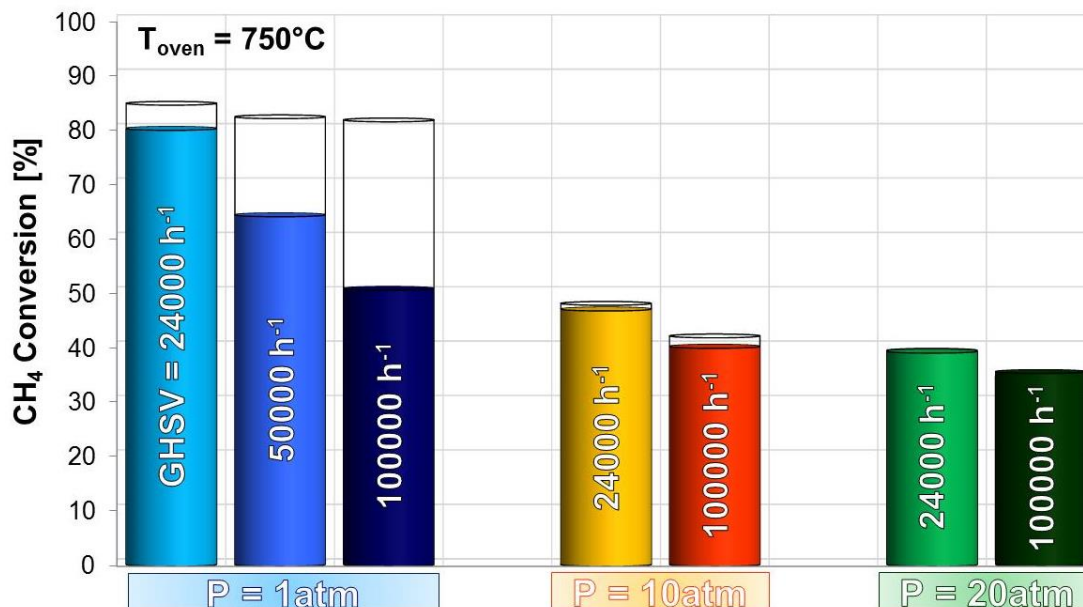


Fig. 3.70. Activity of Rh1IWI_CZO-m750-R750 sample in the oxy-reforming conditions in function of P and GHSV

The Rh1IWI_CZO-m750-R750 is better than its equivalent sample calcined at 900°C also regarding the deactivation degree, as shown in Fig. 3.71. From a direct comparison with the deactivation degree relative to the Rh1IWI_CZO-m900-R750 catalyst (Fig. 3.42), the Rh1IWI_CZO-m750-R750 sample results more stable at high temperature, showing a decrease of CH₄ conversion lower than 1% after 13 hours of reaction (against $\approx 4\%$ after 15 hours showed by Rh1IWI_CZO-m900-R750) and a further decrease of only about 3% after 22 hours of reaction is observed (against 7% after 34 hours showed by Rh1IWI_CZO-m900-R750). Therefore the improvement deriving from the decrease of the calcination temperature of the support is clearly evident also concerning the stability, reaching with the Rh1IWI_CZO-m750-R750 system the best compromise, up to now, in terms of activity at low and high temperatures, and stability towards deactivation.

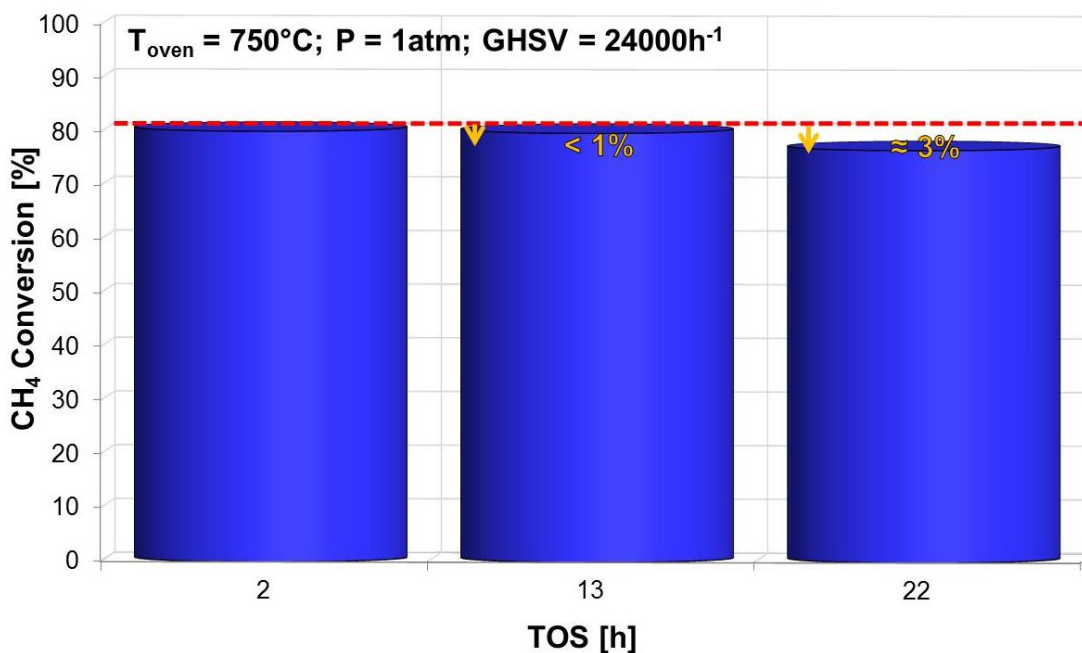


Fig. 3.71. Deactivation degree of the Rh1IWI_CZO-m750-R750 sample at high temperature in function of time on stream

On the same support (CZO-m750) Ru (1% w/w) was also impregnated and its H₂-TPR profiles are reported in Fig. 3.72. Focusing on the first reduction profile and comparing it with those relative to the Ru1IWI_CZO-m900 sample (Fig. 3.28) is possible to assert that these profiles are similar. Both of them are characterized by a first intense peak at about 150 – 160°C attributable to the reduction of surface Ru oxide species, and another at about 175 – 185°C ascribable to the reduction of some RuO₂ particles interacting stronger with the support. The main difference between the two profiles lay in this second peak, which, in the case of Ru1IWI_CZO-m750 is more intense and centered at a slightly higher temperature (188°C) than those characterizing the sample composed by the CZO-m900 support (175°C). Probably during the thermal treatment at 500°C carried out after the metal impregnation, the higher defectivity characterizing the support calcined at lower temperature (CZO-m750) allows an higher mobility of the RuO₂ particles leading to a stronger interaction between them and the support. After the oxidation cycle until 950°C, the reduction profile change significantly showing several peaks in a wide range of temperature (170 – 300°C). The peaks at about 170 – 200°C become very less intense than in the first profile and other two peaks at 240°C and 300°C are detected. This mean that during the oxidation cycle Ru interacts strongly with the support, reducing themselves at higher temperatures. The number of peaks detected, however, indicates that the Ru dispersion on the CZO-m750 support is not good like those characterizing the equivalent Rh-based catalyst (Rh1IWI_CZO-m750 –

Fig. 3.68 a) and it is even worse than those characterizing the Ru1IWI_CZO-m900 sample (Fig. 3.28).

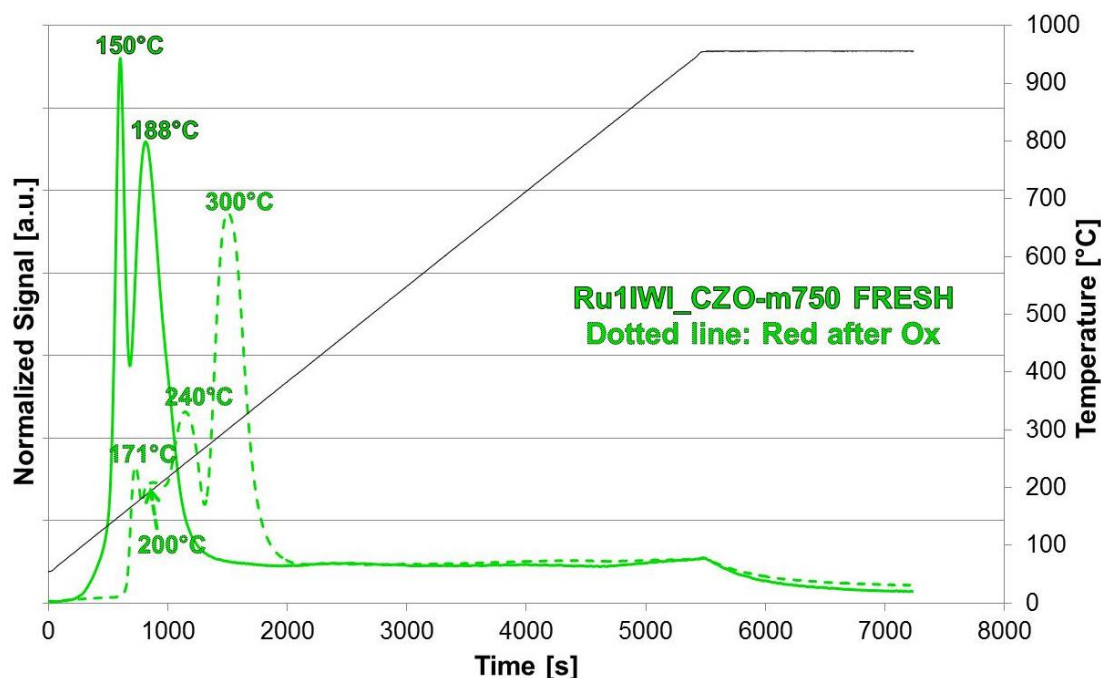


Fig. 3.72. H₂-TPR profiles recorded during a TPR/O/R cycle on the Ru1IWI_CZO-m750 sample

From the first test at $T_{\text{oven}} = 500^{\circ}\text{C}$ under LT-SRM conditions, a very low activity of this system can be observed. In fact, Ru1IWI_CZO-m750-R750 shows a CH₄ conversion in this condition of about 19% against a value of about 31% recorded in the case of Ru1IWI_CZO-m900-R750 (Fig. 3.52). For this reason, it was decided not to carry out further LT-SRM tests in order to avoid the occurrence of deactivation phenomena related to metal oxidation phenomena of Ru, favoured in these conditions. The activity of Ru1IWI_CZO-m750-R750 at high temperature is reported in Fig. 3.73. Also in the oxy-reforming conditions, its activity is lower than those exhibit by the equivalent sample calcined at 900°C (Fig. 3.50), showing CH₄ conversions of about 5% – 6% lower in all of the conditions tested. Even at 10 atm and 24000 h^{-1} the Ru1IWI_CZO-m750-R750 catalyst does not reach the equilibrium, and the effect of the GHSV is significant also at high pressures. Thus, in the case of Ru a decrease in the calcination temperature of the support acts negatively in terms of catalytic activity. Probably this is due to the higher mobility of the Ru on the defective mixed oxide matrix obtained by low temperature thermal treatment which can increase the Ru sintering. This hypothesis is confirmed if the Ru1IWI_CZO-m750-R750 behavior towards deactivation is considered. As shown in Fig. 3.74 this sample is more sensitive towards deactivation than the Ru1IWI_CZO-m900-R750 (Fig. 3.51), showing a decrease of the CH₄ conversion of about 10% already

after 13 hours of reaction (against 3% after 14 hours of the Ru1WI_CZO-m900-R750), which increase to a value close to 14% after 22 hours of reaction.

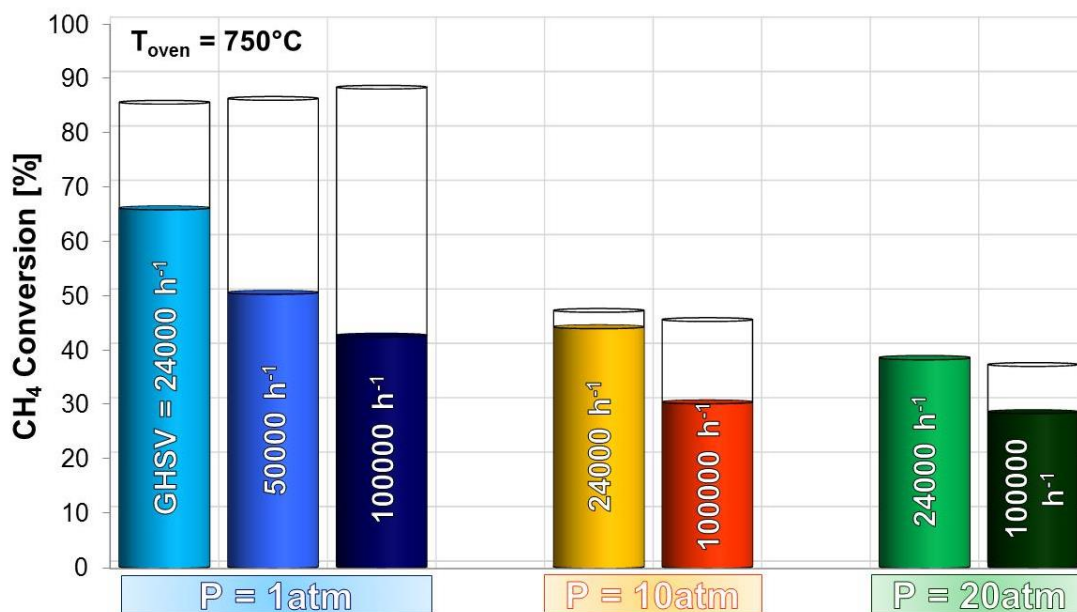


Fig. 3.73. Catalytic activity of Ru1WI_CZO-m750-R750 sample in function of pressure and GHSV

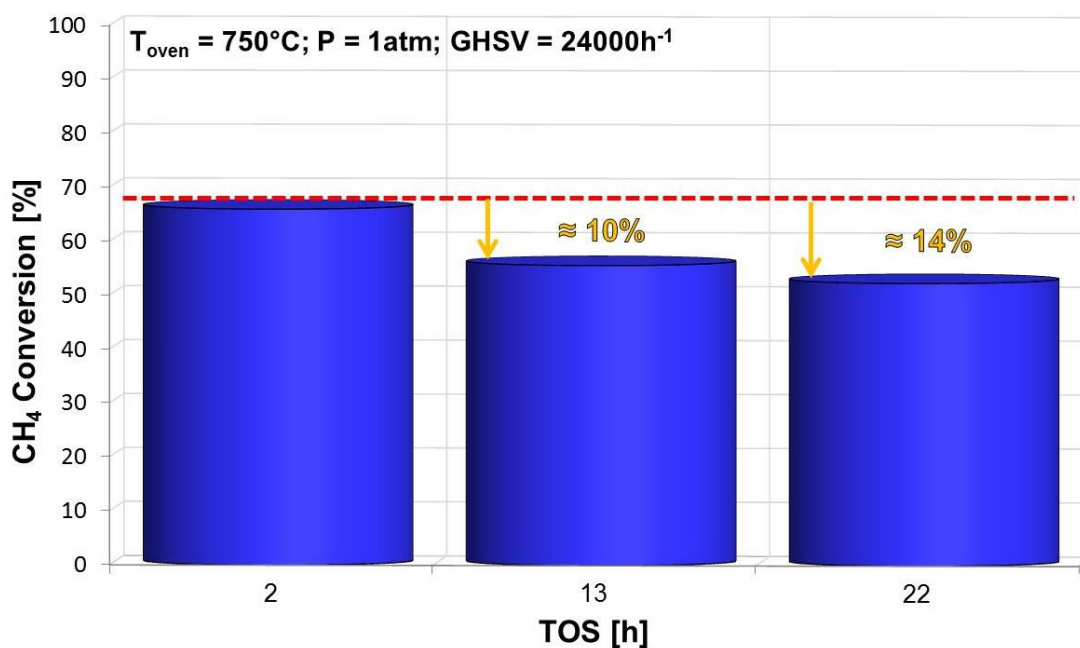


Fig. 3.74. Deactivation degree of Ru1WI_CZO-m750-R750 sample in function of the time on stream

3.4.7 Effect of the reduction temperature

A further feature that could play an important role in terms of the metal support interaction and size of the metal particles on the support is the temperature at which the reduction step is carried out. This investigation is performed only on the most promising catalytic system obtained up to now especially at high temperature, i.e. the Rh1IWI_CZO-m750 one.

The “standard” temperature involved during the activation/reduction process of the catalysts has been set at 750°C, i.e. equal to the maximum temperature reached during the catalytic tests, in order to avoid some structural transformations that could occur during reaction. But, lower reduction temperatures, for instance 500°C, could probably affect the dispersion and the activity of a catalyst. At the same time it is important that this temperature is high enough in order to reach a system in which the metal particles are well-stabilized on the support in order to avoid sintering during the operative reaction conditions.

The Rh1IWI_CZO-m750 catalyst is reduced at 500°C (Rh1IWI_CZO-m750-R500) and its activity, both at low and high temperature, is compared to those exhibited by the equivalent catalytic system reduced at 750°C (Rh1IWI_CZO-m750-R750). First of all the performances at low temperature (LT-SRM) are investigated and the results are reported in Fig. 3.75 a (Rh1IWI_CZO-m750-R750) and b (Rh1IWI_CZO-m750-R500). The trend of the experimental CH₄ outlet percentages exhibited by the catalyst reduced at 500°C (Fig. 3.75 b) is closer to those calculated at the thermodynamic equilibrium with respect to the case of the system reduced at higher temperature (Fig. 3.75 a), indicating that a milder reduction process leads to a more active catalytic system, at least at low temperature. The Rh1IWI_CZO-m750-R500 shows, already at about 350°C, a CH₄ outlet amount lower than 70% (≈ 66%), a value not even reached in the case of Rh1IWI_CZO-m900-R750 (≈ 73% - Fig. 3.45), considered up to now the most active system in this LT-SRM conditions. Also at about 400°C the sample reduced at 500°C shows the lowest CH₄ outlet percentage (≈ 52%) against a value of about 58% relative to the catalyst reduced at 750°C and at around 440°C the equilibrium is reached by the former system, which maintains the same trend also at the highest temperature of about 490°C. Probably a lower reduction temperature leads to the formation of a system characterized by smaller metal particles with a narrow size distribution than those that are subjected to a more severe activation process at 750°C.

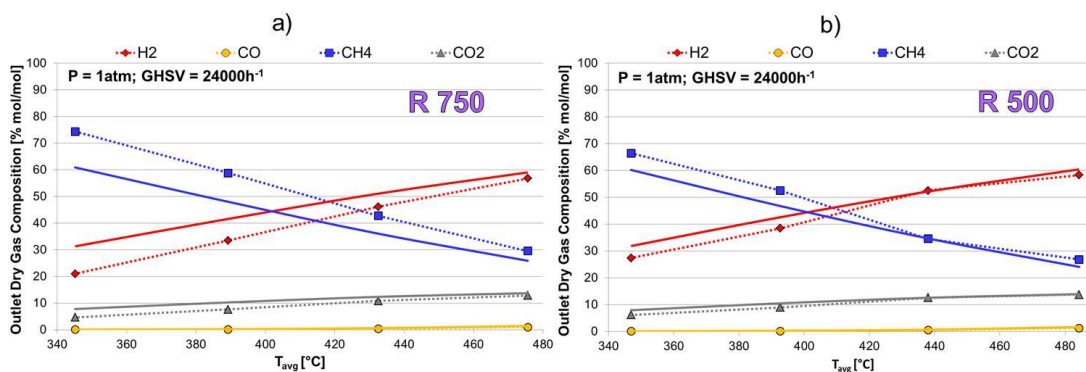


Fig. 3.75. Catalytic activity at LT-SRM conditions of the Rh1IWI_CZO-m750 samples reduced at: a) 750°C and b) 500°C

These catalysts are also tested at high temperature carrying out the oxy-reforming tests, in order to find out whether the improvement deriving from the different reduction conditions observed at low temperature occur even at high temperature and what is the effect on the catalyst deactivation. As shown in Fig. 3.76 the performances exhibit by the sample reduced at 500°C (Fig. 3.76 b), in these conditions, are slightly worse than those relative to the catalyst reduced at 750°C (Fig. 3.76 a), which, is the most active system at high temperature. The difference is however small, and can be observed only in the most discriminating conditions, i.e. at 1 atm, while at high pressures the behavior of the two catalysts is practically the same. Focusing on the tests carried out at 1 atm the Rh1IWI_CZO-m750-R500, the two samples are very similar also in terms of deactivation. More in details, the sample reduced at lower temperature (Fig. 3.77) shows a stability slightly lower than those relative to the Rh1IWI_CZO-m750-R750 (Fig. 3.71), with a decrease in the CH₄ conversion of about 5% after 20 hours of reaction, against a value of 3% after 22 hours displayed by Rh1IWI_CZO-m750-R750.

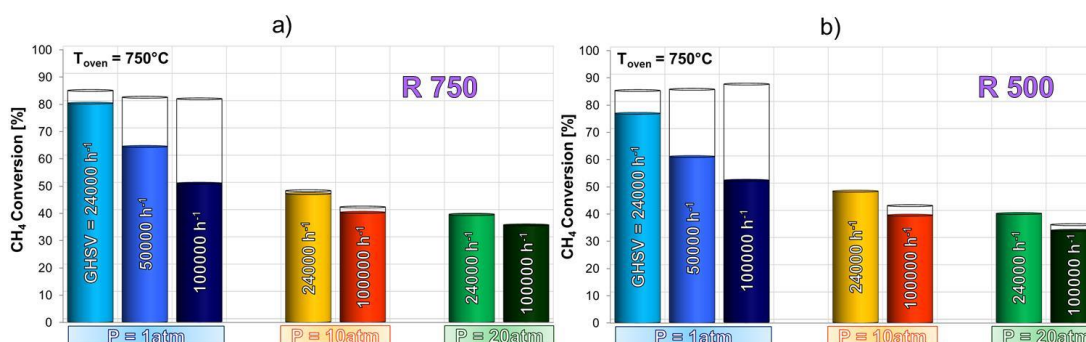


Fig. 3.76. Catalytic activity at oxy-reforming conditions of the Rh1IWI_CZO-m750 samples reduced at: a) 750°C; b) 500°C

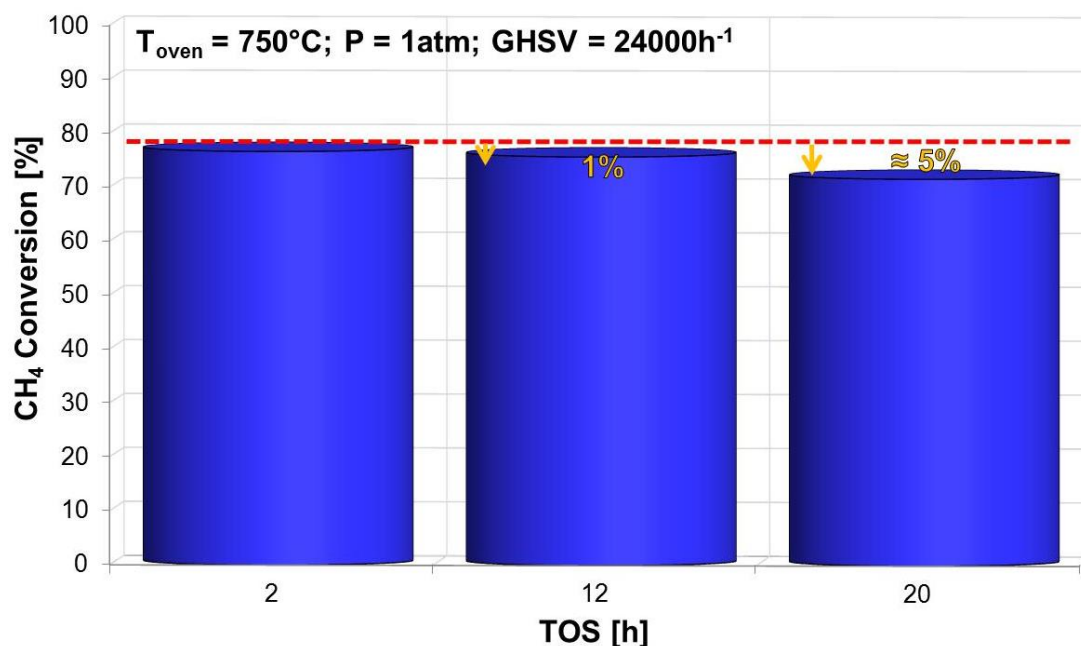


Fig. 3.77. Deactivation degree of the sample Rh1IWI_CZO-m750-R500 in function of time on stream

The two samples are therefore very similar in the whole series of tests. Nevertheless can be stated that at high reaction temperature, the system reduced at 750°C is slightly better, on the contrary at low temperature, the differences are more evident, indicating a slightly higher activity of the catalytic sites reduced at 500°C.

In the light of these results, is possible to affirm that the calcination temperature parameter has surely a more significant effect on the dispersion of the active metal on the support surface and hence on the catalytic than those depending on the reduction temperature. The most promising catalytic system seems to be the Rh1IWI_CZO-m750-R750 one, which satisfy the best compromise between a good catalytic activity at both high (oxy-reforming conditions – Fig. 3.70) and low temperatures (LT-SRM conditions – Fig. 3.69) and a really good stability (Fig. 3.71) showing a deactivation degree very low ($\approx 3\%$) even after more than 20 hours of time on stream.

3.4.8 Preliminary tests with membrane reactor (MBr)

The best catalytic system (Rh1IWI_CZO-m750-R750) was tested also with the integration of a membrane reactor (MBr). As shown in Fig. 2.7 the membrane separation module is placed downstream of the reactor and the outlet gas mixture produced during reaction inside the catalytic reactor, is feeded to the MBr. The procedure can be repeated after separation giving rise to a multistep H₂ production configuration like those schematically showed in Fig. 3.37. This part of the work is now developing in collaboration with the University of Messina, having high experience in the preparation of the membranes to be tested in the oxy-reforming and even in the LT-SRM processes.

The membrane is placed into a steel reactor like those represented in Fig. 2.6, which works following the scheme showed in Fig. 3.78. The outlet gaseous mixture of non – converted CH₄ and H₂O, CO, CO₂ and mainly H₂ get into the MBr maintained at 400°C, where occurs the H₂ separation through the dense Pd film deposited on the internal wall of the Al₂O₃ support, following the mechanism mentioned in paragraph 1.1.6. In this way two different stream are created; the retentate stream, which is composed mainly by the gases that are not able to pass through the Pd membrane (H₂O, CH₄, CO and CO₂), getting out from the opposite side of the reactor, and the permeate stream, which is composed mainly of H₂ which is able to pass through the membrane, separated from the other gases. The driving force which allows the separation of H₂ from the retentate side to the permeate one is the different partial pressure of the two sides of the membrane. This ΔP is created maintaining the retentate side at a slightly higher pressure (3 atm) than what characterizing the permeate one, being at atmospheric pressure. For this reason the tests with the integration of MBr, are carried out at a minimum pressure of 3 atm.

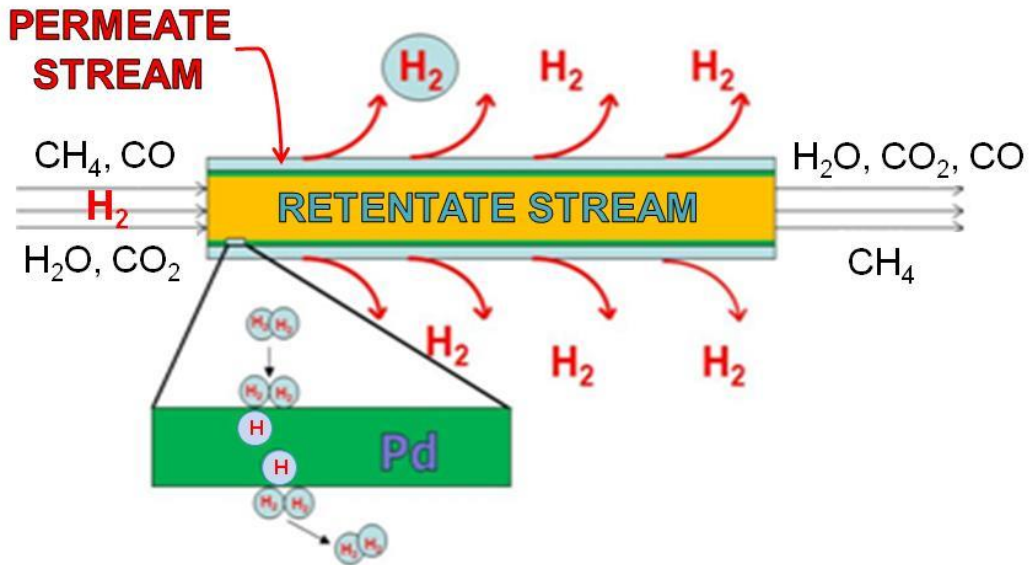


Fig. 3.78. Schematic representation of H₂ separation mechanism inside the Pd-based dense membrane

One of the problems related to these kind of system is the adhesion of Pd film on the internal wall of the ceramic support, which should be optimal and free from defects in order to perform the best H₂ permeation. This problems derive from the very different nature of the materials composing the membrane film (Pd) and the ceramic support (Al₂O₃), mainly in terms of physico – chemical properties. Especially during the heating up of the membrane module, is very important to increase the temperature following a very slow rate (1°C/min) in order to avoid the formation of defects that could originate at the Pd/Al₂O₃ interface because of the different coefficient of thermal expansion characterizing these two materials. Al₂O₃ has a coefficient of thermal expansion ($8.4 \cdot 10^{-6}/^{\circ}\text{C}$) lower than those characterizing Pd ($11.8 \cdot 10^{-6}/^{\circ}\text{C}$). Thus, it is necessary to control the possible formation of defects in the Pd film after the heating of the membrane until 400°C. This check is made carrying out the so called H₂ permeability test, through which is possible to determine the permeance of the membrane, which is a fundamental parameter in order to determine the good or bad membrane operation; higher is the permeance, better is its performances mainly in terms of selectivity of separation and permeate flow rate. Therefore, the H₂ permeability tests are carried out before starting the reaction and after each catalytic test, in order to understand if the reaction conditions (GHSV, composition of the outlet gaseous mixture) tarnish the membrane or not.

The membrane physical characteristics are listed in Table 3.9.

M154 Physical Properties		
Length	[cm]	13
External diameter	[cm]	1
Internal diameter	[cm]	0.7
Amount of Pd deposited	[mg]	132
Surface Area of Pd layer	[cm ²]	21
Thickness of Pd layer (δ)	[μ m]	5
Dependence factor of the H ₂ flux on the H ₂ partial pressure (n)	-	0,5

Table 3.9. Physical properties of the membrane

After reaching 400°C flowing N₂ (\approx 500 mL/min) inside the membrane, the permeate flow is checked in order to make sure that N₂ doesn't pass through the Pd membrane indicating that there aren't present defects in the Pd film through which could pass other gases in addition to H₂. This N₂ permeability is performed monitoring the permeate flow increasing the pressure in the retentate side following steps of 0,5 atm each, starting from 1 atm reaching 3.5 atm. At any pressure the N₂ flow rate in the permeate side was lower than 1 mL/min, indicating the good conditions of the membrane. After this, the same procedure is followed in order to carry out the H₂ permeability test, feeding to the MBr an H₂ flow rate of 2250 mL/min, measuring at each pressure the permeate flow rate and the retentate one. The data obtained are reported in Table 3.10. Considering the equation (4) reported in paragraph 1.1.6is possible to calculate the permeance of the membrane assuming that when the pressures involved are relatively low, $n = 0.5$ and equation (4) becomes the Sieverts – Fick law (33):

$$J_{H_2, Sieverts} = \frac{Pe_{H_2} \cdot (p_{H_2, ret}^{0.5} - p_{H_2, perm}^{0.5})}{\delta} \quad (33)$$

where $J_{H_2, Sieverts}$ can be named permeance and corresponds to the slope of the interpolation line of the data arising from the relation between the H₂ permeation flux (J), normalized in function of the surface area of the membrane, and the difference among the H₂ partial pressures at the retentate and permeate sides ($p_{H_2, ret}^{0.5} - p_{H_2, perm}^{0.5}$). If the H₂ separation through the membrane occurs following the Sieverts – Fick law, the dependence between these two parameters will be linear, as shown in Fig. 3.79 where are reported the permeability data relative to the membrane. The permeance of this membrane is very high, showing a value of about 126 mL·cm⁻²·min⁻¹·atm^{-0.5}.

Pressure [atm]	Permeate flow [mL/min]	Retentate flow [mL/min]
1.5	606	1656
2	1102	1162
2.5	1538	701
3	1929	263

Table 3.10. Permeate and retentate flow rates obtained during the first H₂ permeability test carried out on the membrane

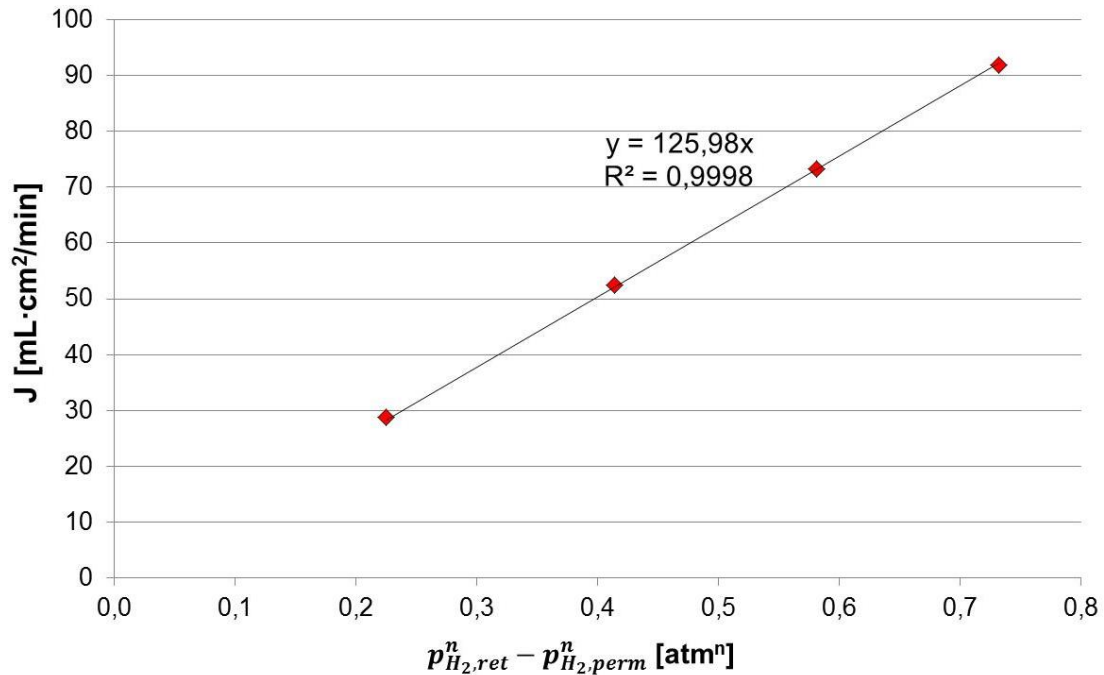


Fig. 3.79. Data obtained during the first permeability test of the M154 sample

The performance of the membrane in the oxy-reforming conditions are tested carrying out a first test at $T_{oven} = 750^\circ\text{C}$, $GHSV = 24000 \text{ h}^{-1}$ and $P = 3 \text{ atm}$ in order to create the driving force necessary for the H₂ separation. The outlet dry gas mixture is firstly analyzed by-passing the membrane in order to understand its composition, which will be those characterizing the feed of the membrane reactor. As shown in Fig. 3.80 in these operative conditions is obtained an outlet gas composed by 65% of H₂, 17% CO, 12% CH₄ and 6% CO₂. These data are useful in order to determine the performances of the membrane in terms of separation selectivity and understand if are present some limiting parameters that don't allow the maximum H₂ separation. This outlet gaseous mixture is conveyed to the membrane reactor and sequentially the permeate and retentate compositions are analyzed. As expected, the permeate stream is practically composed by pure H₂ with all the other gases percentage tended to 0, but a significant amount of H₂ ($\approx 40\%$) is present also in the retentate stream, index of a non-complete separation of H₂ from the other gases. In order to understand better this consideration is necessary to consider other parameters involved such as, the distinct flow rates of the

permeate and retentate and the partial pressures of H_2 in each side, reported in Table 3.11.

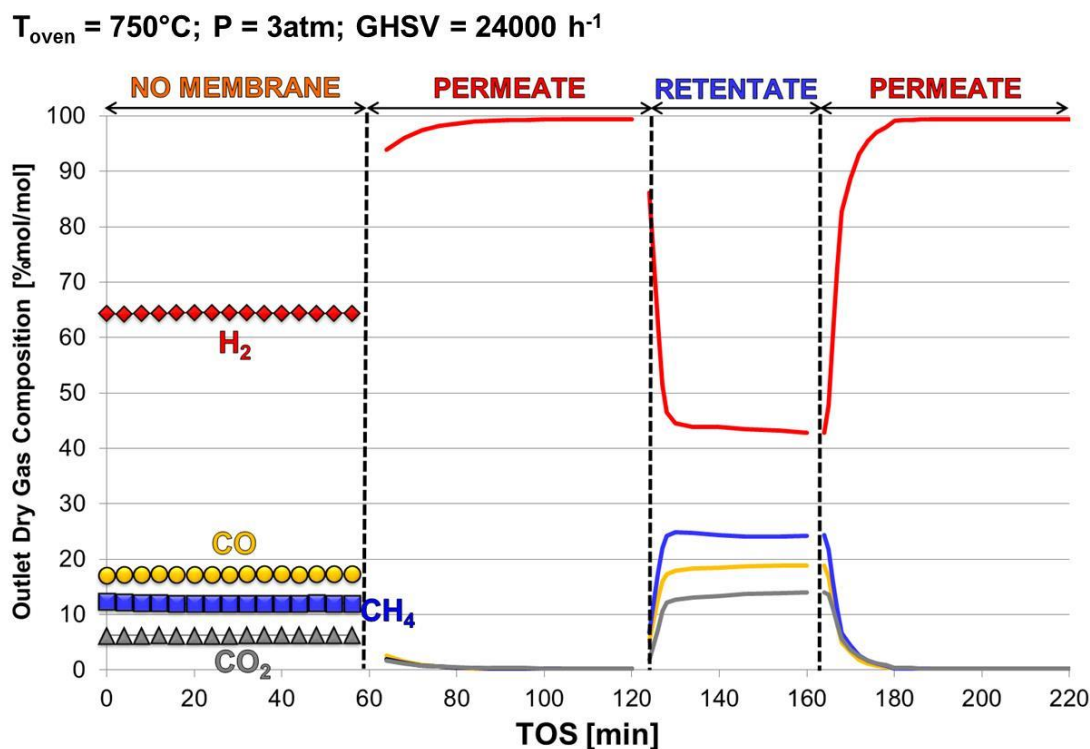


Fig. 3.80. Comparison between the outlet dry gas composition without using the membrane (NO MEMBRANE) and those characterizing the permeate and the retentate streams, recorded during the test at $T_{\text{oven}} = 750^{\circ}\text{C}$; $P = 3\text{ atm}$; $\text{GHSV} = 24000\text{ h}^{-1}$

The outlet gaseous mixture gets into the MBr at a pressure of 3 atm with a H_2 amount of 64.4%, corresponding to a H_2 partial pressure of 1.9 atm. This means that at the beginning (t_0) of the experiment the ΔP between the H_2 partial pressure of the retentate side (1.9 atm) and those of the permeate side (0 atm) is about 2 atm. From the moment in which the H_2 separation through the Pd membrane start to occurs, the permeate gradually become rich of H_2 and, since the permeate side is maintained at an absolute pressure of 1 atm, the maximum H_2 partial pressure possible at this side is 1 atm. Furthermore the partial pressure along the membrane decrease in the retentate side. Considering the data relative to the permeability test reported in Table 3.10, even if in this case a pure H_2 flow is feeded ($\approx 2250\text{ mL/min}$) to the MBr, when the ΔP is equal to 0.5 ($P = 1.5\text{ atm}$) the separation efficiency is about of 27% while at a ΔP value of 2 ($P = 3\text{ atm}$) the efficiency increase to a value of about 86%. Making the same considerations considering the data obtained during reaction, and in particular focusing on those relative to the retentate analysis, is possible to calculate the separation efficiency of the membrane in this conditions, approximately equal to 53%. This value is quite in accordance to those relative to the permeability tests just cited. As already mentioned is

possible to hypothesized that along the membrane, as a consequence of the transfer of H₂ from the retentate to the permeate side, the ΔP decrease from an high value (≈ 2 atm) at the beginning until a lower value of about 0.3 atm, after equilibration at the end of the membrane tube.

Anyhow, considering the preliminary nature of these tests, is possible to assert that they are encouraging, especially if they are connected to the original configuration, which provided a multistep H₂ separation configuration like those schematized in Fig. 1.21.

	NO MEMB	PERMEATE	RETENTATE	PERMEATE
H ₂ [%]	64.4	99.4	43.4	99.4
CO [%]	17.3	0.1	18.6	0.1
CH ₄ [%]	11.9	0.2	24.3	0.2
CO ₂ [%]	6.3	0.3	13.6	0.3
Total flow rate [mL/min]	259.8	88.7	156.1	89.3
H ₂ flow rate [mL/min]	167.3	88.2	67.8	88.8
p_{H_2} [atm]	1.9	1	1.3	1

Table 3.11. Outlet gas composition, flow rate and H₂ partial pressure without and with the use of membrane ($T_{oven} = 750^\circ\text{C}$; $P = 3$ atm; $GHSV = 24000$ h⁻¹)

After this test the membrane was disassemble from the MBr and inside of the membrane was find a significant quantity of carbon on the side of the reaction gas mixture and also present also in the retentate line which get out from the membrane reactor. Probably its formation derive from the low temperature at which is maintained the MBr (400°C) that, together with the decrease of the H₂ content in the retentate during the occurrence of the separation, create the favourable conditions for the carbon formation. In fact, the progressive H₂ transfer from the retentate to the permeate side, lead to a drastic drop of the H₂/C ratio and increase in the CO in the retentate, conditions at which the carbon formation, through mainly Boudouard reaction catalyzed by the Pd membrane sites, is favored. Furthermore, the H₂O amount involved in these conditions of low GHSV, is not high enough in order to contrast significantly this phenomenon. After cleaning the same membrane is also tested at higher GHSV (100000 h⁻¹), where the flow rates involved are higher and probably able to contrast in a more marked way the formation of carbon powder inside of the membrane.

The results obtained at 100000 h⁻¹ are graphically reported in Fig. 3.81 and also listed in Table 3.12. The increase of the flow rates doesn't influence the performances of the membrane, on the contrary the results obtained are incredibly similar to those recorded at lower GHSV (24000 h⁻¹). Obviously at higher GHSV the CH₄ conversion results lower than those obtained at 24000 h⁻¹, therefore the H₂ amount produced during

reaction, and hence those which will be fed to the MBr, is lower of about 10 percentage ($\approx 54\%$ against $\approx 65\%$). This generate a lower H_2 partial pressure in the retentate side (≈ 1.6 atm) and considering that the permeate one remains constantly at 1 atm, this lead to a lower ΔP between the two sides of the membrane. In accordance with a lower driving force, the separation efficiency is lower ($\approx 38\%$) than the previous case ($\approx 53\%$) but is important to notice that in terms of the H_2 flow rate at high space velocity, the membrane is able to separate an higher amount of H_2 , nevertheless having a lower efficiency also the retentate H_2 flow rate is higher. Focusing on the retentate composition, is possible to notice how the H_2 percentage ($\approx 43.2\%$) is practically the same relative to the previous test carried out at 24000 h^{-1} ($\approx 43.4\%$), which correspond to a final ΔP of H_2 partial pressure equal to 0.3 atm. These results, confirming the same values of the previous test, allow to draw the hypothesis that below a certain ΔP value, the H_2 separation become very slow due to the decrease of the driving force and the H_2 remain in the retentate; this value seems have a limit equal to 0.3 atm which was found as final difference of partial pressure in the two tests.

Also after this test the MBr is disassembled and this time a much lower amount of carbon powder is observed. This is in accordance with the higher flow rates involved in this test rather than those characterizing the previous one. in fact higher flow rates generate lower methane and steam conversion. Therefore, together with the constant separation performances of the membrane, these conditions lead to higher amount (in terms of flow rate, i.e. mL/min) of H_2 and vapor and lower amount of CO in the retentate stream. Notwithstanding the H_2 separation, the retentate has a composition which can inhibit the carbon formation.

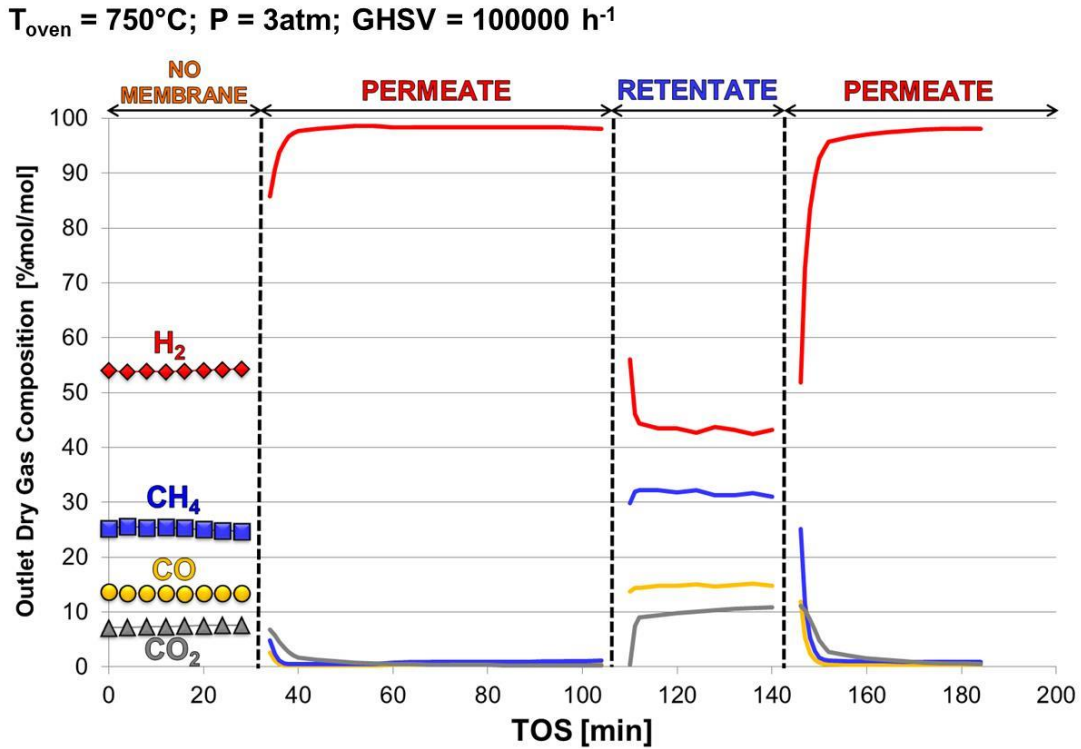


Fig. 3.81. Comparison between the outlet dry gas composition without using the membrane (NO MEMBRANE) and those characterizing the permeate and the retentate streams, recorded during the test at $T_{\text{oven}} = 750^{\circ}\text{C}$; $P = 3\text{ atm}$; $\text{GHSV} = 100000\text{ h}^{-1}$

	NO MEMB	PERMEATE	RETENTATE	PERMEATE
H_2 [%]	54.0	98.3	43.2	98.1
CO [%]	13.4	0.3	14.9	0.4
CH_4 [%]	25.2	0.8	31.6	0.9
CO_2 [%]	7.4	0.5	10.3	0.6
Total flow rate [mL/min]	829.9	171.7	658.1	174.0
H_2 flow rate [mL/min]	448.1	168.8	284.3	170.7
p_{H_2} [atm]	1.6	1	1.3	1

Table 3.12. Outlet gas composition, flow rate and H_2 partial pressure without and with the use of membrane ($T_{\text{oven}} = 750^{\circ}\text{C}$; $P = 3\text{ atm}$; $\text{GHSV} = 100000\text{ h}^{-1}$)

4 CONCLUSIONS

This work is mainly focused on the achievement of a new catalytic system to be used in reforming reactions based on $\text{CeO}_2 - \text{ZrO}_2$ mixed oxide obtained through the water-in-oil (w/o) microemulsion method. In particular the main process in which the catalysts prepared are tested is the oxy-reforming one, i.e. a new hydrogen and syngas ($\text{H}_2 + \text{CO}$) production process which occurs in non-conventional CPO and reforming reaction conditions characterized by a low S/C ratio (0.7) and O_2/C ratio (0.21). The present research is mainly aimed towards the improvements of the activity and stability of the catalytic system and the characterization of the catalysts in order to understand how some important parameters such as preparation method, active phase, thermal treatments affect in the oxygen support mobility, the dispersion and the metal – support interaction.

Generally, reforming reactions are carried out in conditions at which carbon formation and thermal sintering phenomena are favored, hence a catalyst characterized by a good activity accompanied by an high stability towards deactivation, is already a challenge not completely resolved. $\text{CeO}_2 - \text{ZrO}_2$ mixed oxides (CZO) could be a material with the right characteristics in order to contrast these kind of deactivation effects. In fact, ZrO_2 confers an high thermal stability while the peculiar redox properties characterizing the CeO_2 could be decisive in order to contrast the carbon formation on the active metal surface. CZO oxides are characterized by an high oxygen mobility capacity of the oxygen atoms present in the surface layers of the material that can migrate on the metal, get in contact with the carbonaceous deposits and oxidized them. In this way, the active surface become free again and available for the reaction increasing the lifetime of the catalysts. CZO mixed system is composed by several stable and metastable phases present as in function of temperature and preparation conditions. Among them, those that are claimed to have the higher oxygen mobility is the $\text{Ce}_{0.5}\text{Zr}_{0.5}\text{O}_2$ phase, which is the most difficult to obtained pure through classical synthesis method. For these reasons the w/o microemulsion method have been developed for the synthesis of this specific CZO phase and it is compared with a classical co-precipitation route.

The microemulsion synthesis procedure is taken from literature [159] but a wide study, mainly focused on the microemulsion containing the precipitating agent (usually TMAH-m), is performed in order to understand stability limit of the starting solution and possibly to obtain a final stable microemulsion system with the precipitated Ce and Zr hydroxides inside the micelles. Several parameters (pH of the aqueous solutions, R_w

ratio, nature of the precipitating agent, the relative amount of organic compounds) are systematically changed and the stability of the systems obtained is controlled through DLS analysis, that always confirm the valuation carried out by optical observation, i.e. an higher turbidity of the system imply the formation of a microemulsion characterized by micelles composing the microemulsion. Anyway, all of the tests carried out lead to the formation of a final microemulsion system where worse than those obtained through the original procedure reported in literature either in terms of yield of the precipitate and stability of the CZO mixed oxide. Interestingly results have been nevertheless obtained using NH_3 3 M solution, as precipitating agent, in microemulsion with which only at a temperature of 900°C some difference in terms of phase stability have been observed.

The solid powders obtained through the reference microemulsion and the coprecipitation method (CZO-m and CZO-cp) are firstly treated through a calcination process at high temperatures ($550 - 700 - 900^\circ\text{C}$) and deeply characterized by means of several techniques such as XRD, TPR/O/R, Raman Spectroscopy, porosimetry and TEM. Microemulsion and coprecipitate sample show an analogous reflection pattern and different position of the XRD reflections allows to identify the microemulsion phase composition as the desired $\text{Ce}_{0.5}\text{Zr}_{0.5}\text{O}_2$ phase, while the coprecipitated sample is characterized by the $\text{Ce}_{0.6}\text{Zr}_{0.4}\text{O}_2$. This compositional difference is further confirmed by TPR/O/R and Raman analysis that respectively show an higher reducibility of the CZO-cp sample deriving from the higher amount of Ce present in the crystalline phase and the presence of a specific tetragonal distorted phase (t'') in CZO-m, while a more cubic character is present in the coprecipitated sample (CZO-cp). TPR/O/R characterization further determine a lower degree of homogeneity of the CZO-cp sample with respect to the CZO-m one. Porosimetric analysis show difference in terms of pore volume and especially in terms of pore diameter (5 times larger for the microemulsion sample). The morphological difference is also observed through TEM characterization. Therefore the w/o microemulsion procedure allows to obtain a solid characterized by the desired crystalline phase with an high compositional and morphological homogeneity and larger pore.

The insertion of the active metal (Rh, Ru or Ni) on the support is another crucial feature and the method followed for its addition can influence significantly the properties of the supported systems and, in turns, their catalytic activity. Specifically the metal insertion is performed through two techniques: the Incipient Wetness Impregnation (IWI) and the bulk one. The differences deriving from these methods influence mainly the metal dispersion and the interaction between metal and support (MSI). The parameters are mainly studied through TPR and Raman characterizations. The impregnation

technique lead to a good dispersion of the active metal on the surface in the case of Rh (Rh1IWI_CZO-m900) and of Ru (Ru1IWI_CZO-m900), but the support has a limit in the preparation of high loading, due to low pore volume. Therefore in the case of Ni (5% and 10% w/w) this effect is clearly evident and more than five impregnation procedure are required to reach the desired loading, inducing a low dispersion of the Ni, detectable from XRD.

Rh-based bulk sample (Rh1bulk_CZO-m900) is characterized by the insertion of Rh inside the CZO lattice creating further structural distortions, detectable through Raman spectroscopy. In this way Rh results less reducible and therefore available on the support surface, having a negative influence on the catalytic activity of this bulk system. Regarding Ru-based bulk sample, the metal is not totally present inside the CZO lattice, furthermore a thermal sintering effect, which lead to low metal dispersion, is detected from the analysis of the H₂-TPR profiles relative to the Ru1bulk_CZO-m900 sample.

The decrease in the calcination temperature (750°C and 500°C) lead to an higher mobility of the cation in the bulk lattice, increasing the reducibility of the Rh, which increase the metal availability on the surface. The metal dispersion increase both in the case of Rh-based catalysts (Rh1bulk_CZO-m750 and Rh1bulk_CZO-m500), and Ru-based ones (Ru1bulk_CZO-m750 and Ru1bulk_CZO-m500) These effect, deriving from a lower calcination temperature have been analyzed also in also the IWI samples. CZO-m support is calcined at 750°C and 500°C in order to determine if a significant increase of the surface area and especially of the pores volume occurs. Nevertheless the pores volume remain too low for the impregnation of the high Ni loading. Thus the Ni-based samples have also synthesized following the bulk insertion technique and calcined at 750°C. TPR analysis showed a very high MSI effect, displaying reduction peaks at very high temperatures, symptom of the occurrence of the Ni insertion inside of the CZO lattice. This hypothesis is further confirmed by XRD because the patterns of Ni5bulk_CZO-m750 and Ni10bulk_CZO-m750 don't reveal any reflections relative to NiO crystalline phases, like in the case of the equivalent IWI samples characterized by the CZO-m900 support.

The catalytic activity of the catalysts prepared is studied in two processes: the oxy-reforming, carried out at relative high temperature ($T_{oven} = 750^{\circ}\text{C}$) in a pressure range within 1 – 20 atm and a GHSV range from 24000 h⁻¹ to 100000 h⁻¹; and the steam reforming at low temperature (LT-SRM), conducted in a temperature range between 350°C and 500°C maintaining constant the pressure (1 atm) and GHSV (24000 h⁻¹). Is important to develop a catalyst active enough also in these latter conditions with the aim to allow a multistep process starting with a low temperature step which decrease the

oxygen consumption, and in future can work using an integrated system configuration in which occurs simultaneously the H₂ production, through the steam reforming reaction, and its separation by means of the membrane technology.

The Rh-based catalysts prepared by microemulsion, result the best ones in all of the conditions tested and also in terms of deactivation they reveal the lowest decrease in the activity even after long period of time. In the microemulsion sample characterized by the Ce_{0.5}Zr_{0.5}O₂ no carbon formation is detected by TPO and TEM analysis confirmed the effect of the high oxygen mobility which contrast deactivation phenomena mainly related to carbon formation.

The decrease of the calcination temperature, improve significantly the activity of the bulk samples. In fact Rh- and Ru-based bulk samples calcined at 900°C showed a very low activity in the oxy-reforming conditions that increase for the samples calcined at 750°C and 500°C, reaching values comparable to those obtained testing the equivalent impregnated samples and, for Rh, even better in drastic reaction conditions. These catalyst represent a new class of system studied for the first time during the present work and this achievement is especially important regarding Ru-based systems that are those that, usually, show problems in terms of activity and stability through sintering.

That the low thermal treatment procedure have been extended to impregnated systems which show an improvement of the catalytic activity both at high and low temperature. In particular the Rh1IW1_CZO-m750-R750 catalyst, in all the reaction conditions, results very close to the thermodynamic equilibrium and very stable during time on stream.

This catalyst have been used to perform some preliminary tests with the integration of a Pd dense membrane placed downstream of the reactor in which the oxy-reforming reaction carried out, in order to separate H₂ from the other gases composing the outlet gas mixture. This part of the work is developed in collaboration with the University of Messina, where the actual membrane preparation is performed and optimized. The data obtained allow to reach a good separation degree accompanied by an optimal separation selectivity, which lead to a permeate stream composed by 100% of pure H₂. Nevertheless the overall hydrogen separation is limited by the operative pressure of the membrane (3 atm) and the difference in the partial pressure obtained during separation between retentate and permeate (0.3 atm). Finally an integrated configuration in which the catalyst is present into the membrane inside of which occurs simultaneously the reaction and the H₂ separation, could be the next step to be studied using the catalyst developed during the present work having high activity even at low temperature.

5 REFERENCES

-
- [1] I. Wender, *Fuel Processing Technology* 48 (1996) 189
- [2] E4Tech, *Review of Technologies for Gasification of Biomass and Wastes NNFCC Project 09/008* (2009) Available via www.nnfcc.co.uk.
- [3] Progressive Energy and CNG Services, *Bio-SNG Feasibility Study e Establishment of a Regional Project*. Available at: <http://www.northeastbiofuels.com/reports>
- [4] C. Higman, M. van der Burgt, *Gasification, Elsevier/GPP*, (2008)
- [5] K.S. Weil, *Energy* 163 (EN1) 7
- [6] AMEC, *Engineering Design and Capture Technologies for Carbon Capture and Storage in the Tees Valley*, (2010) Available at: <http://nepic.co.uk>
- [7] Haag, W.O., Kuo, J.C. and Wender, I., *Gasification for Synthesis of Fuels and Chemicals. Chap. 5 in Coal Gasification: Direct Application and Syntheses of Chemicals and Fuels*, DOE/ER-0326, (1987) 117
- [8] K. Liu, C. Song, V. Subramani, *Hydrogen and syngas production and purification technologies*, published by J. Wiley & Sons, Inc., (2010)
- [9] A. Paula. G. Peres, B. H. Lunelli, R. M. Filho, *Chem. Eng. Transaction*, 32 (2013) 589
- [10] Ni M., Leung D.Y.C., Leung M.K.H., Sumathy K., *Fuel Processing Technology*, 87 (2006), 461
- [11] Arni S.A., Bosio B., Arato E., *Renewable Energy*, 35 (2010), 29
- [12] Garcia L., Salvador M.L., Arauzo J., Bilbao R., *Journal of Analytical and Applied Pyrolysis*, 58–59 (2001), 491
- [13] Lin Y.C., *International Journal of Hydrogen Energy*, 38 (2013), 2678
- [14] Chang A.C.C., Chang H.F., Lin F.J., Lin K.H., Chen C.H., *International Journal of Hydrogen Energy*, 36 (2011), 14252
- [15] Xie Q., King S., Liu Y., Zeng H., *Bioresource Technology*, 110 (2012), 603
- [16] Gao N., Li A., Quan C., Qu Y., Mao L., *International Journal of Hydrogen Energy*, 37 (2012), 9610
- [17] Nipattummakul N., Ahmed I.I., Kerdsuwan S., Gupta A.K., *Applied Energy*, 92 (2012), 778
- [18] Lv P., Yuan Z., Wu C., Ma L., *Energy Conversion and Management*, 48 (2007), 1132
- [19] Skoulou V. K., Zabaniotou A. A., *Journal of Analytical and Applied Pyrolysis*, 99 (2013), 110
- [20] Huang B.S., Chen H.Y., Chuang K.H., Yang R.X., Wey M.Y., *International Journal of Hydrogen Energy*, 37 (2012), 6511
- [21] Ahmed I., Gupta K., *International Journal of Hydrogen Energy*, 36 (2011), 4340
- [22] Simone M., Nicoletta C., Tagnotti L., *Chemical Engineering Transactions*, 24 (2011), 19

-
- [23] Yoon S.J., Choi Y.C., Son Y.I., Lee S.H., Lee J.G., *Bioresource Technology*, 101 (2010), 1227
- [24] Dalai A.K., Batta N., Eswaramoorthi I., Schoenau G.J., *Waste Management*, 29 (2009), 252
- [25] IEA, *World Energy Outlook*, (2011)
- [26] Crompton, S., 'European LNG Pricing Uncertainty's Threat to Investment', *Petroleum Economist*, (2010)
- [27] Dempsey, J., 'Eastern Europe, seeking energy security, turns to shale gas', *New York Times*, (2010)
- [28] Hulbert, M., Unconventional Gas: Producer Pickle or Consumer Curse?, *CSS Analysis in Security Policy No. 76*, (2010) (Zürich: CSS ETH)
- [29] Jaffe, A., 'How shale gas is going to rock the world', *Wall Street Journal*, (2010)
- [30] Komduur, R., 'Europe Not Ready for Unconventional Gas, Yet', *European Energy Review*, (2010)
- [31] Von Kluechtzner, L., 'Unconventional Gas: A Game Changer for LNG', *Middle East Economic Survey*, 53 – 29 (2010)
- [32] Stevens P., 'The Shale Gas Revolution: Hype and Reality', *Chatman House Report*, (2010)
- [33] IEA, *World Energy Outlook*, (2009)
- [34] H. Rogers, *Oxford Review of Economic Policy*, 27 – 1,, (2011), 117
- [35] Available on "The Economist online" (2012) - <http://www.economist.com/blogs/graphicdetail/2012/06/focus>
- [36] Tsafos, N., 'The US: A Deep Liquid LNG Market', *Petroleum Economist*, (2010)
- [37] Jensen J. T., 'LNG: Its Role in the Internationalization of Gas Markets', *presentation to Columbia School of International and Public Affairs*, (2009)
- [38] Meagher, J., 'LNG's Unexpected, Unconventional Shift', *Petroleum Economist*, (2010)
- [39] BP, *BP Statistical Review of World Energy*, (2010)
- [40] M.J.A. Tijmenses, A.P.C. Faaij, Hamelkinck, et al., *Biomass and Bioenergy* 23 (2) (2002) 129
- [41] F. Fischer, *Industrial and Engineering Chemistry* 17 (1925) 574
- [42] D. J. Roddy, *Applied Thermal Engineering* 53 (2013) 299
- [43] Basini L.; Bartolini A.; Lupi G.; Clerici G. C. E. *Catalytic partial oxidation process for producing synthesis gas. US7368482*, 06 May 2008
- [44] Barbera D., Innovative process for syngas production, *PhD Thesis* (2013)
- [45] A. Solbakken, *Stud. Surf. Sci. Catal.*, 61 (1991) 447
- [46] H. Topsoe, *Hydrocarbon Processing*, 67 (1988) 77
- [47] Palo, D. R., *Chem. Reviews* 107 (2007), 3992
- [48] Mundschau, M. V., *Catal. Today* 118 (2006), 12
- [49] Paglieri, S., *NonporousInorganicMembranes* (2006), 77

-
- [50] Gao, H., *I&EcResearch* 43 (2004) 6920
- [51] Uemiya, S., *Topics In Catal.* 29 (2004), 79
- [52] Baker, R. W., *I&Ec Research* 41 (2002), 1393
- [53] W. J. Koros, Y. H. Ma, T. Shimidzu, *J. Membrane Sci.* 120 (1996), 149
- [54] Basile A., Gallucci F., *Membranes for Membrane Reactors: Preparation, Optimization and Selection*, (2011) John Wiley & Sons
- [55] Fuertes A. B., Centeno T. A., *J. Membrane Sci.* 144 (1998), 105
- [56] Cejka J., Van Corna H., Corma A, Schuth F., *Introduction to zeolite science and practice, Studies in surface science and catalysis* 168 (2007)
- [57] Saracco G., Specchia V., *Catal. Rev. Sci. Eng.* 36 (1994), 305
- [58] Kapoor A., Yang R. T., Wong C., *Catal. Rev.* 31 (1989), 129
- [59] Lee K. H., Hwang T., *J. Coll. Int. Sci.* 110 (1986), 544
- [60] Ulhorn R. J. R., Keizer K., Burggraaf A. J., *J. Membrane Sci.* 66 (1992), 259
- [61] Barelli L., Bidini G., Gallorini F., Servili S., *Energy* 33 (2008), 554
- [62] Ritter J. A., Ebner A. D., *Sep. Sci. Techn.* 42 (2007), 1123
- [63] Rustrup-Nielsen J. R. *Stud. Surf. Sci. Catal.*, 147 (2004), 121
- [64] Lutz, A. E.; Bradshaw, R. W.; Keller, J. O.; Witmer, D. E. *Int. J. Hydrogen Energy*, 28 (2003), 159
- [65] Twigg, M. V. *Catalyst Handbook. 2nd. Ed. [S.L.]*: Wolf Publishing, 1989
- [66] Jarosch, K.; El Solh, T.; De Lasa, H. *I. Chem. Eng. Sci.* 57 (2002), 3439
- [67] Wei, J.; Iglesia, E. *Journal Of Catalysis*, 224 (2004), 370.
- [68] Wei, J.; Iglesia, E. *Journal Of Catalysis*, 225 (2004), 116
- [69] Matsumura, Y.; Nakamori, T. *Appl. Catal. A*, 258 (2004). 107
- [70] Choudary, T. V.; Goodman, D. W. *J. Molec. Catal. A*, 163 (2000), 9
- [71] Alstrup, B.; Clausen, S.; Olsen, C.; Smits, R. H. H.; Rustrup-Nielsen, J. R., *Stud. Surf. Sci. Catal, Natural Gas Conversion V*, 119 (2002), 5
- [72] Takeira, K.; Shishido, T.; Kondo, M. *Journal Of Catalysis*, 207 (2002), 307
- [73] Tsyganok, A. I.; Tsunoda, T.; Hamakawa, S.; Suzuki, K.; Takehira, K.; Hayakawa, T. *Journal Of Catalysis*, 213 (2003), 213
- [74] Takehira, K.; Shishido, T.; Shouro, D.; Murakami, K.; Honda, M.; Kawabata, T.; Takaki, K., *App. Catal. A*, 279 (2005), 41
- [75] Ohi, T.; Miyata, T.; Li, D.; Shishido, T.; Kawabata, T.; Sano, T.; Takehira, K. *App. Catal. A*, 308 (2006), 194
- [76] Fonseca, A.; Assaf, E. M. *J. Power Sources*, 142 (2005), 154
- [77] Foletto, E. L.; Alves, R. W.; Jahn, S. L. *J. Power Sources*, 161 (2006), 531

-
- [78] Keghouche, N.; Chettibi, S.; Latrèche, F.; Bettahar, M. M.; Belloni, J.; Marignier, J. L. *Radiation Physics And Chemistry*, 74 (2005), 185
- [79] Siswana, N. P.; Trimm, D. L.; Cant, N. W., *Stud. Surf. Sci. Catal., Natural Gas Conversion V*, 119 (1998), 789
- [80] Dong, W.; Roh, H.; Jun, K.; Park, S.; Oh, Y., *Appl. Catal. A*, 226 (2002), 63
- [81] Oh, Y.; Roh, H.; Jun, K.; Baek, Y., *Intern. J. Hydrogen Energy*, 28 (2003), 1387
- [82] Roh, H.; Jun, K.; Park, S., *Appl. Catal. A*, 251 (2003), 275
- [83] Urasaki, K.; Sekine, Y.; Kawabe, S.; Kikuchi, E.; Matsukata, M., *Appl. Catal. A*, 286 (2005), 23
- [84] Wang, J. S. B.; Tai, Y. L.; Dow, W. P.; Huang, T., *J. Appl. Catal. A*, 218 (2001), 69
- [85] Wang, J. B.; Kuo, L. E.; Huang, T., *J. Appl. Catal. A*, 249 (2003), 93
- [86] Wang, J. B.; Hsiao, S. Z.; Huang, T., *J. Appl. Catal. A*, 246 (2003), 197
- [87] Wang H. Y., Ruckenstein E., *Appl. Catal. A: Gen.* 204 (2000), 143
- [88] Liu Y., Hayakawa T., Ishii T., Kumagai M., Yasuda H., Suzuki K., Hamakawa S., Murata K., *Appl. Catal. A: Gen.* 210 (2001), 301
- [89] Montoja J.A., Romero-Pascual E., Gimón C., Del Angel P., Monzon A., *Catal. Today* 63 (2000), 71
- [90] Wang S., Lu G. Q., *Appl. Catal. B: Env.*, 19 (1998), 267
- [91] Montoja J. A., Romero – Pasual E., Monzon A., Guimon C., *Stud. Surf. Sci. Catal.* 130D (2000), 3669
- [92] Roh H.-S., Jun K.-W., Dong W.-S., Park S.-E., Baek Y.-S., *Catal. Lett.* 74 (2001), 31
- [93] Noronha F. B., Fendley E. C., Soares R. R., Alvarez W. E., Resasco D. E., *Chem. Eng. J.*, 82 (2001), 21
- [94] C. Descorme, D. Duprez, *Applied Catalysis A: General* 202 (2000) 231
- [95] S. Menad P. Ferreira-Aparicio, O. Cherifi, A. Guerrero-Ruiz, and I. Rodríguez-Ramos, *Catalysis Letters.*, 89 (2003), 63
- [96] Boutonnet M., Lögdberg S., Svensson E. E., *Current Opinion in Colloid & Interface Science* 13 (2008), 270
- [97] Eriksson S, Nylén U, Rojas S, Boutonnet M., *ApplCatal A: Gen* 265 (2004), 207
- [98] Capek I., *Advances in Colloid and Interface Science* 110 (2004), 49
- [99] A.Martinez-Arias, M. Fernandez-Garcia, V. Ballesteros, L. N. Salamanca, J. C: Conesa, C. Otero and J. Soria, *Langmuir*, 15 (1999) 4796
- [100] Schulman JH, Stoeckenius W, Prince LM., *J PhysChem*; 63 (1959), 1677
- [101] Ivanova A. S., *Kinetics and Catalysis*, 50 No. 6 (2009), 797
- [102] Duwez, P. and Odell F, *J. Am. Ceram. Soc.*, 35 (1952), 107
- [103] Yashima M, Arashi H, Kakihana M and Yoshimura M, *J. Am. Ceram. Soc.*, 77 (1994), 1067

- [104] Meriani S., *J. Phys.*, 47 (1986), 485
- [105] Meriani S., *Mater. Sci. Eng., A*, 109 (1989), 121
- [106] Meriani S., *Mater. Sci. Eng.*, 71 (1985), 369
- [107] Fornasiero P., Balducci G., Di Monte R., Kaspar J., Sergio V., Gubitosa G., Ferrero A. and Graziani M., *J. Catal.*, 164 (1996), 173
- [108] Vlaic G., Di Monte R., Fornasiero P., Fonda E., Kaspar J., and Graziani M., *J. Catal.*, 182 (1999), 378
- [109] Turko, G.A., Ivanova, A.S., Plyasova, L.M., Litvak, G.S., Rogov, V.A., *Kinet. Catal.*, 46 No. 6 (2005), 932
- [110] S.J. Tauster, S.C. Fung, R.L. Garten, *J. Am. Chem. Soc.* 100 (1978) 170
- [111] S.J. Tauster, *Acc. Chem. Res.* 20(11) (1987) 389
- [112] G.L. Haller, D.E. Resasco, *Adv. Catal.* 36 (1989) 173
- [113] M. Primet, M. El Azhar, R. Frety and M. Guenin, *Appl. Catal.* 59 (1990) 153
- [114] J.L. Duplan and H. Praliaud, *Appl. Catal.* 67 (1991) 325
- [115] A. Trovarelli, G. Dolcetti, C. Leitenburg, J. Kaspar, P. Finetti and A. Santoni, *J. Chem. Soc., Faraday Trans.* 88 (1992) 1311
- [116] S. Bernal, G.A. Cifredo, J.J. Calvino, J.M. Rodríguez-Izquierdo, V. Perrichon and A. Laachir, *J. Chem. Soc. Chem. Commun.* (1992) 460
- [117] J.R. Katzer, A.W. Sleight, P. Gajardo, M. Edwar, F. Gleason and S. Mc Millan, *Discuss. Faraday Soc.* 72 (1982) 121
- [118] S. Bernal, F.J. Botana, J.J. Calvino, M.A. Cauqui, G.A. Cifredo, A. Jobacho, J.M. Pintado and J.M. Rodríguez-Izquierdo, *J. Phys. Chem.* 97 (1993) 4118
- [119] J.L.G. Fierro, J. Soda, J. Sanz and J.M. Rojo, *J. Solid State Chem.* 66 (1987) 154
- [120] A. Laachir, V. Perrichon, A. Badri, J. Lamotte, E. Catherine, J.C. Lavalley, J. El Fallah, L. Hilaire, F. Le Normand, E. Quéméré, G.N. Sauvion and O. Touret, *J. Chem. Soc., Faraday Trans.* 87 (1991) 1601
- [121] S. Bernal, J.J. Caivino, G.A. Cifredo, J.M. Gatica, J.A. Pérez Omil and J.M. Pintado, *J. Chem. Soc. Faraday Trans.* 89 (1993) 3499
- [122] A. Badri, J. Lamotte, J.C. Lavalley, A. Laachir, V. Perrichon, O. Touret, G.N. Sauvion and E. Quéméré, *Europ. J. Solid State Chem.* 28 (1991) 445
- [123] C. Li, Y. Sakata, T. Arai, K. Domen, K. Maruya and T. Onishi, *J. Chem. Soc. Faraday Trans.* 1 85 (1989) 929
- [124] C. Li, Y. Sakata, T. Arai, K. Domen, K. Maruya and T. Onishi, *J. Chem. Soc. Faraday Trans.* 1, 85 (1989) 1451
- [125] S. Bernal, G.A. Cifredo, J.J. Calvino, J.M. Rodríguez-Izquierdo, V. Perrichon and A. Laachir, *J. Catal.* 137 (1992) 1
- [126] C. Binet, A. Jadi, J.C. Lavalley and M. Boutonet-Kizling, *J. Chem. Soc. Faraday Trans.* 88 (1992) 2079

-
- [127] J. Barrault, A. Alouche, V. Paul-Boncour, L. Hilaire and A. Percheron-Guegan, *Appl. Catal.* 46 (1989) 269
- [128] M. Guenin, P.N. Da Silva and R. Frety, *Appl. Catal.* 27 (1986) 313
- [129] J. Cunningham, S. O'Brien, J. Sanz, J.M. Rojo, J. Sofia and J.L.G. Fierro, *J. Mol. Catal.* 57 (1990) 379
- [130] S. Bernal, J.J. Calvino, G.A. Cifredo, A. Laachir, V. Perrichon and J.M. Herrmann, *Langmuir* 10 (1994) 717
- [131] P. Meriaudeau, J.F. Dutel, M. Dufaux and C. Naccache, *Stud. Surf. Sci. Catal.* 11 (1982) 95
- [132] D. Kalakkad, A.K. Datye and H. Robota, *Appl. Catal. B: Environmental* 1 (1992) 191
- [133] S. Bernal, J.J. Calvino, M.A. Cauqui, J.M. Gatica, C. LópezCartes, J.A. Pérez Omil, J.M. Pintado, *Catal. Today* 77 (2003) 385
- [134] H.D. Cochrane, J.L. Hutchinson, D. White, G.M. Parkinson, C. Dupas and A.J. Scott, *Ultramicroscopy* 34 (1990) 10
- [135] S. Bernal, F.J. Botana, R. Garcia, Z. Kang, M.L. Lopez, M. Pan, F. Ramirez and J.M. Rodriguez-Izquierdo, *Catal. Today*, 2 (1988) 653
- [136] S. Bernal, F.J. Botana, G.A. Cifredo, J.J. Calvino, R. Garcia and J.M. Rodriguez-Izquierdo, *Ultramicroscopy*, 34 (1990) 60
- [137] S. Bernal, J.J. Calvino, M.A. Cauqui, G.A. Cifredo, A. Jobacho and J.M. Rodriguez-Izquierdo, *Appl. Catal. A: General*, 99 (1993) 1
- [138] M. Pan, R. Garcia, D.J. Smith, J.M. Cowley, and G.A. Cifredo, in G.W. Bailey (Editor), *Proceedings 47th Meeting of the Electron Microscopy Society of America, San Francisco*, (1989) 256
- [139] M. Pan, *Ph.D. Thesis*, Arizona State University (1991)
- [140] S. Bernal, F.J. Botana, J.J. Calvino, G.A. Cifredo, J.A. Pérez-Omil, J.M. Pintado, *Catal. Today* 23 (1995) 219
- [141] Bartholomew, C. H., *Appl. Catal. A*, 212 (2001), 17
- [142] Bartholomew, C. H., *Catal. Rev. – Sci. Eng.*, 24 (1982), 67
- [143] Rostrup-Nielsen, J. R., *Catal. Today* 37 (1997), 225
- [144] Armor, J. N.; Martenak, D. J., *Appl. Catal. A* 206 (2001), 231
- [145] Wanke S. E. and Flynn, P.C., *Catal. Rev. Sci. Eng.* 12 No.1 (1975), 93
- [146] Campbell, C. T.; Parker, S. C.; Starr, D. E., *Science* 298 (2002), 811
- [147] Sehested, J.; Gelten, J. A. P.; Remediakis, I. N.; Bengaard, H.; Norskov, J. K., *J. Catal.*, 223 (2004), 432
- [148] Sehested, J., *J. Catal.* 217 (2003), 417
- [149] Choudhary, V. R.; Sansare, S. D.; Mamman, A. S., *Appl. Catal. A*, 90 (1992)
- [150] Ferreira-Aparicio, P.; Benito, M. J.; Sanz, L., *J. Catalysis Reviews* 47 (2005), 491
- [151] Hu, Y. H.; Ruckenstein, E., *Adv. Catal.* 48 (2004), 297

- [152] Choudhary, V. R.; Rajput, A. M.; Prabhakar, B., *Catal. Lett.* 15 (1992), 363
- [153] Choudhary, V. R.; Rajput, A. M.; Prabhakar, B., *J. Catal.* 139 (1993), 326
- [154] Choudhary, V. R.; Rajput, A. M.; Rane, V. H., *Catal. Lett.* 16 (1992), 269
- [155] Choudhary, V. R.; Rajput, A. M.; Rane, V. H., *J. Phys. Chem* 96 (1992), 8686
- [156] Hu, Y. H.; Ruckenstein, E., *Ind. Eng. Chem. Res.* 37 (1998), 2333
- [157] Basile, F.; Fornasari, G., Vaccari A., *Catal. Today* 64 (2001), 54
- [158] Hickman, D. A.; Schmidt, L. D., *J. Catal.* 138 (1992), 267
- [159] Martinez-Arias A., Fernandez-Garcia M., Ballesteros V., Salamanca L. N., Conesa J. C., Otero C., Soria J., *Langmuir* 15 (1999), 4796
- [160] Bond G.; Tahir S. F., *Appl. Catal.*, 1 (1991). 71
- [161] Augustine R. L., *New York: Marcel Dekker, Inc.* (1996) 287
- [162] Avila, M. S. Catalizadores de Platino Soportado Sobre Óxidos Reducibles Para La Eliminación De Compuestos Orgánicos Volátiles. PhD. Thesis (2011). Disponible en: <<http://bibliotecavirtual.unl.edu.ar:8180/tesis/handle/1/322?locale=es>>
- [163] Berne, B.J.; Pecora, R., *Courier Dover Publications* (2000)
- [164] Powder Diffraction Files - Inorganic Phase, ICDD (International Centre for Diffraction Data)
- [165] S. Gregg, K.S.W. Sing, *Adsorption, Surface Area and Porosity* 2nd edition, (1982)
- [166] A. Bumajdad et al., *Journal of Colloid and Interface Science* 355 (2011) 282
- [167] G. Colon, M. Pijolat, F. Valdivieso et al., *J. Chem. Soc., Faraday Trans.*, 94 (1998), 3717
- [168] G. Colon, F. Valdivieso, M. Pijolat, R.T. Baker, J.J. Calvino and S. Bernal, *Catal. Today.*, 50 (1999), 271
- [169] Zhang F., Chen C-H, Hanson JC, Robinson RD, Herman LP, Chan S-W, *J. Am. Ceram. Soc.* 89, (2006) 1028
- [170] J. E. Spanier, R. D. Robinson, F. Zhang, S.-W. Chan, and I. P. Herman, *Phys. Rev. B*, 64, (2001) 245407
- [171] A. Mineshige, T. Taji, Y. Muroi, M. Kobune, S. Fujii, N. Nishi, M. Inaba, and Z. Ogumi, *Solid State Ionics*, 135 (2000), 481
- [172] P. Fornasiero, G. Balducci, R. DiMonte, J. Kaspar, V. Sergo, G. Gubitosa, A. Ferrero, M. Graziani, *J. Catal.* 164 (1996), 173
- [173] P. Barberis, T. Merle-Mejean, P. Quintard, *J. Nucl. Mat.* 246 (1997), 232
- [174] J.I. Gutierrez-Ortiz, B. de Rivas, R. Lopez-Fonseca, J.R. Gonzalez-Velasco, *Appl. Catal. A* 269 (2004) 147
- [175] M. Boaro, M. Vicario, C. de Leitenburg, G. Dolcetti, A. Trovarelli, *Catal. Today* 77 (2003) 407
- [176] G. Balducci, J. Kaspar, P. Fornasiero, M. Graziani, *J. Phys. Chem. B* 101 (1997) 1750
- [177] J.I. Gutierrez-Ortiz, B. de Rivas, R. Lopez-Fonseca, J.R. Gonzalez-Velasco, *Catal. Today* 107–108 (2005) 933

-
- [178] J.A. Wang, T. Lopez, X. Bokhimi, O. Novaroc, *Journal of Molecular Catalysis A*, 239 (2005) 249–256
- [179] S. Brunauer, L.S. Deming, W.S. Deming, E. Teller, *J. Am. Chem. Soc.* 62 (1940), 1723
- [180] S.J. Gregg, K.S.W. Sing, *Adsorption, Surface Area and Porosity*, 2nded., Academic Press, London (1974), 285
- [181] S.J. Gregg, K.S.W. Sing, *Adsorption, Surface Area and Porosity*, Academic Press, London, (1967)
- [182] A.J. Lecloux, in: J.R. Anderson, M. Boudart (Eds.), *Catal.-Sci. Technol.*, vol. 2, Springer-Verlag, Berlin (1981), 171
- [183] S.J. Gregg, in: J. Rouquerol, K.S.W. Sing (Eds.), *Adsorption at the Gas–Solid and Liquid–Solid Interface*, Elsevier, Amsterdam (1982), 153
- [184] P. Fornasiero, R. Di Monte, G.R. Rao, J. Kaspar, S. Meriani, A. Trovarelli, M. Garziani, *J. of Catal.* 151 (1995) 168
- [185] A. Trovarelli, G. Dolcetti, C. de Leintenburg, J. Kaspar, P. Finetti, A. Santoni, *J. Chem. Soc. Faraday Trans88* (1992) 1311
- [186] J. Chen, Q. Wu, J. Zhang, J. Zhang, *Fuel* 87 (2008) 2901
- [187] P. Kumar, Y. Sun, R.O. Idem, *Energy Fuels* 21 (2007) 3113
- [188] H.S. Roh, H.S. Potdar, K.W. Jun, J.W. Kim, Y.S. Oh, *Appl. Catal. A: Gen.* 276 (2004) 231
- [189] J.A. Montoya, E. Romero-Pascual, C. Gimón, P. Del Angel, A. Monzon, *Catal. Today* 63 (2000) 71
- [190] H.S. Roh, K.W. Jun, W.S. Dong, S.E. Park, Y.S. Baek, *Catal. Lett.* 74 (2001) 31
- [191] T. Takeguchi, S. Furukawa, M. Inoue, *J. Catal.* 202 (2001) 14
- [192] A. Kambolis, H. Matralis, A. Trovarelli, Ch. Papadopoulou, *Appl. Catal. A: Gen.* 377 (2010) 16
- [193] S. Tang, J. Lin, K.L. Tan, *Catal. Lett.* 51 (1998) 169
- [194] Rosetti V., *Catalysts for H₂ production* (2007)
- [195] Korup O.; Goldsmith C. F.; Weinberg G.; Geske M.; Kandemir T.; Schlögl R.; Horn R. *Catalytic partial oxidation of methane on platinum investigated by spatial reactor profiles, spatially resolved spectroscopy, and microkinetic modeling* 297 (2013), 1
- [196] Basile F.; Fornasari G.; Trifirò F.; Vaccari A., *Partial oxidation of methane: Effect of reaction parameters and catalyst composition on the thermal profile and heat distribution* 64 (2001), 245
- [197] P. Fornasiero, G. Balducci, R. Di Monte, J. Kašpar, V. Sergo, G. Gubitosa, A. Ferrero, M. Graziani, *J. Catal.* 164 (1996), 173
- [198] Y. Nagai, T. Yamamoto, T. Tanaka, S. Yoshida, T. Nonaka, T. Okamoto, A. Suda, M. Sugiura *Catal. Today* 74 (2002), 225